

# Cell-type-specific transcriptomes and the Allen Atlas (II): discussion of the linear model of brain-wide densities of cell types

Pascal Grange<sup>1,\*</sup>, Jason W. Bohland<sup>2</sup>, Benjamin Okaty<sup>3</sup>,  
Ken Sugino<sup>4</sup>, Hemant Bokil<sup>5</sup>, Sacha Nelson<sup>6</sup>,  
Lydia Ng<sup>7</sup>, Michael Hawrylycz<sup>7</sup>, Partha P. Mitra<sup>5</sup>

<sup>1</sup> Xi'an Jiaotong-Liverpool University, Department of Mathematical Sciences, Suzhou 215021, China

<sup>2</sup> Boston University, College of Health & Rehabilitation Sciences,  
Boston, MA 02215, United States

<sup>3</sup> Department of Genetics, Harvard Medical School, Boston, MA 02215, United States

<sup>4</sup> Janelia Farm Research Campus, Howard Hughes Medical Institute,  
Ashburn, VA 20147, United States

<sup>5</sup> Cold Spring Harbor Laboratory, Cold Spring Harbor, NY 11724, United States

<sup>6</sup> Department of Biology and Center for Behavioral Genomics,  
Brandeis University, Waltham, Massachusetts, United States

<sup>7</sup> Allen Institute for Brain Science, Seattle, WA 98103, United States

\*E-mail: [pascal.grange@polytechnique.org](mailto:pascal.grange@polytechnique.org)

## Abstract

The voxelized Allen Atlas of the adult mouse brain (at a resolution of 200 microns) has been used in [arXiv:1303.0013] to estimate the region-specificity of 64 cell types whose transcriptional profile in the mouse brain has been measured in microarray experiments. In particular, the model yields estimates for the brain-wide density of each of these cell types. We conduct numerical experiments to estimate the errors in the estimated density profiles. First of all, we check that a simulated thalamic profile based on 200 well-chosen genes can transfer signal from cerebellar Purkinje cells to the thalamus. This inspires us to sub-sample the atlas of genes by repeatedly drawing random sets of 200 genes and refitting the model. This results in a random distribution of density profiles, that can be compared to the predictions of the model. This results in a ranking of cell types by the overlap between the original and sub-sampled density profiles. Cell types with high rank include medium spiny neurons, several samples of cortical pyramidal neurons, hippocampal pyramidal neurons, granule cells and cholinergic neurons from the brain stem. In some cases with lower rank, the average sub-sample can have better contrast properties than the original model (this is the case for amygdalar neurons and dopaminergic neurons from the ventral

midbrain). Finally, we add some noise to the cell-type-specific transcriptomes by mixing them using a scalar parameter weighing a random matrix. After refitting the model, we observe that a mixing parameter of 5% leads to modifications of density profiles that span the same interval as the ones resulting from sub-sampling.

# Contents

<b>1</b>	<b>Introduction and notations</b>	<b>4</b>
<b>2</b>	<b>Simulations with missing cell types</b>	<b>5</b>
2.1	Simulation scenario . . . . .	5
2.2	Results . . . . .	7
<b>3</b>	<b>Error estimates for the predicted density profiles</b>	<b>10</b>
3.1	Theoretical bounds on the error as a function of noise . . . . .	10
3.2	Repeated sub-sampling of gene space . . . . .	15
3.2.1	Simulation scenario . . . . .	15
3.2.2	Variability of density profiles between the original and sub-sampled models	16
3.2.3	Confidence thresholds for the density of cell types . . . . .	21
3.2.4	Discussion of errors estimates obtained through sub-sampling . . . . .	23
3.3	Error estimates on the anatomical analysis of profiles . . . . .	26
3.4	Discussion of results by brain regions . . . . .	27
3.4.1	Cerebral cortex . . . . .	27
3.4.2	Olfactory areas . . . . .	30
3.4.3	Hippocampus . . . . .	30
3.4.4	Striatum . . . . .	31
3.4.5	Pallidum . . . . .	31
3.4.6	Thalamus . . . . .	31
3.4.7	Midbrain . . . . .	32
3.4.8	Medulla . . . . .	32
3.4.9	Cerebellum . . . . .	32
3.4.10	"Basic cell groups and regions" . . . . .	33
3.5	Repeated sub-sampling of gene space (II): random splitting of the data set in two equal parts . . . . .	34
<b>4</b>	<b>Numerical experiments with noise added</b>	<b>37</b>
4.1	Simulation scenario . . . . .	37
4.2	Results . . . . .	38
<b>5</b>	<b>Tables: cell-type-specific transcriptomes</b>	<b>41</b>
5.1	Description, labeling and anatomical origin of cell-type-specific transcriptomes .	41
5.2	Cell-type-specific transcriptomes, ordered by overlap between estimated density and average sub-sampled density . . . . .	44
<b>6</b>	<b>Figures: predicted and sub-sampled profiles: statistics of overlaps and localization scores in the ARA, and visualization</b>	<b>47</b>
<b>7</b>	<b>Figures for sub-sampled profiles (II): random splitting of the genes</b>	<b>112</b>

# 1 Introduction and notations

The present note is a quantitative discussion of the model presented in [1]. Let us briefly review the data and computations. The Allen Brain Atlas (ABA), the first Web-based, genome-wide atlas of gene expression in the adult mouse brain (eight-week old C57BL/6J male mouse brain), was obtained using an unified automated experimental pipeline [3, 4, 5, 6, 7, 8, 9]. The resulting data set consists of *in situ* hybridization (ISH) digitized image series for thousands of genes. These image series are co-registered to the Allen Reference Atlas (ARA) [10]. In the digitized version of the ARA we use, the mouse brain is partitioned into  $V = 49,742$  cubic voxels of side 200 microns. For a voxel labeled  $v$ , the *expression energy* of the gene labeled  $g$  is defined [11] as a weighted sum of the greyscale-value intensities of pixels intersecting the voxel. We developed the Brain Gene Expression Analysis (BGEA) MATLAB toolbox [13, 14], which allows to manipulate the gene-expression energies of the brain-wide ABA on the desktop as matrices [15, 16].

A complementary (cell-based) approach to the study of gene-expression energy in the brain uses microarray experiments to study co-expression patterns in a small set of brain cells of the same type. We studied cell-type-specific microarray gathered from different studies [17, 18, 19, 20, 21, 22, 23, 24], analyzed comparatively in [25], for  $T = 64$  cell types.

We determined the set of genes that are represented in *both* data sets (there are  $G = 2,131$  such genes). The ISH data of the Allen Atlas are arranged in a *voxel-by-gene* matrix  $E$ , and the cell-type-specific microarray data are arranged in a *type-by-gene* matrix  $C$ . The columns of both matrices correspond to the same set of genes, ordered in the same way:

$$E(v, g) = \text{expression of gene labeled } g \text{ in voxel labeled } v, \quad (1)$$

$$C(t, g) = \text{expression of gene labeled } g \text{ in cell type labeled } t. \quad (2)$$

We proposed a linear model to attempt a decomposition of the signal at each voxel (taking all genes into account), over cell-type-specific samples<sup>1</sup>:

$$\forall v \in [1..V], \quad (\rho_t(v))_{1 \leq t \leq T} = \operatorname{argmin}_{\nu \in \mathbf{R}_+^T} \sum_{g=1}^G \left( E(v, g) - \sum_{t=1}^T \nu(t) C_t(g) \right)^2. \quad (3)$$

We solved these quadratic optimization problems with positivity constraints (one per voxel), using the CVX toolbox for convex optimization [27, 28].

The results were presented graphically in the tables of [1] for all cell types. It is clear from visual examination that some cell types are predicted to have density profiles with striking anatomical features, while others are more amorphous. Moreover, there is intrinsic heterogeneity between the two data sets (ISH and microarrays), missing cell types, and missing genes

---

<sup>1</sup>We will sometimes use a dot to denote an index that takes all the possible values in a range that is well-defined from the context. For example, the symbol  $E(v, \cdot)$  denotes the vector  $(E(v, g))_{1 \leq g \leq G}$ , an element of  $\mathbf{R}^G$ , and the symbol  $\rho \cdot (v)$  denotes the vector  $(\rho_t(v))_{1 \leq t \leq T}$ , an element of  $\mathbf{R}^T$ .

due to the fact that the coronal ABA does not cover the whole genome. We therefore have to estimate how stable our estimates are against these sources of errors.

The present note is organized as follows. In section 2 we simulate a missing cell type in a thalamus in order to study the errors induced by one missing cell type. It turns out that a deviation from the average transcriptome profile for only 200 genes (roughly 10 % of our data set) is enough to induce the expected transfer of density from a class of Purkinje cells (labeled  $t = 52$ ) to the simulated cell type. In section 2 we repeatedly draw random samples of 200 genes from the data set, refit the model, thereby simulating the distribution of densities of cell types in sub-sampled models. We study the distribution of overlaps with the densities predicted in the original model, which gives rise to a ranking of cell types. The most visually striking anatomical (and least sparse) patterns tend to rank higher than the very sparse and amorphous patterns. The sub-sampling procedure also gives rise to a simulation of localization scores of the density profiles in the brain regions defined by the ARA. Cumulative distribution functions of the overlaps, distributions of localization scores and heat maps of average density profiles from sub-samples are presented graphically in section 6. However, this approach does not take into account the variation of stability properties from voxel to voxel for a given cell type. We perform random splitting of the data set into two equal parts (section 3.2), and compute the probability at each voxel of detecting each cell type from one sample, conditional on detecting it from the complementary sub-sample. This gives rise to spatial profiles estimating the stability properties of the predictions for each cell type. The results are presented graphically in the form of heat maps in section 7 (where density profiles threshold at 99% and 75% of conditional probability are plotted for each cell type. In section 4 we add noise to the cell-type-specific transcriptome profiles by mixing them in a Gaussian way, weighted by a scalar noise parameter. Adjusting the value of the parameter allows us to approximately recover the distribution of overlaps obtained from sub-sampling, which gives rise to a self-consistent estimate of the level of noise giving rise to the same amount of instability as missing genes.

**Convention and notation.** In this note we will work with the type-by-gene matrix of cell-type-specific transcriptomes obtained by subtracting the smallest entry of  $C$  from  $C$ , as this matrix has been shown in section 4.3 [1] to give rise to lower residual terms than the original microarray data (moreover, none of the original microarray data are zero, whereas all genes and voxels in the Allen Atlas contain some zeroes. For the sake of brevity of notation, this matrix will be denoted by  $C$  again.

## 2 Simulations with missing cell types

### 2.1 Simulation scenario

One of the surprising features of the results comes from the Purkinje cells labeled  $t = 52$  (see section 5 for tables containing the correspondence between cell types and labels), that were dissected from the cerebellum, but whose estimated profile  $\rho_{52}$  is mostly supported in the thalamus (the correlation between  $C_{52}$  and thalamic voxels is also remarkably high). There are two

other samples of Purkinje cells from the cerebellum in our data set. We verified that refitting the model with only one Purkinje cell sample left (the one labeled  $t = 52$ ), leads to a transfer of the cerebellar signal of the other Purkinje cell samples to this cell type, while the large density spot in the thalamus is conserved. Although the high value of the correlation is independent from our linear model, we conjecture that the high estimated density of Purkinje cells ( $\rho_{52}$ ) in the thalamus is due to a missing transcriptome from the thalamus: given the choice between  $C_{52}$  and a genuine thalamic transcriptome profile  $C_{\text{thalamus}}$ , we expect that most thalamic voxels would choose  $C_{\text{thalamus}}$  rather than  $C_{52}$ .

We do not have such data available, but the model suggests a simulation strategy: using ISH data for  $G = 2,131$  or roughly 10 percent of the genome allowed us to recover some striking anatomical density patterns. We can use this fraction of the genes at the scale of our data set (i.e. 200 genes) to simulate missing transcriptomes. Let us assume that a thalamic transcriptome<sup>2</sup> would only need to deviate from the average cell type  $\bar{C}$  in a suitably chosen set of 200 genes, *and in a competitive way with  $C_{52}$* , to inherit the thalamic signal from  $C_{52}$ . If the deviation is well chosen, this cell type should be able to inherit thalamic signal from  $t = 52$  upon refitting the model, providing a test of our conjecture<sup>3</sup>.

To simulate the missing transcriptome  $C_{\text{thalamus}}$ , we appended a simulated transcriptome  $C_{T+1}$  to the fitting panel, defined from mixtures of transcriptomes by the following pseudocode:

1. Initialize  $C_{T+1}$  at the average transcriptome,  $C_{T+1} = \bar{C} = \sum_{t=1}^C (t, \cdot) / T$ .
2. Find the voxel  $v_{th}$  in the thalamus with highest value of  $\rho_{52}$ :  
 $v_{th} := \operatorname{argmax}_{v \in \text{thalamus}} \rho_{52}(v)$ .
3. Rank the  $G$  entries in  $E(v_{th}, \cdot)$  by decreasing value:  
 $E(v_{th}, g_1) \geq E(v_{th}, g_2) \geq \dots \geq E(v_{th}, g_{T-1}) \geq E(v_{th}, g_T)$ .
4. For each of the 200 highest-ranking genes, replace the entry in  $C_{T+1}$  by the entry in  $C_{52}$ , modified by some dilation parameter  $\phi$  taken between 0 and 1:

$$\forall i \in [1..200], C_{T+1}^{(\phi)}(g_i) = (1 + \phi)C_{52}(g_i). \quad (4)$$

The last instruction in the pseudocode aims to ensure that the simulated profile  $C_{T+1}^{(\phi)}$  deviates from the average transcriptome in the 10% of genes that matter most in some thalamic voxels, and that it does so in a more intense way than  $C_{52}$ . Fitting the model to the above-defined panel of  $T + 1 = 65$  transcriptomes yields a new estimated voxel-by-type density matrix, denoted by  $\rho^{(\phi)}$ . If  $\phi$  grows from 0 to some critical value, we expect the thalamic density to

---

<sup>2</sup>A trivial simulation would involve choosing  $C_{T+1} = E(v_{Th}, \cdot)$ , where  $v_{Th}$  is a voxel from thalamus such that  $\rho_{52}(v_{Th})$  is large. This guarantees a perfect fit at this voxel:  $\rho_t(v_{Th}) \sim \delta_{t, T+1}$ ; we checked that this is the case numerically, and that the other voxels with positive densities at cell type labeled  $T + 1$  are all in the thalamus, and that the densities of other cell types are well-conserved, apart from  $t = 52$  loosing its density in the thalamus. But given the heterogeneity between microarray and ISH data, this check is more akin to a clustering property of the rows of  $E$  than to a test of the model, and we have to build  $C_{T+1}$  out of microarray data to run a more realistic simulation.

<sup>3</sup>See the next section on random sub-sampling for further tests of this idea using random samples of 200 genes from the data set.

transfer smoothly from  $t = 52$  to  $t = T + 1$ , and the thalamic voxels should be mostly affected.

## 2.2 Results

To test this conjecture, we ran simulations for growing values of  $\phi$ , starting from 0.01. The thalamic signal is indeed gradually transferred from  $t = 52$  to  $t = 65$  when  $\phi$  grows (see Fig. 1), and for sufficiently low values of  $\phi$ , the support of  $\rho_{T+1}^\phi$  is confined to the thalamus. However, as  $\phi$  continues to grow beyond 0.05,  $\rho_{T+1}$  develops positive density in other areas of the brain (see Fig. 2), and its values in the thalamus become larger than the values of  $\rho_{52}$  at  $\phi = 0$ .

This simulation of a missing cell type extends the qualitative logic that was unveiled by refitting the model to a panel containing a single composite pyramidal cell type [1], but it does so in a more refined way in the sense that the new fitting panel contains more transcriptomes than the original one. In the particular case of missing thalamic cell types, we showed that adding a cell type that is closer than the available ones to some voxels leads to a continuous transfer of signal to the new cell type (and 200 genes are enough to observe this regime of transfer). Hence a class of errors inherent to our model (the abusive prediction of a positive density of a given cell type in a region of the brain far from where it was extracted), can probably be checked against when new cell-type-specific transcriptomes become available and are included in the fitting panel.

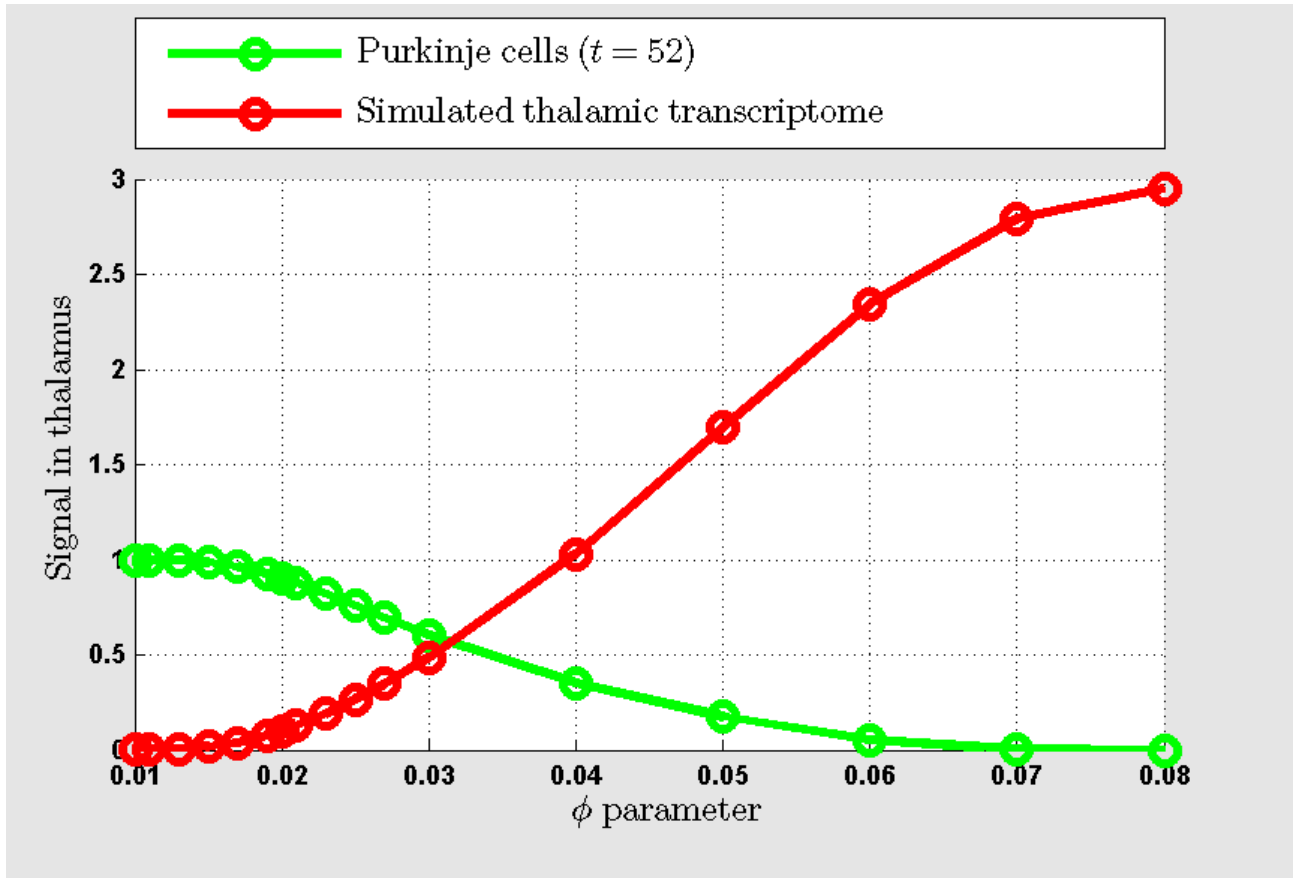


Figure 1: Thalamic signals for Purkinje cells and simulated thalamic transcriptome, as a function of the simulation parameter  $\phi$  (Eq. 4). The thalamic signal is transferred from Purkinje cells to the simulated thalamic transcriptome  $C_{T+1}$ . See Fig. 2 for visualization of the entire profiles at some values of  $\phi$ . The signals are normalized by the value  $\sum_{v \in \text{thalamus}} \rho_{52}(v)$  of the thalamic signal in Purkinje cells  $t = 52$  at  $\phi = 0$ , hence the start of the green curve at 1.

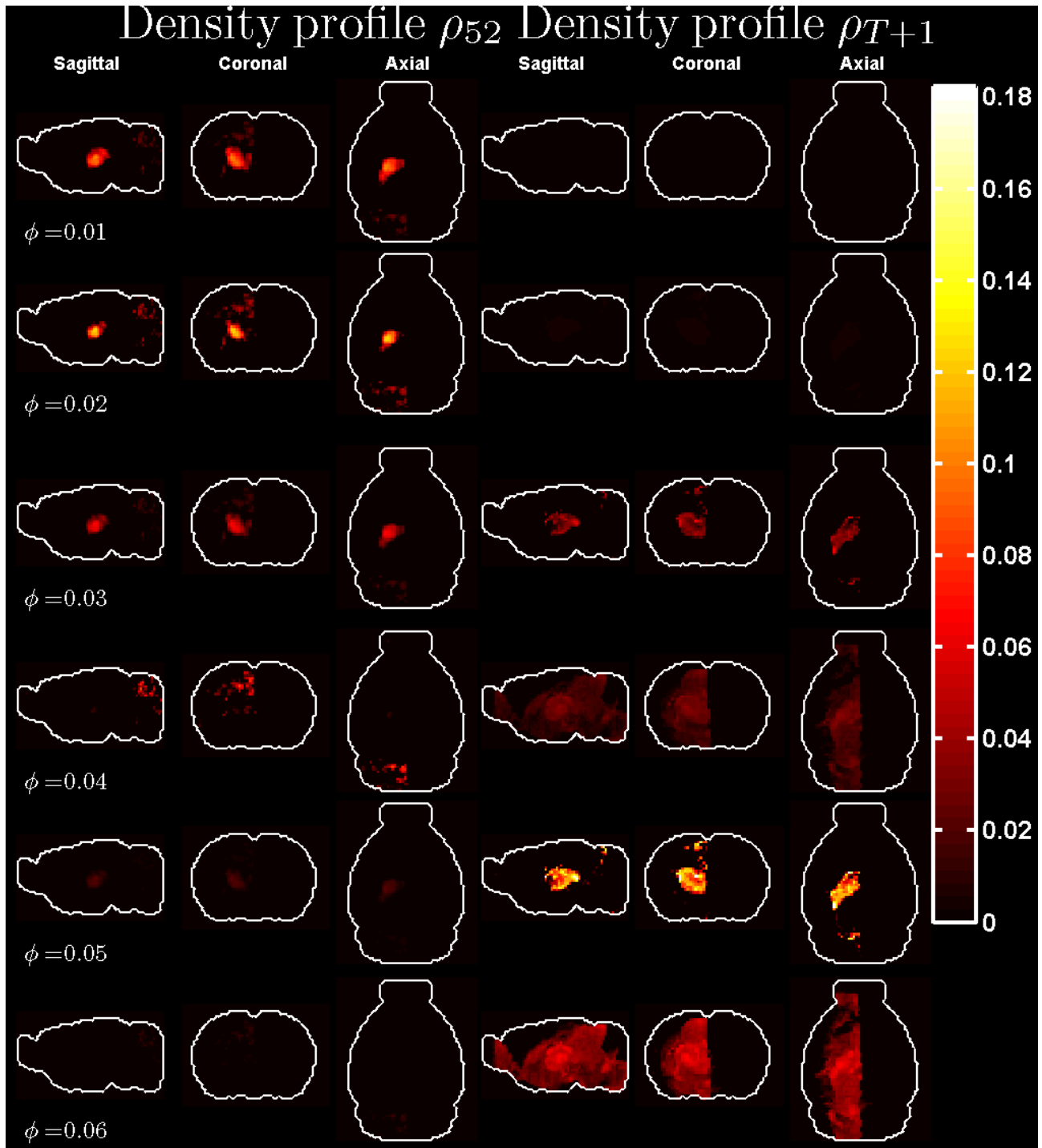


Figure 2: Maximal-intensity projections of the profiles  $\rho_{52}^\phi$  (first three columns) and  $\rho_{T+1}^\phi$  (last three columns). The signal in thalamic voxels is transferred from  $\rho_{52}^\phi$  to  $\rho_{T+1}^\phi$  as  $\phi$  grows.

### 3 Error estimates for the predicted density profiles

Subtracting a uniform term from the matrix of microarray data led to results [1] that present similar anatomical aspects for many cell types, and fit the ABA in a closer way. This raises the issue of the accuracy of the model. Some of the  $T = 64$  cell types have striking neuroanatomical profiles in our results, some others have non-zero density at very few voxels, but how vulnerable are these anatomical properties to errors introduced by missing data and noise? This is a difficult statistical problem, but we can perform a few numerical experiments to address it, and work out statistical bounds from theoretical results. In this section we will repeatedly refit the model to sub-sampled sets of genes in order to simulate the impact of missing genes on density estimates.

#### 3.1 Theoretical bounds on the error as a function of noise

Bounds have been provided recently by Meinshausen in [32] on the discrepancy between the signed-constrained estimates  $\rho$  obtained by minimizing quadratic discrepancies (as we did), and the quantity  $\rho^*$  such that

$$E(v, \cdot) = \sum_{t=1}^T C(t, \cdot) \rho_t^*(v) + \sigma \Xi(v, \cdot), \quad (5)$$

where the last term is drawn from a Gaussian distribution:

$$\Xi(v, \cdot) \sim \mathcal{N}(0, 1), \quad (6)$$

The voxel index  $v$  is fixed in Eq. 5. The vector  $E(v, \cdot)$  corresponds to the vector  $\mathbf{Y}$  in the notations of [32], and the matrix  $C$  corresponds to  $X^T$ , while our  $\rho$  corresponds to  $\hat{\beta}$ , and our  $\rho^*$  corresponds to  $\beta^*$ . Before stating the theorem and checking the hypotheses, let us note that the upper bound on  $\|\rho(v) - \rho^*(v)\|_1$  proven in [32] scales as the inverse square root of the number of genes  $G$ , which makes the bounds narrower when more genes are taken into account. As we are taking genetic data into account collectively, we are in an encouraging regime.

The covariance matrix  $\hat{\Sigma}$  is built from the matrix  $X$  obtained by  $L^2$ -normalizing the columns of  $C^T$ :

$$X(g, t) = \frac{C(t, g)}{\sqrt{\sum_{g=1}^G C(t, g)^2}}, \quad (7)$$

$$\hat{\Sigma} = \frac{1}{G} X^T X. \quad (8)$$

An upper bound on the  $L^1$ -norm of the difference between the vectors  $(\rho_t(v))_{1 \leq t \leq T}$ , and  $(\rho_t^*(v))_{1 \leq t \leq T}$  is given by Theorem 3 in [32] as a linear function of the noise parameter  $\sigma$ , with a coefficient given in terms of the properties of the matrix  $\hat{\Sigma}$ , which depends on the number of non-zero entries in  $\rho^*(v)$ , denoted by

$$S := \{k \in [1..T], \beta_k^* \neq 0\}, \quad (9)$$

which depends on the voxel label  $v$  in our case.

The first hypothesis of the theorem is the following *compatibility condition*:

$$\exists \phi_\infty > 0, \quad \min \left\{ |S| \frac{\beta^T \hat{\Sigma} \beta}{\|\beta\|_1^2}, \beta \in \mathcal{R}(0, S) \right\} \geq \phi_\infty, \quad (10)$$

where  $\|\cdot\|_1$  denotes the  $L^1$ -norm, and  $\mathcal{R}(0, S)$  is the set of vectors in  $\mathbf{R}^T$  that have zero entries outside the support  $S$ :

$$\forall L > 0, \quad \mathcal{R}(L, S) := \left\{ \beta, \sum_{k \in \bar{S}} |\beta_k| \leq L \sum_{k \in S} |\beta_k| \right\}. \quad (11)$$

We computed the matrix  $\hat{\Sigma}$ , and found that its entries are all strictly positive (even though there are some zeroes in  $C$  due to the subtraction of the minimum value of microarray data across all genes and cell types, all the entries sit comfortably above zero):

$$\forall s, t \in [1..T], \quad 4.51 \times 10^{-4} \leq \hat{\Sigma}(s, t) \leq 4.70 \times 10^{-4}, \quad (12)$$

hence the existence of a lower bound  $\phi_\infty = |S| \min(\hat{\Sigma})$  proportional to the minimum entry of  $\hat{\Sigma}$ .

The second hypothesis constrains *minimal positive eigenvalue* of  $\hat{\Sigma}$ , defined as<sup>4</sup>:

$$\phi_{pos,S}^2(\hat{\Sigma}) = \min \left\{ \frac{\beta^T \hat{\Sigma} \beta}{\|\beta\|_1^2}, \beta \in \mathbf{R}^T, \min_{k \in \bar{S}} \beta_k \geq 0 \right\}, \quad (13)$$

where  $\bar{S}$  denotes the complement in  $[1..T]$  of the support  $S$  of  $\beta^*$  defined in Eq. 9. If there exists some  $\kappa > 0$  such that  $\phi_{pos,S}^2(\hat{\Sigma}) \geq \kappa$ , then (by Theorem 3 in [32]) for some  $\eta$  chosen in the interval  $]0, 1/5[$ , the following upper bound on the  $L^1$ -norm of the difference between  $\rho(v)$  and  $\rho^*(v)$  holds with probability at least  $1 - \eta$ :

$$\|\rho(v) - \rho^*(v)\|_1 \leq \frac{8Ks\sigma}{\kappa\sqrt{G\phi_\infty}}. \quad (14)$$

Since the hypotheses are formulated in terms of the support  $S$  of  $\rho^*(v)$ , not  $\rho(v)$ , we cannot check them directly in terms of the quantities we computed. However, the inspection of our results across voxels and cell types yields a couple of simple cases (special values of  $v$ , with low values of  $|S|$ ). Indeed there are a few hundreds of voxels  $v$  at which only one cell type is predicted by the model (i.e.  $\rho_t(v) > 0$  for only one cell-type index  $t$ ). Moreover, the two cell types that are detected in this situation are the medium spiny neurons (index  $t = 16$ ) and the hippocampal pyramidal neurons (index  $t = 49$ ), and the corresponding voxels consist of subsets of the striatum and the hippocampus respectively, which are visually striking even if they contain only part of the signal of the two cell types. We plotted the following densities on Fig. 3 for  $t = 16$  and  $t = 49$ :

$$\rho_t^{single}(v) = \rho_t(v) \mathbf{1}(|s \in [1..T], \rho_s(v) > 0| = 1). \quad (15)$$

---

<sup>4</sup>The symbol  $\|\cdot\|_1$  denotes the  $L^1$ -norm in  $\mathbf{R}^T$ , so  $\|x\|_1 = \sum_{k=1}^T |x_k|$ .

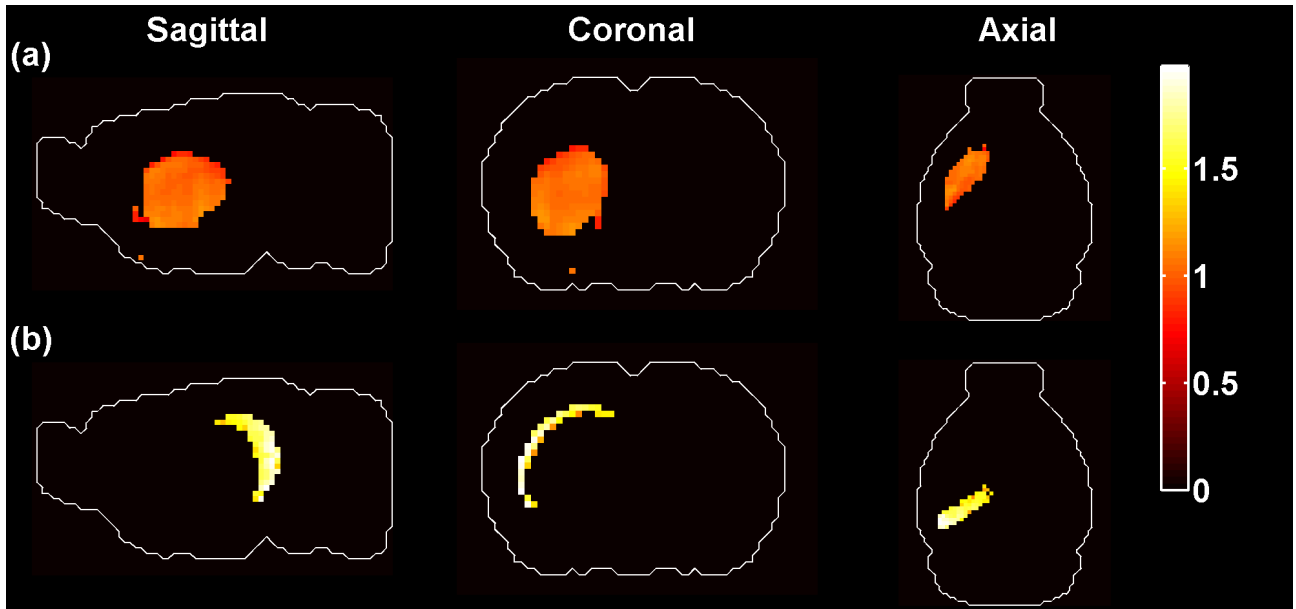


Figure 3: Maximal-intensity projections of density profiles of  $\rho_{16}^{single}$  and  $\rho_{49}^{single}$ , as defined in Eq. 15. (a), Medium spiny neurons  $t = 16$  and (b) hippocampal pyramidal neurons  $t = 49$ , restricted to voxels at which each of them is the only cell type detected by the model.

To get an idea of the values of the upper bounds yielded by 14, let us imagine that the underlying quantities  $\rho^*(v)$  are also supported by just one cell type, with index  $t = 16$  (for some values of  $v$  corresponding to striatal voxels), and with index  $t = 49$  (for some values of  $v$  corresponding to hippocampal voxels). Given that the anatomical origin of these two cell-type-specific transcriptomes (striatum and hippocampus) are guessed correctly by the model, this assumption seems reasonable.

For a voxel  $v$  at which  $\rho^*(v)$  is supported by only one cell type, labeled  $s$  (i.e.  $S = \{s\}$ ), the minimal positive eigenvalue condition can be checked by solving a simple quadratic programming problem. Indeed, if the support consists only of cell-type labeled  $s$  at a given voxel, the quantity to minimize to check the hypothesis on the minimal positive eigenvalue is the following:

$$\mathcal{Q}(\beta) = \frac{\beta^T \hat{\Sigma} \beta}{\|\beta\|_1^2}, \quad (16)$$

on the space of vectors  $\beta$  with positive entries at all indices except  $s$ . We can take care of the denominator in Eq. 3.1 by rewriting  $\mathcal{Q}(\beta)$  as a quadratic form in the  $L^1$ -normalized vector

$$\beta^{norm} = \left( \beta_1, \dots, \beta_{s-1}, \pm(1 - \sum_{t \neq s} \beta_t), \beta_{s+1}, \dots, \beta_T \right), \quad (17)$$

where the expression at the  $s$ -th entry follows from the fact that  $\beta_t = |\beta_t|$  for any  $t \neq s$ . Hence, we can bound the expression in Eq. from below as follows

$$\mathcal{Q}(\beta) = \beta^{norm T} \hat{\Sigma} \beta^{norm} \geq \mathcal{Q}'(\beta_1, \dots, \beta_{s-1}, \beta_{s+1}, \dots, \beta_T), \quad (18)$$

where the expression  $\mathcal{Q}'(\beta_1, \dots, \beta_{s-1}, \beta_{s+1}, \dots, \beta_T)$  is a quadratic form in the vector

$$\beta^{\bar{s}} = (\beta_1, \dots, \beta_{s-1}, \beta_{s+1}, \dots, \beta_T), \quad (19)$$

with positive entries. As the entries of the (symmetric) covariance matrix  $\hat{\Sigma}$  are all positive, the expression of  $\mathcal{Q}'$  in the lower bound of Eq. 18 is as follows:

$$\mathcal{Q}'(\beta^{\bar{s}}) = \beta^{\bar{s} T} \hat{\Sigma}_{\bar{s}\bar{s}} \beta^{\bar{s}} + \hat{\Sigma}_{ss} \left( 1 - \sum_{t \neq s} \beta_t \right)^2 - 2 \left( 1 - \sum_{t \neq s} \beta_t \right) \sum_{t \neq s} \hat{\Sigma}_{st} \beta_t, \quad (20)$$

where  $\hat{\Sigma}_{\bar{s}\bar{s}}$  is the  $(T - 1)$ -by- $(T - 1)$  matrix obtained by destroying the  $s$ -th column and the  $s$ -th row in  $\hat{\Sigma}$ . We minimized  $\mathcal{Q}'$  over positive vectors  $\beta^{\bar{s}}$  in  $\mathbf{R}_+^{T-1}$ , and found it to be strictly positive for all values of  $s$ . In particular, with  $s = 16$  and  $s = 49$ , choosing  $\eta = 0.15$ , the upper bound of [32] are linear functions of the noise parameter  $\sigma$  plotted on Fig. 4 (divided by the value of  $\|\rho(v)\|_1$  for each voxel  $v$ , hence the voxel-dependent lines on the figure).

The regime of noise corresponding to narrow bounds even in this simple case of single-supported voxel is quite low (at  $\sigma < 10^{-5}$ ), whereas the average entry in  $E(v, \cdot)$  at the

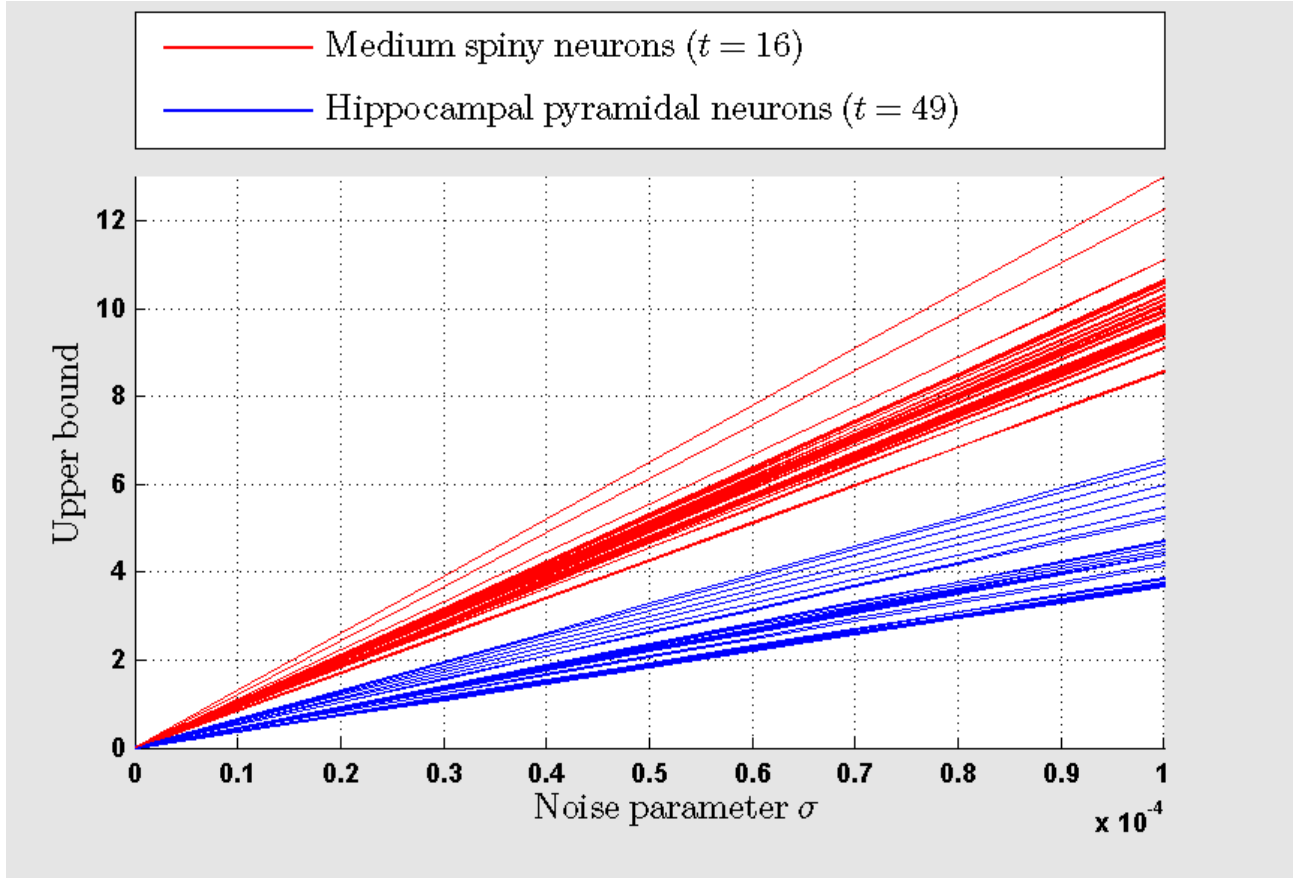


Figure 4: The upper bound on the discrepancy between  $\rho_t$  and  $\rho_t^*$  as a function of noise, for the two values of  $t$  for which the model predicts the largest number of voxels to have support with  $s = 1$ . We normalized the bounds by  $\|\rho(v)\|_1$ , so the interesting regime of noise is the one for which the values in the vertical axis are below 1.

voxels plotted in Fig. 3 is larger than 4. Hence we found the theoretical upper bounds to be very large, assuming the simplest possible support ( $s = 1$ ). This confirms the difficulty of theoretical approaches to the problem, even though our data set verifies the strong assumptions of Theorem 3 of [32] in the case of  $|S| = 1$ . This triggers us to conduct simulations to assess more quantitatively with which probability the support of densities  $\rho^*(v)$  in voxel space (index  $v$ ) and in the space of cell types (index  $t$ ) is correctly identified.

## 3.2 Repeated sub-sampling of gene space

### 3.2.1 Simulation scenario

As our data set contains only  $G = 2,131$  genes (those with data both the coronal ABA and in all transcriptomes), our results are based on roughly 10% of the mouse genome. One obvious source of error is therefore the incompleteness of the coverage of gene space. Given a cell type with a striking predicted density pattern, it is easy to imagine ways to append thousands of columns to the matrices  $E$  and  $C$  (collectively labeled  $g_{new}$ ), such that the new entries  $E(v, g_{new})$  and  $C(t, g_{new})$  are anticorrelated, for voxels  $v$  where cell type  $t$  has a positive predicted density,  $\rho_t(v) > 0$ . Refitting the model to this larger data set could destroy the anatomical pattern of the estimated density (bringing  $\rho_t(v)$  to 0) if the uncorrelated entries in the appended columns are large enough.

However, detailed neurobiological knowledge presided over the choice of the genes included in the coronal ABA [3]: genes found to have striking expression patterns in preliminary data, and genes of particular interest in the neuroscience literature, were prioritized. There must therefore be more genes with region-specific expression pattern among our  $G$  genes than expected by chance. The mathematical scenario with large anti-correlated extra columns in matrices  $E$  and  $C$  should therefore be made improbable by the design of the coronal ABA, but this scenario suggests a simulation technique to assess how badly our anatomical conclusions can be affected by missing genes. Indeed we can sub-sample the available gene space, taking random sets of genes into account, each containing only 200 genes (a little less than 10% of the data set, which is approximately the scaling of the data set compared to the complete genome). Repeating this operation yields a random family of density estimates for each cell type. The results of the sub-samplings are all of the same voxel-by-type format, and their distribution in the space of matrices  $\mathcal{M}_{\mathbf{R}_+}(V, T)$  can be studied to estimate confidence intervals on the densities, one per transcriptome profile (i.e. one per column).

The following pseudocode helps introduce notations:

for  $s$  in [ 1..S ]

1. draw a random set of 200 integers from [1..G], without replacement;

2. construct the matrices  $C^{(s)}$  and  $E^{(s)}$  by concatenating the columns of  $C$  and  $E$  corresponding to these integers;

3. compute  $(\rho_t^{(s)}(v))_{1 \leq t \leq T}$  at each voxel:

$$(\rho_t^{(s)}(v))_{1 \leq t \leq T} = \operatorname{argmin}_{\phi \in \mathbf{R}_+^T} (\| \|E^{(s)}(v, \cdot) - \sum_t \phi_t C^{(s)}(t, \cdot)\|^2).$$

end

### 3.2.2 Variability of density profiles between the original and sub-sampled models

The situation studied theoretically in the article [32] is identical to ours (we have one instance of this situation at each voxel). We observed that it is difficult to predict the values of the densities, and even their support in type space (the number of indices  $t$  for which  $\rho_t(v) > 0$  at a fixed value of the voxel index  $v$ ). When we consider all values of the voxel index  $v$  for a fixed value of the cell-type index  $t$ , which is what we do when we plot estimated densities of a cell type, it is therefore difficult to know which voxels have positive densities for type  $t$  (the support of cell-type labeled  $t$  in gene space). However, the estimated profile  $\rho_t$  can be visualized compared to of the average sub-sampled profile

$$\bar{\rho}_t(v) = \frac{1}{S} \sum_{s=1}^S \rho_t^{(s)}(v). \quad (21)$$

To compare density profiles in the original and sub-sampled models, we first observe that the density profiles in the original model, denoted by  $(\rho_t(v))_{1 \leq t \leq T, 1 \leq v \leq V}$  are rather sparse in voxel space, in the sense that for all values of  $t$ , the number of voxels in the support  $\text{Supp}(t)$  of cell type labeled  $t$ , defined<sup>5</sup> as follows:

$$\text{Supp}(t) = \{v \in \text{Brain Annotation}, \rho_t(v) > 0\}, \quad (22)$$

corresponds to 6.52% of the brain on average, and never exceed 32% . The sorted values of the fraction

$$\xi(t) = \frac{|\text{Supp}(t)|}{\sum_{v \in \text{Brain Annotation}} 1} \quad (23)$$

are plotted in Fig. 5. The values of the fractions defined in Eq. 23 are also typical of the densities obtained after sub-sampling.

We can use the support  $\text{Supp}(t)$  of cell type labeled  $t$  as a control set, and compute how much of the signal of the second profile (which for us will be the profile  $\rho_t^{(s)}$  of the same cell type in the  $s$ -th sample) is supported in  $\text{Supp}(t)$  . We computed the following quantity  $\mathcal{I}(s, t)$  for each sub-sample  $s$  and each cell type  $t$ , which is an overlap ranging from 0 (when the two

---

<sup>5</sup>We used the set of voxels belonging to the set of voxels annotated in the digitized Allen Reference Atlas to belong to the left hemisphere. This set consists of 25,155 voxels. This convention corresponds to the one used to determine the *top region by density* in the coarsest annotation of the mouse brain in the ARA, which covers the left hemisphere. Moreover, we chose to study the left hemisphere in order to be able to conduct more simulations, as the model involves the solution of one quadratic optimization problem per voxel. As the results of the model can be observed to have a large degree of left-right symmetry, at least for the cell types with large predicted densities, this choice of annotation should give a reasonable simulation of brain-wide prediction errors, assuming these errors are also left-right symmetric. The analysis can easily be extended to the entire brain by doubling the allotted computation time.

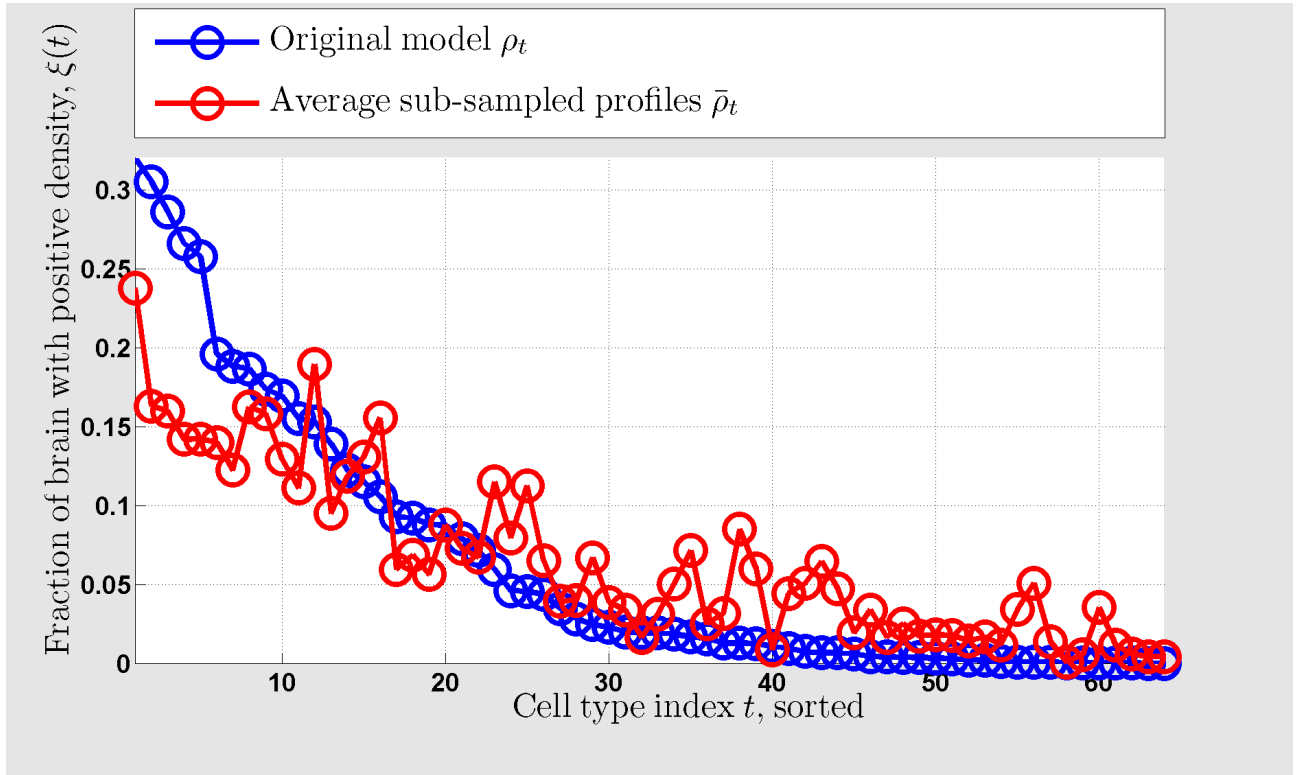


Figure 5: Sorted values of the fraction of the volume of the brain annotation in the ARA (Eq. 23) supporting the total density of each of the  $T = 64$  cell types in the study. The largest value corresponds to  $t = 40$ , cortical pyramidal neurons, whose support occupies 32% of the left hemisphere, and corresponds roughly to the entire left cerebral cortex.

profiles have disjoint supports), to 1 (when the signal of the sample  $s$  is entirely supported by the support of  $\rho_t$ ):

$$\mathcal{I}(s, t) := \frac{1}{\sum_v \rho_t^{(s)}(v)} \sum_v \mathbf{1}(\rho_t(v) > 0) \rho_t^{(s)}(v). \quad (24)$$

For each cell type labeled  $t$ , the repeated sub-sampling approach simulates the distribution of the overlaps  $\mathcal{I}(\cdot, t)$ . The closer to 1 this distribution is concentrated, the more stable on average the estimate of the density of cell type labeled  $t$  is under sub-sampling. This simulation of the distributions of the overlaps  $\mathcal{I}(\cdot, t)$  for all values of  $t$  can be used to rank the transcriptome profiles by decreasing level of average overlap between  $\rho_t$  and sub-samples density profiles:

$$\bar{\mathcal{I}}(t) := \frac{1}{S} \sum_{s=1}^S \mathcal{I}(s, t). \quad (25)$$

Let us denote the corresponding ranking by  $(r_t^{signal})_{1 \leq t \leq T}$ , which is defined by the following inequalities:

$$\bar{\mathcal{I}}(r_1^{signal}) \geq \bar{\mathcal{I}}(r_2^{signal}) \geq \dots \geq \bar{\mathcal{I}}(r_T^{signal}). \quad (26)$$

The index  $t = 40$  is ranked first:  $r_1^{signal} = 40$ , followed by  $t = 16$ , medium spiny neurons. The results of the simulations are presented graphically in the 64 figures of section 6 (the cell-type indices  $t$  are ordered from 1 to  $T$  as in the other tables for the sake of consistency, but the ranking of each cell type induced by Eq. 26 can be found in Tables 6 and 7), for which the following four densities are plotted, following the format of Figs. 6 and 7:

- (a) As a reminder, the original density  $\rho_t$ .
- (b) The average sub-sampled profile  $\bar{\rho}_t$ .
- (c) The part of the average sub-sampled profile that is supported by the support of  $\rho_t$ , obtained by applying a Boolean mask to it:

$$\bar{\rho}_t^{(supported)}(v) = \bar{\rho}_t(v) \mathbf{1}(\rho_t(v) > 0). \quad (27)$$

- (d) The part of the average sub-sampled profile that is supported outside the support of  $\rho_t$ :

$$\bar{\rho}_t^{(unsupported)}(v) = \bar{\rho}_t(v) \mathbf{1}(\rho_t(v) = 0). \quad (28)$$

If the overlap  $\bar{\mathcal{I}}(t)$  is close to 1, the density profiles (a), (b) and (c) will look very similar, and the density profile (c) will look empty. Examples taken from the top two cell types of the ranking  $r^{signal}$  are shown on Figs. 6 and 7.

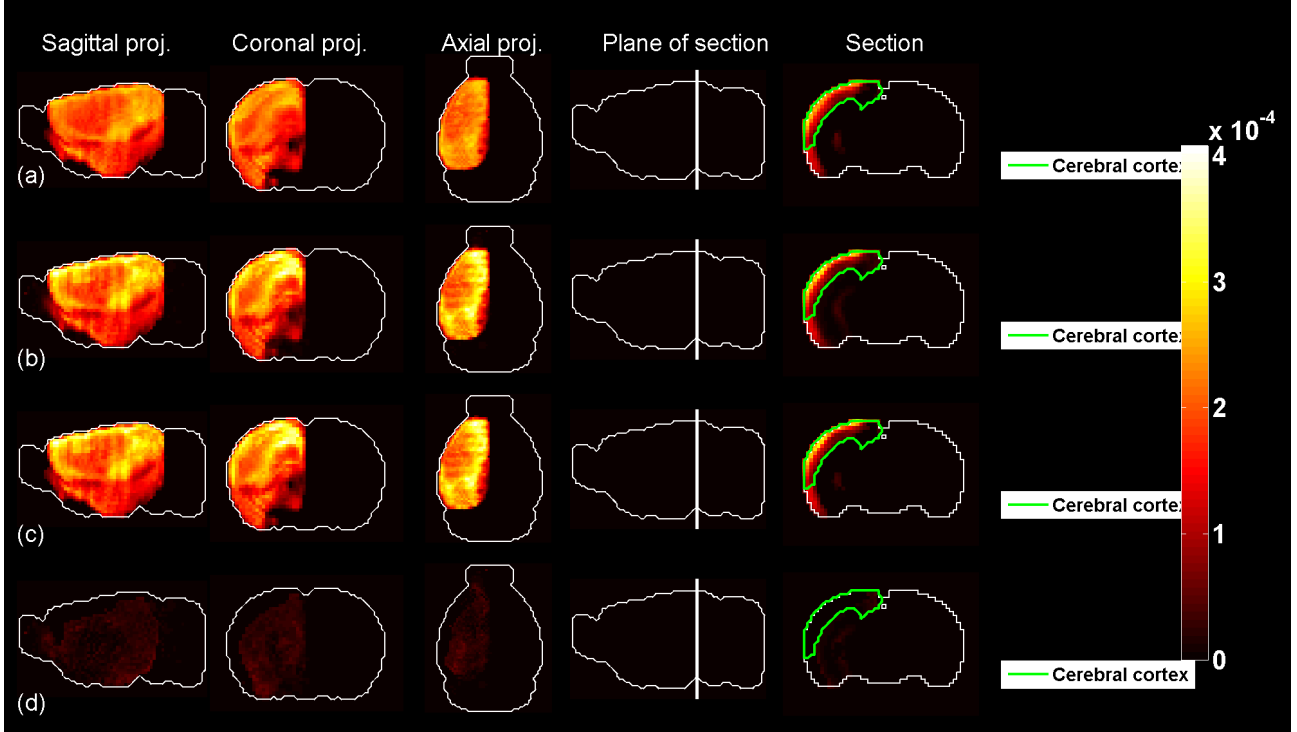


Figure 6: Density profiles for cell type labeled  $t = 40$ , cortical pyramidal neurons, which has the highest overlap ( $r_1^{signal} = 40$ ) between the predicted profile  $\rho_t$  and the average sub-sampled profile  $\bar{\rho}_t$ . (a) The predicted density profile  $\rho_{40}$ . (b) The average sub-sampled profile  $\bar{\rho}_{40}$ . (c) The part of  $\bar{\rho}_{40}$  supported in the same voxels as  $\rho_{40}$ , Eq. 27. (d) The part of  $\bar{\rho}_{40}$  that does not overlap with the support of  $\rho_{40}$ , Eq. 28. The ranking of cell-type-specific transcriptomes induced by the sub-sampling procedure and Eq. 26 is supposed to rank highly the cell types for which the profiles (a), (b) and (c) look very similar, while (d) looks close to zero.

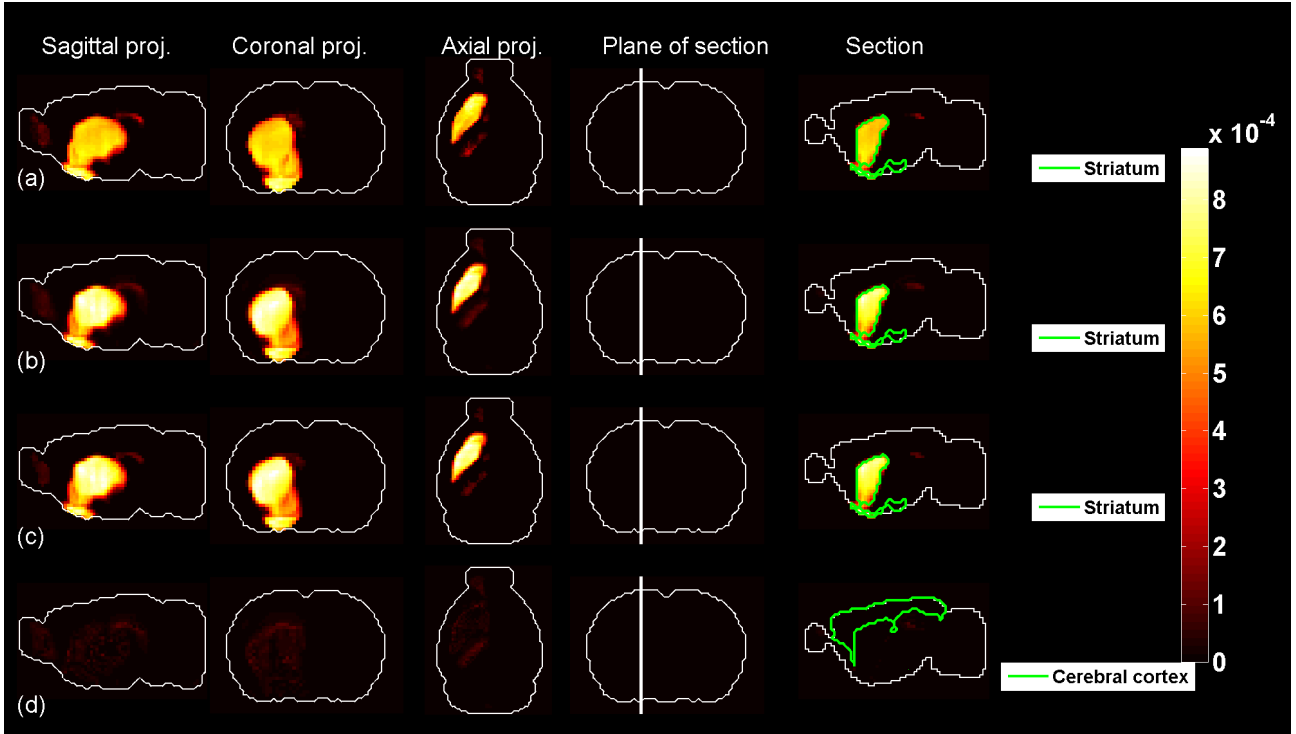


Figure 7: Density profiles for cell type labeled  $t = 16$  medium spiny neurons, which has the second highest overlap ( $r_2^{signal} = 16$ ) between the predicted profile  $\rho_t$  and the average sub-sampled profile  $\bar{\rho}_t$ . (a) The predicted density profile  $\rho_{16}$ . (b) The average sub-sampled profile  $\bar{\rho}_{16}$ . (c) The part of  $\bar{\rho}_{16}$  supported in the same voxels as  $\rho_{16}$ , Eq. 27. (d) The part of  $\bar{\rho}_{16}$  that does not overlap with the support of  $\rho_{40}$ , Eq. 28.

### 3.2.3 Confidence thresholds for the density of cell types

Having simulated the distribution of the sub-sampled densities of all the  $T$  cell-type specific transcriptomes in our data set, we can estimate confidence thresholds in two ways, for a cell type labeled  $t$ .

(1) Impose a threshold  $\alpha$  in the interval  $[0, 1]$  on the overlap with the density  $\rho_t$  estimated in the linear model, and work out the probability  $p_{t,\alpha}$  of reaching that threshold from the sub-samples:

$$p_{t,\alpha} := P(\mathcal{I}(\cdot, t) \geq \alpha) = \frac{1}{S} |\{s \in [1..S], \mathcal{I}(s, t) > \alpha\}|. \quad (29)$$

For a cell type labeled  $t$ , the distribution of the overlaps  $\mathcal{I}(\cdot, t)$  can be visualized using the cumulative distribution function  $\text{CDF}_t$  (in the space  $[0, 1]$  of the values of the overlap between  $\rho_t$  sub-sampled profiles  $\rho_t^{(s)}$ ):

$$\text{CDF}_t(\alpha) = \frac{1}{S} |\{s \in [1..S], \mathcal{I}(s, t) \leq \alpha\}|. \quad (30)$$

The value  $\text{CDF}_t(u)$  is related to the probability defined in Eq. 29 as follows:

$$p_{t,\alpha} = 1 - \text{CDF}_t(\alpha). \quad (31)$$

(2) Impose a threshold  $\beta$  in the interval  $[0, 1]$  on the fraction of sub-samples, and work out which overlap  $\mathcal{I}_{thresh}(t, \beta)$  with the estimated density  $\rho_t$  is reached by that fraction of the sub-samples. The threshold value of the intercept  $\mathcal{I}_{thresh}(t, \beta)$  is readily expressed in terms of the inverse of the cumulative distribution function:

$$\mathcal{I}_{thresh}(t, \beta) = \text{CDF}_t^{-1}(\beta). \quad (32)$$

The more stable the prediction  $\rho_t$  is against sub-sampling, the more concentrated the values of  $\mathcal{I}(\cdot, t)$  are at high values (close to 1), the slower the take-off of the cumulative function  $\text{CDF}_t$  is, the lower the value of  $\text{CDF}_t(\alpha)$  is, and the larger the probability  $p_{t,\alpha}$  is (for a fixed value of  $\alpha$  in  $[0,1]$ ).

For a fixed cell type labeled  $t$ , the values of  $p(t, \cdot)$  and  $\mathcal{I}_{thresh}(t, \cdot)$  can therefore be readily read off from a plot of the cumulative distribution function  $\text{CDF}_t$  (this plot is in the  $\alpha\beta$  plane in our notations). For the sake of visualization of results for all cell types, we constructed the matrix  $\mathcal{C}$ , whose columns correspond to cell types, and whose rows correspond to values of the threshold  $\alpha$ :

$$\mathcal{C}(\alpha, t) := \text{CDF}_{r_t^{signal}}(\alpha), \quad (33)$$

where the index  $r_t^{signal}$  in the r.h.s. means that the cell types are ordered by decreasing order of overlap between the average sub-sampled profile and the predicted profile. If the entries of the matrix  $\mathcal{C}$  are plotted as a heat map (see Fig. 8), the hot colors will be more concentrated in the left-most part of the image. For a fixed column, the more concentrated the hot colors are in the heat map, the more stable the corresponding cell type is.

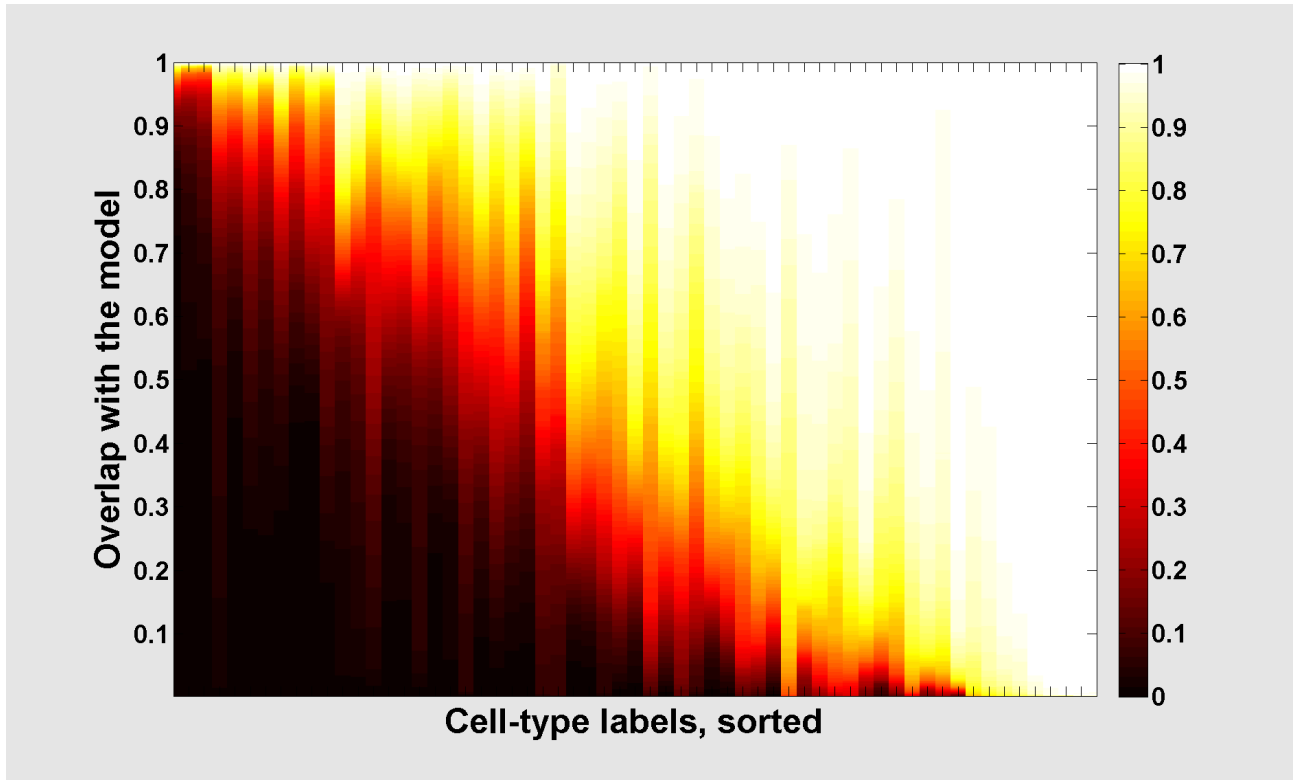


Figure 8: **Heat map of the CDFs of the overlaps between sub-sampled densities and the result of the model, ordered as in the matrix  $\mathcal{C}$  (Eq. 33).** One cell type per column, the columns are sorted by decreasing order of the average value of the overlap defined in 26. Each of the columns of this heat map is plotted as a function at the end of this note (in the figures of section 6), next to the visual rendering of the average sub-sampled profile.

### 3.2.4 Discussion of errors estimates obtained through sub-sampling

The large bright area in the heat map of Fig. 8 makes it clear that quite a few cell types in the present data set (at the bottom of the ranking by average overlap) have a very unstable signal across sub-samples. In particular, nearly all the sub-samples for types such that  $r_t^{signal} > 45$  have profiles with empty overlap with the original profile  $\rho_t$  predicted by optimizing over the full gene space. The ranked list of cell types is given in tables, but we can study how the rankings  $r^{signal}$  and error bars correlate with features of the predicted profiles, and with the metadata.

Taking a look at the cell types  $t$  at the first ranks (for example the pyramidal neurons  $t = 40$  and medium spiny neurons  $t = 16$ ) one notices that their support tends to be larger (even though they are always confined to less than a third of the voxels), and also more localized in neuroanatomical areas defined in the ARA, whereas the ones at the bottom of the ranking tend to have sparser profiles, which can be restricted to just a few voxels. The value of the overlap between a random profile and a fixed profile is biased upwards by the size of the support of the profile. If one considers the ensemble of random subsets of  $[1..V]$  (or equivalently random subsets of the voxels in the ARA), of fixed size  $W$ , denoted by  $\nu$  as follows:

$$\nu_v = \pm 1, \quad v \in [1..V], \quad \sum_{v=1}^V \nu_v = W, \quad (34)$$

and if one considers the ensemble of brain-wide profiles  $\chi$  supported on these voxels (with some uniform value  $\phi$ ), that is

$$\chi(v) = \phi \mathbf{1}(\nu_v = 1), \quad (35)$$

then the average overlap of these profiles with  $\rho_t$  averages at the fraction of the brain supporting  $\rho_t$ , assuming independence between the random support  $\nu$  and the support of  $\rho_t$ :

$$\mathcal{U}_t^{rand} := \left\langle \frac{1}{\sum_{v=1}^V \chi(v)} \sum_{w=1}^V \chi(w) \mathbf{1}(\rho_t(w) > 0) \right\rangle = \frac{1}{W} \sum_{w=1}^V \frac{W}{V} \frac{|\text{Supp}(t)|}{V} = \xi(t), \quad (36)$$

where  $\xi(t)$  is the fraction of voxels in the brain annotation supporting the estimated profile  $\rho_t$  (see Eq. 22) which is one reason for which cell types largest supports tend to be on the left of the heat map of Fig. 8. The crude estimate  $\mathcal{U}_t^{rand}$  also provides a reference for the expectation by chance to which the values or  $\bar{\mathcal{I}}(t)$  can be compared these two quantities, and again rank the cell-type-specific transcriptomes by decreasing values of this differences. The types with high positions above the diagonal (such as  $t = 1, 12, 16, 40, 26$ ) tend to be conserved between scatter-plots 9 and 10, even though the exact shape of the cloud of points change.

The indices that are higher above the diagonal in the scatter-plot 9, (resp. high in the vertical direction in the scatter-plot 10), are the ones whose densities are the most stable under sub-sampling (resp. the ones whose stability properties deviate more than what would be expected by chance, based on random independent profiles). Not surprisingly, the medium spiny

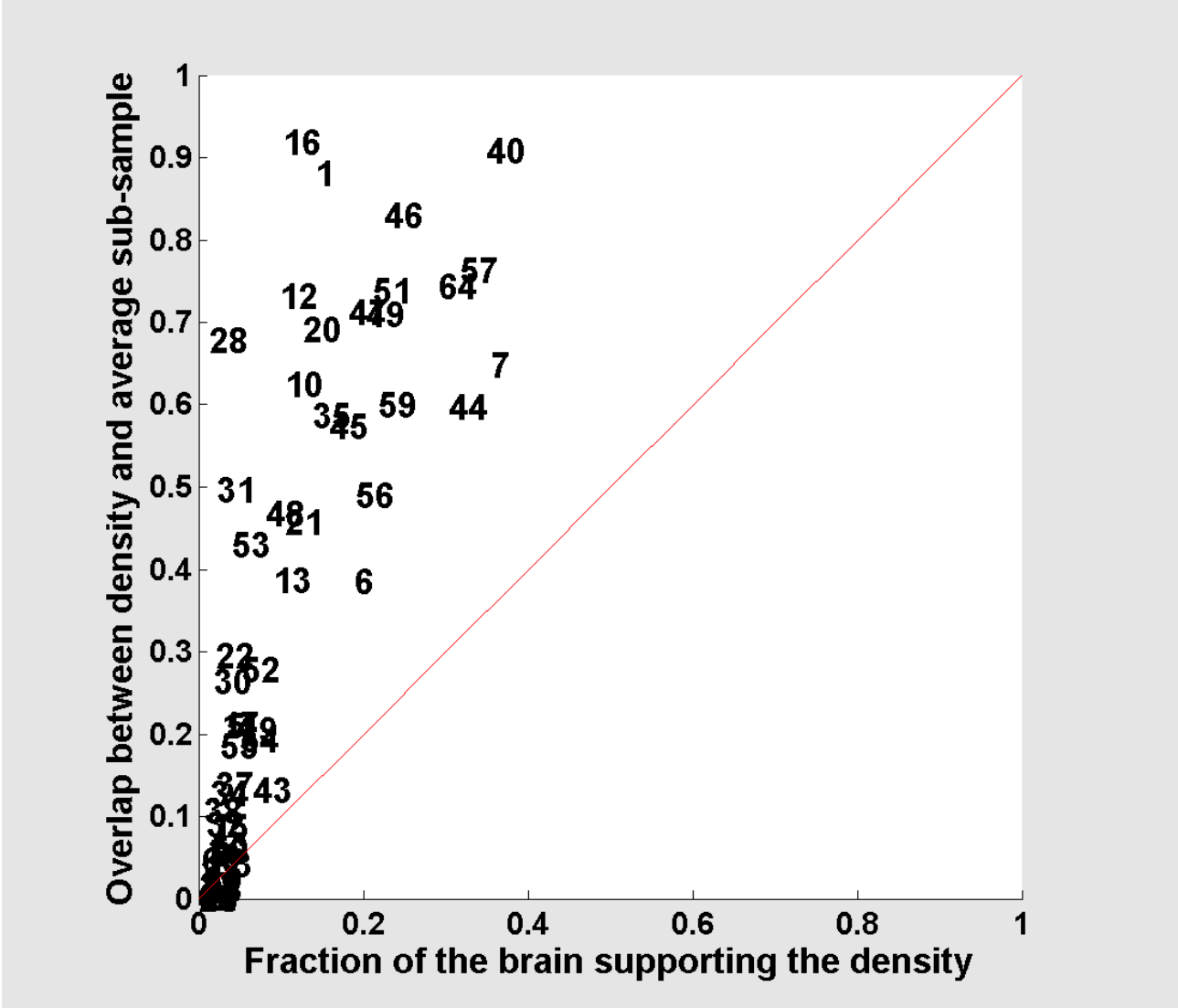


Figure 9: Scatter-plot of overlaps  $\bar{I}(t)$  against fraction of voxels supporting the predicted density,  $\xi(t)$ .

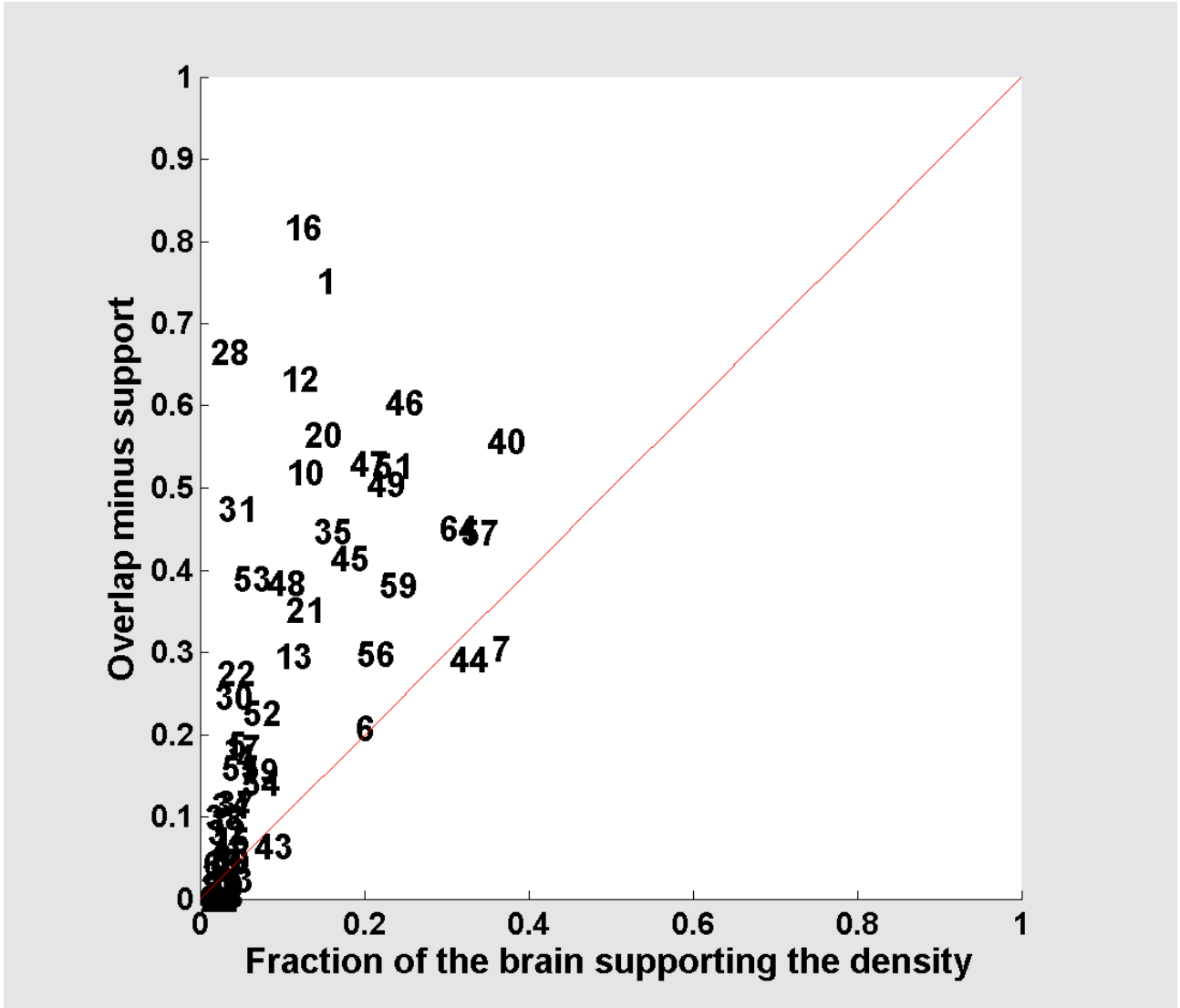


Figure 10: Scatter-plot of differences between overlaps and supports  $\bar{\mathcal{I}}(t) - \xi(t)$  against fraction of voxels supporting the predicted density,  $\xi(t)$ . Medium spiny neurons ( $t = 16$ ) appear on top of the scatter-plot.

neurons labeled  $t = 16$  are singled out by these scatter-plot.

So far the analysis of results has been very general and abstract. The support analysis is just one possible quantitative approach to the ranking of cell-type-specific transcriptomes by the amplitude of errors, and we have to look at the results for each of the cell types. However, we can notice that the transcriptomes that are ranked highly by our procedure tend to be ones that one would have singled out by eye for anatomical reasons before the sub-sampling procedure was carried out, because these transcriptomes tend to:

1. have a density profile  $\rho_t$  that highlight a known neuroanatomical region,
2. come from cells that were indeed microdessected from these regions.

Moreover, we can compute the localization scores of the average sub-sample on the same bar diagram as the ones of the predicted profile, in order to see if the fraction of signal in the average sub-sample that is not supported by the prediction changes radically the ranking of regions in the ARA by density of cell-type  $t$  or not. A bar diagram of these localization scores is presented in the figures for every cell type in part (b) of the figure containing the plot of the cumulative distribution functions of the overlaps.

### 3.3 Error estimates on the anatomical analysis of profiles

The brain-wide density profiles  $\rho$  (or rather any quantity defined in the left hemisphere, where the so-called Big12 annotation<sup>6</sup> is defined), can be confronted to classical neuroanatomy using a bar diagram of the localization scores of  $\rho$  in the regions of the 'Big12' annotation. A number of these bar diagrams were presented in [1]. Let us recall the definition of the localization scores [16] of  $\rho$  in region  $\omega$ :

$$\lambda_\omega(\rho) = \frac{\sum_{v \in \omega} \rho_t(v)^2}{\sum_{v \in \text{Brain Annotation}} \rho_t(v)^2} \quad (37)$$

The (squared)  $L^2$ -norm is only one possible choice of norm in the fraction 37. It happens to have a generalization to sums of functions chosen from a family, that maps the maximization of localization scores to a generalized eigenvalue problem (using the  $L^1$ -norm instead does not lead to major changes in the designation of the top region by density). The important thing in the present discussion is that we can repeat the computation of localization scores for each cell type labeled  $t$ . We can complement the bar diagram of localization scores  $(\lambda_\omega(\rho_t))_{\omega \in \text{Big12}}$  by the bar diagram of localization scores of the average sub-sampled profile,  $(\lambda_\omega(\bar{\rho}_t))_{\omega \in \text{Big12}}$ . Moreover, we can compute the whole family of localization scores of all the sub-sampled profiles  $(\lambda_\omega(\rho_t^{(s)}))_{\omega \in \text{Big12}, s \in [1..S]}$ . The more peaked the distribution of these scores is around  $(\lambda_\omega(\bar{\rho}_t))_{\omega \in \text{Big12}}$  for each region  $\omega$ , and the closer the values  $(\lambda_\omega(\bar{\rho}_t))_{\omega \in \text{Big12}}$  are to  $(\lambda_\omega(\rho_t))_{\omega \in \text{Big12}}$ , the more stable

---

<sup>6</sup>This annotation is the coarsest annotation in the ARA, and consists of 12 regions together with the so-called 'Basic cell groups and regions'. The regions are designated by the following symbols in the plots: Basic cell groups and regions = Basic, Cerebral cortex = CTX, Olfactory areas = OLF, Hippocampal region = HIP, Retrohippocampal region = RHP, Striatum = STR, Pallidum = PAL, Thalamus = TH, Hypothalamus = HY, Midbrain = MB, Pons = P, Medulla = MY, Cerebellum = CB

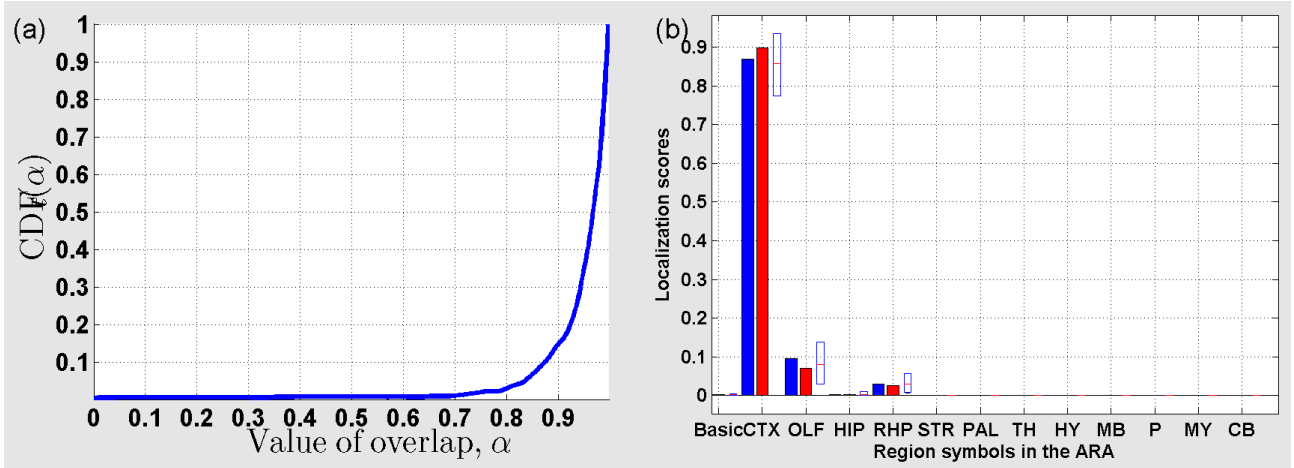


Figure 11: **Cumulative distribution function of overlaps and distribution of localization scores for cortical pyramidal neurons,  $t = 40$ .** (a) The function  $CDF_t$  for  $t = 40$ . (b) Localization scores in the 'Big12' annotation. The top region of the density is the cerebral cortex both in the original model and in the average sub-sampled density. Moreover, the localization score in the cortex is larger than 78% in 75% of the samples, which allows to distinguish the cortex from any other region with non-zero signal (such as the olfactory areas and the hippocampus).

the anatomical properties of the density profile  $\rho_t$  are under sub-sampling. For visualization purposes, the bar diagrams of the localization scores of  $\rho_t$  and  $\bar{\rho}_t$  are supplemented on the same graph by a box plot of the localization scores of samples, showing the median of the distribution, and extending vertically between the first and third quartiles of the distribution  $(\lambda_\omega(\rho_t^{(s)}))_{s \in [1..S]}$  for each region  $\omega$ . A stable prediction results in two very similar bar diagrams, with very small boxes appended to their right. Not surprisingly, the cell types labeled  $t = 40$  and  $t = 16$ , which were ranked first and second by the overlap analysis, give rise to such plots (see Figs. 11 and 12). Analogous figures for all values of  $t$  can be found at the end of the present note (section 6).

### 3.4 Discussion of results by brain regions

#### 3.4.1 Cerebral cortex

The cerebral cortex is the largest region in the coarsest version of the ARA. It is also the one from which the largest number of cell types were dissected (see the subsection on 'Basic cell groups and regions' for a separate discussion of some cell-type-specific samples dissected from the cerebral cortex, and the subsection on olfactory areas for a separate discussion of indices  $t = 48$  and  $t = 53$ , that were dissected from the amygdala). This subsection discusses a group of 28 cortical cell types which contains both (1) samples that have striking cortical profiles  $\rho_t$  in the model and good stability properties under sub-sampling and (2) samples that have very sparse and 'amorphous' profiles  $\rho_t$  in the model and bad stability properties.

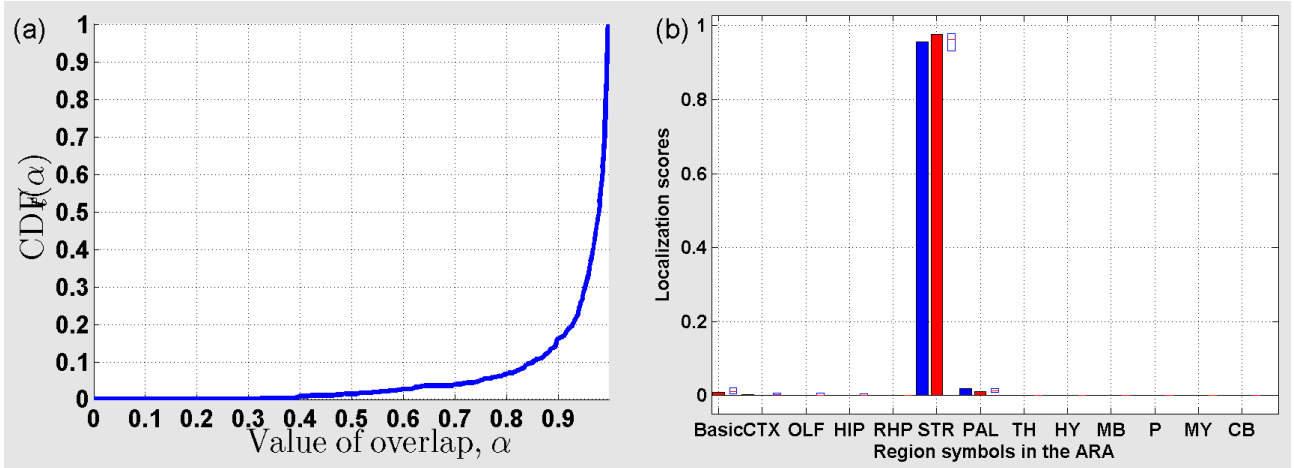


Figure 12: **Cumulative distribution function of overlaps and distribution of localization scores for medium spiny neurons,  $t = 16$ .** (a) The function  $CDF_t$  for  $t = 16$ . (b) Localization scores in the 'Big12' annotation. The top region of the density is the striatum both in the original model and in the average sub-sampled density. Moreover, the localization score in the striatum is larger than 90% in 75% of the samples. All other regions score less than 5% on average.

A more detailed composition of these groups is as follows:

1. A set of cortical pyramidal neurons, some which with striking cortical patterns ( $t = 40$ , Pyramidal Neurons, Callosally projecting, P14, are ranked first by average overlap with the model ( $r_1^{signal} = 40$ ), and 85% of the sub-sampled profiles have at least 90 % overlap with the model, followed by  $t = 46$  and  $t = 47$  in the top ten cell types by average overlap), and also some GABAergic interneurons whose density profiles is mostly subcortical, and distributed among many brain regions.
2. A set of cell types that have very sparse profiles, and tend to have less sparse profiles in the sub-samples. For some cell types such as the mixed neurons (index  $t = 9$ ), the average sub-sample is much more credible as it returns a cortical pattern rather than an isolated voxel (the ranking is of course very low,  $r_{61}^{signal} = 9$ ). The low ranking of some cell-type-specific transcriptomes that come from non-adult animals could correspond to the fact that these cell types mature early and therefore fit poorly to the entire atlas. This developmental effect may differ from gene to gene, and when subsets of genes are taken into account, they can happen to offer a better fit to the cortex, hence a cortical contribution to  $\bar{\rho}_t$ . However, this lack of conservation of anatomical properties under sub-sampling is not a sure way to detect non-adult transcriptomes, as the pyramidal neurons at the top of the overlap distribution correspond to P14.

Rank	Cell type	Index $t$	Overlap $\bar{I}(t)$ (%)
1	Pyramidal Neurons, Callosally projecting, P14	40	94.1
4	Pyramidal Neurons	46	84.5
6	GABAergic Interneurons, PV+	64	80.7
10	Pyramidal Neurons	47	76.2
12	Pyramidal Neurons	7	67.3
15	Pyramidal Neurons, Corticotectal, P14	44	66
17	Pyramidal Neurons	45	64.8
21	GABAergic Interneurons, SST+	56	55.6
24	Pyramidal Neurons	6	53.6
28	Astrocytes	30	32.7
32	GABAergic Interneurons, VIP+	55	25.5
33	GABAergic Interneurons, VIP+	54	25.3
36	Pyramidal Neurons, Corticospinal, P14	43	18.8
37	Oligodendrocyte Precursors	37	17.4
38	Pyramidal Neurons, Callosally projecting, P3	38	16.7
41	Pyramidal Neurons	8	10.7
42	Pyramidal Neurons	50	9.4
44	GABAergic Interneurons, PV+, P7	60	8.5
45	Mixed Neurons	33	8
47	GABAergic Interneurons, PV+, P25	63	7.3
48	Pyramidal Neurons, Callosally projecting, P6	39	7.1
51	Pyramidal Neurons, Corticospinal, P6	42	3.4
52	GABAergic Interneurons, PV+	58	1.8
53	GABAergic Interneurons, PV+, P10	61	1.5
54	Pyramidal Neurons	3	1
55	Pyramidal Neurons	2	0.6
56	Pyramidal Neurons, Corticospinal, P3	41	0.3
57	Neurons	26	0.2
58	GABAergic Interneurons, PV+, P13-P15	62	0.1
59	Interneurons	14	0.1
61	Mixed Neurons	9	0
64	Mixed Oligodendrocytes	24	0

Table 1: **Table of cell types extracted from the cortex, ranked by average overlap.** The cell types whose profile is localized mostly in the 'Basic cell groups and regions' of the ARA are included in Table 3. The index called "rank" (first column), at a fixed value of  $t$  (third column), denotes the integer  $k$  such that  $r_k^{signal} = t$ .

### 3.4.2 Olfactory areas

There is no cell-type-specific transcriptome labeled to have been dissected from olfactory areas in Tables 4 and 5, but two (pyramidal neurons labeled  $t = 48$ , and glutamatergic neurons,  $t = 53$ ) were extracted from the amygdala, and the amygdala is split between the cortex and the olfactory areas in the finer versions of the ARA. Visual inspection of Figures 111 and 121 shows rather striking contrast between the amygdala and the rest of the brain (especially in pyramidal neurons).

However the two cell types are only ranked 19 th and 20th out of 64 ( $r_{19}^{signal} = 48$  and  $r_{20}^{signal} = 53$ ), but the procedure is more sensitive to the support of  $\rho_t$  than to the contrast inside this support (see Figs. 191 and 196 in section 7 for thresholded heat maps of  $\rho_{48}$  and  $\rho_{53}$  at 99% of conditional probability of detecting cell types  $t = 48$  and  $t = 53$ ; they both show distinct amygdalar sets of voxels). With  $t = 48$ , we are clearly in a case where a small set of voxels inside the support of  $\rho_t$  concentrates a large fraction of the signal. In the average sub-samples profiles  $\bar{\rho}_{48}$  and  $\bar{\rho}_{53}$ , the support is more extended across the brain (for instance there are more hippocampal voxels with non-zero signal in  $\bar{\rho}_{53}$  than in  $\rho_{53}$ , and they make up for about 3 % of the signal in  $\bar{\rho}_{53}$ ), but the same set of voxels shows high contrast. The olfactory areas are the top region by localization score both in  $\bar{\rho}_{53}$  and  $\rho_{53}$  at about 60% and 54% respectively, followed by the cerebral cortex at 30 % and 33 % respectively; inspection of Figs. 120 121 illustrates the fact that in both the original and sub-sampled profiles, these scores come largely from voxels in the amygdala.

### 3.4.3 Hippocampus

The transcriptome of hippocampal pyramidal neurons labeled  $t = 49$  is one of the cell types for which the density  $\rho_t$  provides the most spectacular guess of the anatomical origin (with more than 85% of the signal in the hippocampal or retrohippocampal regions of the ARA). These localization scores are even a few percentage points higher for  $\bar{\rho}_{49}$ , and 75 % of the sub-samples have more than 80% overlap with  $\rho_{49}$ . Moreover, the ranking by average overlap is 9 out of 64 ( $r_9^{signal} = 49$ ).

Perhaps more surprisingly, the other cell-type-specific transcriptome extracted from the hippocampus (GABAergic neurons, SST+  $t = 57$ ), which on the contrary has low localization score in the hippocampus, ranks similarly high ( $r_8^{signal} = 57$ ), and the rather complex sub-cortical pattern of localization scores is rather well-conserved (see Figs. 128 and 129). Looking at the results of  $T = 64$  confirms that there is stronger solidarity between densities of GABAergic interneurons than between any of them and the particular region from which they were dissected.

### 3.4.4 Striatum

The sample of medium spiny neurons labeled  $t = 16$  ranks second according to  $r^{signal}$ , and indeed the density profiles  $\rho_{16}$  and  $\bar{\rho}_{16}$  look very similar, with 97 and 98% of the signal in the striatum respectively (see Figs. 46 and 47). Moreover, 83% of the samples have an overlap of more than 90% with  $\rho_{16}$ .

Interestingly, the other sample of medium spiny neurons in the fitting panel ( $t = 15$ ), ranks only 39 out of 64. Looking at Figs. 44 and 45) shows that  $\bar{\rho}_{15}$  is much more localized in the striatum than the prediction  $\rho_{15}$  (about 67% of the signal is in the striatum, compared to about 13 % for  $\rho_{15}$ , which makes for a correct prediction of the anatomical origin of the sample (as was the case for  $\rho_{16}$  and  $\bar{\rho}_{16}$ ). We showed in [1] that the densities  $\rho_{15}$  and  $\rho_{16}$  are anti-correlated at each voxel, in the sense that  $C_{15}$  and  $C_{16}$ , being very close to each other in gene space, compete for the same signal. Refitting the whole model (using the full set of genes), but just one of the two medium spiny neurons present in the fitting panel, lead to densities of medium spiny neurons that are close to  $\rho_{16} + \rho_{15}$ . Here we kept all samples but refitted the models repeatedly to various sub-samples of the atlas, and therefore gave the two samples more chances to compete for the signal, hence a fuller profile for  $\bar{\rho}_{15}$  than for  $\rho_{15}$ . The sub-sampling procedure is therefore a useful complement to the full model, as it reveals a source of uncertainty in the predictions (high similarities between transcriptomes lead to negative correlations between results): having  $\rho_{15}$  and  $\bar{\rho}_{15}$  yields an error bar on  $\rho_{15}$  at each voxel.

As for the cholinergic neurons  $t = 13$  extracted from the striatum, they are ranked  $r_1^{signal} 3 = 25$ , and the average profile is more localized in the medulla, and less in the pallidum, than the prediction  $\rho_{13}$ . Just as the one of  $\rho_{13}$ , the spatial profile  $\bar{\rho}_{13}$  is quite complex, spread over several brain regions, of which the striatum is far from being the most important.

### 3.4.5 Pallidum

Only one cell type (cholinergic projection neurons,  $t = 11$ ), was dissected from the pallidum. Its predicted profile  $\rho_{11}$  is almost identically zero, and the c.d.f. of overlaps with sub-sampled profiles therefore jumps quickly to 1, but the results in individual sub-samples are highly sparse and unstable, resulting in the (less sparse but still hardly conclusive) profile  $\bar{\rho}_{11}$ , see Figs. 36 and 37).

### 3.4.6 Thalamus

Only one cell type (cholinergic projection neurons, PV+,  $t = 59$ ), was dissected from the thalamus (which region visibly begs for other cell types in the panel, some of which that would probably be close in gene space to the Purkinje cells ( $t = 52$ , see the first section and the discussion of the sub-sampling results in the cerebellum). The thalamus is not the top region by density in  $\rho_{59}$ , as it is ranked below midbrain. The larger contribution of the dorsal midbrain is also observed in the average sub-sampled profile  $\bar{\rho}_{59}$ . About 60% of the sub-samples have an overlap of at least 70% with  $\rho_{59}$ .

### 3.4.7 Midbrain

The A9 and A10 dopaminergic neurons (indices  $t = 4$  and  $t = 5$ ), have a better visual contrast between ventral midbrain and its neighborhood in the average sub-samples  $\bar{\rho}_4$  and  $\bar{\rho}_5$  than in  $\rho_4$  and  $\rho_5$  (this pair of transcriptome profiles has a high similarity in gene space, just as the pair of medium spiny neurons, hence the better anatomical properties of the average sub-sample, which gives the profiles  $C_4$  and  $C_5$  more opportunities to compete for signal).

The midbrain cholinergic neurons  $t = 10$  are ranked 13 out of 64 (60% of the sub-samples have an overlap of at least 70% with the original profile  $\rho_{10}$ ). The signal is more contrasted and more concentrated in the medulla than in the midbrain in  $\bar{\rho}_{10}$ , but in both cases pons, midbrain and medulla concentrate more than 90 % of the signal. Interestingly  $\bar{\rho}_{10}$  could be visually mistaken for  $\bar{\rho}_{12}$ . However, the two profiles differ by the component in midbrain, which is proper to  $\bar{\rho}_{10}$ . As both transcriptomes  $t = 10$  and  $t = 12$  correspond to cholinergic neurons, with  $t = 10$  extracted from the midbrain and  $\rho_{12}$  from the medulla, this similarity is consistent with prior biological knowledge.

### 3.4.8 Medulla

Only one cell type in our data set can be assigned to this brain region, as it was dissected from the brain stem (Motor Neurons, Cholinergic Interneurons,  $t = 12$  ). The corresponding profile  $\rho_{12}$  returns indeed the medulla as the best guess for the anatomical origin of the sample (more than 65 % of the signal is in the medulla, and 30 % in the neighboring pons). These scores are conserved within 2% in the average profile  $\bar{\rho}_{12}$  (see Fig. 38b, and the coronal sections through the top-region by density in Fig. 39a,b,c, which all cut through the medulla), and this cell type is ranked 7th out of 64 samples ( $r_7^{signal} = 12$ ) for the average overlap between sub-samples and the model, and 75% of the sub-samples (resp. 48%) have at least an overlap of at least 80% (resp. 90%) between the model and the average sub-sample (see Fig. 38a).

Moreover, the contrast between groups of voxels inside the medulla is stronger in the average sub-sample than in the original model, but singles out the same set of voxels, with three connected components in the left hemisphere.

### 3.4.9 Cerebellum

The cerebellar cell types are ranked as follows by  $r^{signal}$ :

- rank 3, Purkinje cells,  $t = 1$ ,
- rank 11, granule cells,  $t = 20$ ,
- rank 14, astroglia,  $t = 28$ , pattern close to the white-matter pattern (see the next subsection),
- rank 23, mature oligodendrocytes,  $t = 21$ ,
- rank 27, Purkinje cells,  $t = 52$ , in which case  $\bar{\rho}_{52}$  has more signal in the cerebellum than in the thalamus, hence a correct prediction of the cerebellum as the origin of the sample,
- rank 31, stellate basket cells,  $t = 19$ , in which more of the signal is localized in the cerebellum

Rank	Cell type	Index $t$	Overlap $\bar{\mathcal{I}}(t)$ (%)
3	Purkinje Cells	1	91
11	Granule Cells	20	73.1
23	Mature Oligodendrocytes	21	53.6
27	Purkinje Cells	52	33.1
31	Stellate Basket Cells	19	25.9
34	Golgi Cells	17	24.6
43	Unipolar Brush cells (some Bergman Glia)	18	9.1
49	Bergman Glia	27	3.8
60	Purkinje Cells	25	0
63	Mixed Oligodendrocytes	23	0

Table 2: **Table of cell types extracted from the cerebellum, ranked by average overlap with the predicted profiles.** The cell types whose profile is localized mostly in the 'Basic cell groups and regions' of the ARA are included in Table 3. The index called "rank" (first column), at a fixed value of  $t$  (third column), denotes the integer  $k$  such that  $r_k^{signal} = t$ .

in the average sub-sample than in the original density,

- rank 34, Golgi cells,  $t = 17$ , where the medulla is the top region both in the average sub-sample than in the original density,
- rank 43, unipolar brush cells (some Bergman glia),  $t = 18$ ,
- rank 49, Bergman glia,  $t = 27$ , where the cerebellum is the top region by density in the average sub-sample  $\bar{\rho}_{27}$ , and not in  $\rho_{27}$
- rank 60, Purkinje cells,  $t = 25$ , for which the very low rank is a consequence of the almost zero profile  $\rho_{25}$ , whereas the average profile  $\bar{\rho}_{25}$  has the cerebellum as its top region by density,
- rank 63, mixed oligodendrocytes,  $t = 23$ , where the original profile  $\rho_{63}$  is zero and the average sub-sample rather amorphous.

### 3.4.10 "Basic cell groups and regions"

The set of voxels labeled "Basic cell groups of regions" in the ARA contains subcortical white matter and the *arbor vitae*, and several cell types labeled as astrocytes and dissected from other regions of the brain, in particular the cerebral cortex (see Tables 4 and 5), can be expected to be typical of white matter, and indeed a pattern coinciding with basic cell groups and regions (and containing the *arbor vitae*), was noticed to appear for a number of cell types (see Table 3). This pattern survives to a certain extent in the average sub-sampled profiles, which can be illustrated graphically by plotting the sum of the profiles for which "Basic cell groups and regions" is the top region by density for in the original model, namely the cell types labeled  $t \in \mathcal{T}_{basic}$  defined by:

$$t \in \mathcal{T}_{basic} \text{ iff } \operatorname{argmax}_{\omega \in \text{ARA}} (\lambda_{\omega}(\rho_t)) = \text{'Basic cell groups'} \quad (38)$$

Rank	Cell type	Index $t$	Overlap $\bar{\mathcal{I}}(t)$ (%)
14	Astroglia	28	67.2
18	Mature Oligodendrocytes	35	63.5
22	Astrocytes	31	54.8
26	Mature Oligodendrocytes	22	44
35	Mixed Neurons	34	23.6
40	Astrocytes	32	13.3
46	Oligodendrocytes	36	7.2
50	Astroglia	29	3.6

Table 3: **Table of cell types for which the top region in the predicted profile  $\rho$  is 'Basic cell groups and regions' in the ARA (they are defined by Eq. 38).** They are extracted either from the cortex or the cerebellum. The index called "rank" (first column), at a fixed value of  $t$  (third column), denotes the integer  $k$  such that  $r_k^{signal} = t$ .

where  $\lambda_\omega(\rho_t)$  is the localization score of  $\rho_t$  in the brain region  $\omega$ :

$$\lambda_\omega(\rho_t) = \frac{\sum_{v \in \omega} \rho_t(v)^2}{\sum_{v \in \text{Brain Annotation}} \rho_t(v)^2}. \quad (39)$$

It can be observed on Fig. 13 that the white-matter pattern of 'Basic cell groups' is still recognizable in the sum of average sub-sampled density profiles plotted in part (b) of the figure, which is almost entirely supported by the support of the original model. Moreover, the contrast between voxels in 'Basic cell groups' is less pronounced in the average sub-sampled profile than in the original model (the intensity in the *arbor vitae* is closer to the intensity in the more frontal component).

### 3.5 Repeated sub-sampling of gene space (II): random splitting of the data set in two equal parts

So far we have obtained a ranking of cell types based on random sub-sampling that provided error estimates from the loss of 90 % of data, which proportion we chose to replicate the scaling of our data set with respect to the full genome of the mouse. An alternative, more symmetric sub-sampling procedure is the following: repeated splitting of the data set into two sets of genes of equal sizes, followed by refitting of the model in each of the resulting sub-samples, allows to study the probability of detecting a cell type at each voxel (conditional on the detection of it from the symmetric sub-sample).

The following pseudo-code helps establish notations:

```

for j in [1..J]
draw a random permutation  $\sigma$  of [1..G] (without replacing);
construct the following matrices extracted from the Allen Atlas and cell-type-specific

```

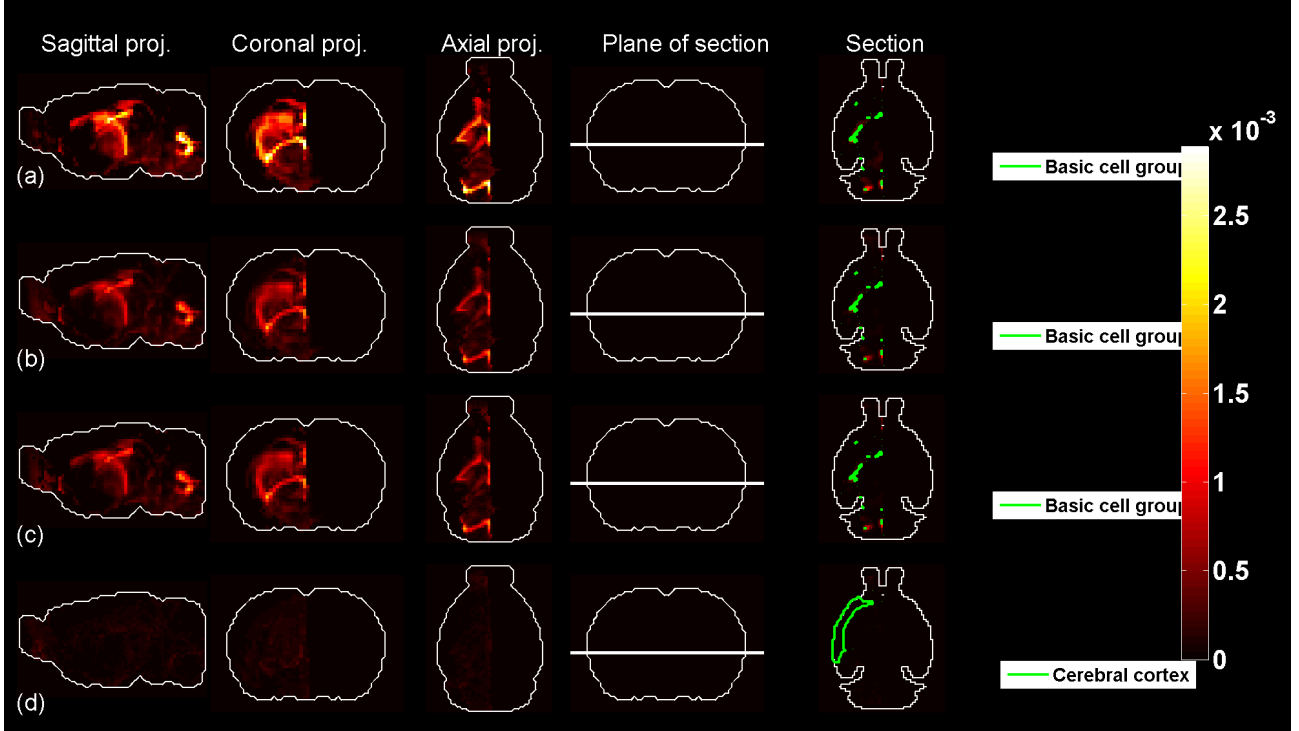


Figure 13: **The sum of density profiles (labeled  $t \in \mathcal{T}_{basic}$  of the cell types listed in Table 3).** (a) The sum of profiles in the original model,  $\rho_{basic} = \sum_{t \in \mathcal{T}_{basic}} \rho_t$ . (b) The sum of average sub-sampled profiles,  $\bar{\rho}_{basic} = \sum_{t \in \mathcal{T}_{basic}} \bar{\rho}_t$ . (c) The part of  $\bar{\rho}_{basic}$  in the voxels supporting  $\rho_{basic}$ , or  $\bar{\rho}_{basic}^{supported}(v) = \sum_{t \in \mathcal{T}_{basic}} \bar{\rho}_t(v) \mathbf{1}(\rho_{basic}(v) > 0)$ . (d) The difference  $\bar{\rho}_{basic} - \bar{\rho}_{basic}^{supported}$ .

transcriptomes:

fit the model to the two sets of genes  $\{g_{\sigma_1}, \dots, g_{\sigma_{[G/2]}}\}$  and  $\{g_{\sigma_{[G/2]+1}}, \dots, g_{\sigma_G}\}$ :

$$E^{(j,1)} = (E(v, g_{\sigma_i})_{1 \leq v \leq V, 1 \leq i \leq [G/2]}, E^{(j,2)} = (E(v, g_{\sigma_i})_{1 \leq v \leq V, [G/2]+1 \leq i \leq G}, \quad (40)$$

$$C^{(j,1)} = (C(t, g_{\sigma_i})_{1 \leq t \leq T, 1 \leq i \leq [G/2]}, C^{(j,2)} = (C(t, g_{\sigma_i})_{1 \leq t \leq T, [G/2]+1 \leq i \leq G}, \quad (41)$$

fit the model to these two data sets

$$(\rho_t^{(j,1)}(v))_{1 \leq t \leq T} = \operatorname{argmin}_{\phi \in \mathbf{R}_+^T} \left( E^{(j,1)}(v, \cdot) - \sum_t \phi_t C^{(j,1)}(t, \cdot) \right). \quad (42)$$

$$(\rho_t^{(j,2)}(v))_{1 \leq t \leq T} = \operatorname{argmin}_{\phi \in \mathbf{R}_+^T} \left( E^{(j,2)}(v, \cdot) - \sum_t \phi_t C^{(j,2)}(t, \cdot) \right). \quad (43)$$

end

This approach has one less parameter than the sub-sampling procedure described above, and the fact that the sub-samples all have the same size (and come in pairs), invites us to estimate stability properties of the results in terms of conditional probabilities. For each voxel labeled  $v$  and each cell type labeled  $t$ , there are two random variables, namely  $\rho_t^{(j,1)}(v)$  and  $\rho_t^{(j,2)}(v)$ , corresponding to the random permutation of genes labeled  $j$ . The cell-type label  $t$  is detected at voxel  $v$  (an element of the set  $S$  in the terminology of [32], see Eq. 9) in sub-sample  $(j, 1)$  (resp.  $(j, 2)$ ) if  $\rho_t^{(j,1)}(v) > 0$  (resp.  $\rho_t^{(j,2)}(v) > 0$ ). We can compute the probability of cell type  $t$  being a detected at voxel  $v$  in a sub-sample  $(j, 1)$  conditional on the probability of it being detected in the complementary sub-sample  $(j, 2)$ :

$$\mathcal{P}_{12}(t, v) = \frac{|j \in [1..J], \rho_t^{(j,1)}(v) \rho_t^{(j,2)}(v) > 0|}{|j \in [1..J], \rho_t^{(j,2)}(v) > 0|} \quad (44)$$

$$\mathcal{P}_{21}(t, v) = \frac{|j \in [1..J], \rho_t^{(j,1)}(v) \rho_t^{(j,2)}(v) > 0|}{|j \in [1..J], \rho_t^{(j,1)}(v) > 0|} \quad (45)$$

If  $J$  equalled the total number of permutations of  $[1..G]$ , the two quantities  $\mathcal{P}_{12}$  and  $\mathcal{P}_{21}$  defined above would be equal for symmetry reasons, but for small values of  $J$  they will be different (but hopefully close), and we will evaluate both of them. For a fixed value of  $t$ , they can be plotted as brain-wide profiles (or hemisphere-wide profiles, as will be the case again for the sake of maximizing the number of samples in limited time, again assuming sufficient degree of left-right symmetry), in order to give a visual impression of the voxels at which the cell-type-specific transcriptome labeled  $t$  is a predicting variable. Again, the visual impression of these profiles should be close to the one of  $\rho_t$ . Moreover, the probabilistic nature of the entries of  $\mathcal{P}_{12}$  provides confidence intervals at each voxel for which  $\rho_t$  is strictly positive. Thresholding  $\mathcal{P}_{12}$  at a fixed threshold between 0 and 1 yields a mask that can be applied to  $\rho_t$  in order to keep only the signal that corresponds to predicting variables with probability larger than the threshold.

Going through the plots one by one, one notices that indeed the visual impression is conserved, and that there seems to be a positive correlation between the values of the conditional probabilities and the values of the density profiles in the original model (the thresholded profiles defined above tend to coincide with areas of strongest signal for the cell types that were distinguished for their striking density patterns). To test this idea, let us compute the correlation coefficients between conditional predictor densities and density profiles for each cell types:

$$\text{Corr}_{12}(t) = \text{corr}(\rho_t, \mathcal{P}_{12}(t, \cdot)), \quad \text{Corr}_{21}(t) = \text{corr}(\rho_t, \mathcal{P}_{21}(t, \cdot)) \quad (46)$$

The values are quite large indeed for most cell types (see Fig. ??). This suggests a thresholding procedure of voxels for each cell type based on the conditional probabilities and a chosen threshold  $\eta$  on conditional probabilities:

$$\rho_t^{\text{thresh}, \eta}(v) = \rho_t(v) \mathbf{1}(\min(P_{12}(t, v), P_{21}(t, v)) \geq \eta) \quad (47)$$

For graphical presentation in the figures of section 7, where the threshold  $\eta = 99\%$  and  $\eta = 75\%$  are used.

## 4 Numerical experiments with noise added

### 4.1 Simulation scenario

Having obtained estimates  $\bar{\mathcal{I}}(t)$  for the agreement between the estimated profiles and the average result from repeated sub-sampling, we noticed that these estimates vary across cell types, and tend to be lower for transcriptome profiles that have very low density in the original model. We mentioned that taking 10 percent of the genes in the coronal atlas in each sub-sample probably results in a more severe loss of CNS-specific genes than the one that is incurred by only taking into account the  $G = 2,131$  in the coronal atlas, because the coronal atlas was designed by prioritizing CNS-specific genes. However, we have not given a quantitative estimate of the severity of the sub-sampling in terms of loss of data.

In this section we estimate the impact of sub-sampling in terms of the corresponding intensity of a Gaussian noise added to cell-type-specific transcriptomes. To simulate the influence of noise, we mix the entries of the matrix  $C$  of cell-type-specific transcriptomes using a random mixing matrix denoted by  $M_\sigma$ , and impose a positivity constraint to avoid non-realistic negative entries (which are rare if the amplitude of the noise is small enough, but would penalize the corresponding cell types in the optimization):

$$M_\sigma(t, s) = \delta_{st} + \sigma \Xi(t, s), \quad (48)$$

where

$$\Xi \sim \mathcal{N}(0, 1) \quad (49)$$

and  $\sigma$  models the amplitude of the noise. The original fitting panel corresponds to the case where  $M$  is the identity matrix. Mixing transcriptome profiles together under the influence of

noise amounts to replacing the matrix  $C$  by a matrix  $C'_{M_\sigma}$  whose rows consist of linear combinations of the original transcriptomes:

$$C'_{M_\sigma}(t, g) = \max \left( \sum_{s=1}^T M_\sigma(t, s) C(s, g), 0 \right). \quad (50)$$

We refitted the models at growing values of the noise parameter  $\sigma$ , and found, not surprisingly, that the overlap with the results of the original model is a decreasing function of  $\sigma$ . There is a regime of noise around  $\sigma = 0.05$ , which gives rise to overlap values in the same range (with some transcriptomes close to zero while others are still close to 90%) as the average sub-sample exposed in the previous section. More precisely, we repeatedly drew random "mixing matrices" from the ensemble described by Eq. 48, for  $\sigma = 0.05$ :

$$m_1, \dots, m_U \in \mathbf{R}(T, T), \text{ i.i.d.}, m_i \sim M_\sigma, \sigma = 0.05. \quad (51)$$

A heat map of one of these mixing matrices is shown in Fig. 14.

Again we can summarize the simulations by a pseudocode:

for  $i$  in [ 1..U ]

1. draw a  $T$ -by- $T$  random matrix  $\Xi_i$  with independent, normally distributed entries;

2. compute the mixing matrix  $m_i = \mathbf{I}_T + \sigma \Xi_i$  and the matrix  $C'_{m_i}$

3. compute  $(\rho_t^{(i, noised)}(v))_{1 \leq t \leq T}$  at each voxel:

$$(\rho_t^{(i, noised)}(v))_{1 \leq t \leq T} = \operatorname{argmin}_{\phi \in \mathbf{R}_+^T} (\|E(v, \cdot) - \sum_t C'_{m_i}(t, \cdot) \phi(t)\|^2).$$

end

## 4.2 Results

We fitted the model for each of the corresponding matrices  $C'_{m_i}$ , using the entire data set of  $G$  genes:

$$(\rho_t^{(i, noised)}(v))_{1 \leq t \leq T} = \operatorname{argmin}_{\nu \in \mathbf{R}_+^T} \left( \left\| \sum_{g=1}^G (E(v, g) - \sum_{t=1}^T C'_{m_i}(t, g) \nu(t)) \right\|^2 \right), \quad (52)$$

hence a family of  $U$  random densities of  $T$  cell types, for which one can compute the overlap with the results  $\rho_t$  of the original model, as we did from the random densities computed by sub-sampling the atlas (by substituting  $\rho_t^{i, noised}$  to  $\rho_t^{(s)}$  in 24.

We computed the average cell-type-specific profiles noises as follows:

$$\bar{\rho}_t^{noised}(v) = \frac{1}{U} \sum_{i=1}^U (\rho_t^{i, noised}(v))_{1 \leq t \leq T}. \quad (53)$$

The overlap between  $\bar{\rho}_t^{noised}$  and  $\rho_t$  can be computed for all indices  $t$ :

$$\bar{I}^{noised}(i, t) := \frac{1}{\sum_v \bar{\rho}_t^{(i, noised)}(v)} \sum_v \mathbf{1}(\rho_t(v) > 0) \bar{\rho}_t^{(i, noised)}(v). \quad (54)$$

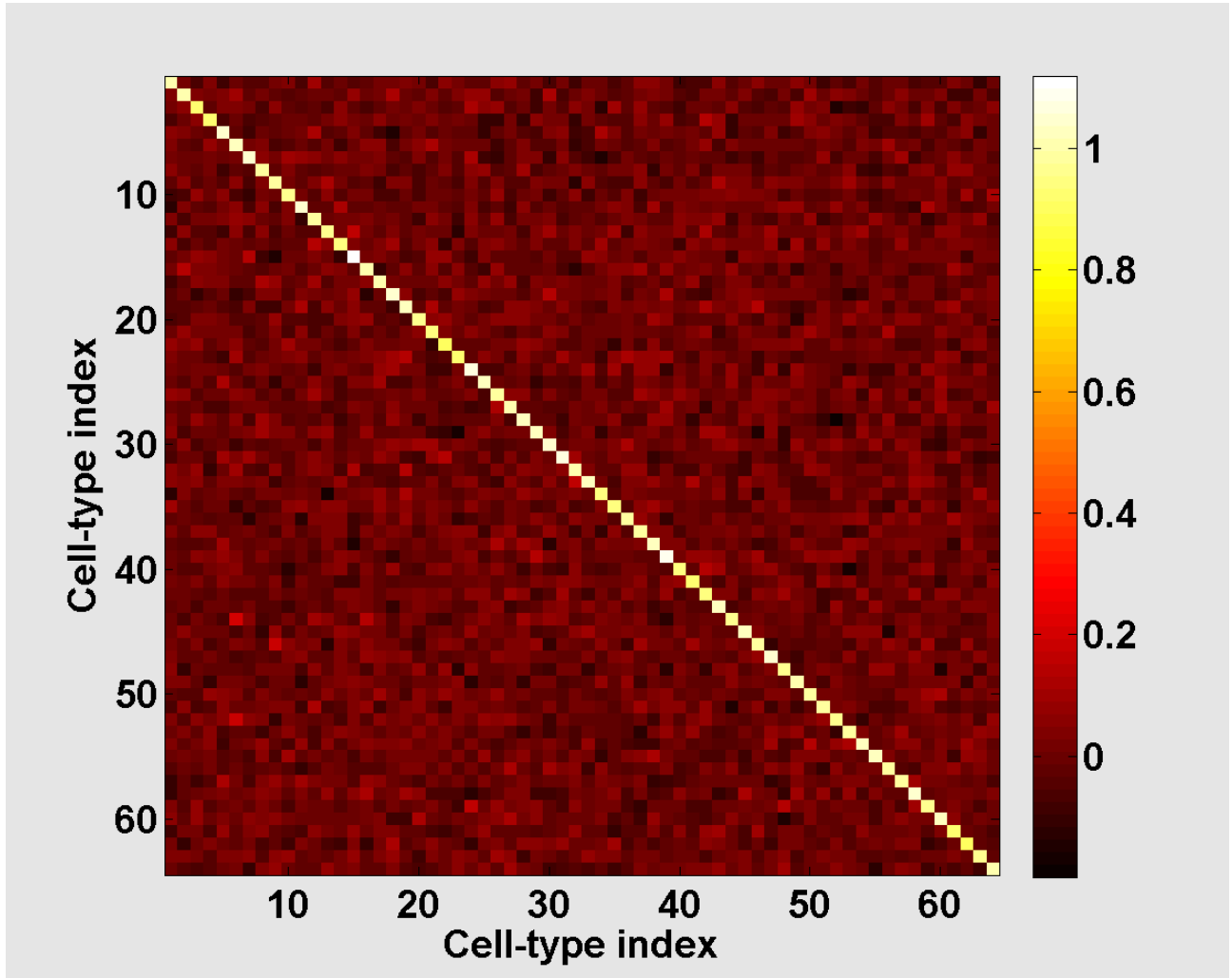


Figure 14: **Heat map of a mixture matrix between cell types.** It is the sum of the identity matrix of size  $T$ , and of a Gaussian noise component, as described by Eq. 48, at  $\sigma = 0.05$ . A perfectly diagonal mixture matrix would correspond to the absence of noise (no mixing between cell types). The color map shows that the mixture matrix is still close to the identity.

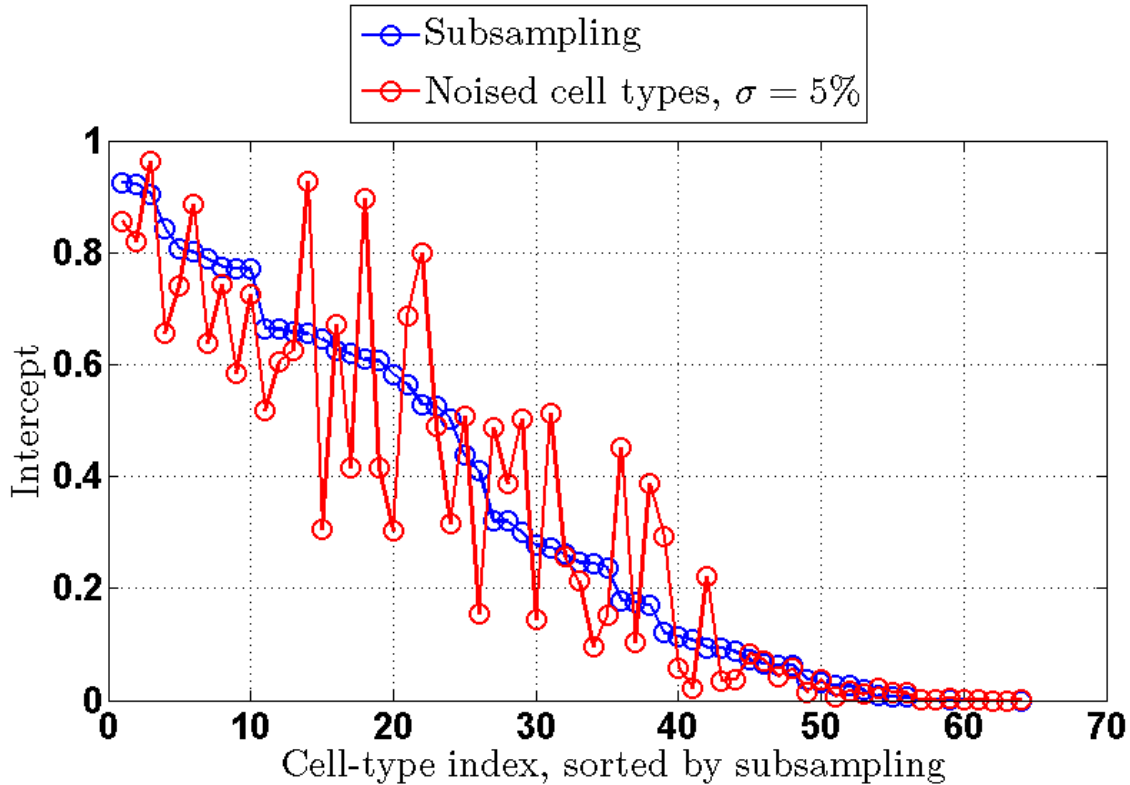


Figure 15: **Overlaps with average sub-sampled densities (with 200 genes per sub-sample), and with average densities estimated from random mixings, with  $\sigma = 5\%$ .** The cell types at the low end of the distribution are the same for both quantities.

These quantities take values in the interval  $[0,1]$ , and a new ranking of cell-type-specific transcriptome is induced by sorting them in decreasing order. Is this ranking compatible with the one induced by the sub-sampling procedure? To look into this graphically, we plotted the values of the average noised overlap  $\bar{\mathcal{I}}^{noised} = \sum_{i=1}^U \bar{\mathcal{I}}^{noised}(i,t)/U$ , ordered according to the ranking of Eq. 26, on the same graph as the sorted overlaps with sub-sampled profiles (Fig. 15). Even though the ranking is not exactly the same as the one induced from sub-sampling, this numerical experiment illustrates the fact that a mixture of cell types deviating from the diagonal by Gaussian random matrices at  $\sigma = 5\%$  noise is empirically close to the result of sub-sampling to 10% of the atlas.

## 5 Tables: cell-type-specific transcriptomes

### 5.1 Description, labeling and anatomical origin of cell-type-specific transcriptomes

For each of the cell-type-specific samples analyzed in this note, the following two tables give a brief description of the cell type, the region from which the samples were extracted according to the coarsest version of the Allen Reference Atlas, and the finest region to which it can be assigned according to the data provided in the studies [17, 18, 19, 20, 21, 22, 23, 24]. The indices in the first columns of the tables are the ones referred to as  $t$ .

Index	Description	Region in the ARA ('big12')	Finest label in the ARA
1	Purkinje Cells	Cerebellum	Cerebellar cortex
2	Pyramidal Neurons	Cerebral cortex	Primary motor area; Layer 5
3	Pyramidal Neurons	Cerebral cortex	Primary somatosensory area; Layer 5
4	A9 Dopaminergic Neurons	Midbrain	Substantia nigra_ compact part
5	A10 Dopaminergic Neurons	Midbrain	Ventral tegmental area
6	Pyramidal Neurons	Cerebral cortex	Cerebral cortex; Layer 5
7	Pyramidal Neurons	Cerebral cortex	Cerebral cortex; Layer 5
8	Pyramidal Neurons	Cerebral cortex	Cerebral cortex; Layer 6
9	Mixed Neurons	Cerebral cortex	Cerebral cortex
10	Motor Neurons, Midbrain Cholinergic Neurons	Midbrain	Peduncolopontine nucleus
11	Cholinergic Projection Neurons	Pallidum	Pallidum_ ventral region
12	Motor Neurons, Cholinergic Interneurons	Medulla	Spinal cord
13	Cholinergic Neurons	Striatum	Striatum
14	Interneurons	Cerebral cortex	Cerebral cortex
15	Drd1+ Medium Spiny Neurons	Striatum	Striatum
16	Drd2+ Medium Spiny Neurons	Striatum	Striatum
17	Golgi Cells	Cerebellum	Cerebellar cortex
18	Unipolar Brush cells (some Bergman Glia)	Cerebellum	Cerebellar cortex
19	Stellate Basket Cells	Cerebellum	Cerebellar cortex
20	Granule Cells	Cerebellum	Cerebellar cortex
21	Mature Oligodendrocytes	Cerebellum	Cerebellar cortex
22	Mature Oligodendrocytes	Cerebral cortex	Cerebral cortex
23	Mixed Oligodendrocytes	Cerebellum	Cerebellar cortex
24	Mixed Oligodendrocytes	Cerebral cortex	Cerebral cortex
25	Purkinje Cells	Cerebellum	Cerebellar cortex
26	Neurons	Cerebral cortex	Cerebral cortex
27	Bergman Glia	Cerebellum	Cerebellar cortex
28	Astroglia	Cerebellum	Cerebellar cortex
29	Astroglia	Cerebral cortex	Cerebral cortex
30	Astrocytes	Cerebral cortex	Cerebral cortex
31	Astrocytes	Cerebral cortex	Cerebral cortex
32	Astrocytes	Cerebral cortex	Cerebral cortex
33	Mixed Neurons	Cerebral cortex	Cerebral cortex
34	Mixed Neurons	Cerebral cortex	Cerebral cortex
35	Mature Oligodendrocytes	Cerebral cortex	Cerebral cortex
36	Oligodendrocytes	Cerebral cortex	Cerebral cortex
37	Oligodendrocyte Precursors	Cerebral cortex	Cerebral cortex

Table 4: Anatomical origin of the cell-type-specific samples (I).

Index	Description	Region in the ARA ('big12')	Finest label in the ARA
38	Pyramidal Neurons, Callosally projecting, P3	Cerebral cortex	Cerebral cortex
39	Pyramidal Neurons, Callosally projecting, P6	Cerebral cortex	Cerebral cortex
40	Pyramidal Neurons, Callosally projecting, P14	Cerebral cortex	Cerebral cortex
41	Pyramidal Neurons, Corticospinal, P3	Cerebral cortex	Cerebral cortex
42	Pyramidal Neurons, Corticospinal, P6	Cerebral cortex	Cerebral cortex
43	Pyramidal Neurons, Corticospinal, P14	Cerebral cortex	Cerebral cortex
44	Pyramidal Neurons, Corticotectal, P14	Cerebral cortex	Cerebral cortex
45	Pyramidal Neurons	Cerebral cortex	Cerebral cortex, Layer 5
46	Pyramidal Neurons	Cerebral cortex	Cerebral cortex, Layer 5
47	Pyramidal Neurons	Cerebral cortex	Primary somatosensory area; Layer 5
48	Pyramidal Neurons	Cerebral cortex	Prelimbic area and Infralimbic area; Layer 5 (Amygdala)
49	Pyramidal Neurons	Hippocampal region	Ammon's Horn; Layer 6B
50	Pyramidal Neurons	Cerebral cortex	Primary motor area
51	Tyrosine Hydroxylase Expressing	Pons	Pontine central gray
52	Purkinje Cells	Cerebellum	Cerebellar cortex
53	Glutamatergic Neuron (not well defined)	Cerebral cortex	Cerebral cortex; Layer 6B (Amygdala)
54	GABAergic Interneurons, VIP+	Cerebral cortex	Prelimbic area and Infralimbic area
55	GABAergic Interneurons, VIP+	Cerebral cortex	Primary somatosensory area
56	GABAergic Interneurons, SST+	Cerebral cortex	Prelimbic area and Infralimbic area
57	GABAergic Interneurons, SST+	Hippocampal region	Ammon's Horn
58	GABAergic Interneurons, PV+	Cerebral cortex	Prelimbic area and Infralimbic area
59	GABAergic Interneurons, PV+	Thalamus	Dorsal part of the lateral geniculate complex
60	GABAergic Interneurons, PV+, P7	Cerebral cortex	Primary somatosensory area
61	GABAergic Interneurons, PV+, P10	Cerebral cortex	Primary somatosensory area
62	GABAergic Interneurons, PV+, P13-P15	Cerebral cortex	Primary somatosensory area
63	GABAergic Interneurons, PV+, P25	Cerebral cortex	Primary somatosensory area
64	GABAergic Interneurons, PV+	Cerebral cortex	Primary motor area

Table 5: Anatomical origin of the cell-type-specific samples (II).

## 5.2 Cell-type-specific trascryptomes, ordered by overlap between estimated density and average sub-sampled density

rank by signal	Cell type	Index $t$	Overlap $\bar{\mathcal{I}}(t)$ (%)	$p_{t,0.75}$ (%)	$\mathcal{I}_{thresh}(t, 0.75)$ (%)
1	Pyramidal Neurons, Callosally projecting, P14	40	94.8	98	98.8
2	Drd2+ Medium Spiny Neurons	16	94.5	94.9	99.4
3	Purkinje Cells	1	93.7	92.8	99.4
4	Pyramidal Neurons	46	84.1	81.6	96.7
5	Tyrosine Hydroxylase Expressing	51	87.5	84	97.3
6	GABAergic Interneurons, PV+	64	82.9	76.3	95.5
7	Motor Neurons, Cholinergic Interneurons	12	86.2	81.1	97.5
8	GABAergic Interneurons, SST+	57	80.3	70.4	93
9	Pyramidal Neurons	49	85.9	78.2	97.7
10	Pyramidal Neurons	47	82	68.2	95.1
11	Granule Cells	20	80.1	69.1	96.7
12	Pyramidal Neurons	7	69.5	38.3	79.5
13	Motor Neurons, Midbrain Cholinergic Neurons	10	70	48.4	83.8
14	Astroglia	28	70.5	56.5	90.2
15	Pyramidal Neurons, Corticotectal, P14	44	71.4	48.3	85.5
16	GABAergic Interneurons, PV+	59	70.7	48.4	84.2
17	Pyramidal Neurons	45	67.4	40.2	84.8
18	Mature Oligodendrocytes	35	71.8	50.7	87.5
19	Pyramidal Neurons	48	69.4	42.9	88.7
20	Glutamatergic Neuron (not well defined)	53	62.5	38	83.8
21	GABAergic Interneurons, SST+	56	60.5	28.2	76.8
22	Astrocytes	31	61.6	36.2	83
23	Mature Oligodendrocytes	21	59.2	27.6	77.3
24	Pyramidal Neurons	6	66	42.1	85.4
25	Cholinergic Neurons	13	49.6	16.3	67.2
26	Mature Oligodendrocytes	22	53.4	25.9	76.8
27	Purkinje Cells	52	39.7	6.5	52.3
28	Astrocytes	30	40.8	7.9	54.1
29	A10 Dopaminergic Neurons	5	40.5	9.6	59.8
30	A9 Dopaminergic Neurons	4	39.5	15.4	60.2
31	Stellate Basket Cells	19	33.2	3.2	43.4
32	GABAergic Interneurons, VIP+	55	34.1	13.6	55.9

Table 6: Ranking of cell types by overlap and agreement for top region (I).

rank by signal	Cell type	Index $t$	Overlap (%) $\bar{\mathcal{I}}(t)$	$p_{t,0.75}$ (%)	$\mathcal{I}_{thresh}(t, 0.75)$ (%)
33	GABAergic Interneurons, VIP+	54	28.7	2.7	40.2
34	Golgi Cells	17	27.7	5.1	39.5
35	Mixed Neurons	34	35	10.4	52.1
36	Pyramidal Neurons, Corticospinal, P14	43	28.1	4.3	37.7
37	Oligodendrocyte Precursors	37	24.7	1.7	34
38	Pyramidal Neurons, Callosally projecting, P3	38	22.4	1.9	35.9
39	Drd1+ Medium Spiny Neurons	15	19.3	1.4	27.9
40	Astrocytes	32	18.4	0.5	25.6
41	Pyramidal Neurons	8	13.6	3.2	17
42	Pyramidal Neurons	50	12.8	1.3	16
43	Unipolar Brush cells (some Bergman Glia)	18	11.6	0.4	16.8
44	GABAergic Interneurons, PV+, P7	60	12.8	1.5	20.3
45	Mixed Neurons	33	11.8	2.4	14.3
46	Oligodendrocytes	36	8.4	-0.2	12.3
47	GABAergic Interneurons, PV+, P25	63	12.7	0.4	15
48	Pyramidal Neurons, Callosally projecting, P6	39	13	1.5	17.4
49	Bergman Glia	27	6.6	0.5	6.8
50	Astroglia	29	6.4	0.7	6.4
51	Pyramidal Neurons, Corticospinal, P6	42	7.7	1.9	7.4
52	GABAergic Interneurons, PV+	58	3.1	0	2.9
53	GABAergic Interneurons, PV+, P10	61	3.4	0.2	1.2
54	Pyramidal Neurons	3	3	0	0.4
55	Pyramidal Neurons	2	1.4	0	0.2
56	Pyramidal Neurons, Corticospinal, P3	41	0.8	-0.2	0.2
57	Neurons	26	0.4	-0.2	0.2
58	GABAergic Interneurons, PV+, P13-P15	62	0.1	-0.2	0.2
59	Interneurons	14	0	-0.2	0.2
60	Purkinje Cells	25	0.2	0	0.2
61	Mixed Neurons	9	0.3	-0.2	0.2
62	Cholinergic Projection Neurons	11	0.1	-0.2	0.2
63	Mixed Oligodendrocytes	23	0	22.4	72.3
64	Mixed Oligodendrocytes	24	0	22.4	72.3

Table 7: Ranking of cell types by overlap and agreement for top region (II).

**6 Figures: predicted and sub-sampled profiles: statistics of overlaps and localization scores in the ARA, and visualization**

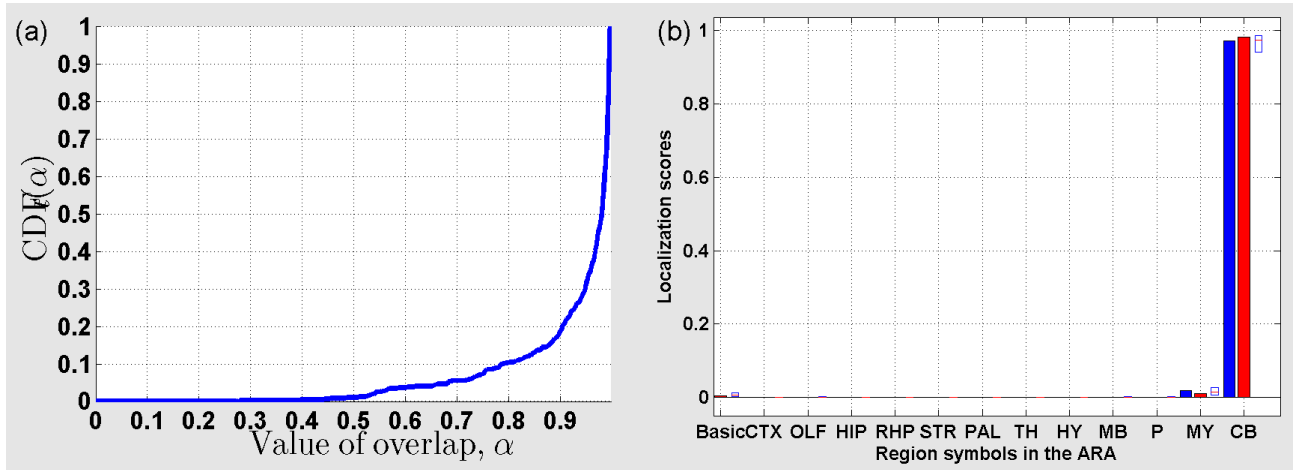


Figure 16: (a) Cumulative distribution function ( $CDF_t$ ) of the overlap between  $\rho_t$  and sub-sampled profiles for  $t = 1$ . (b) Localization scores in the coarsest version of the ARA for  $\rho_t$  (in blue), and  $\bar{\rho}_t$  (in red).

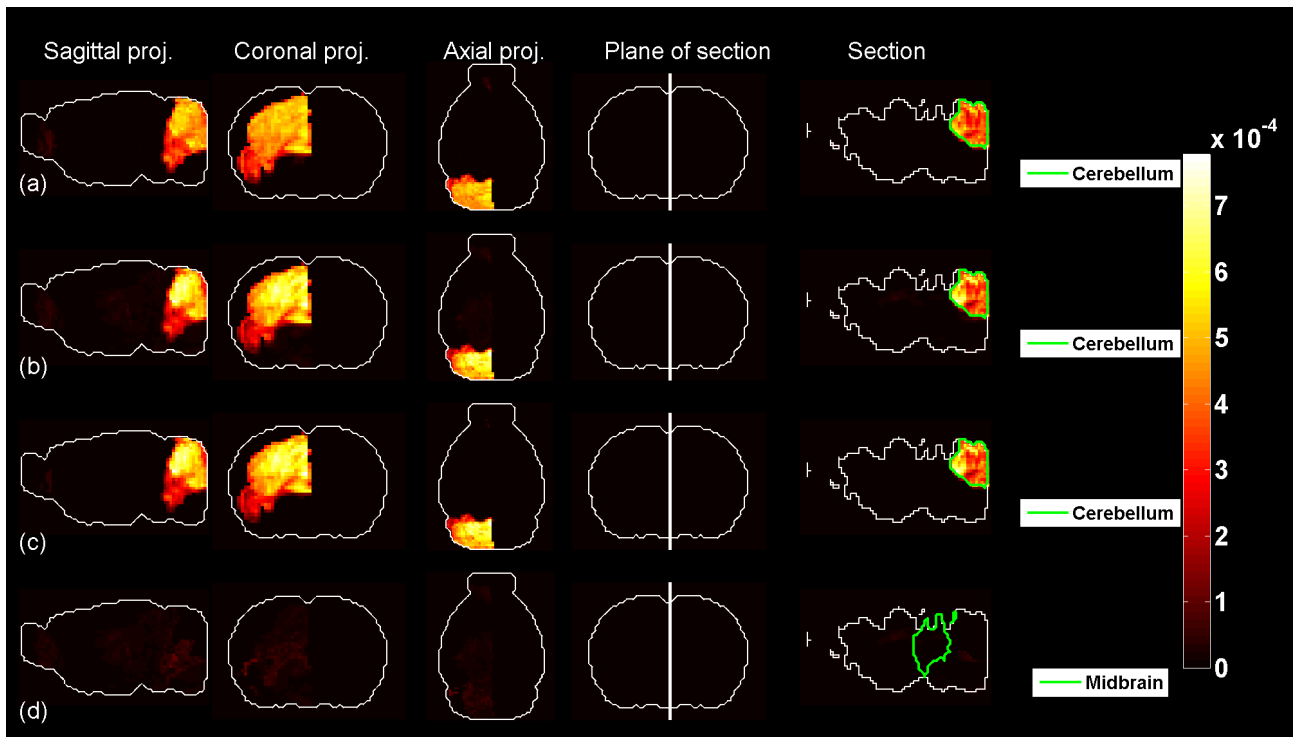


Figure 17: Predicted profile and average sub-sampled profile for  $t = 1$ .

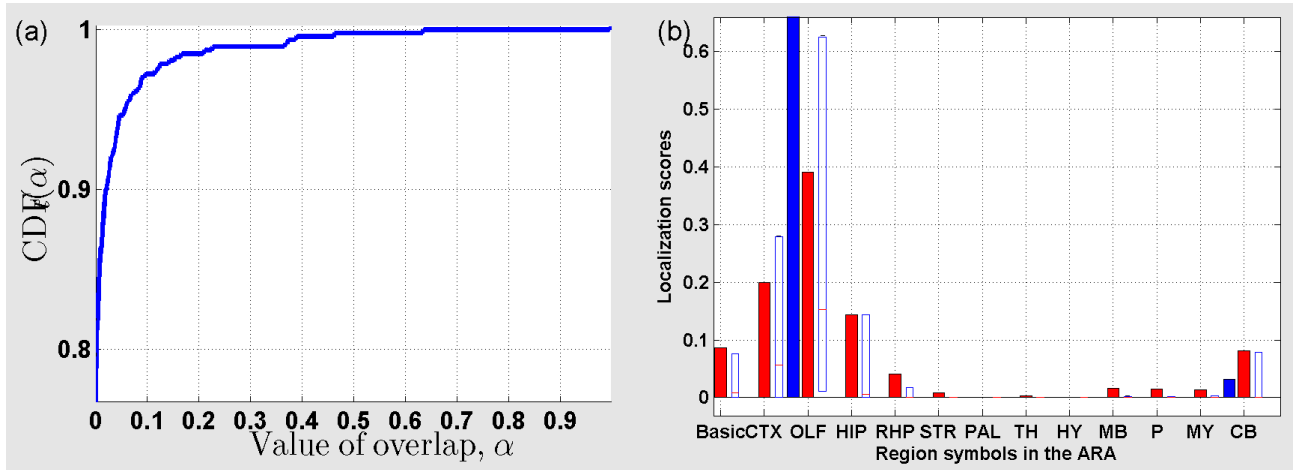


Figure 18: (a) Cumulative distribution function ( $CDF_t$ ) of the overlap between  $\rho_t$  and sub-sampled profiles for  $t = 2$ . (b) Localization scores in the coarsest version of the ARA for  $\rho_t$  (in blue), and  $\bar{\rho}_t$  (in red).

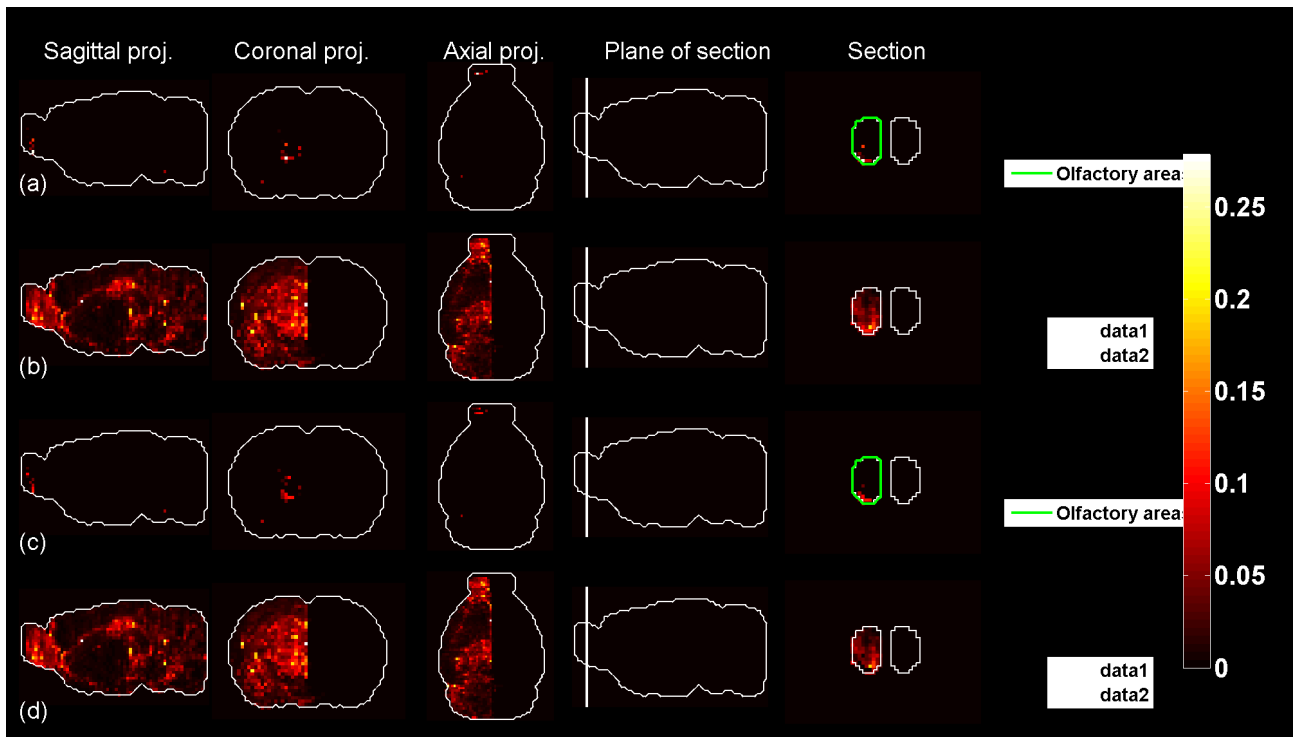


Figure 19: Predicted profile and average sub-sampled profile for  $t = 2$ .

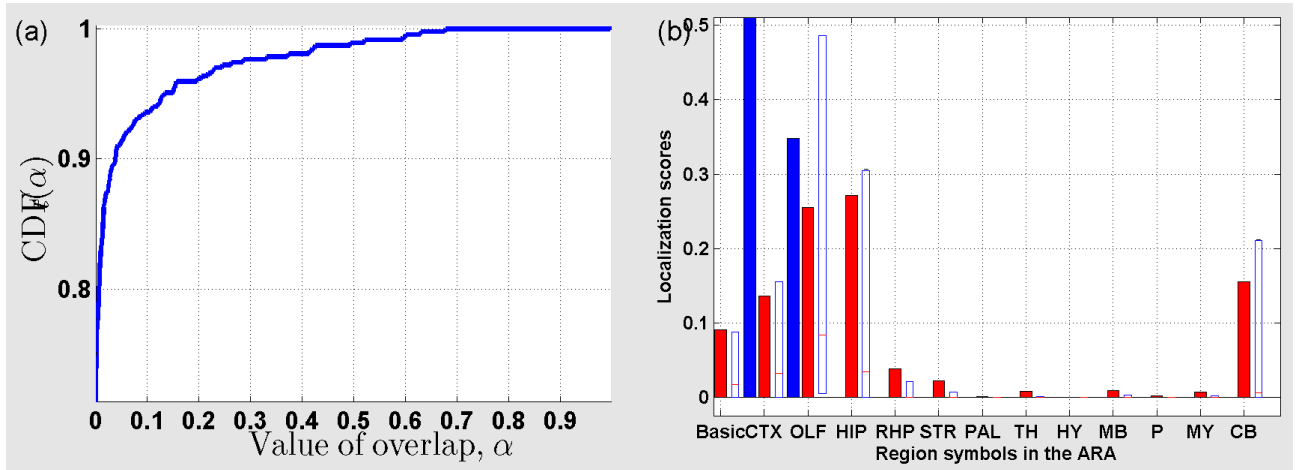


Figure 20: (a) Cumulative distribution function ( $CDF_t$ ) of the overlap between  $\rho_t$  and sub-sampled profiles for  $t = 3$ . (b) Localization scores in the coarsest version of the ARA for  $\rho_t$  (in blue), and  $\bar{\rho}_t$  (in red).

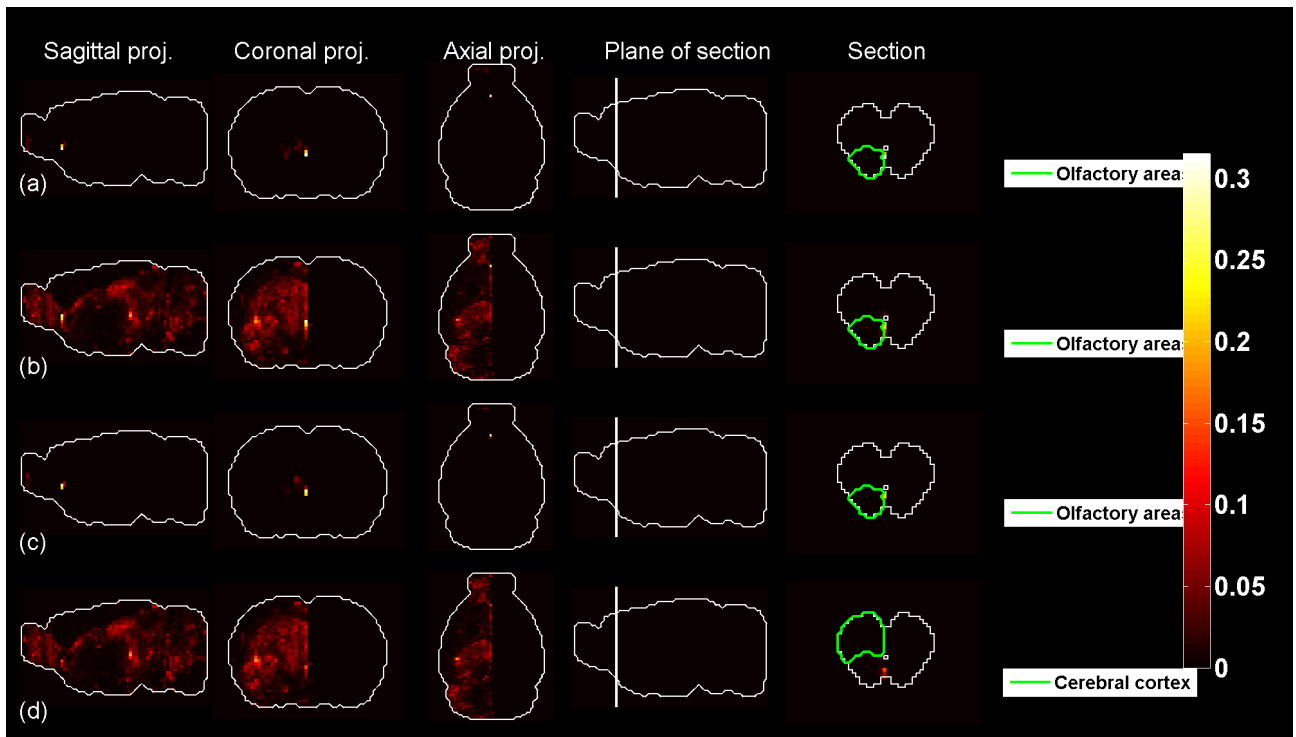


Figure 21: Predicted profile and average sub-sampled profile for  $t = 3$ .

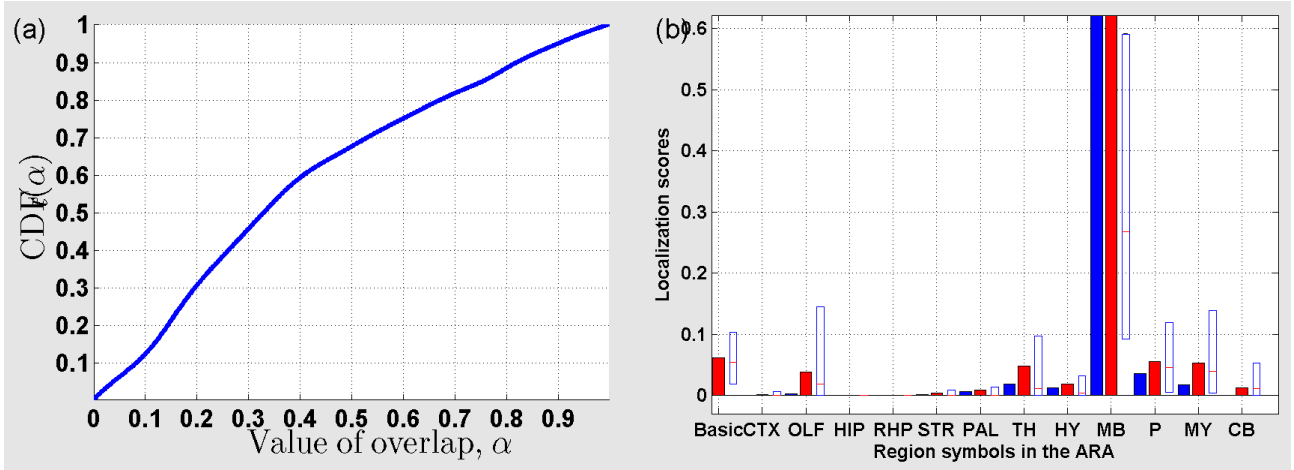


Figure 22: (a) Cumulative distribution function ( $CDF_t$ ) of the overlap between  $\rho_t$  and sub-sampled profiles for  $t = 4$ . (b) Localization scores in the coarsest version of the ARA for  $\rho_t$  (in blue), and  $\bar{\rho}_t$  (in red).

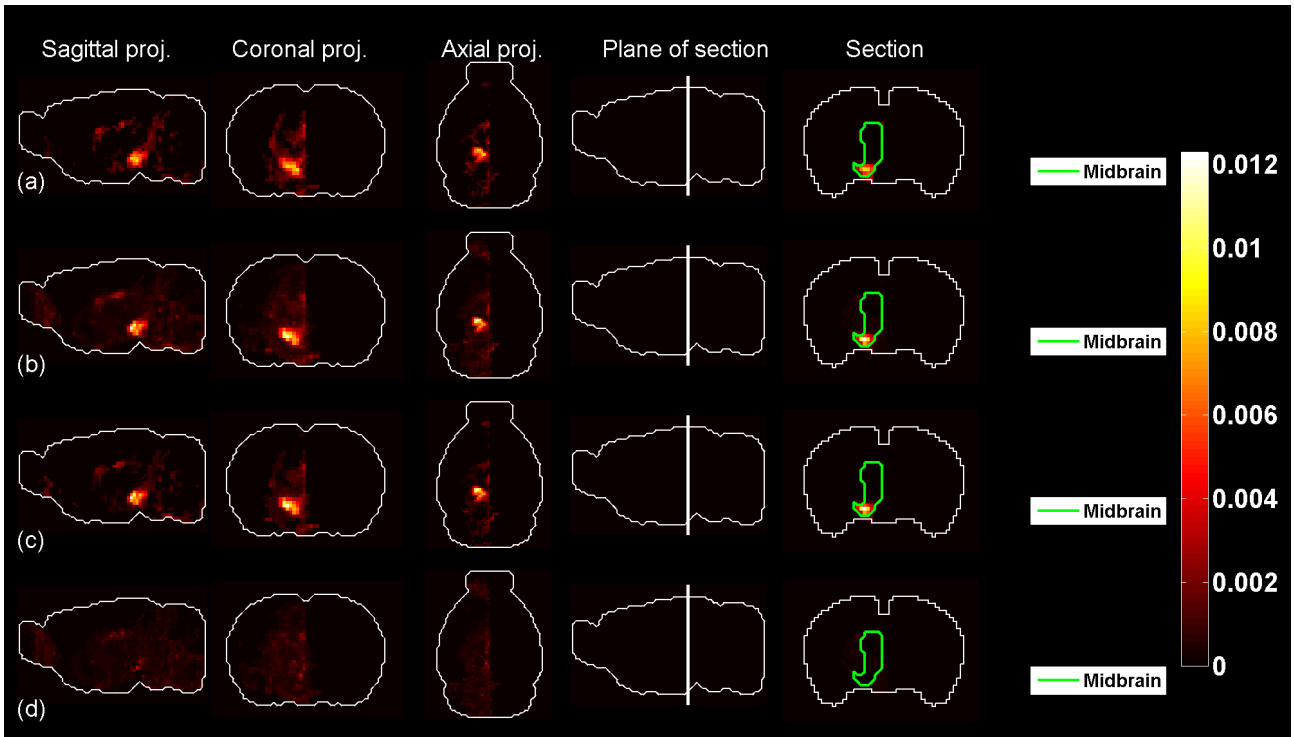


Figure 23: Predicted profile and average sub-sampled profile for  $t = 4$ .

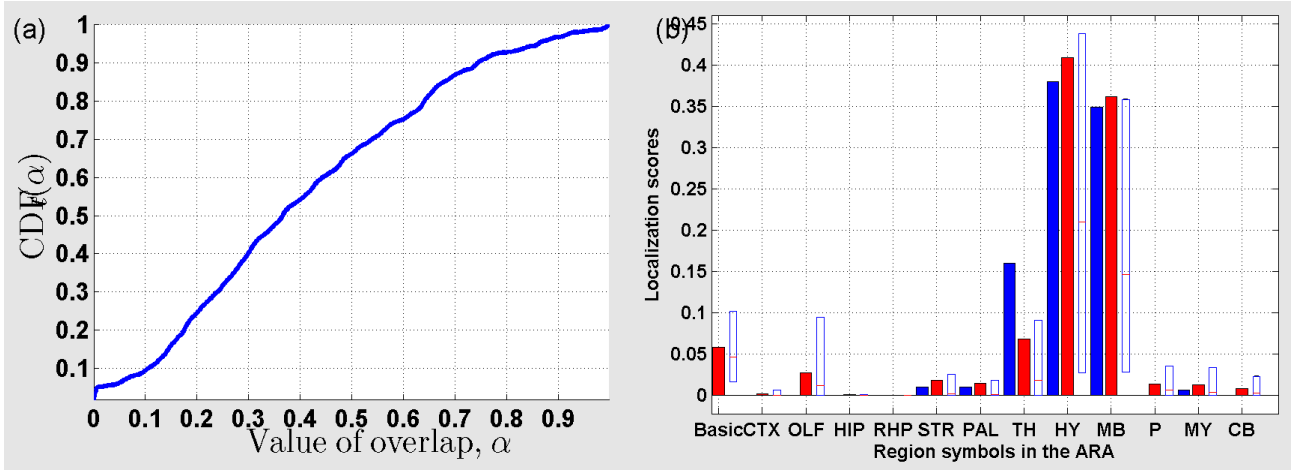


Figure 24: (a) Cumulative distribution function ( $CDF_t$ ) of the overlap between  $\rho_t$  and sub-sampled profiles for  $t = 5$ . (b) Localization scores in the coarsest version of the ARA for  $\rho_t$  (in blue), and  $\bar{\rho}_t$  (in red).

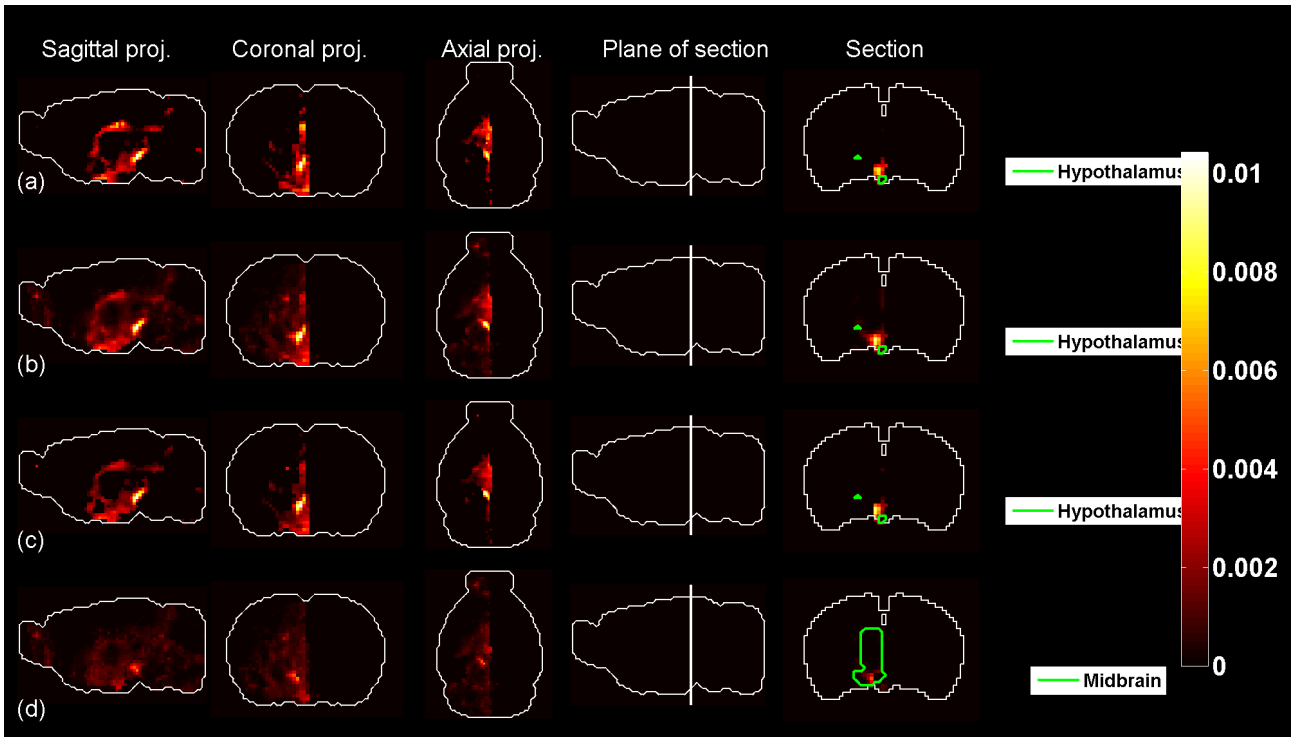


Figure 25: Predicted profile and average sub-sampled profile for  $t = 5$ .

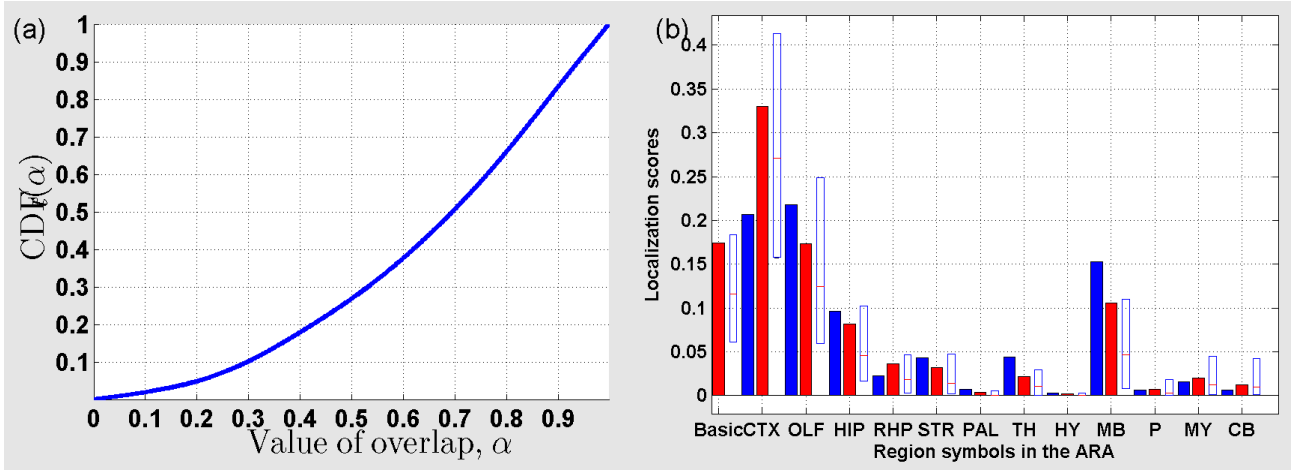


Figure 26: (a) Cumulative distribution function ( $CDF_t$ ) of the overlap between  $\rho_t$  and sub-sampled profiles for  $t = 6$ . (b) Localization scores in the coarsest version of the ARA for  $\rho_t$  (in blue), and  $\bar{\rho}_t$  (in red).

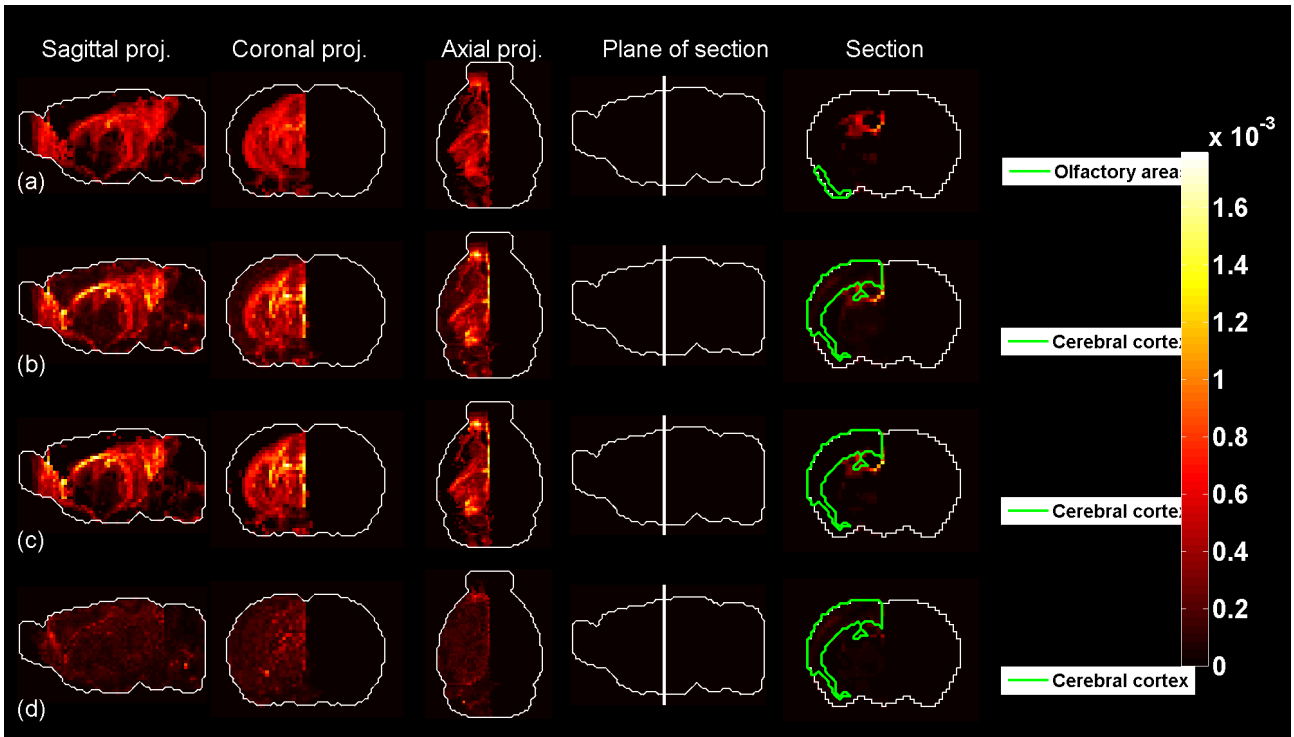


Figure 27: Predicted profile and average sub-sampled profile for  $t = 6$ .

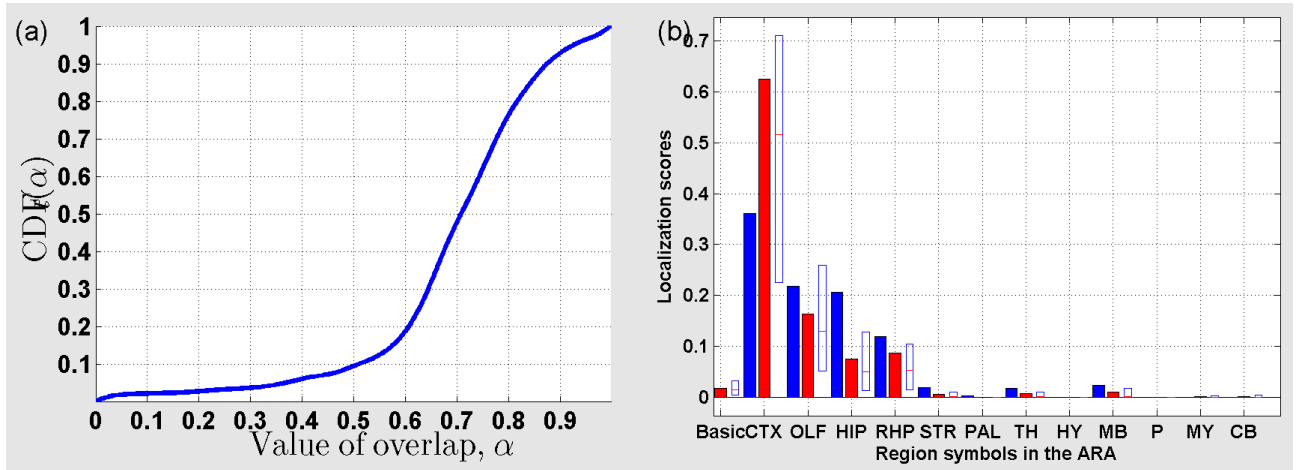


Figure 28: (a) Cumulative distribution function ( $CDF_t$ ) of the overlap between  $\rho_t$  and sub-sampled profiles for  $t = 7$ . (b) Localization scores in the coarsest version of the ARA for  $\rho_t$  (in blue), and  $\bar{\rho}_t$  (in red).

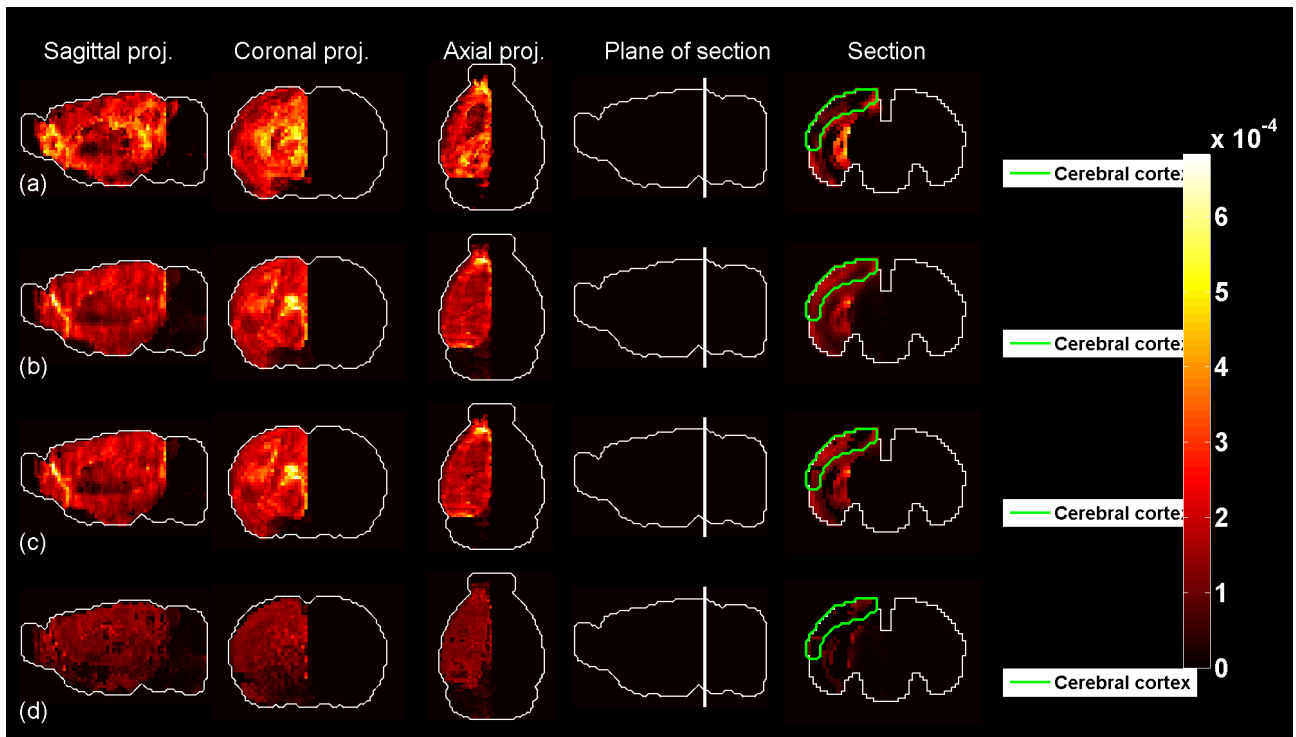


Figure 29: Predicted profile and average sub-sampled profile for  $t = 7$ .

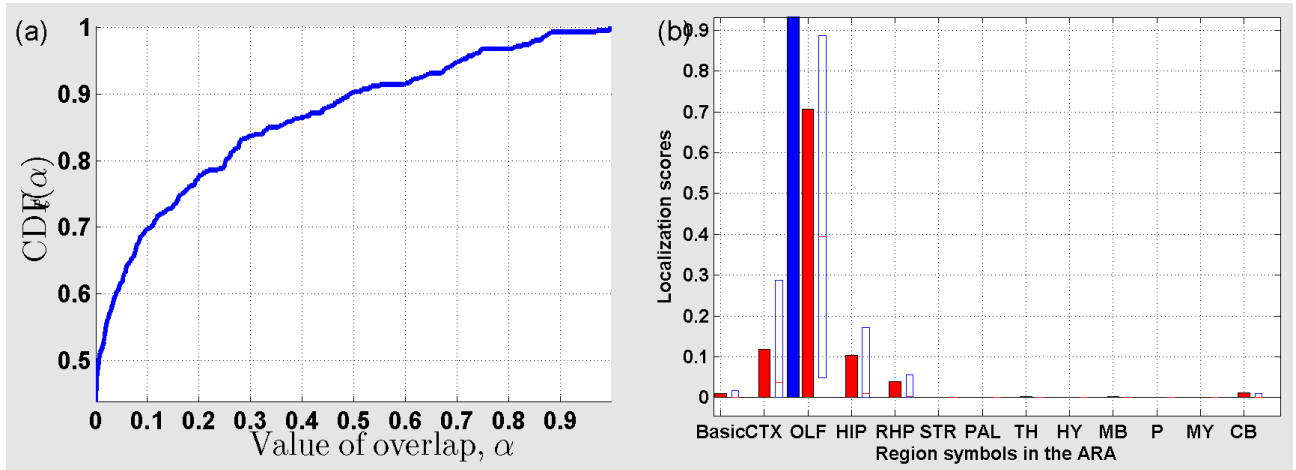


Figure 30: (a) Cumulative distribution function ( $CDF_t$ ) of the overlap between  $\rho_t$  and sub-sampled profiles for  $t = 8$ . (b) Localization scores in the coarsest version of the ARA for  $\rho_t$  (in blue), and  $\bar{\rho}_t$  (in red).

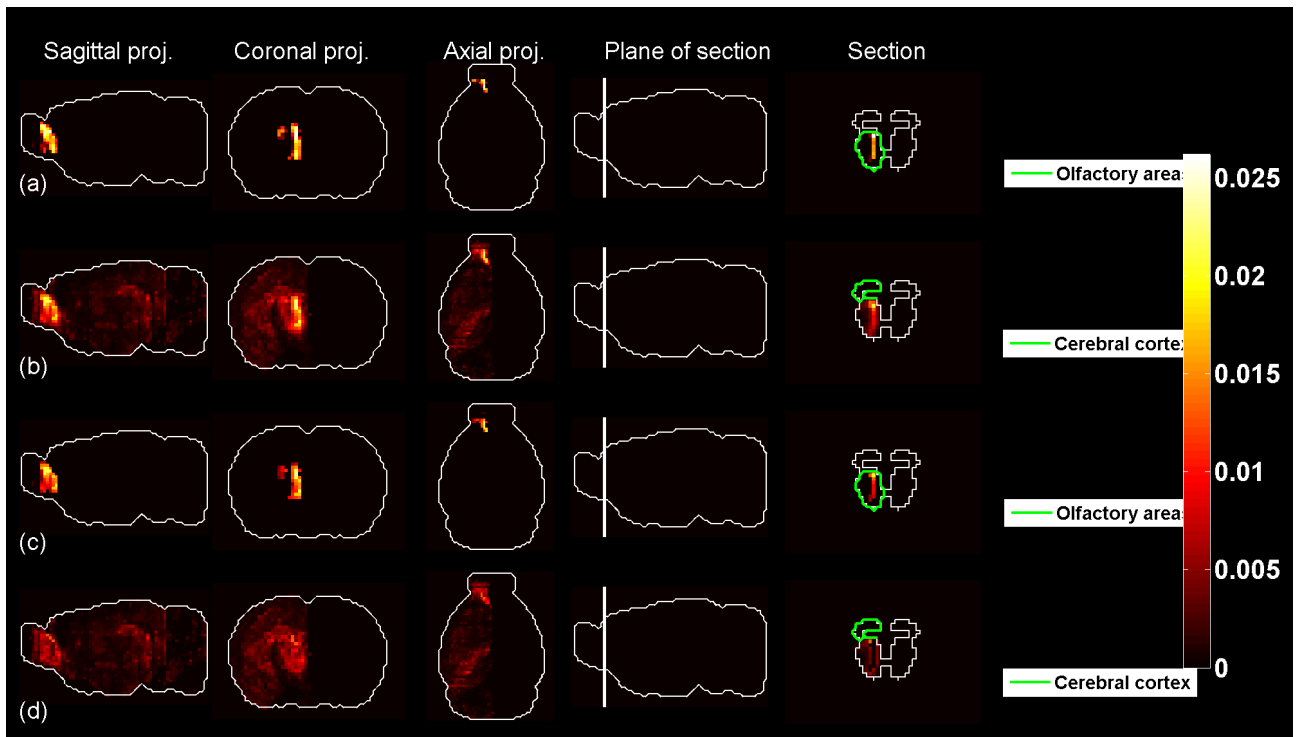


Figure 31: Predicted profile and average sub-sampled profile for  $t = 8$ .

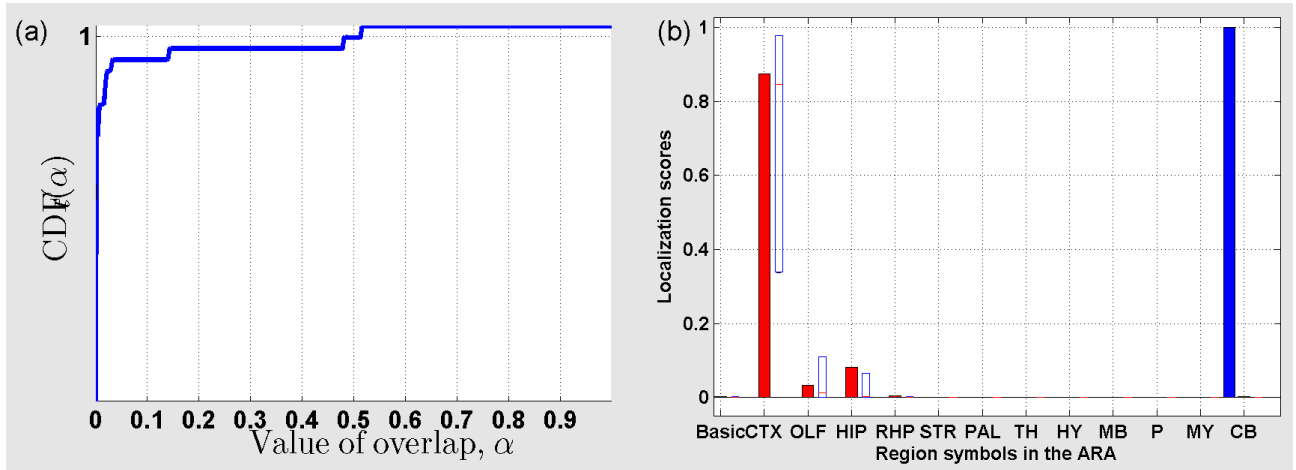


Figure 32: (a) Cumulative distribution function ( $CDF_t$ ) of the overlap between  $\rho_t$  and sub-sampled profiles for  $t = 9$ . (b) Localization scores in the coarsest version of the ARA for  $\rho_t$  (in blue), and  $\bar{\rho}_t$  (in red).

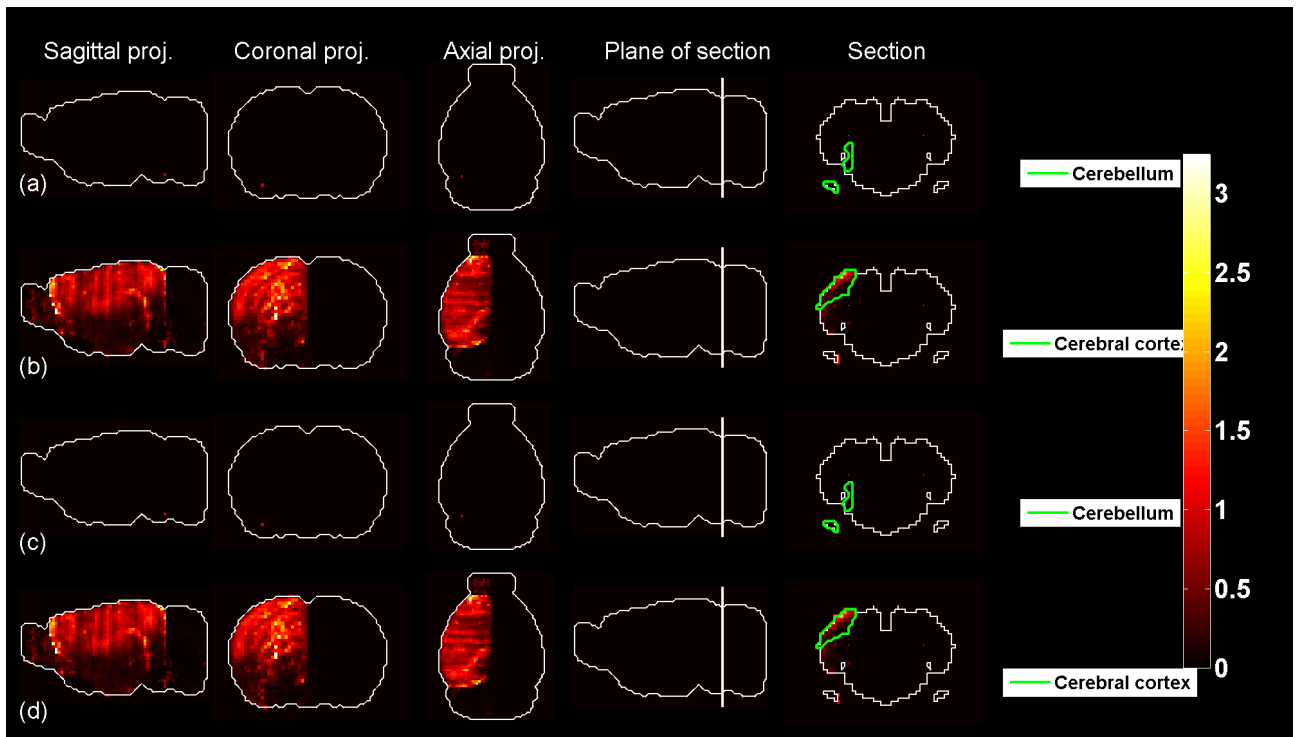


Figure 33: Predicted profile and average sub-sampled profile for  $t = 9$ .

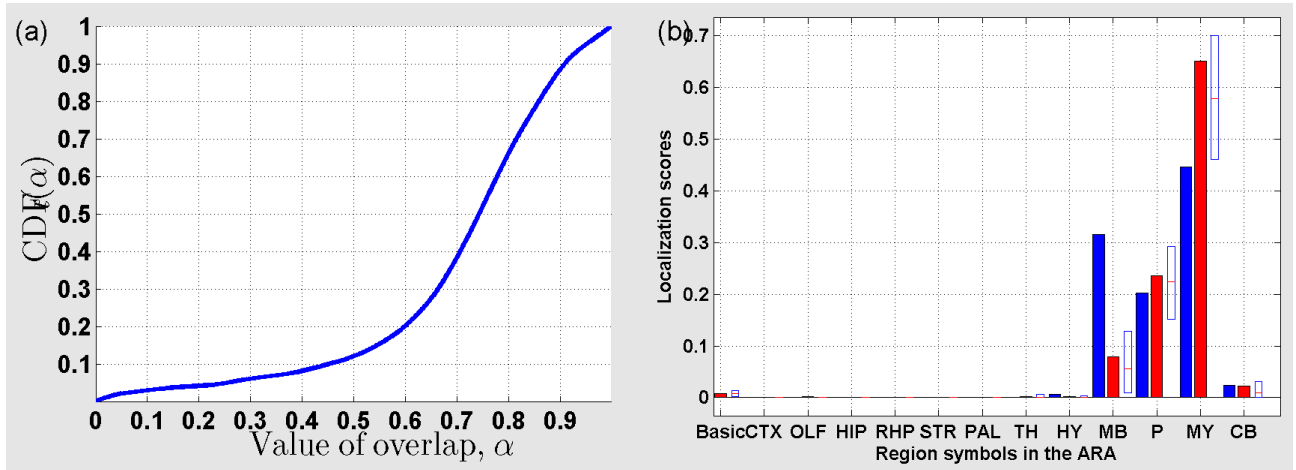


Figure 34: (a) Cumulative distribution function ( $CDF_t$ ) of the overlap between  $\rho_t$  and sub-sampled profiles for  $t = 10$ . (b) Localization scores in the coarsest version of the ARA for  $\rho_t$  (in blue), and  $\bar{\rho}_t$  (in red).

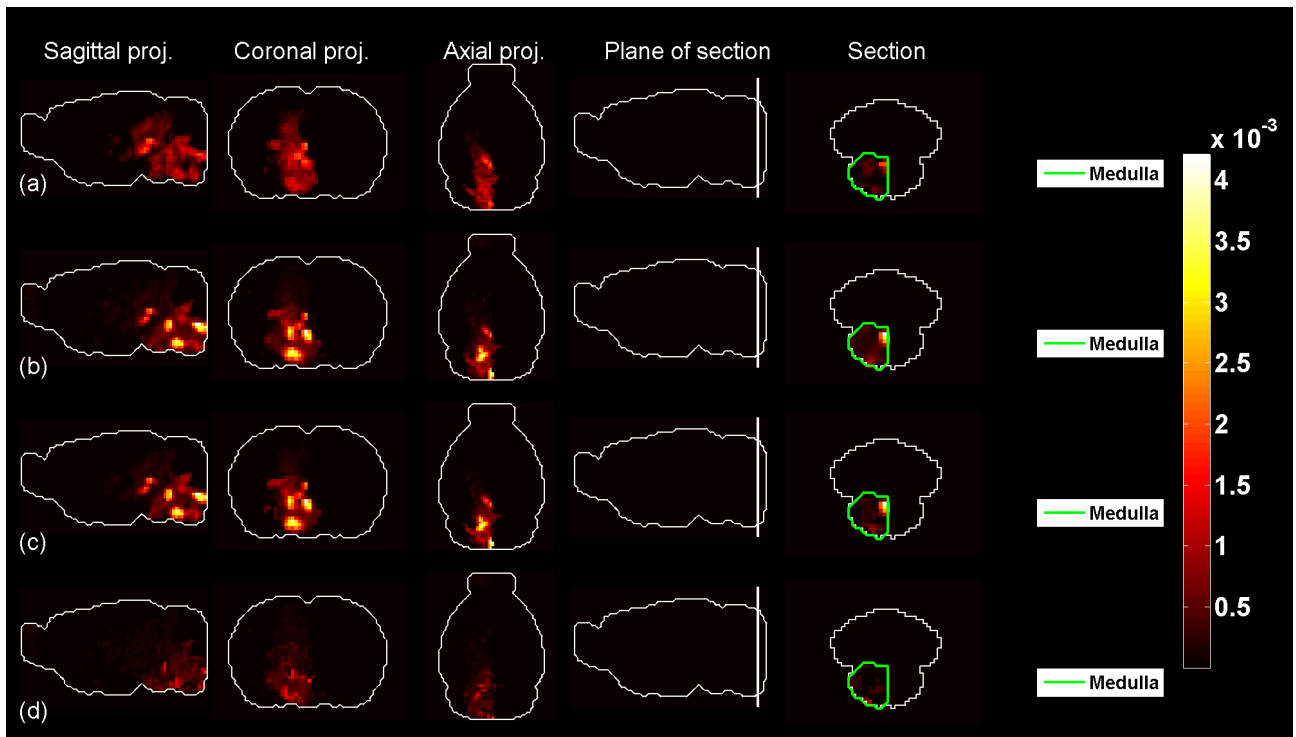


Figure 35: Predicted profile and average sub-sampled profile for  $t = 10$ .

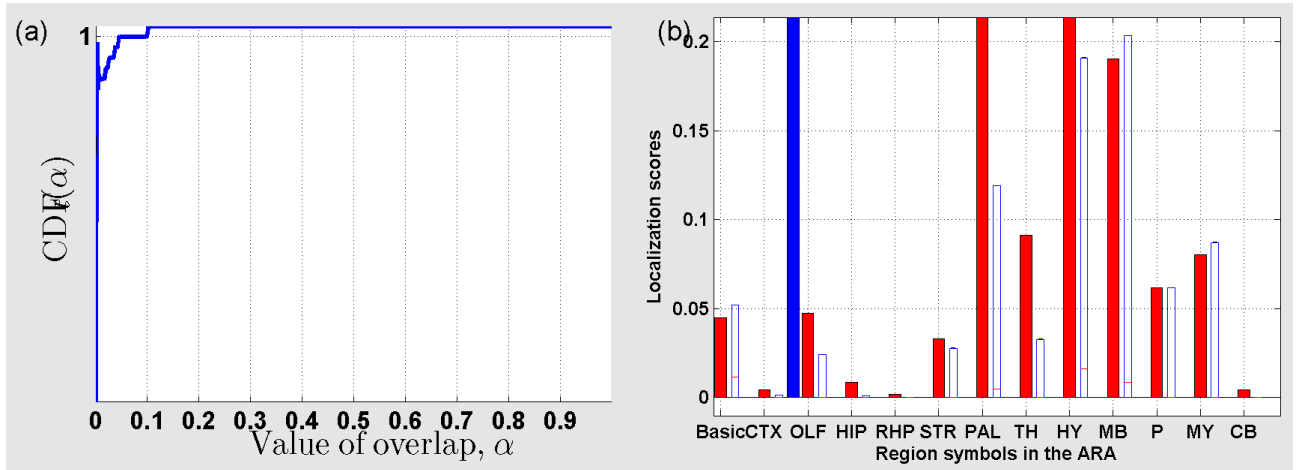


Figure 36: (a) Cumulative distribution function ( $CDF_t$ ) of the overlap between  $\rho_t$  and sub-sampled profiles for  $t = 11$ . (b) Localization scores in the coarsest version of the ARA for  $\rho_t$  (in blue), and  $\bar{\rho}_t$  (in red).

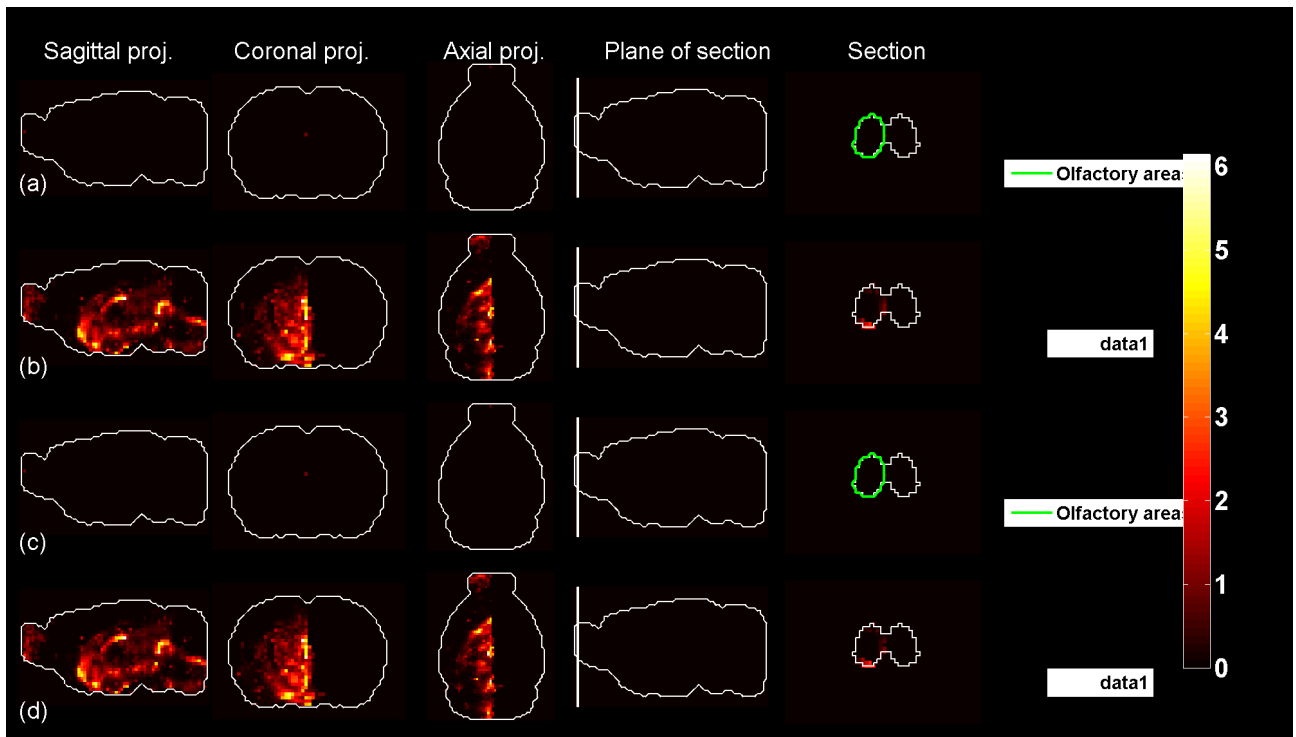


Figure 37: Predicted profile and average sub-sampled profile for  $t = 11$ .

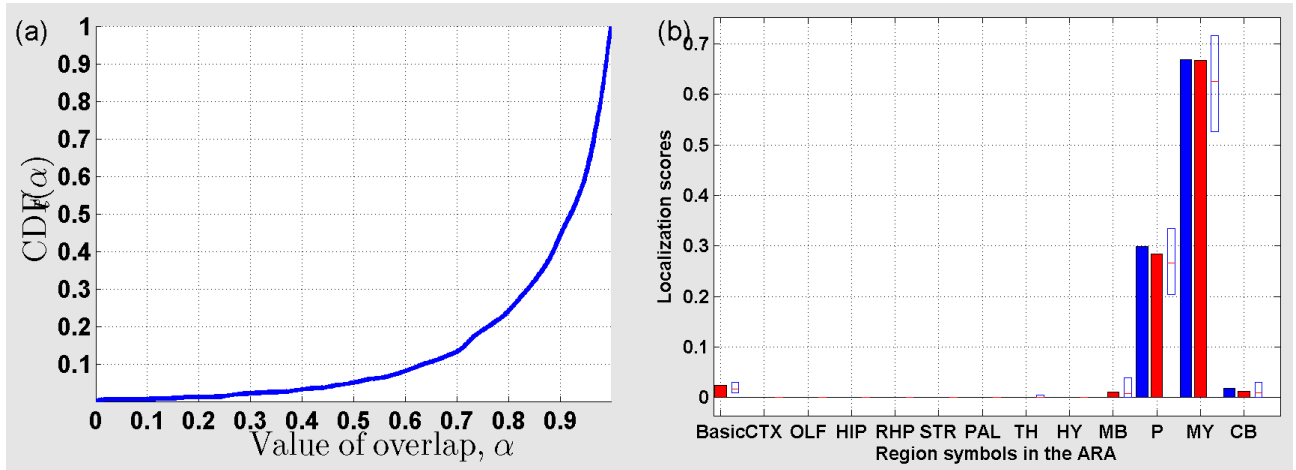


Figure 38: (a) Cumulative distribution function ( $CDF_t$ ) of the overlap between  $\rho_t$  and sub-sampled profiles for  $t = 12$ . (b) Localization scores in the coarsest version of the ARA for  $\rho_t$  (in blue), and  $\bar{\rho}_t$  (in red).

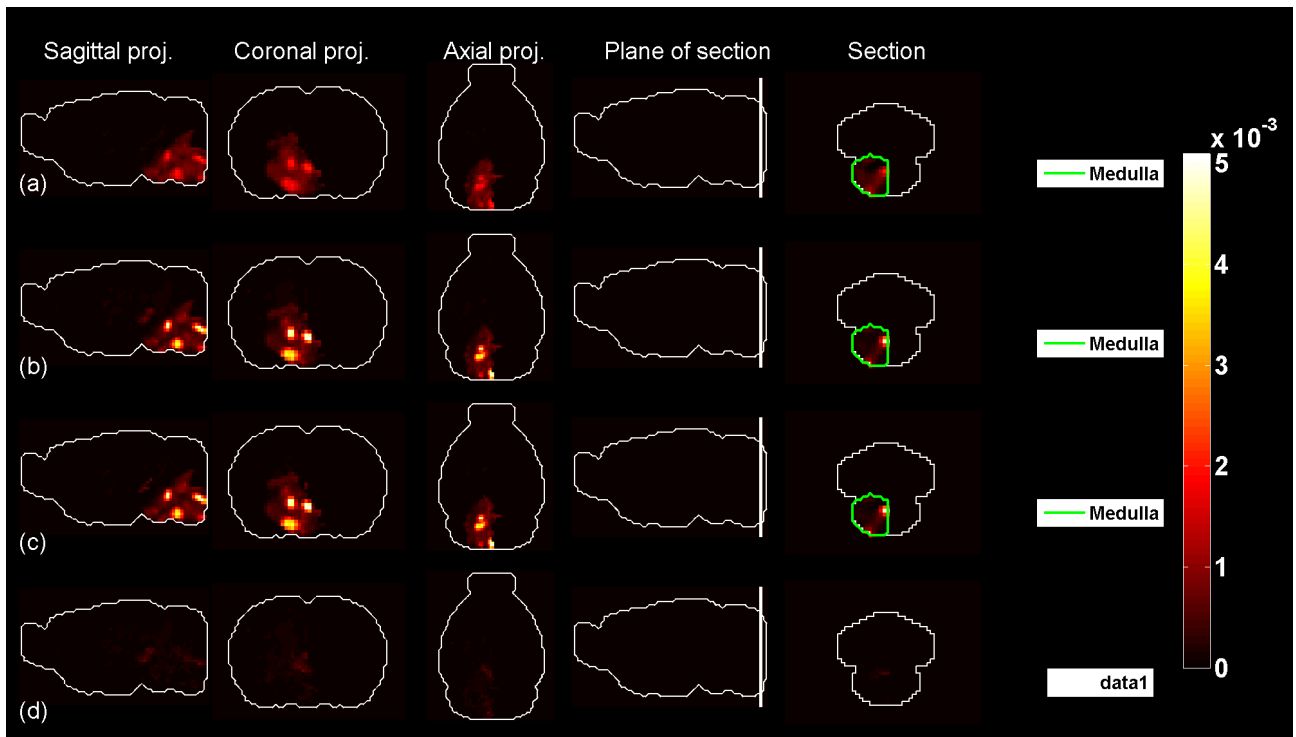


Figure 39: Predicted profile and average sub-sampled profile for  $t = 12$ .

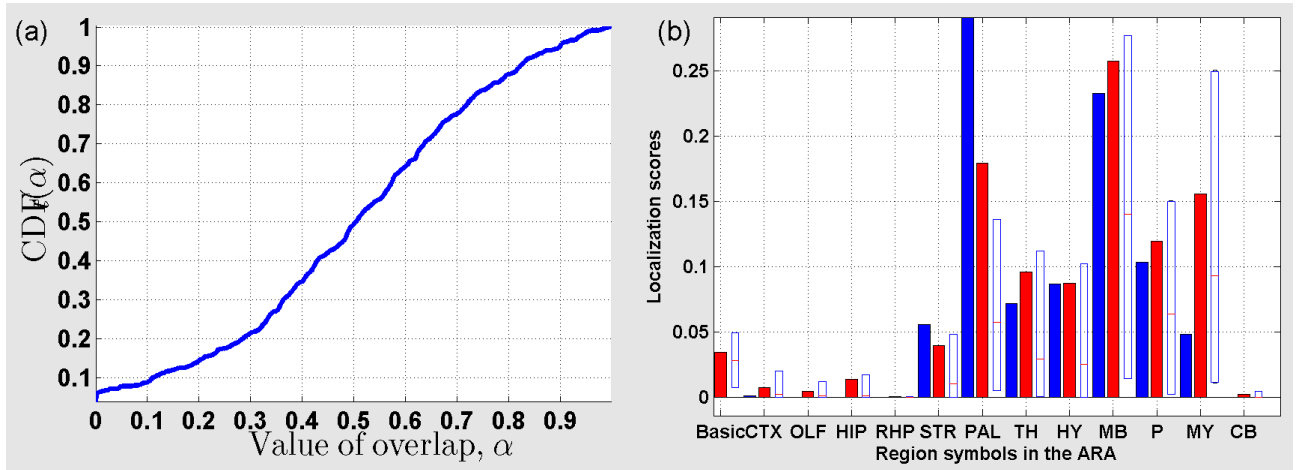


Figure 40: (a) Cumulative distribution function ( $CDF_t$ ) of the overlap between  $\rho_t$  and sub-sampled profiles for  $t = 13$ . (b) Localization scores in the coarsest version of the ARA for  $\rho_t$  (in blue), and  $\bar{\rho}_t$  (in red).

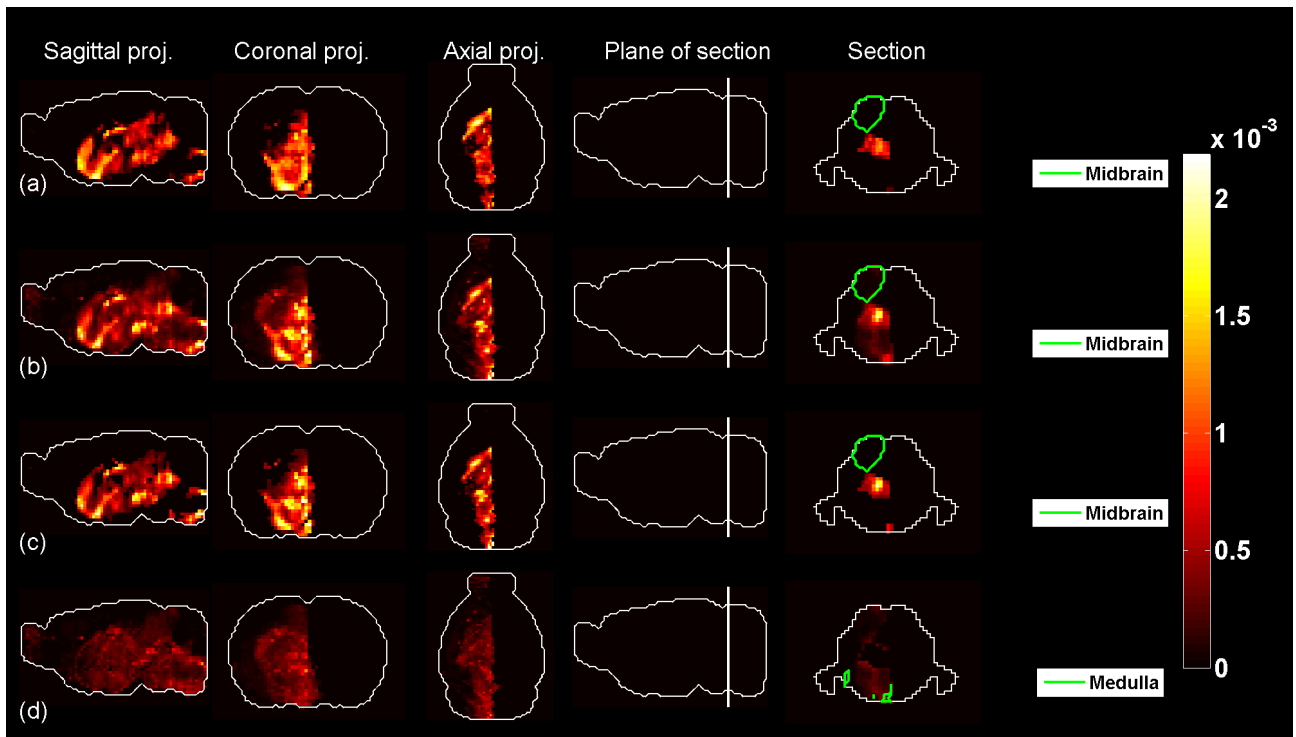


Figure 41: Predicted profile and average sub-sampled profile for  $t = 13$ .

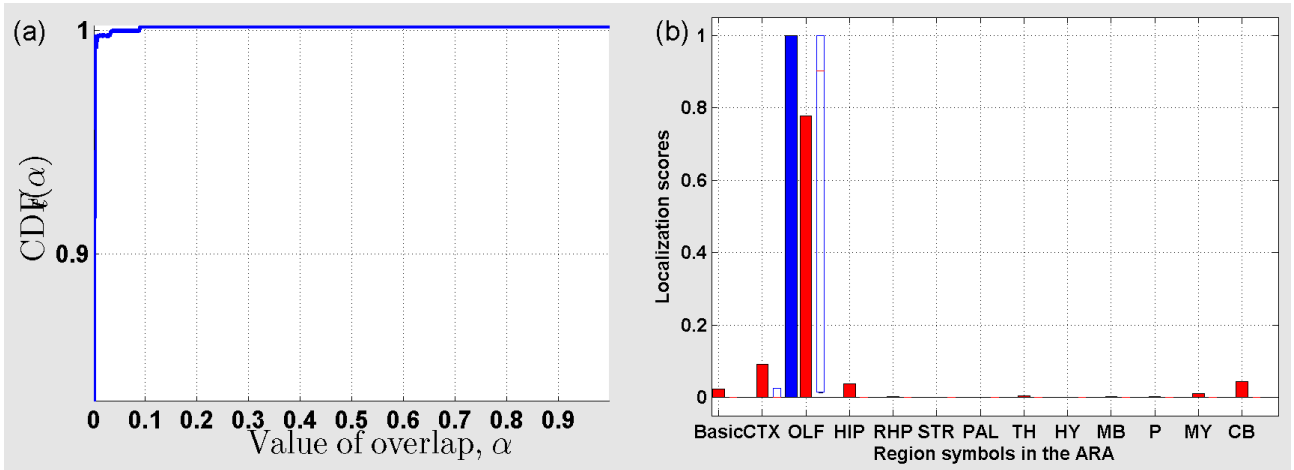


Figure 42: (a) Cumulative distribution function ( $CDF_t$ ) of the overlap between  $\rho_t$  and sub-sampled profiles for  $t = 14$ . (b) Localization scores in the coarsest version of the ARA for  $\rho_t$  (in blue), and  $\bar{\rho}_t$  (in red).

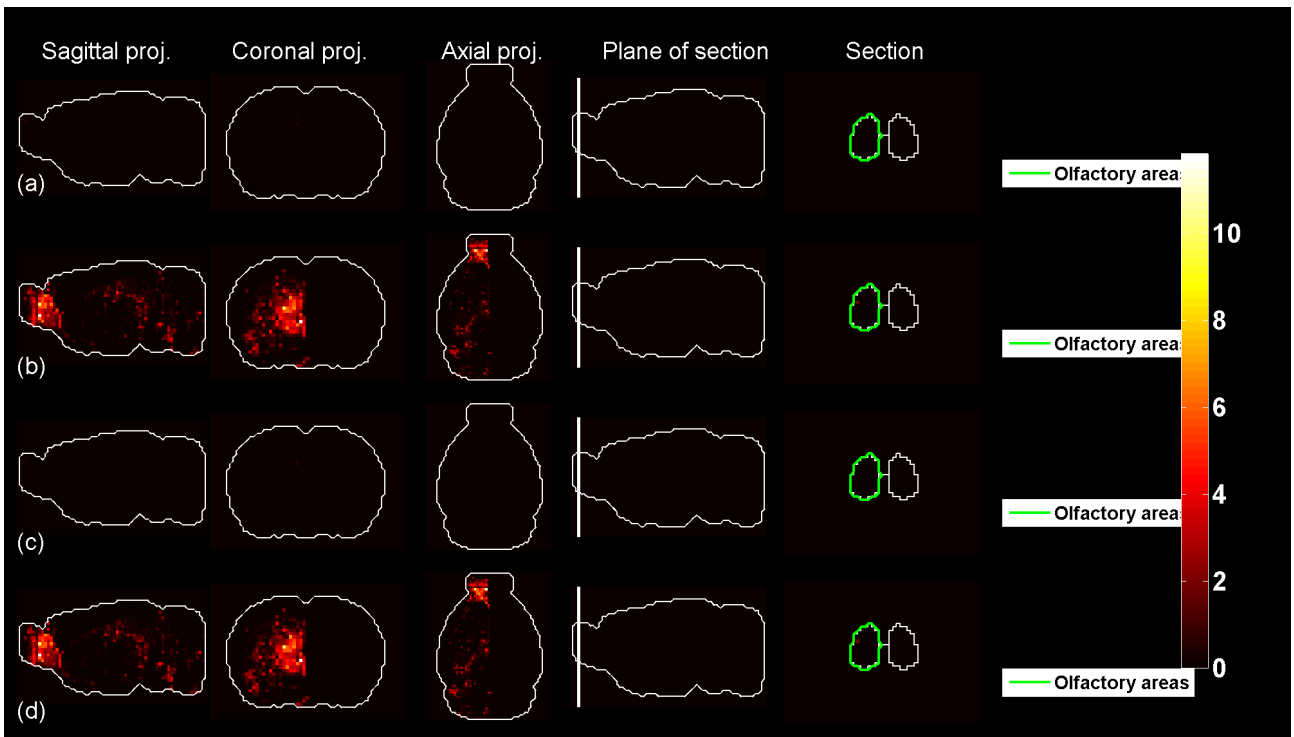


Figure 43: Predicted profile and average sub-sampled profile for  $t = 14$ .

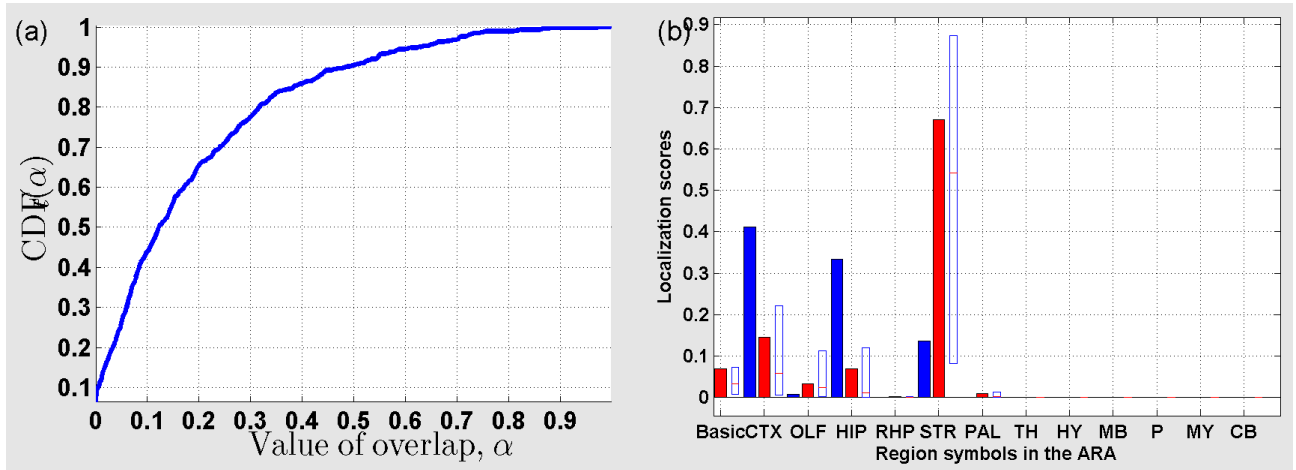


Figure 44: (a) Cumulative distribution function ( $CDF_t$ ) of the overlap between  $\rho_t$  and sub-sampled profiles for  $t = 15$ . (b) Localization scores in the coarsest version of the ARA for  $\rho_t$  (in blue), and  $\bar{\rho}_t$  (in red).

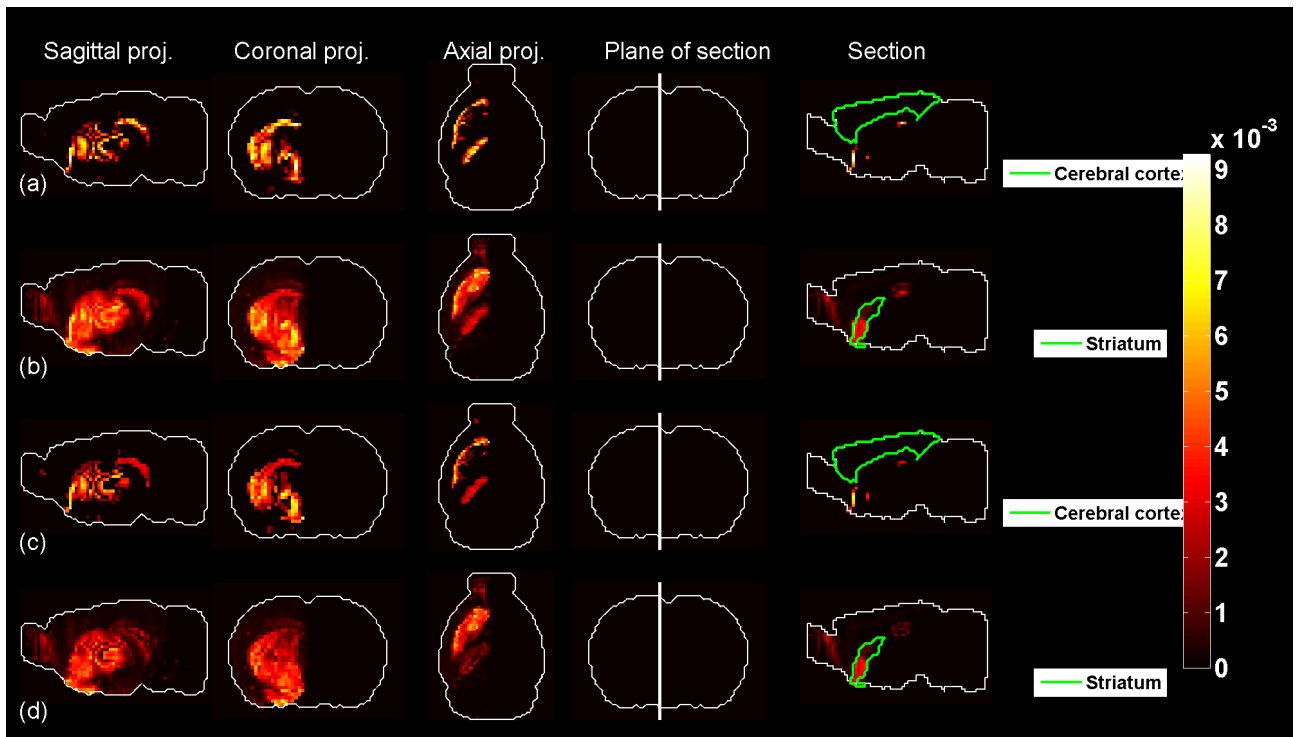


Figure 45: Predicted profile and average sub-sampled profile for  $t = 15$ .

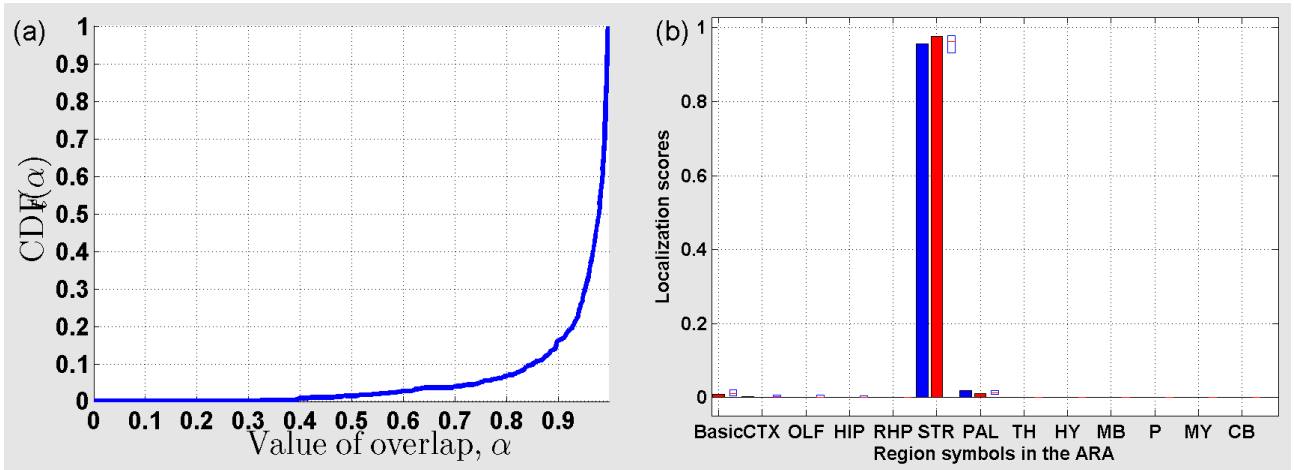


Figure 46: (a) Cumulative distribution function ( $CDF_t$ ) of the overlap between  $\rho_t$  and sub-sampled profiles for  $t = 16$ . (b) Localization scores in the coarsest version of the ARA for  $\rho_t$  (in blue), and  $\bar{\rho}_t$  (in red).

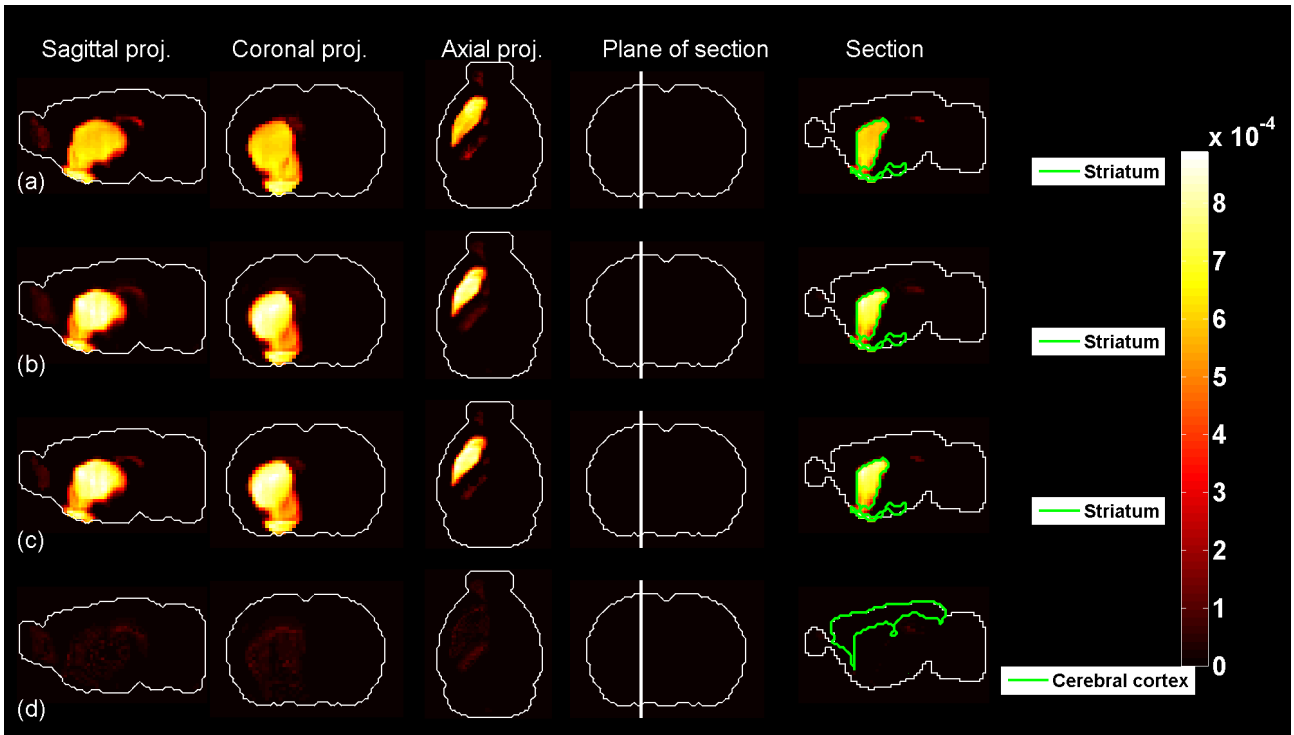


Figure 47: Predicted profile and average sub-sampled profile for  $t = 16$ .

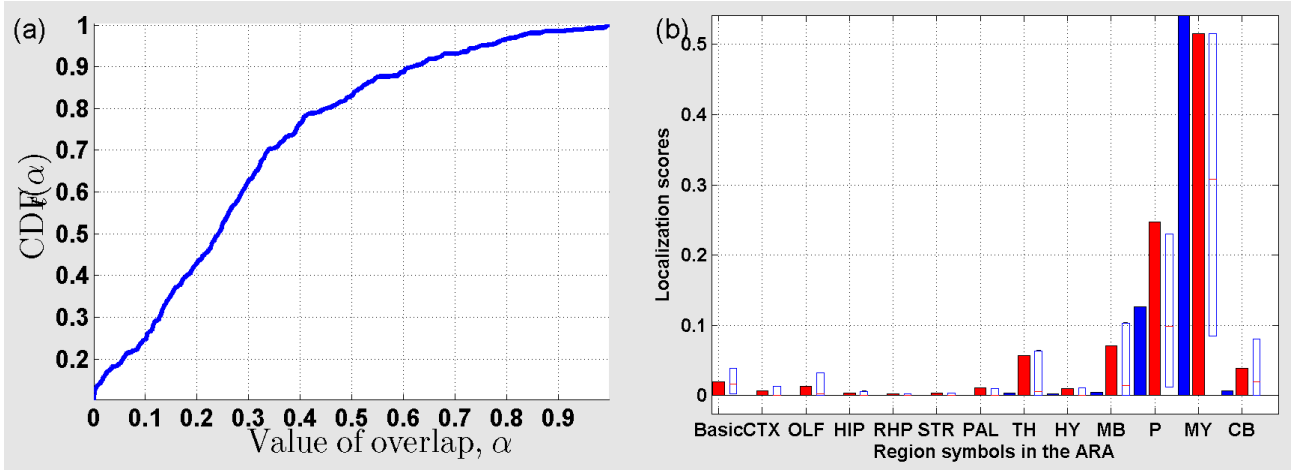


Figure 48: (a) Cumulative distribution function ( $CDF_t$ ) of the overlap between  $\rho_t$  and sub-sampled profiles for  $t = 17$ . (b) Localization scores in the coarsest version of the ARA for  $\rho_t$  (in blue), and  $\bar{\rho}_t$  (in red).

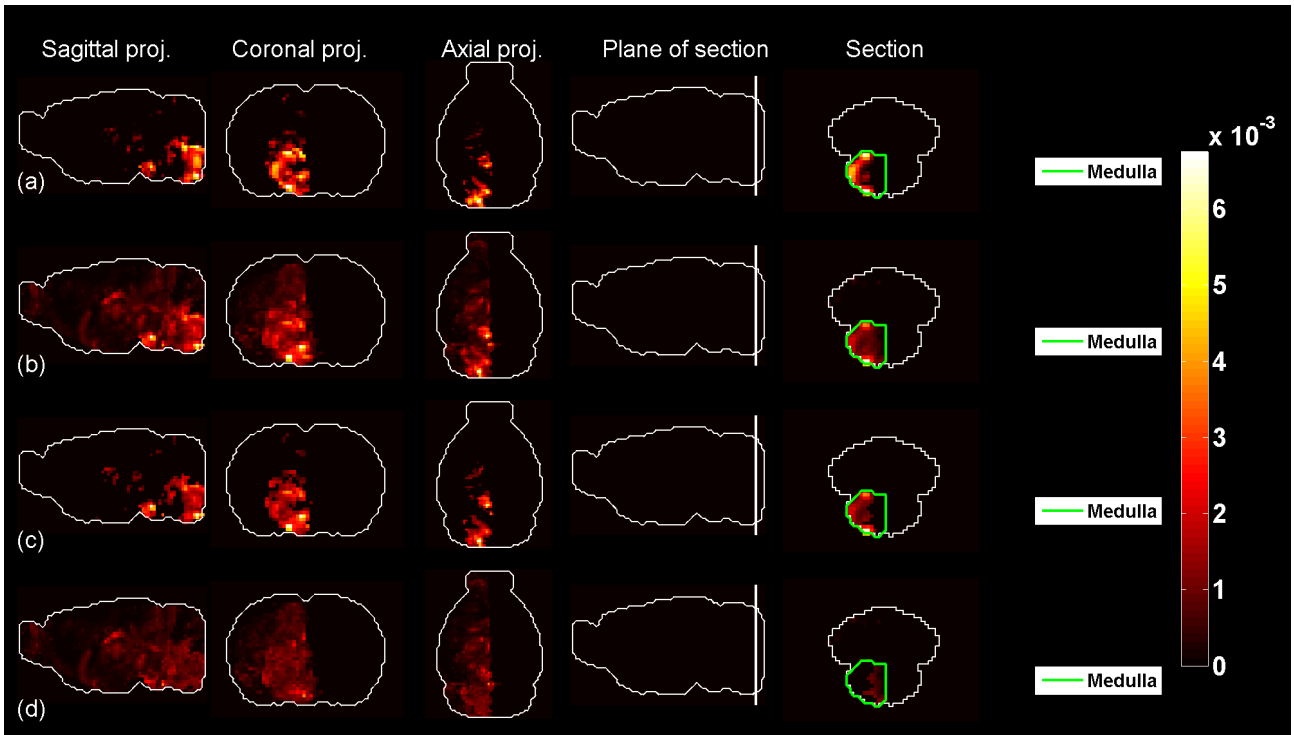


Figure 49: Predicted profile and average sub-sampled profile for  $t = 17$ .

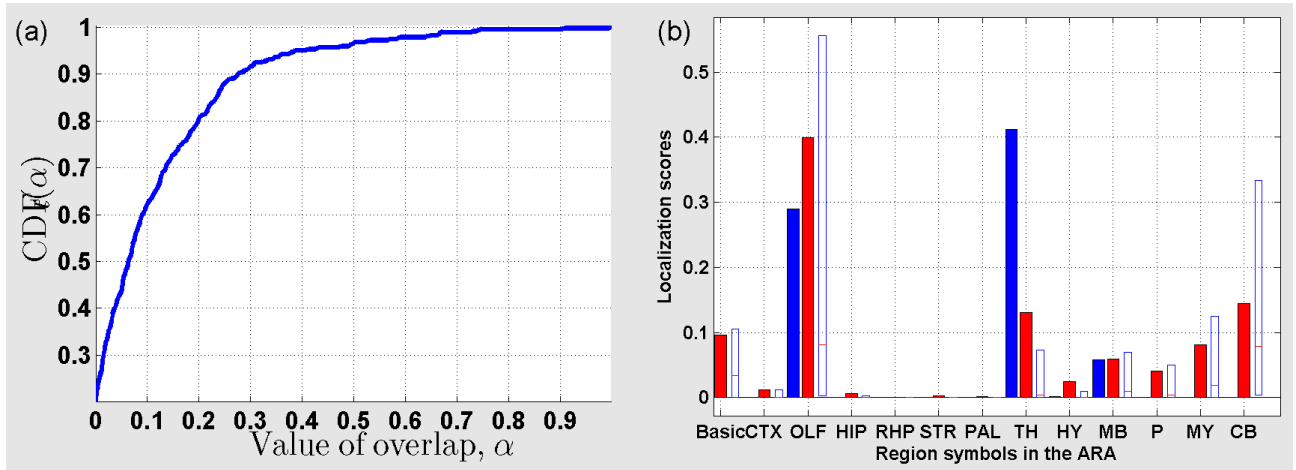


Figure 50: (a) Cumulative distribution function ( $CDF_t$ ) of the overlap between  $\rho_t$  and sub-sampled profiles for  $t = 18$ . (b) Localization scores in the coarsest version of the ARA for  $\rho_t$  (in blue), and  $\bar{\rho}_t$  (in red).

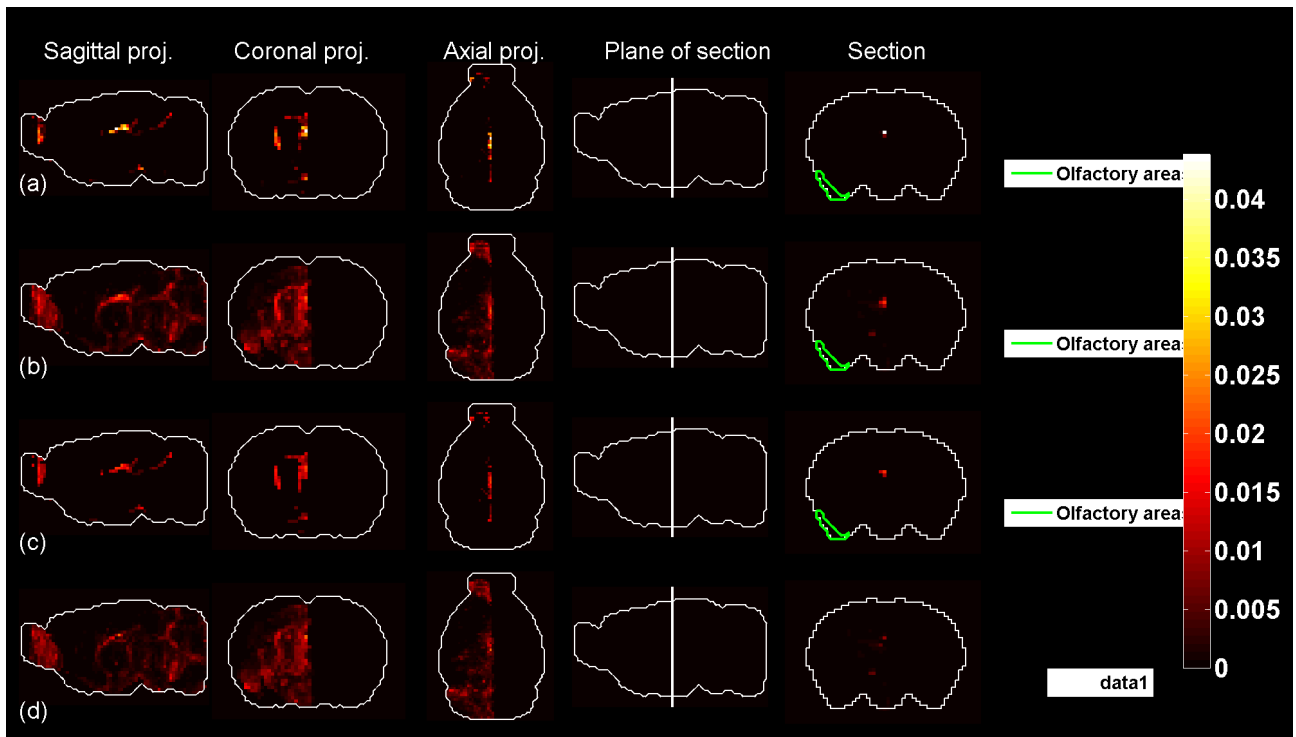


Figure 51: Predicted profile and average sub-sampled profile for  $t = 18$ .

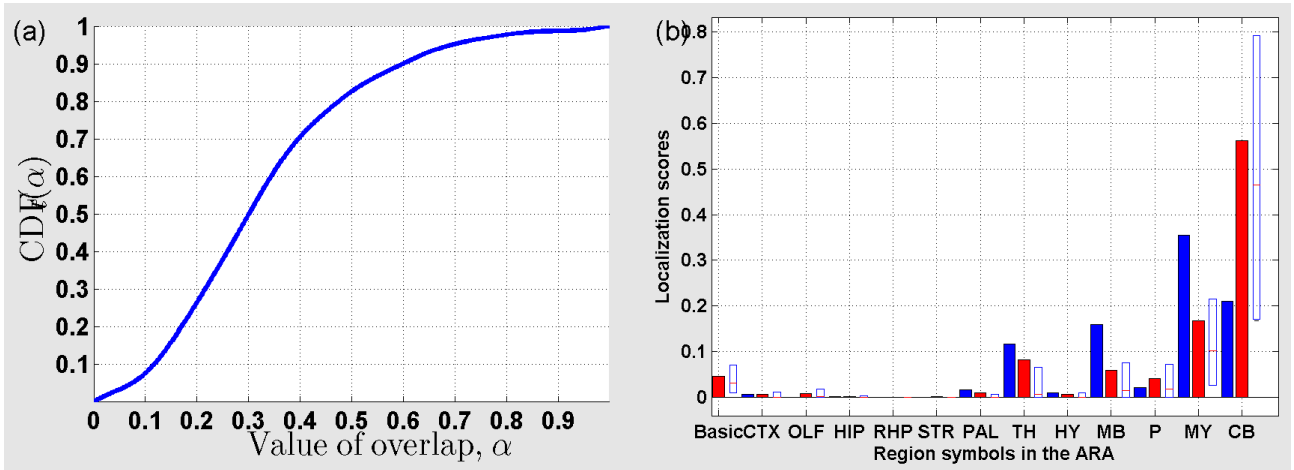


Figure 52: (a) Cumulative distribution function ( $CDF_t$ ) of the overlap between  $\rho_t$  and sub-sampled profiles for  $t = 19$ . (b) Localization scores in the coarsest version of the ARA for  $\rho_t$  (in blue), and  $\bar{\rho}_t$  (in red).

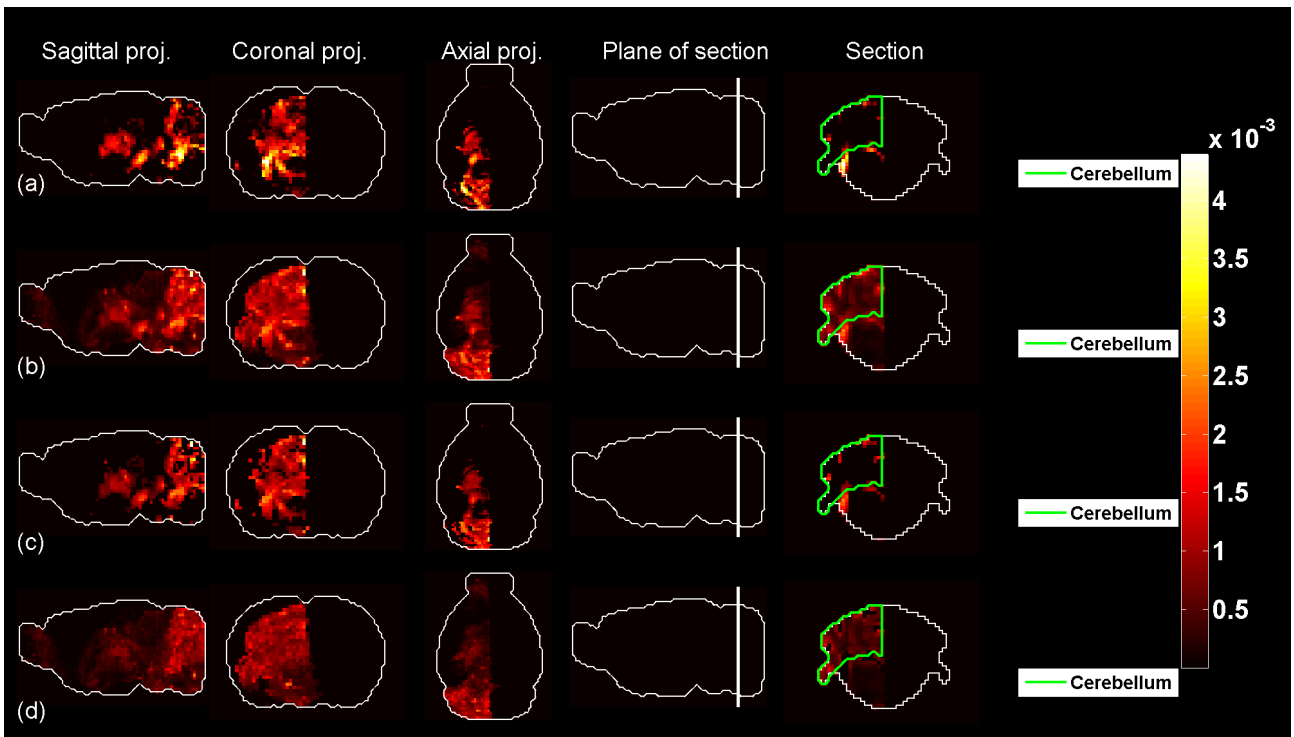


Figure 53: Predicted profile and average sub-sampled profile for  $t = 19$ .

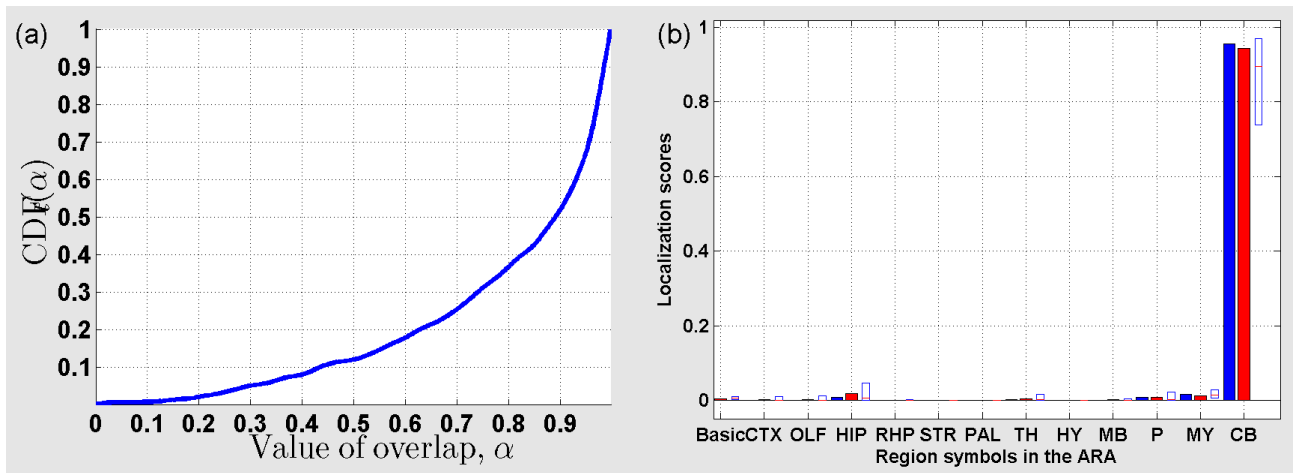


Figure 54: (a) Cumulative distribution function ( $CDF_t$ ) of the overlap between  $\rho_t$  and sub-sampled profiles for  $t = 20$ . (b) Localization scores in the coarsest version of the ARA for  $\rho_t$  (in blue), and  $\bar{\rho}_t$  (in red).

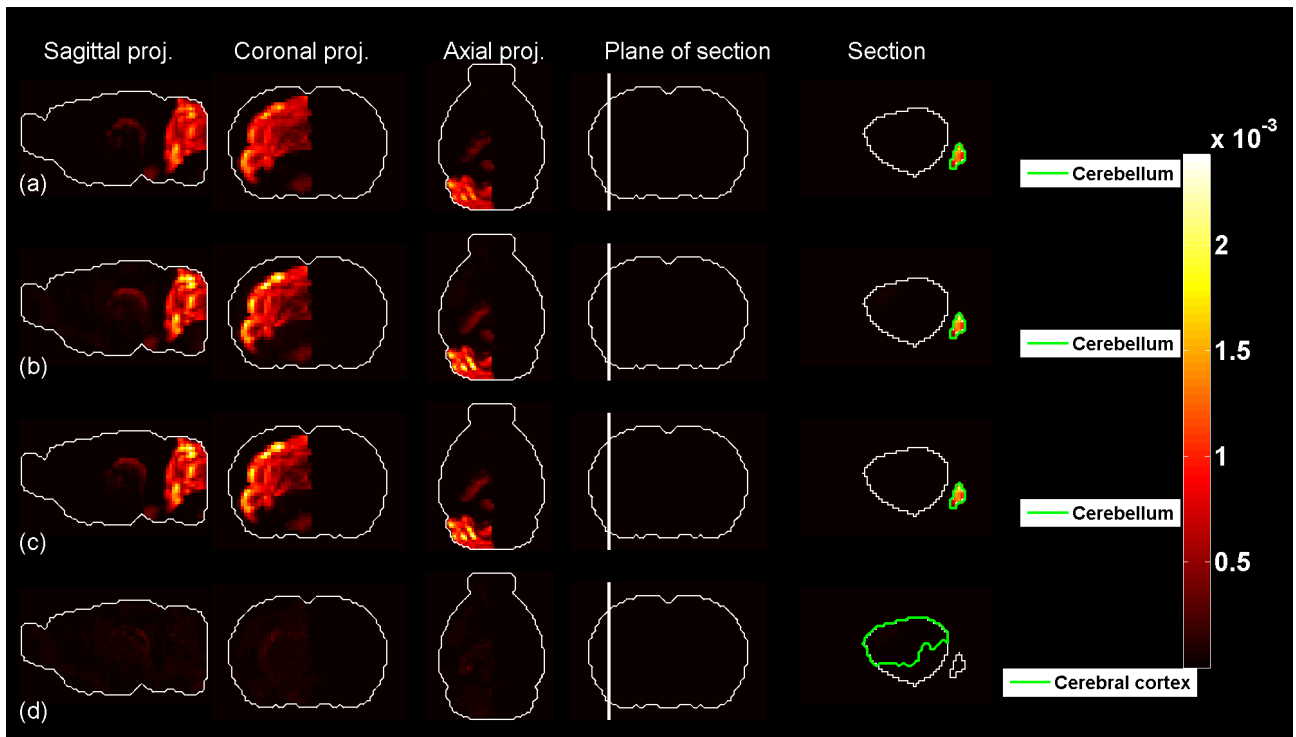


Figure 55: Predicted profile and average sub-sampled profile for  $t = 20$ .

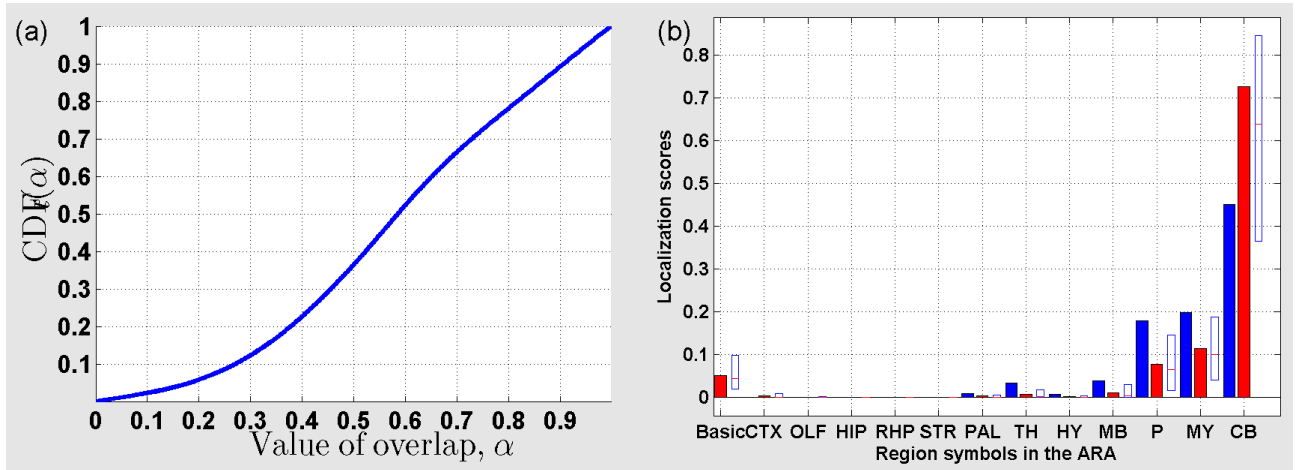


Figure 56: (a) Cumulative distribution function ( $CDF_t$ ) of the overlap between  $\rho_t$  and sub-sampled profiles for  $t = 21$ . (b) Localization scores in the coarsest version of the ARA for  $\rho_t$  (in blue), and  $\bar{\rho}_t$  (in red).

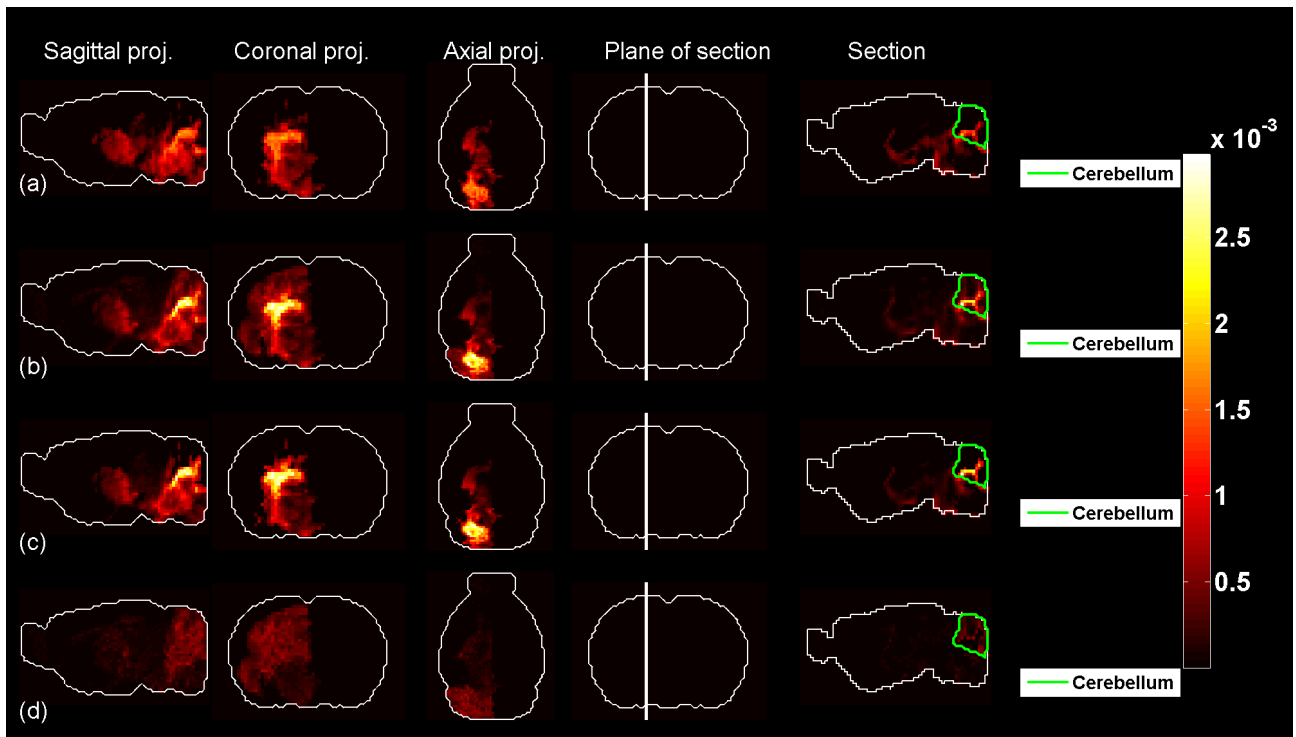


Figure 57: Predicted profile and average sub-sampled profile for  $t = 21$ .

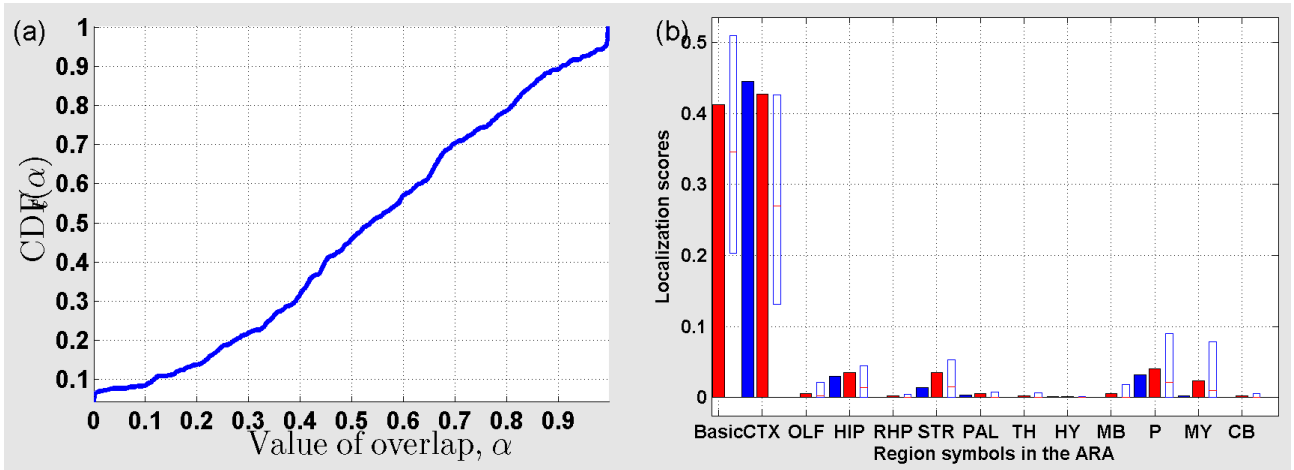


Figure 58: (a) Cumulative distribution function ( $CDF_t$ ) of the overlap between  $\rho_t$  and sub-sampled profiles for  $t = 22$ . (b) Localization scores in the coarsest version of the ARA for  $\rho_t$  (in blue), and  $\bar{\rho}_t$  (in red).

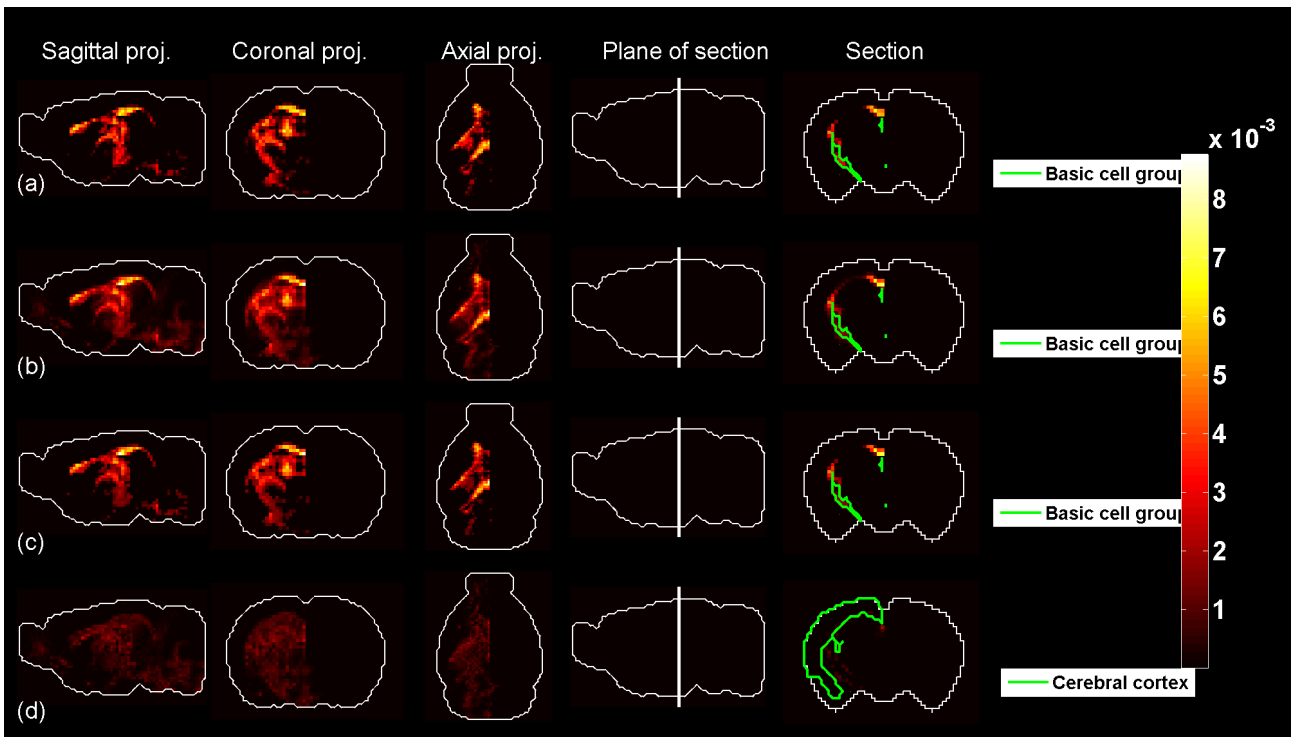


Figure 59: Predicted profile and average sub-sampled profile for  $t = 22$ .

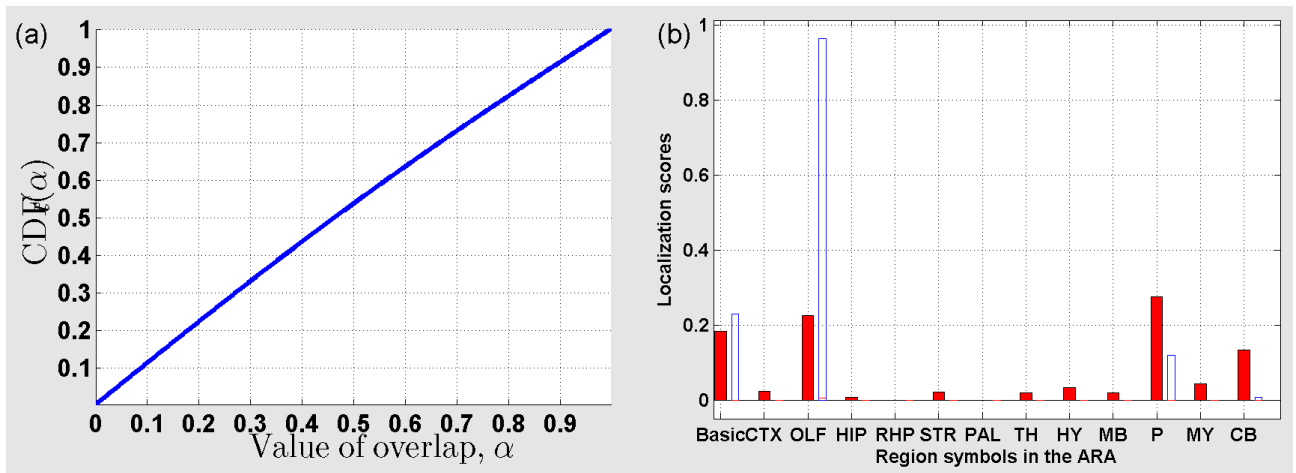


Figure 60: (a) Cumulative distribution function ( $CDF_t$ ) of the overlap between  $\rho_t$  and sub-sampled profiles for  $t = 23$ . (b) Localization scores in the coarsest version of the ARA for  $\rho_t$  (in blue), and  $\bar{\rho}_t$  (in red).

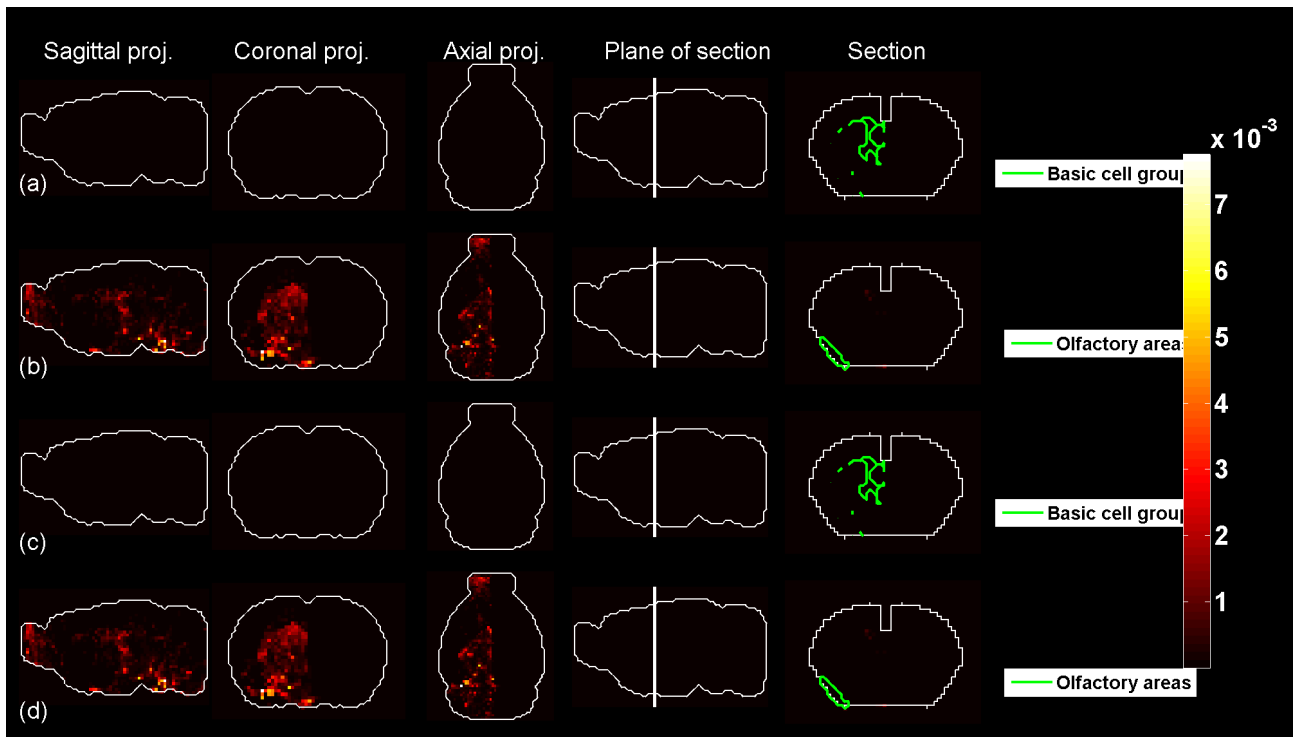


Figure 61: Predicted profile and average sub-sampled profile for  $t = 23$ .

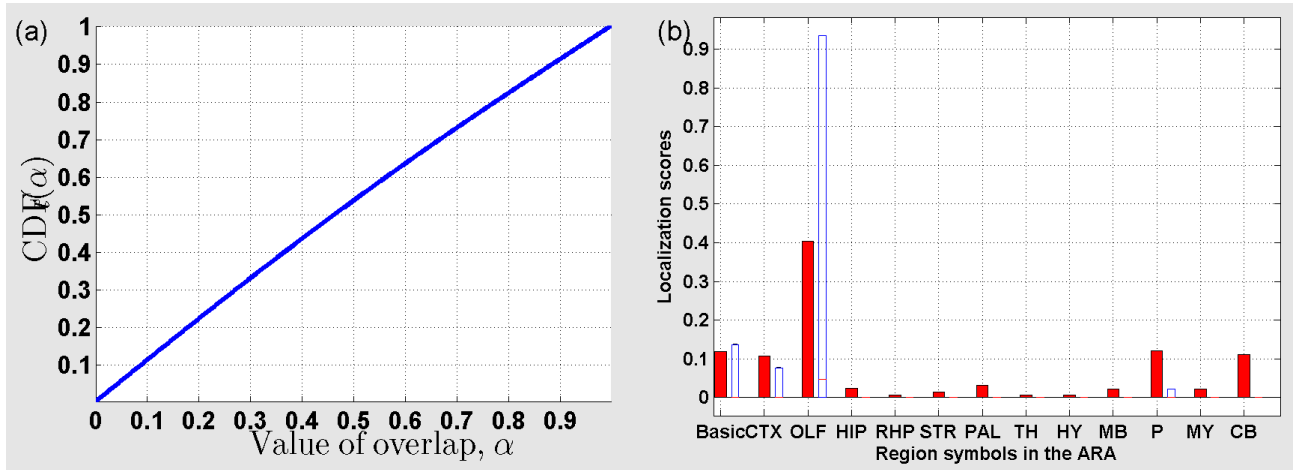


Figure 62: (a) Cumulative distribution function ( $CDF_t$ ) of the overlap between  $\rho_t$  and sub-sampled profiles for  $t = 24$ . (b) Localization scores in the coarsest version of the ARA for  $\rho_t$  (in blue), and  $\bar{\rho}_t$  (in red).

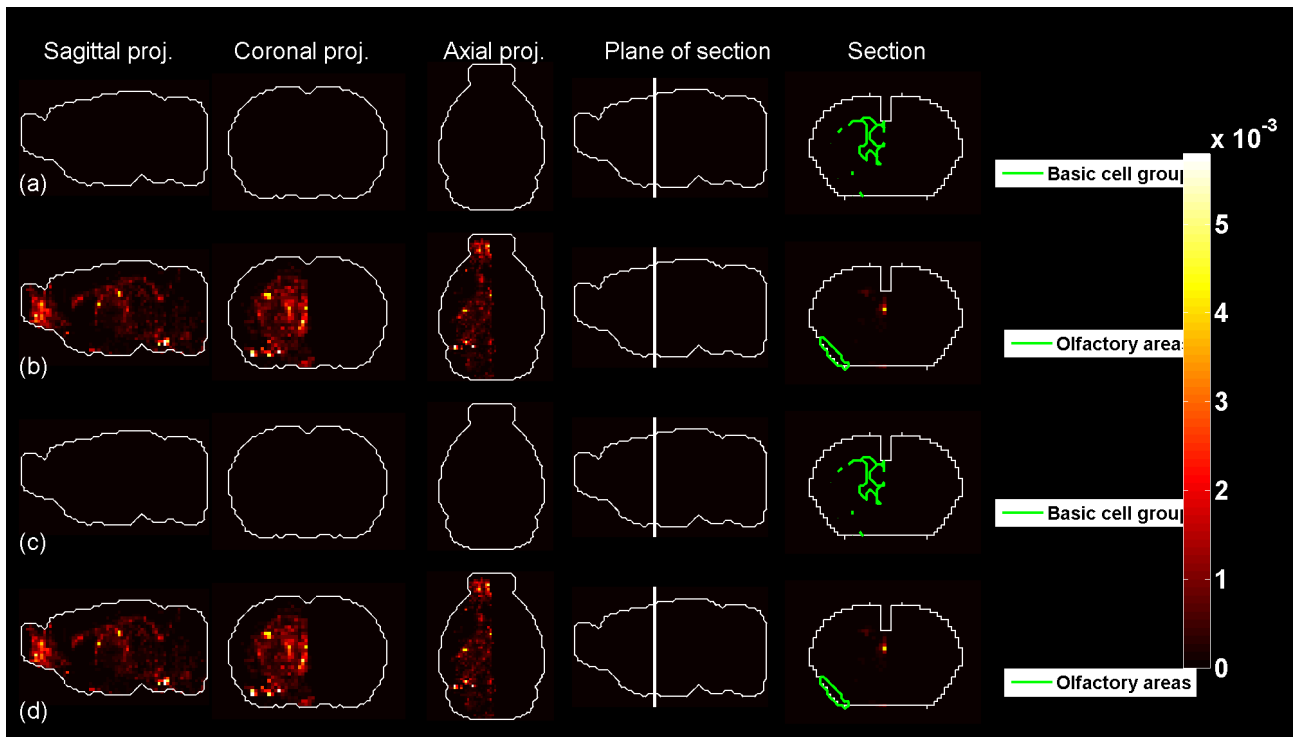


Figure 63: Predicted profile and average sub-sampled profile for  $t = 24$ .

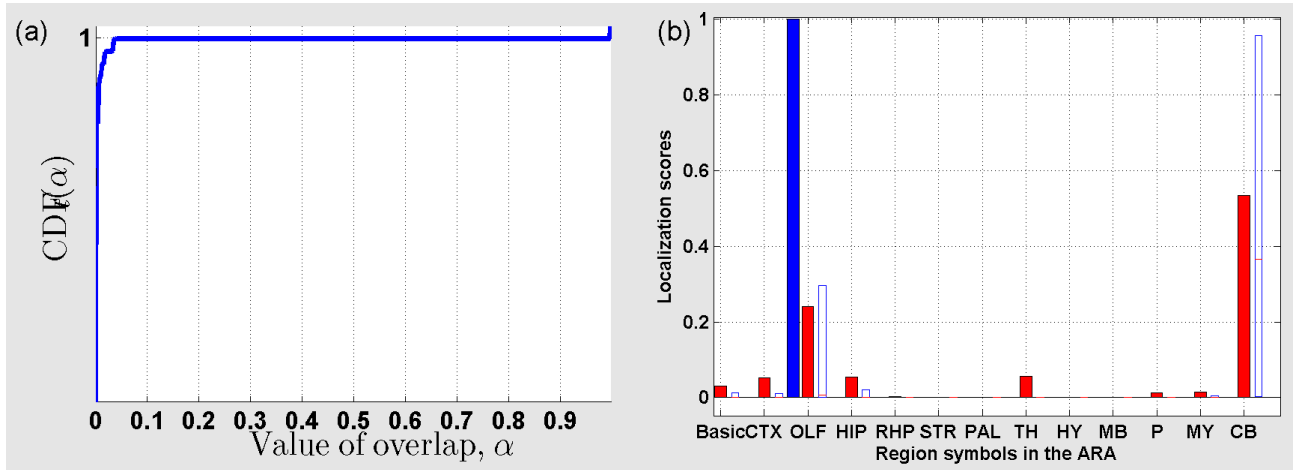


Figure 64: (a) Cumulative distribution function ( $CDF_t$ ) of the overlap between  $\rho_t$  and sub-sampled profiles for  $t = 25$ . (b) Localization scores in the coarsest version of the ARA for  $\rho_t$  (in blue), and  $\bar{\rho}_t$  (in red).

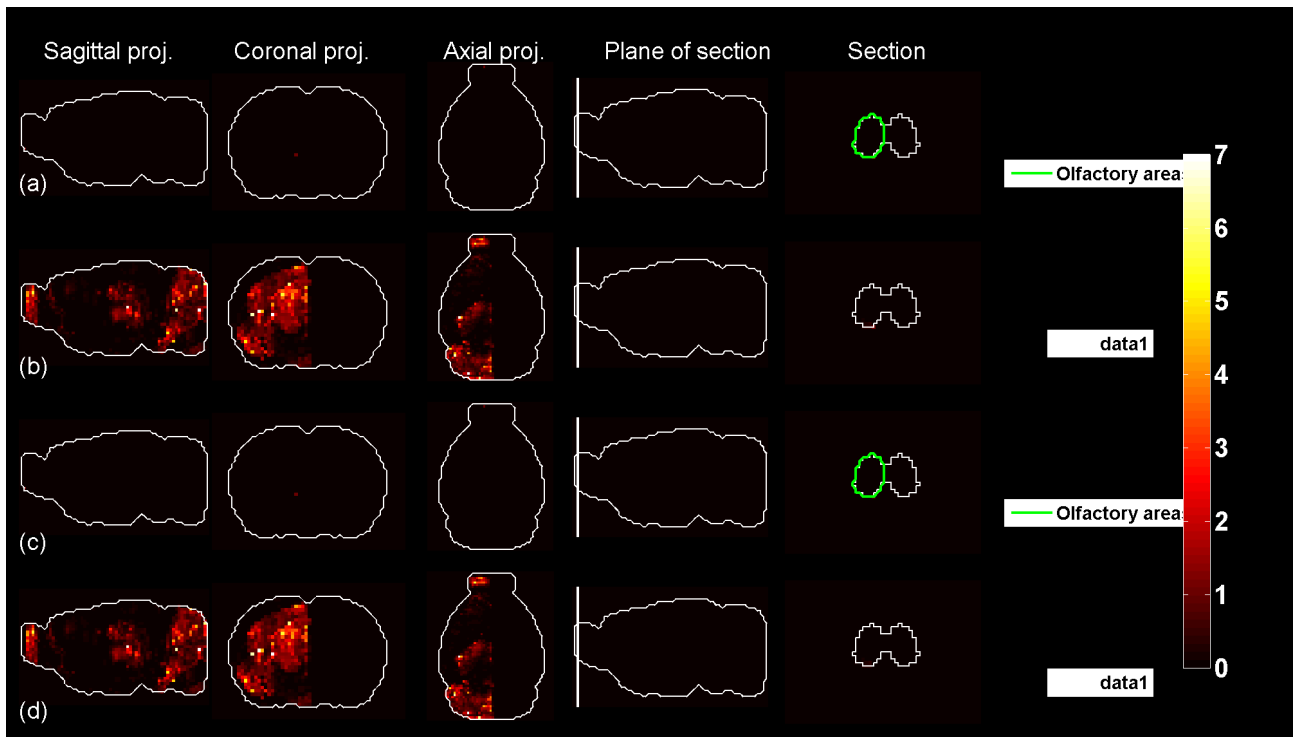


Figure 65: Predicted profile and average sub-sampled profile for  $t = 25$ .

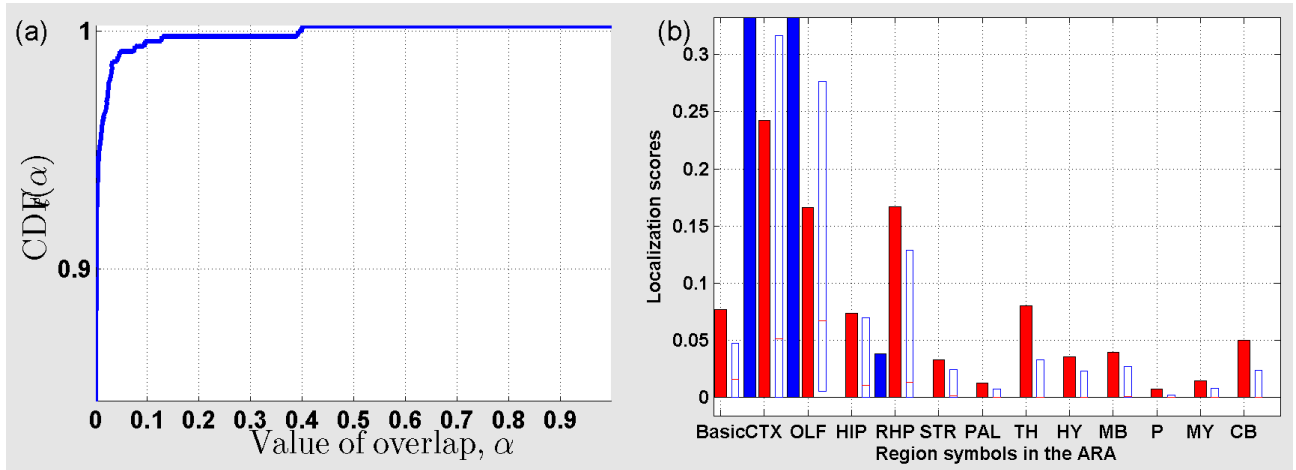


Figure 66: (a) Cumulative distribution function ( $CDF_t$ ) of the overlap between  $\rho_t$  and sub-sampled profiles for  $t = 26$ . (b) Localization scores in the coarsest version of the ARA for  $\rho_t$  (in blue), and  $\bar{\rho}_t$  (in red).

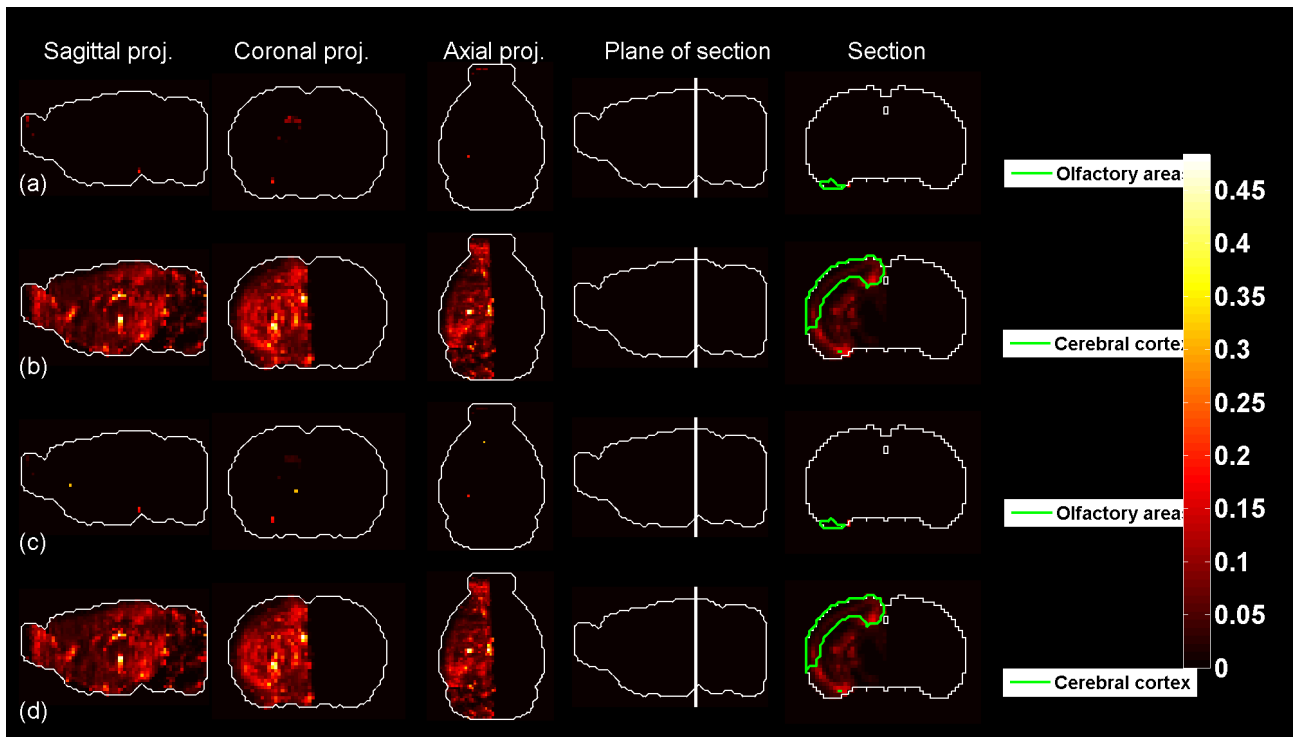


Figure 67: Predicted profile and average sub-sampled profile for  $t = 26$ .

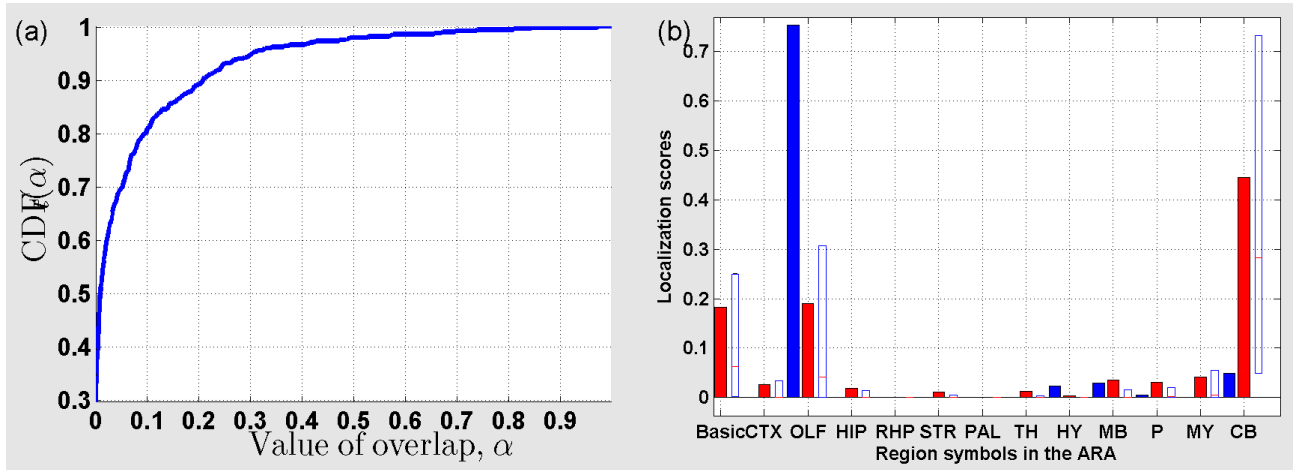


Figure 68: (a) Cumulative distribution function ( $CDF_t$ ) of the overlap between  $\rho_t$  and sub-sampled profiles for  $t = 27$ . (b) Localization scores in the coarsest version of the ARA for  $\rho_t$  (in blue), and  $\bar{\rho}_t$  (in red).

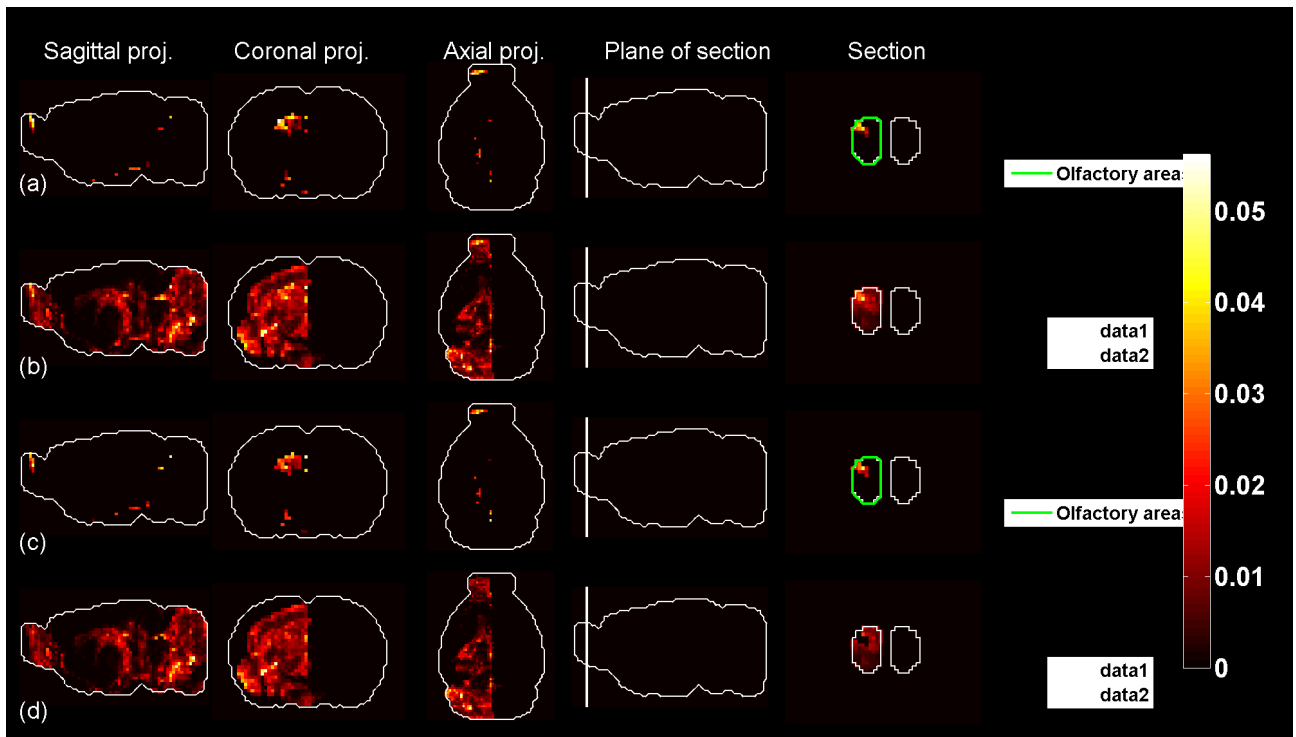


Figure 69: Predicted profile and average sub-sampled profile for  $t = 27$ .

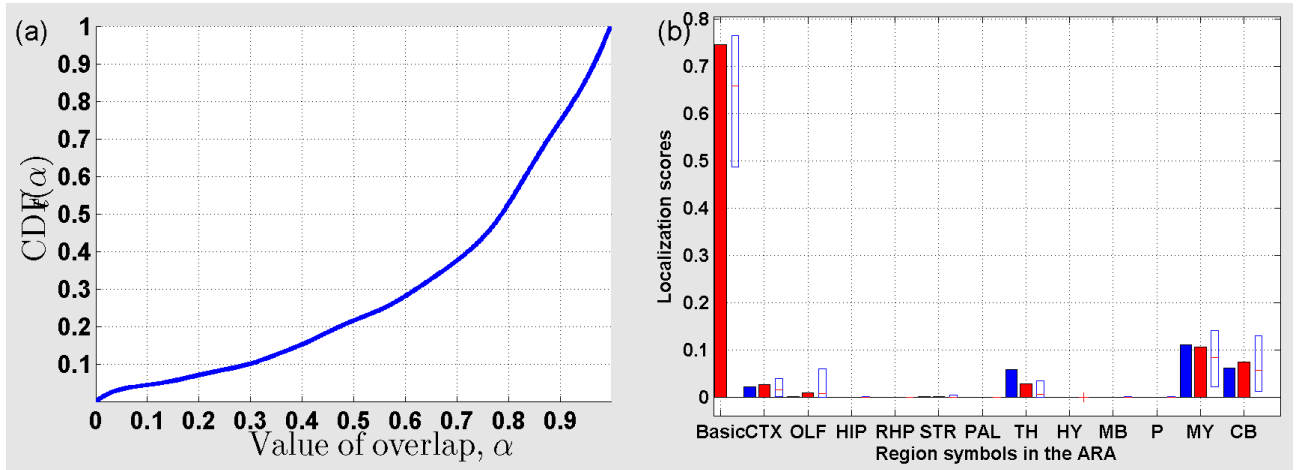


Figure 70: (a) Cumulative distribution function ( $CDF_t$ ) of the overlap between  $\rho_t$  and sub-sampled profiles for  $t = 28$ . (b) Localization scores in the coarsest version of the ARA for  $\rho_t$  (in blue), and  $\bar{\rho}_t$  (in red).

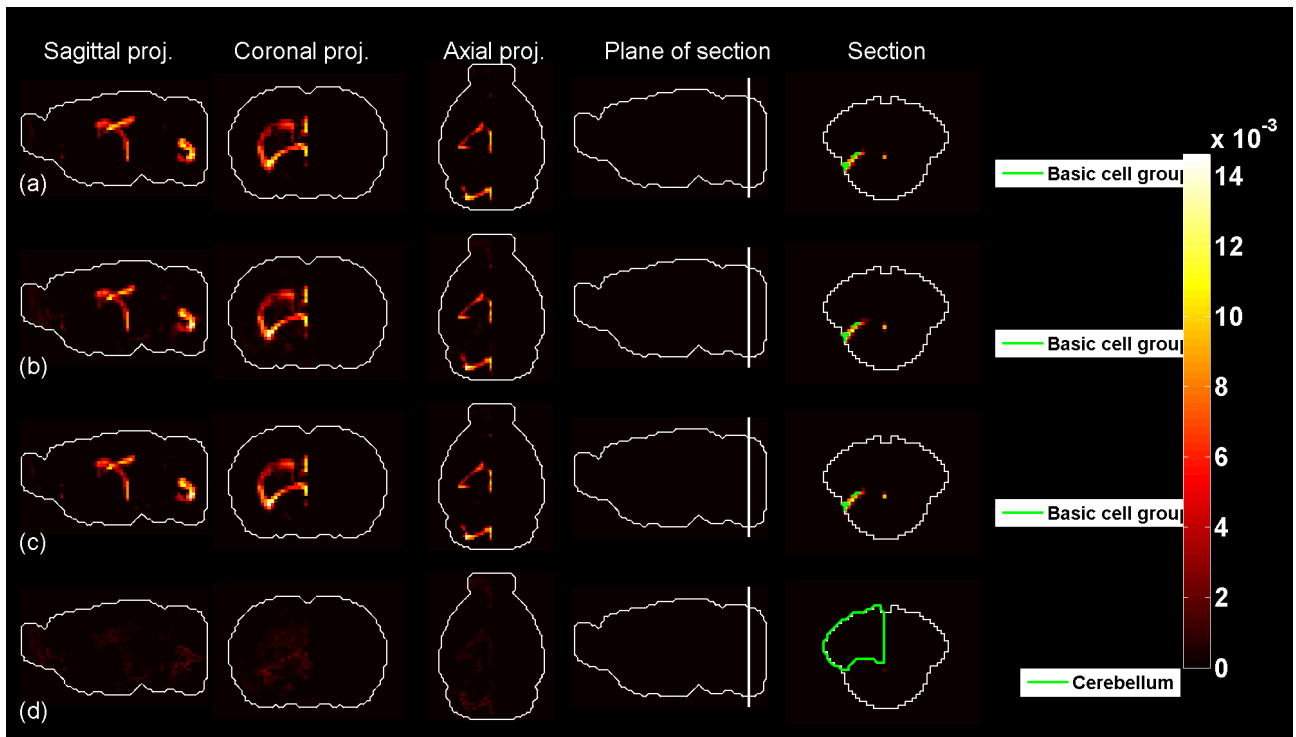


Figure 71: Predicted profile and average sub-sampled profile for  $t = 28$ .

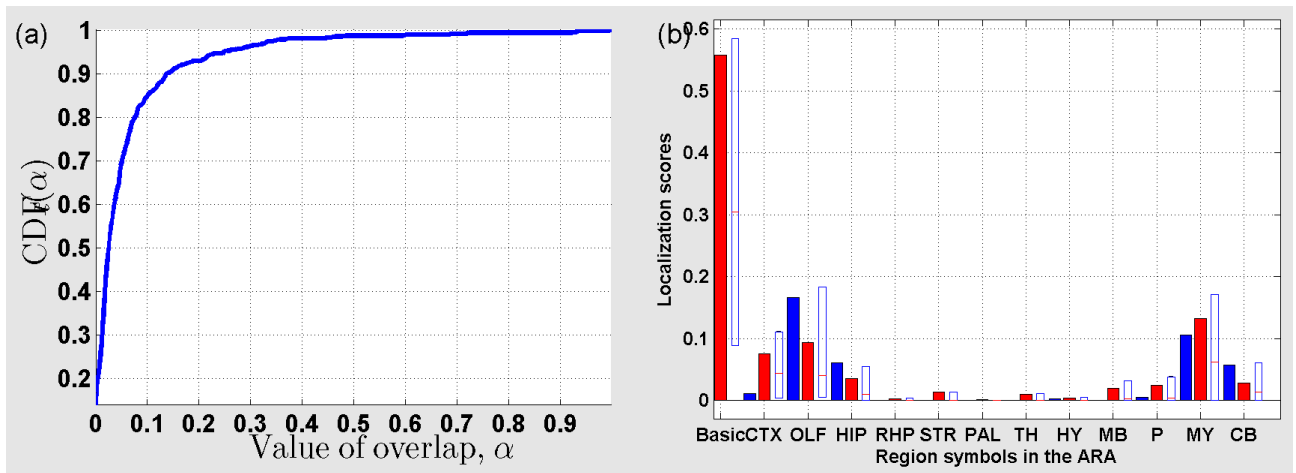


Figure 72: (a) Cumulative distribution function ( $CDF_t$ ) of the overlap between  $\rho_t$  and sub-sampled profiles for  $t = 29$ . (b) Localization scores in the coarsest version of the ARA for  $\rho_t$  (in blue), and  $\bar{\rho}_t$  (in red).

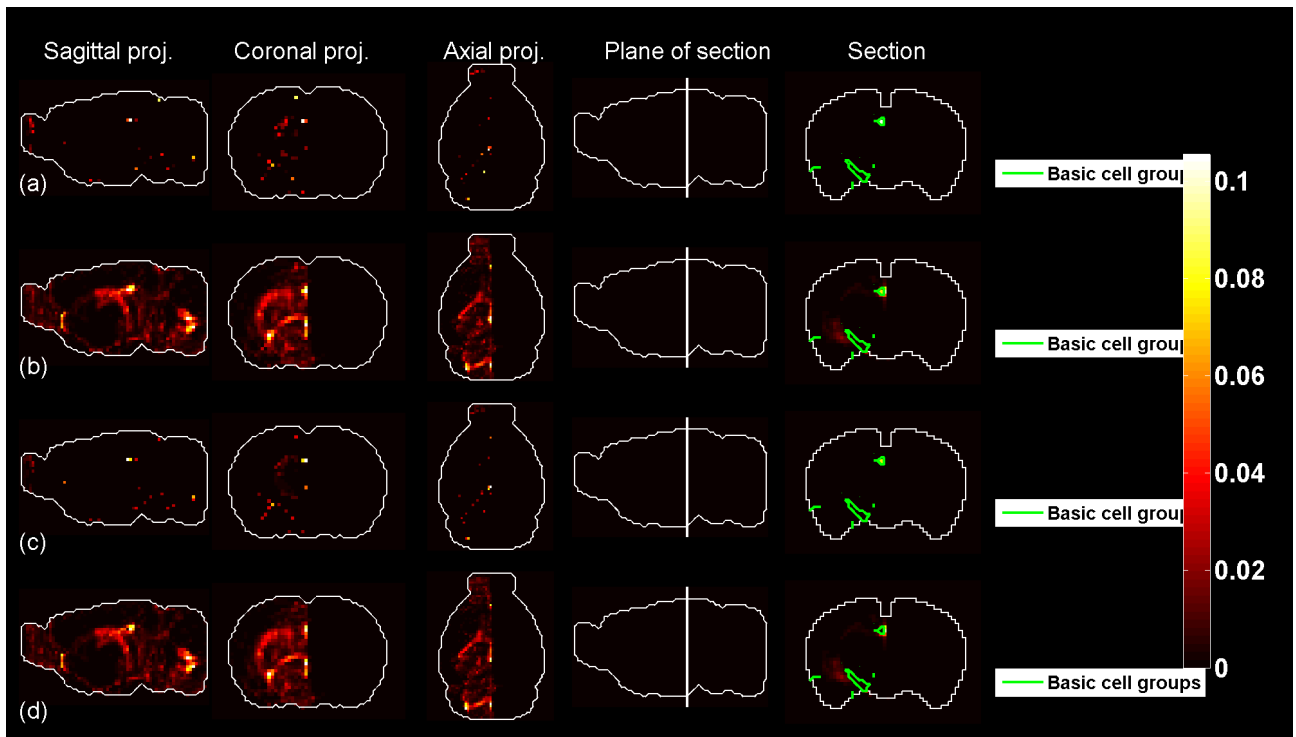


Figure 73: Predicted profile and average sub-sampled profile for  $t = 29$ .

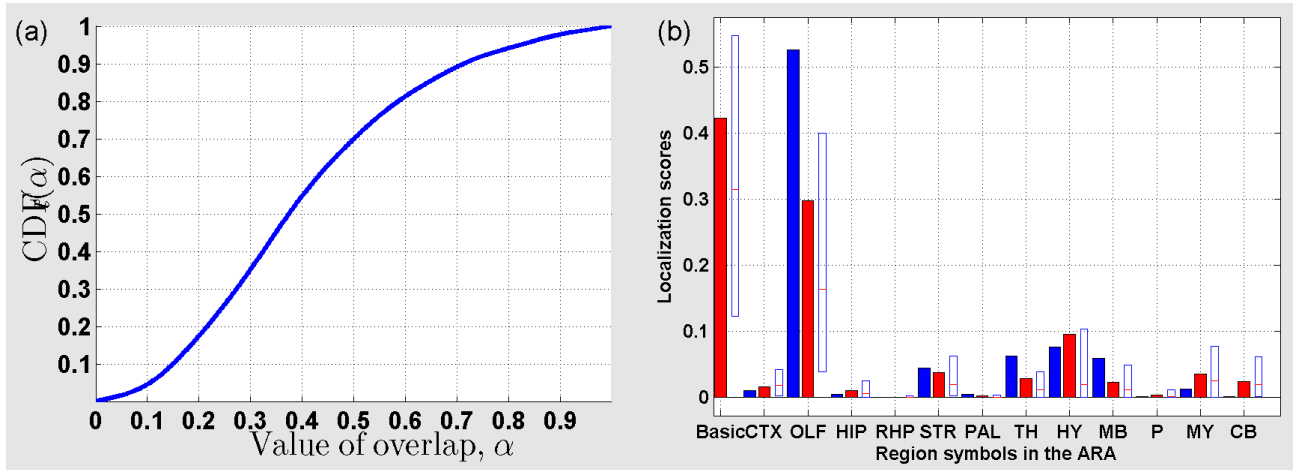


Figure 74: (a) Cumulative distribution function ( $CDF_t$ ) of the overlap between  $\rho_t$  and sub-sampled profiles for  $t = 30$ . (b) Localization scores in the coarsest version of the ARA for  $\rho_t$  (in blue), and  $\bar{\rho}_t$  (in red).

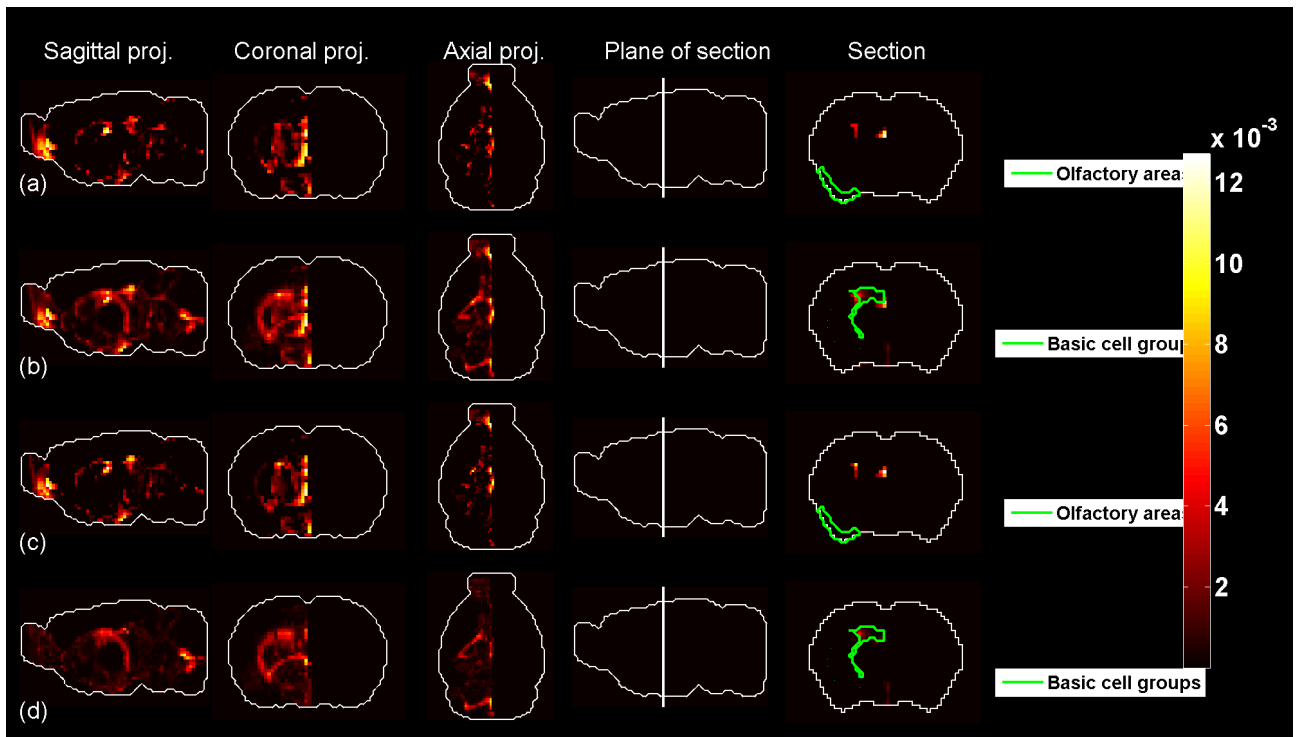


Figure 75: Predicted profile and average sub-sampled profile for  $t = 30$ .

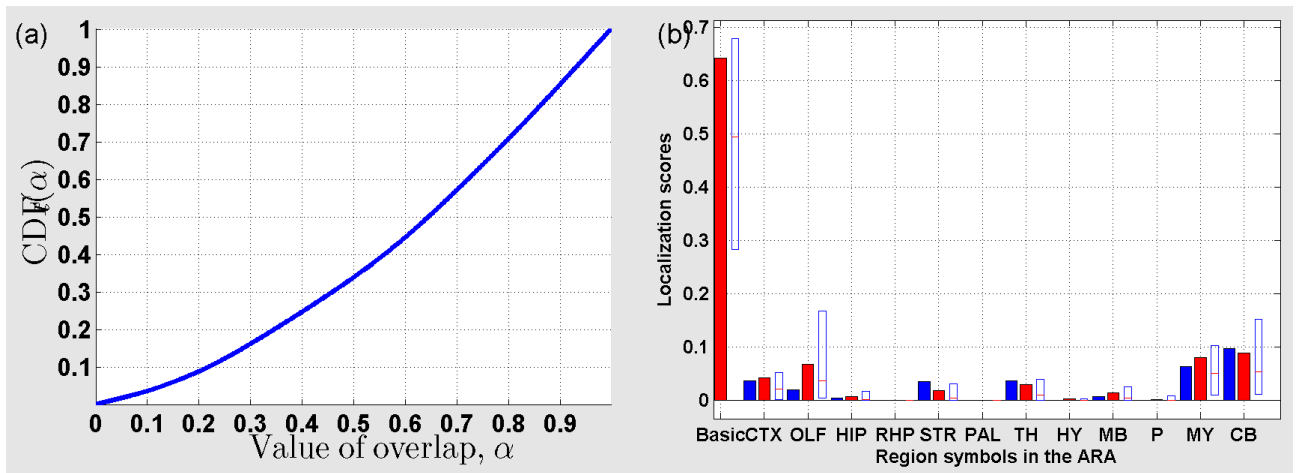


Figure 76: (a) Cumulative distribution function ( $CDF_t$ ) of the overlap between  $\rho_t$  and sub-sampled profiles for  $t = 31$ . (b) Localization scores in the coarsest version of the ARA for  $\rho_t$  (in blue), and  $\bar{\rho}_t$  (in red).

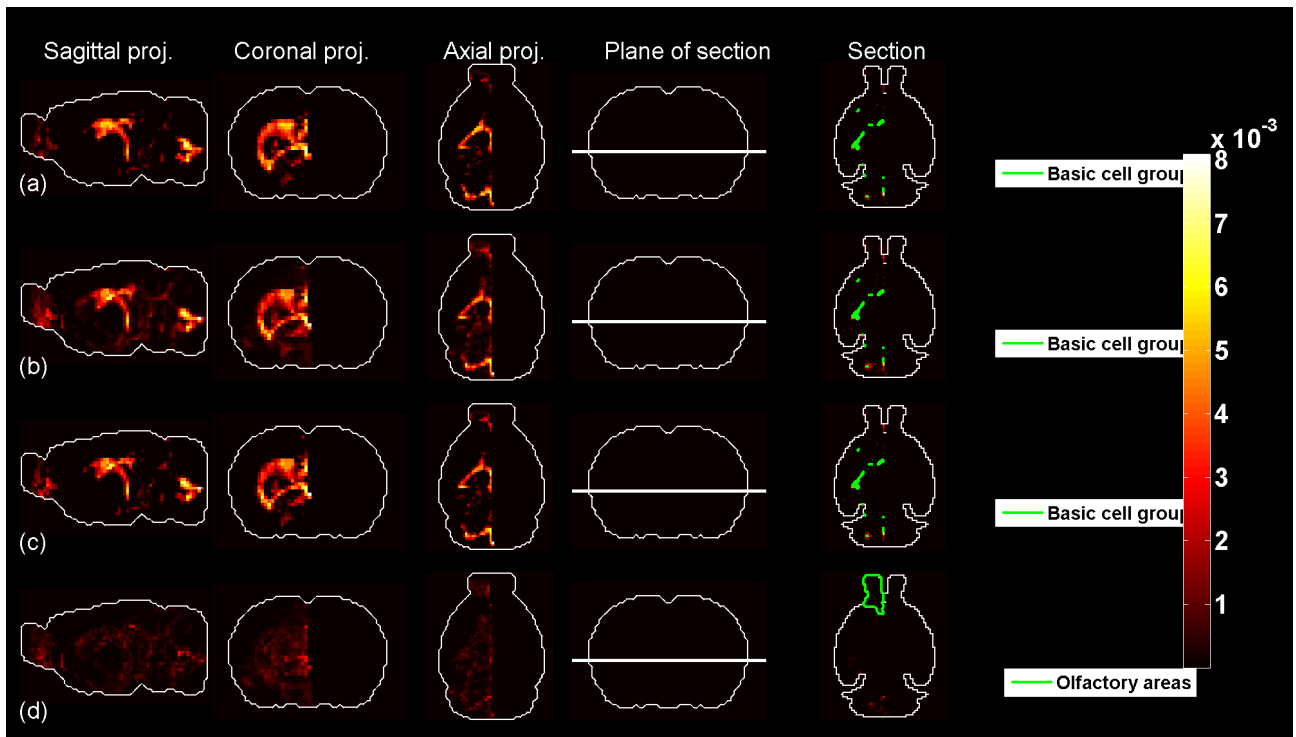


Figure 77: Predicted profile and average sub-sampled profile for  $t = 31$ .

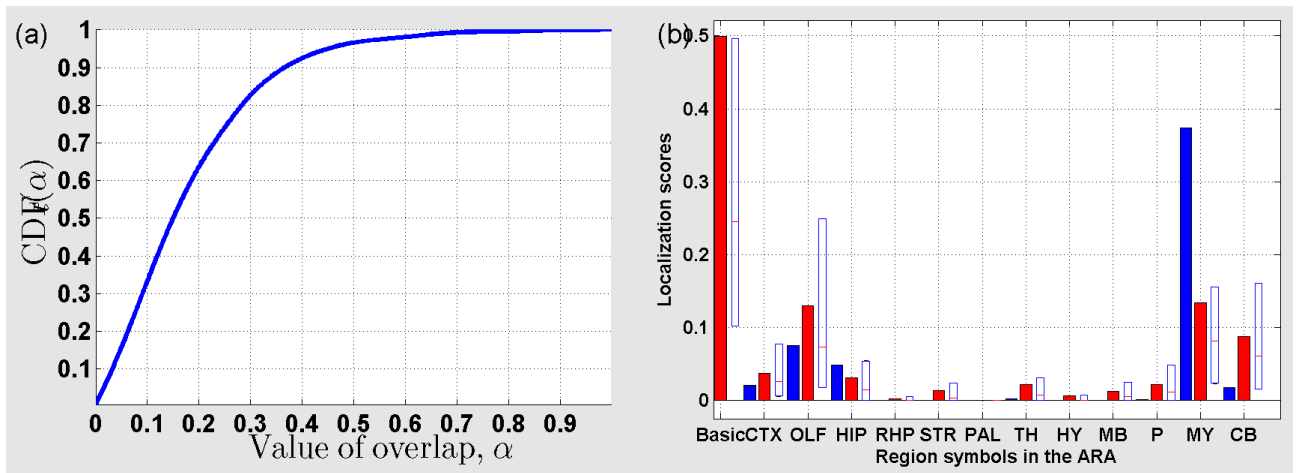


Figure 78: (a) Cumulative distribution function ( $CDF_t$ ) of the overlap between  $\rho_t$  and sub-sampled profiles for  $t = 32$ . (b) Localization scores in the coarsest version of the ARA for  $\rho_t$  (in blue), and  $\bar{\rho}_t$  (in red).

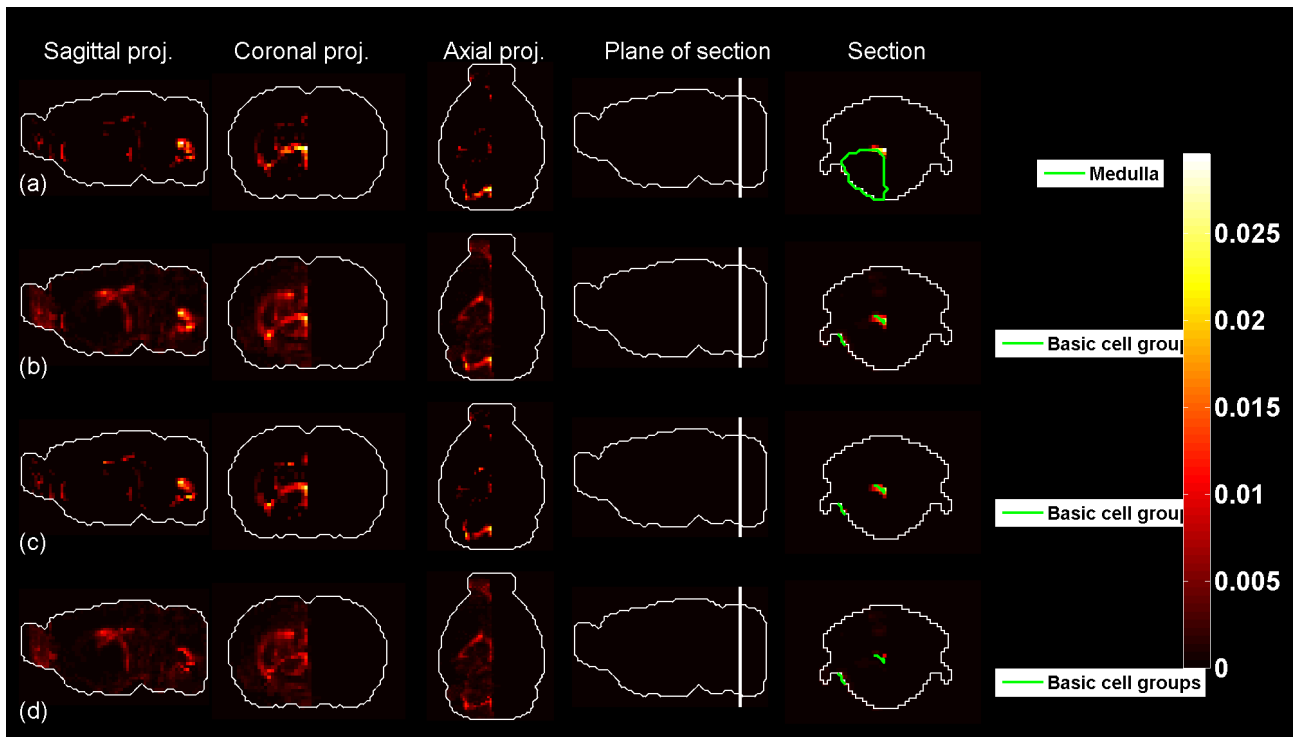


Figure 79: Predicted profile and average sub-sampled profile for  $t = 32$ .

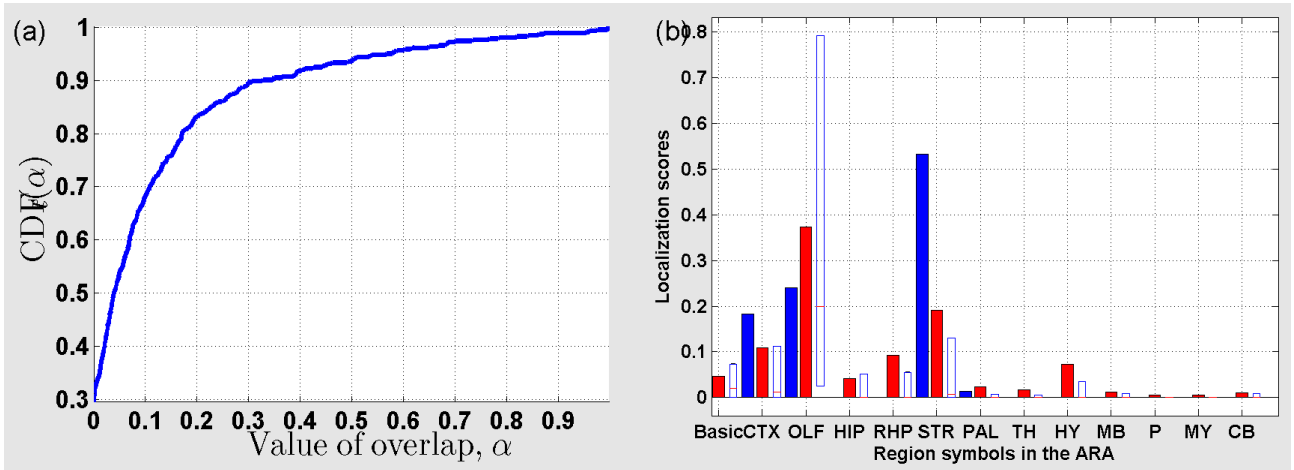


Figure 80: (a) Cumulative distribution function ( $CDF_t$ ) of the overlap between  $\rho_t$  and sub-sampled profiles for  $t = 33$ . (b) Localization scores in the coarsest version of the ARA for  $\rho_t$  (in blue), and  $\bar{\rho}_t$  (in red).

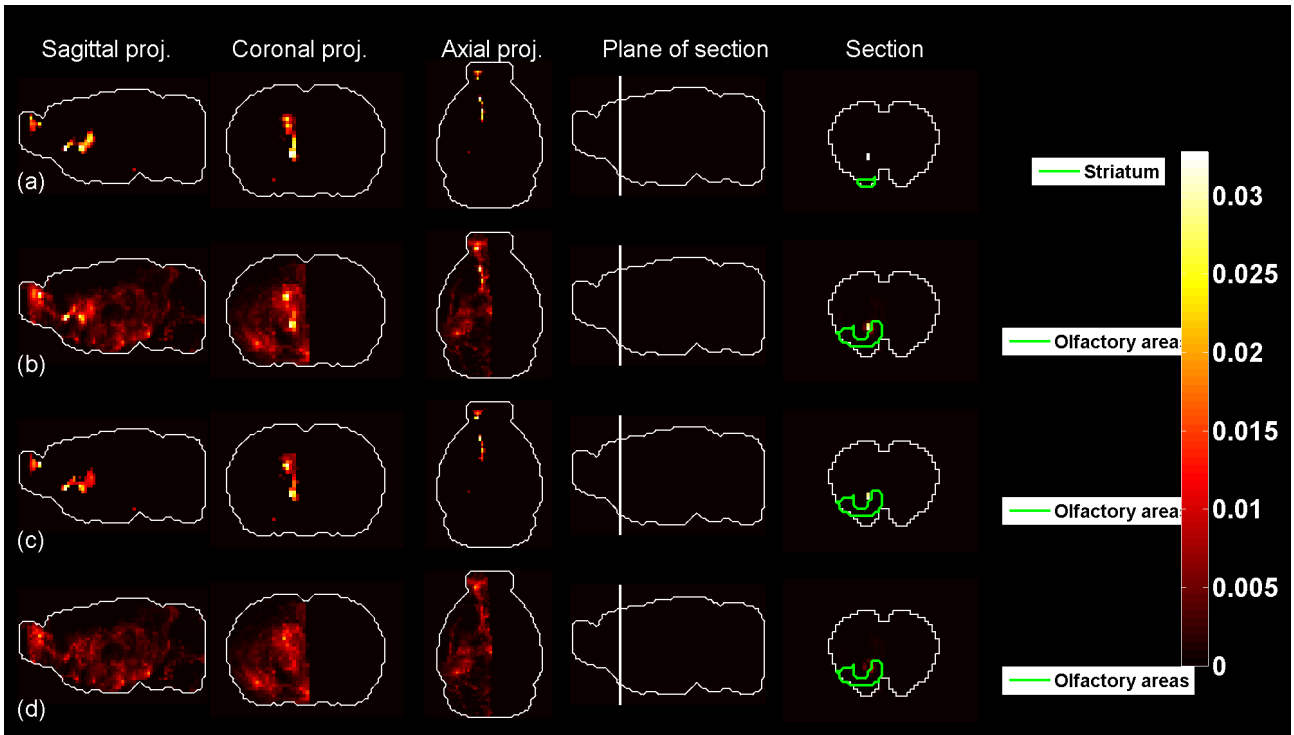


Figure 81: Predicted profile and average sub-sampled profile for  $t = 33$ .

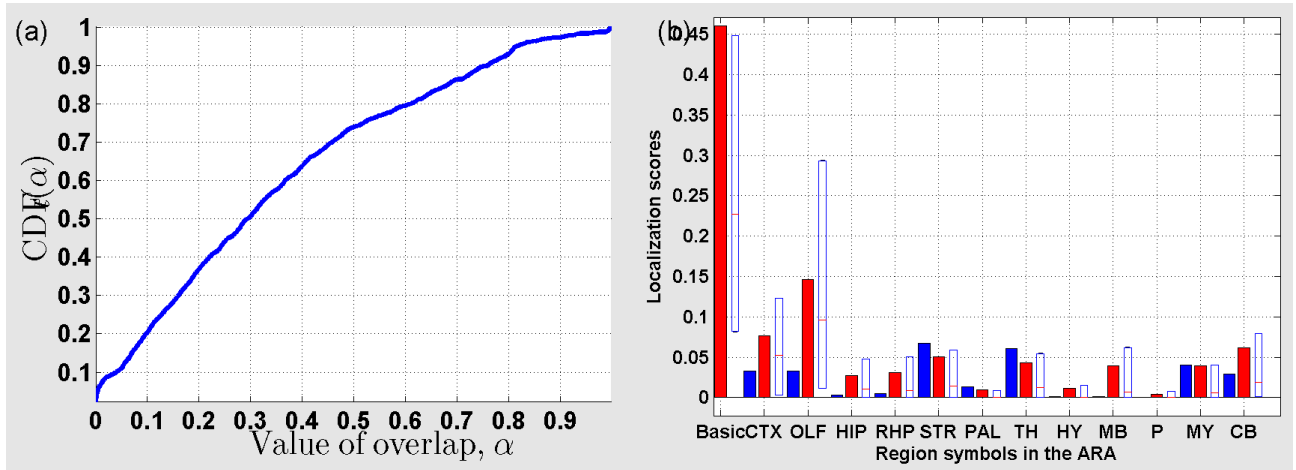


Figure 82: (a) Cumulative distribution function ( $CDF_t$ ) of the overlap between  $\rho_t$  and sub-sampled profiles for  $t = 34$ . (b) Localization scores in the coarsest version of the ARA for  $\rho_t$  (in blue), and  $\bar{\rho}_t$  (in red).

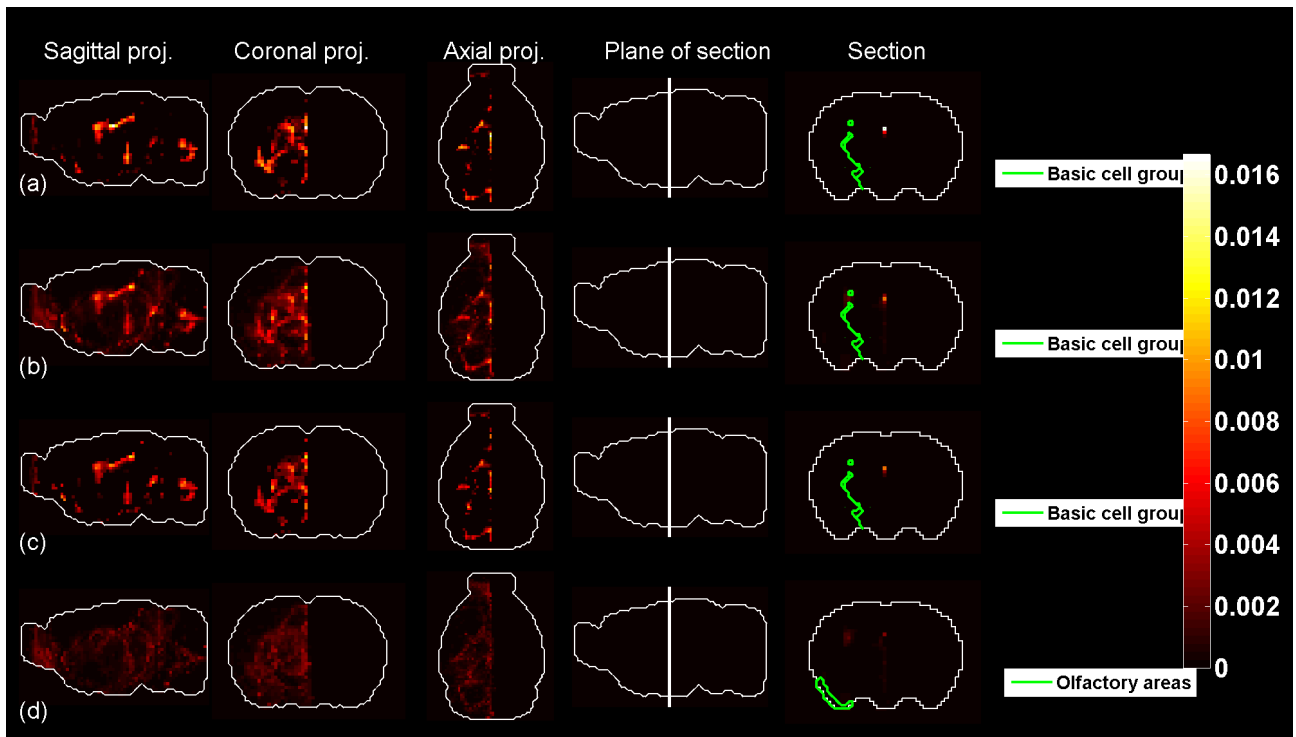


Figure 83: Predicted profile and average sub-sampled profile for  $t = 34$ .

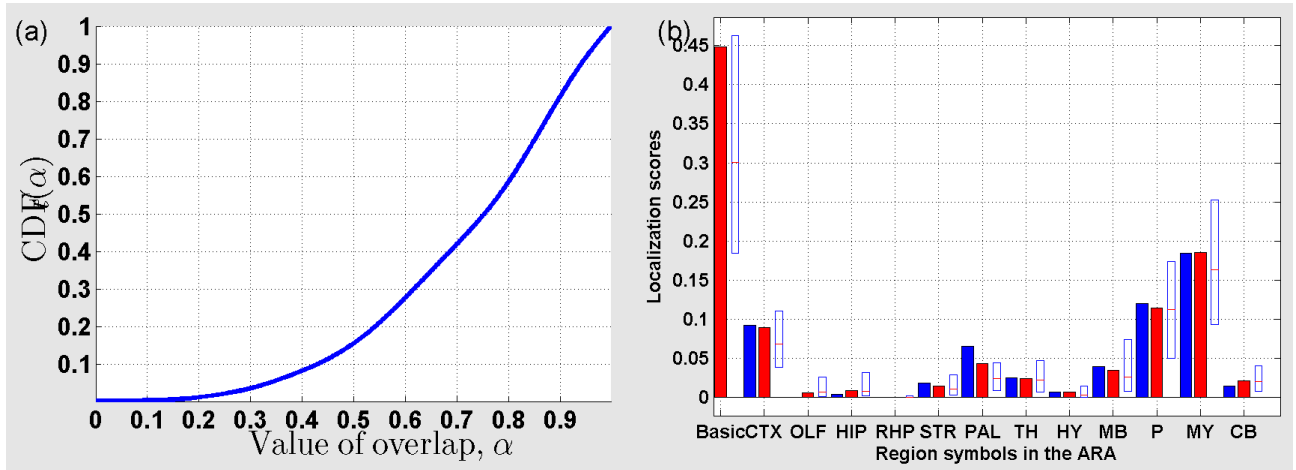


Figure 84: (a) Cumulative distribution function ( $CDF_t$ ) of the overlap between  $\rho_t$  and sub-sampled profiles for  $t = 35$ . (b) Localization scores in the coarsest version of the ARA for  $\rho_t$  (in blue), and  $\bar{\rho}_t$  (in red).

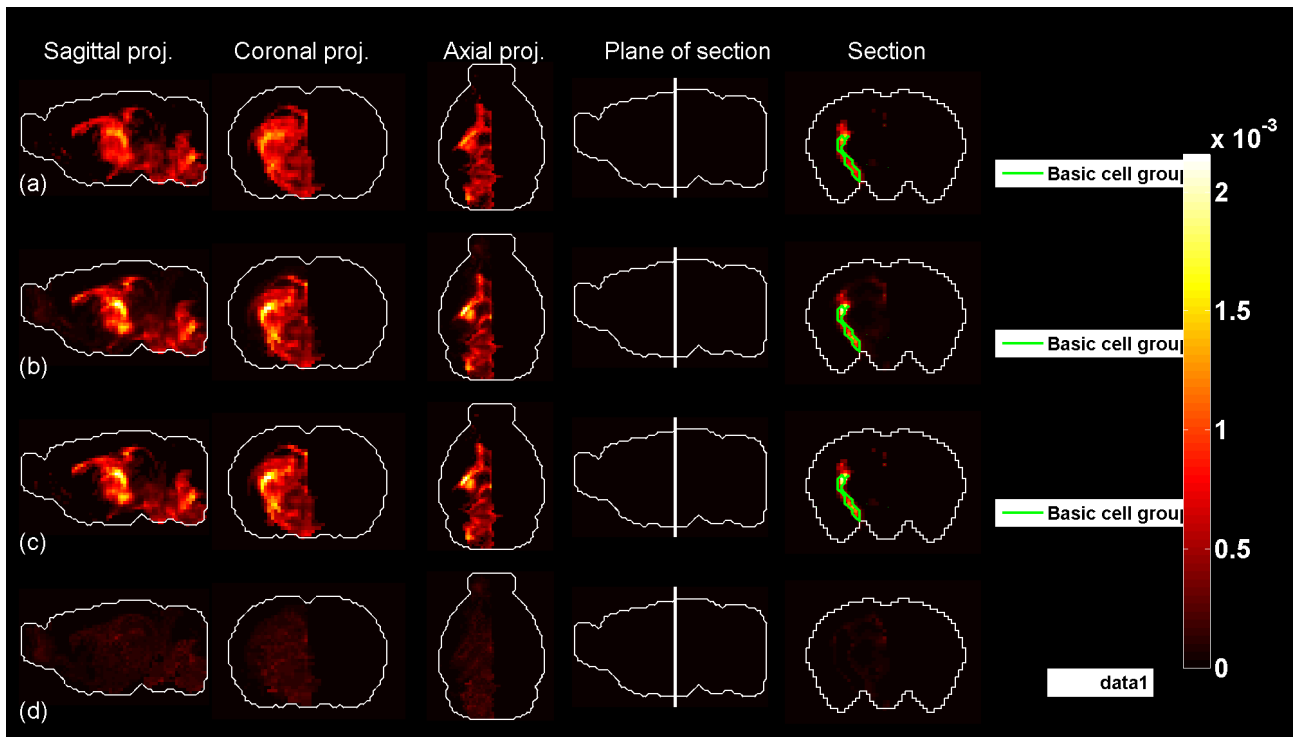


Figure 85: Predicted profile and average sub-sampled profile for  $t = 35$ .

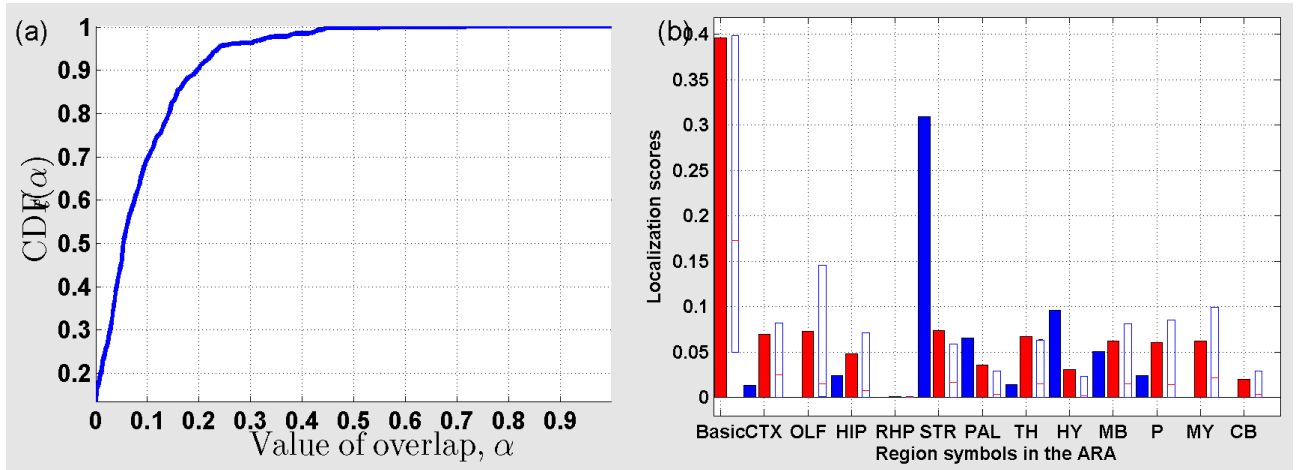


Figure 86: (a) Cumulative distribution function ( $CDF_t$ ) of the overlap between  $\rho_t$  and sub-sampled profiles for  $t = 36$ . (b) Localization scores in the coarsest version of the ARA for  $\rho_t$  (in blue), and  $\bar{\rho}_t$  (in red).

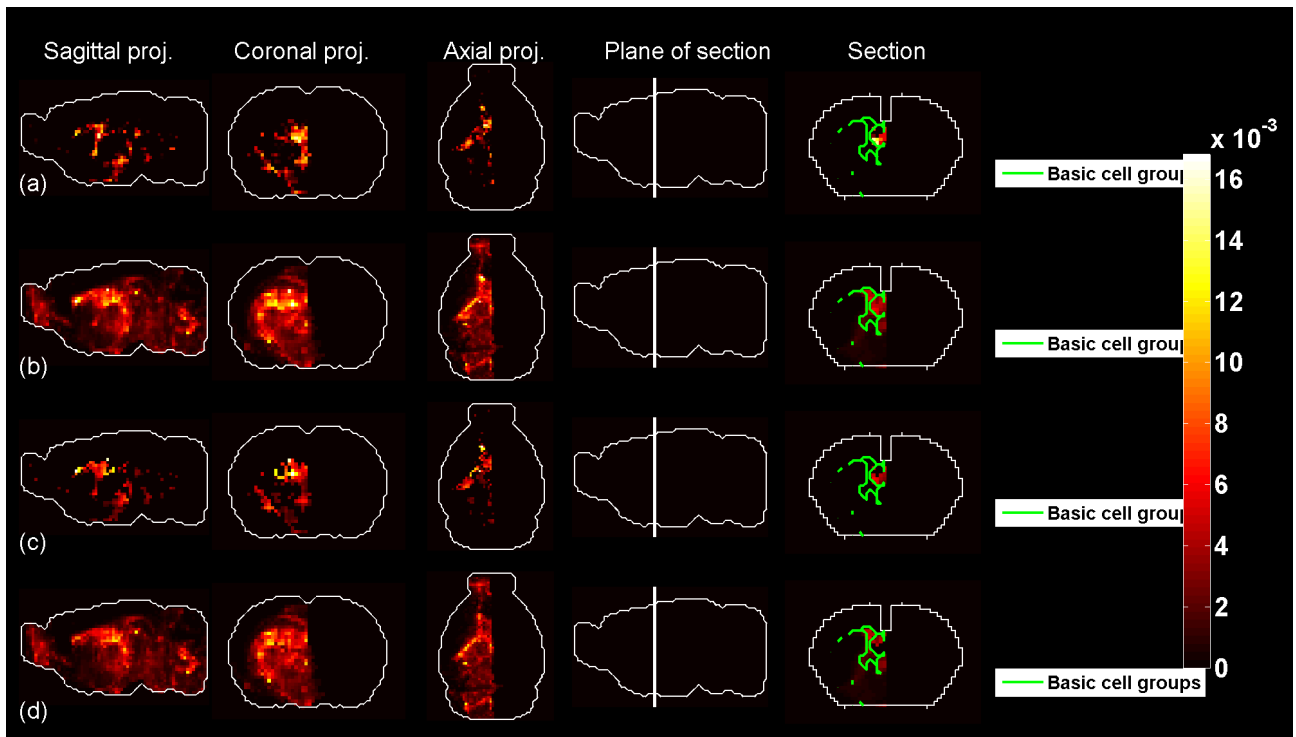


Figure 87: Predicted profile and average sub-sampled profile for  $t = 36$ .

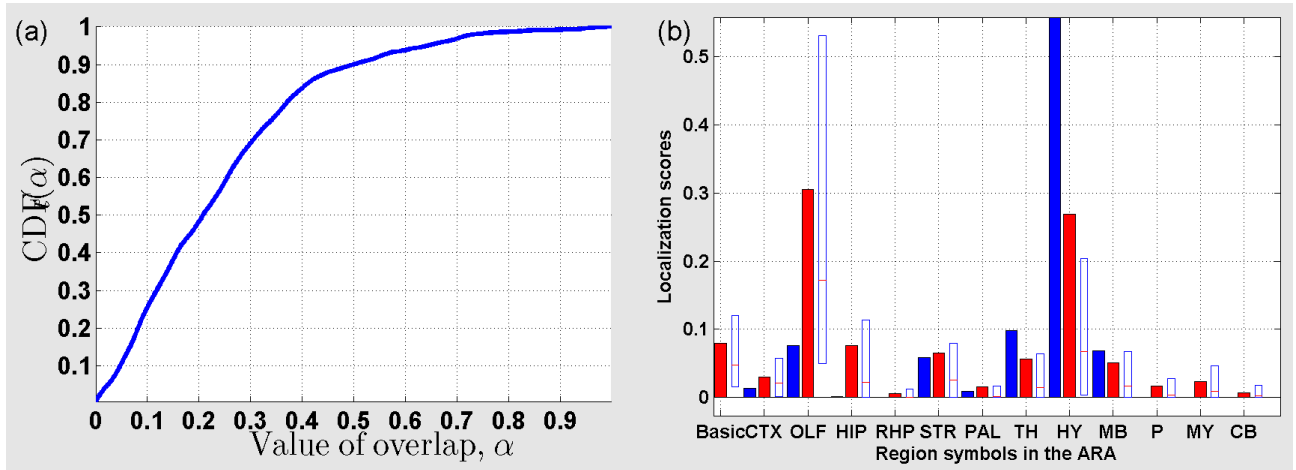


Figure 88: (a) Cumulative distribution function ( $CDF_t$ ) of the overlap between  $\rho_t$  and sub-sampled profiles for  $t = 37$ . (b) Localization scores in the coarsest version of the ARA for  $\rho_t$  (in blue), and  $\bar{\rho}_t$  (in red).

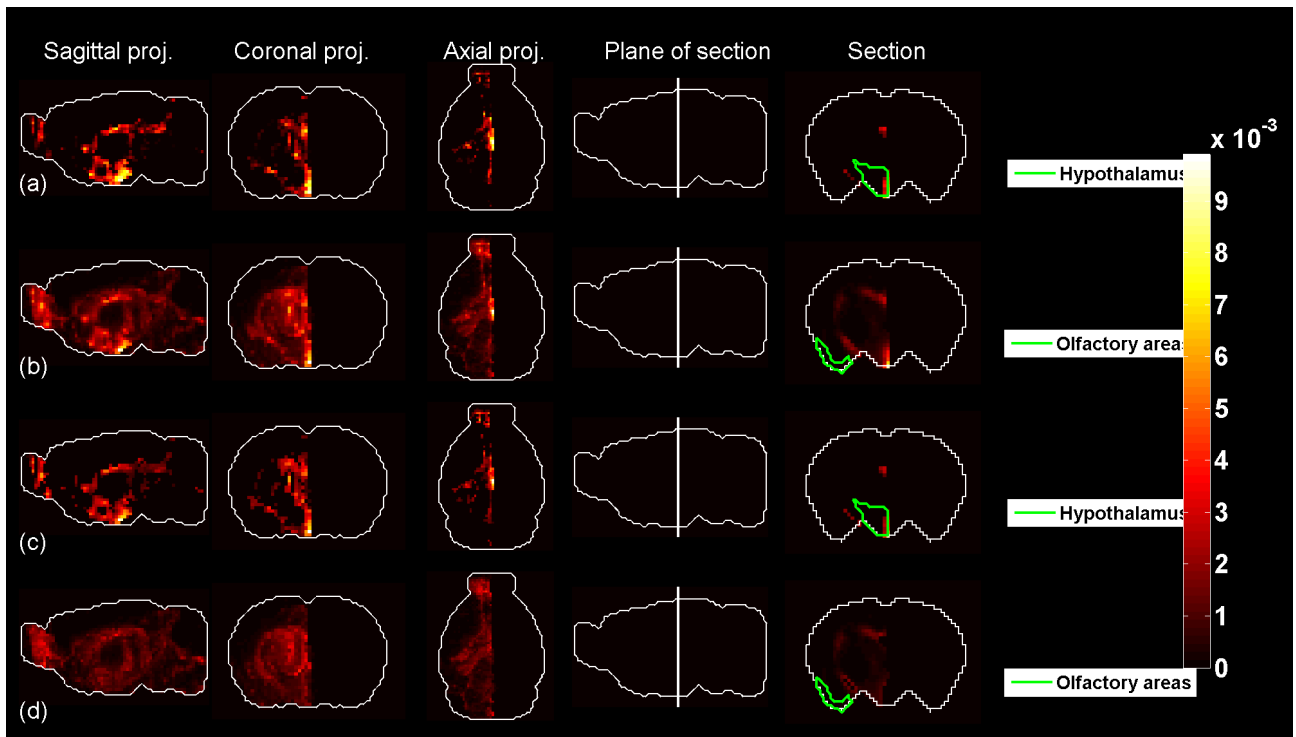


Figure 89: Predicted profile and average sub-sampled profile for  $t = 37$ .

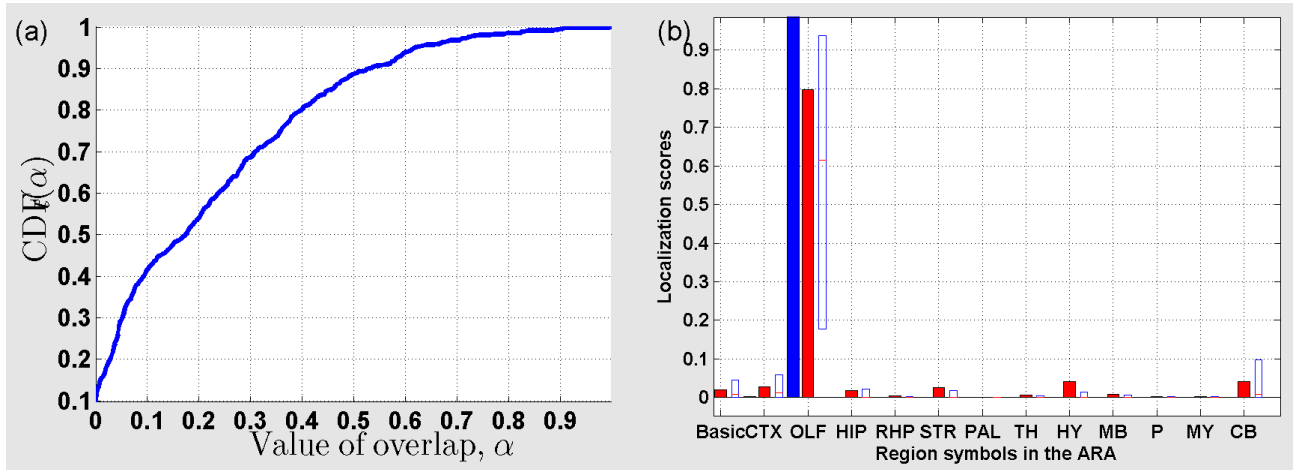


Figure 90: (a) Cumulative distribution function ( $CDF_t$ ) of the overlap between  $\rho_t$  and sub-sampled profiles for  $t = 38$ . (b) Localization scores in the coarsest version of the ARA for  $\rho_t$  (in blue), and  $\bar{\rho}_t$  (in red).

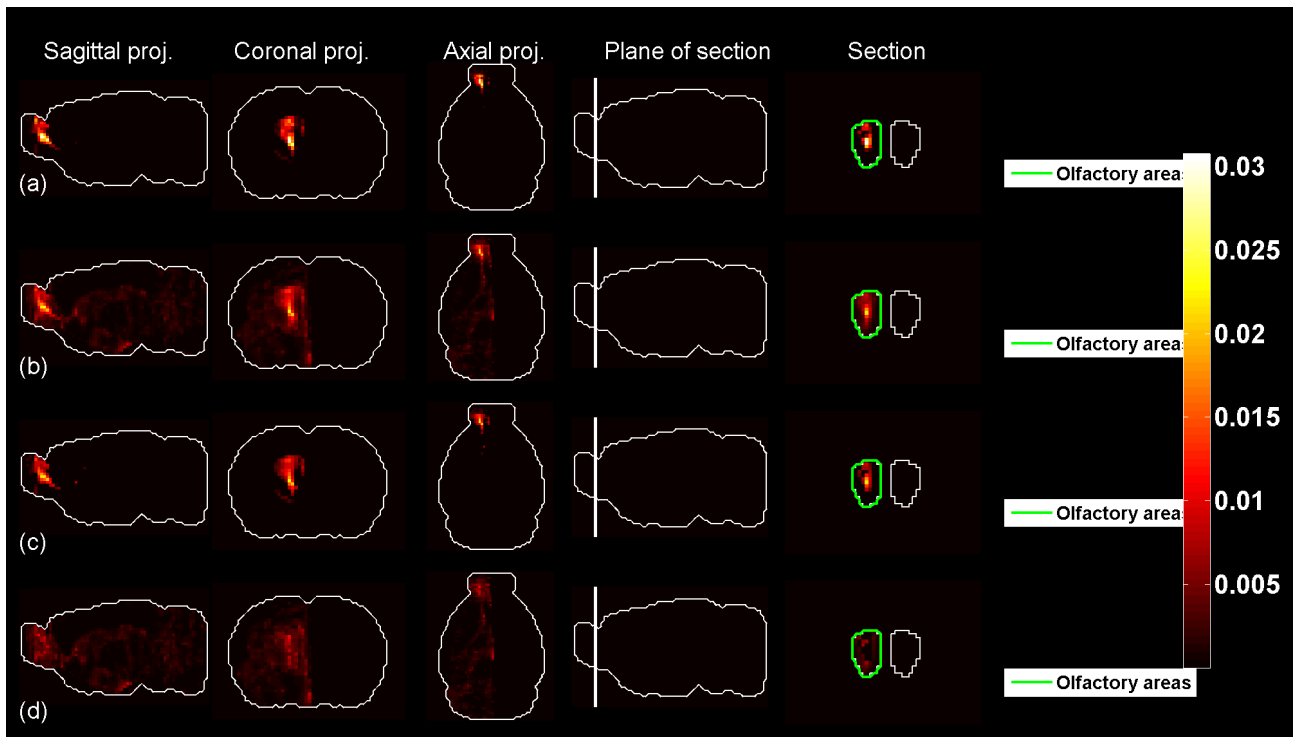


Figure 91: Predicted profile and average sub-sampled profile for  $t = 38$ .

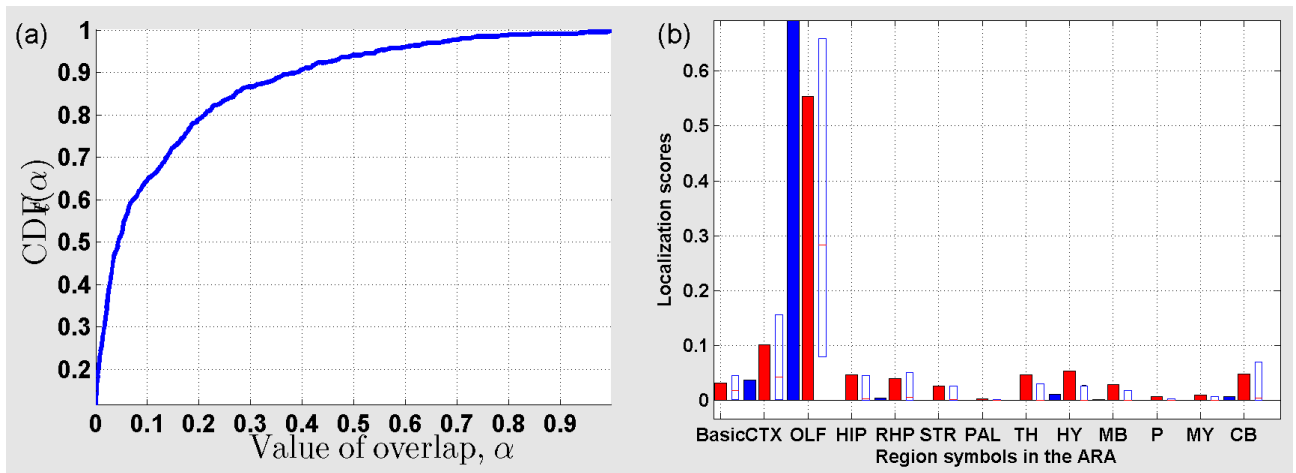


Figure 92: (a) Cumulative distribution function ( $CDF_t$ ) of the overlap between  $\rho_t$  and sub-sampled profiles for  $t = 39$ . (b) Localization scores in the coarsest version of the ARA for  $\rho_t$  (in blue), and  $\bar{\rho}_t$  (in red).

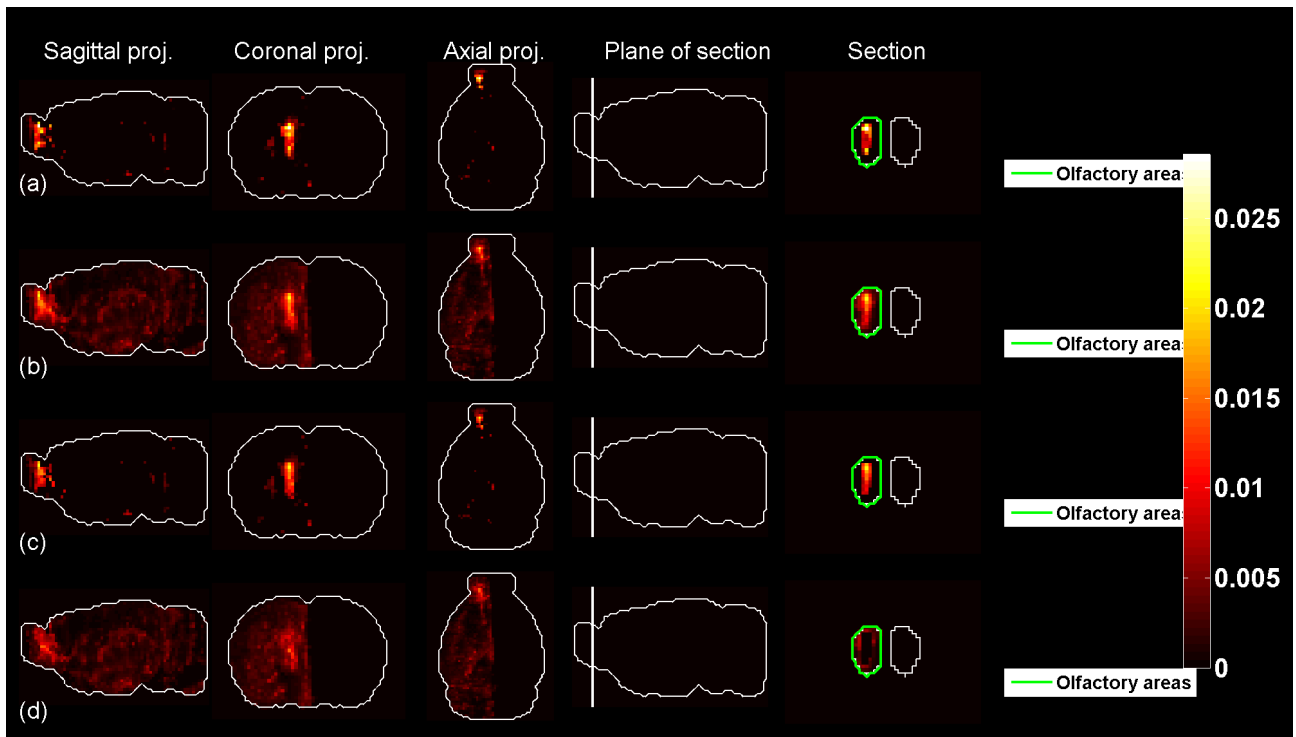


Figure 93: Predicted profile and average sub-sampled profile for  $t = 39$ .

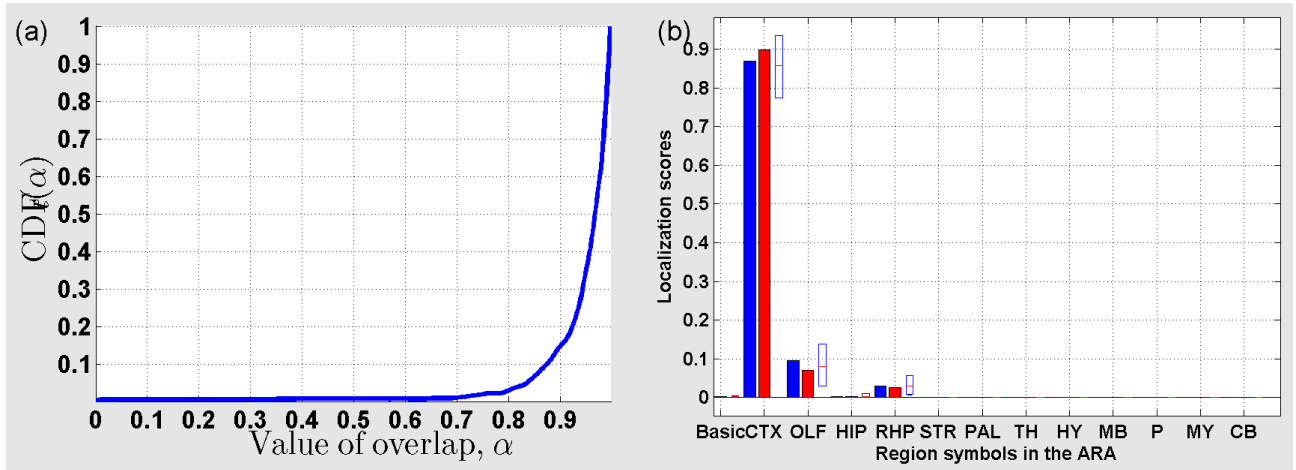


Figure 94: (a) Cumulative distribution function ( $CDF_t$ ) of the overlap between  $\rho_t$  and sub-sampled profiles for  $t = 40$ . (b) Localization scores in the coarsest version of the ARA for  $\rho_t$  (in blue), and  $\bar{\rho}_t$  (in red).

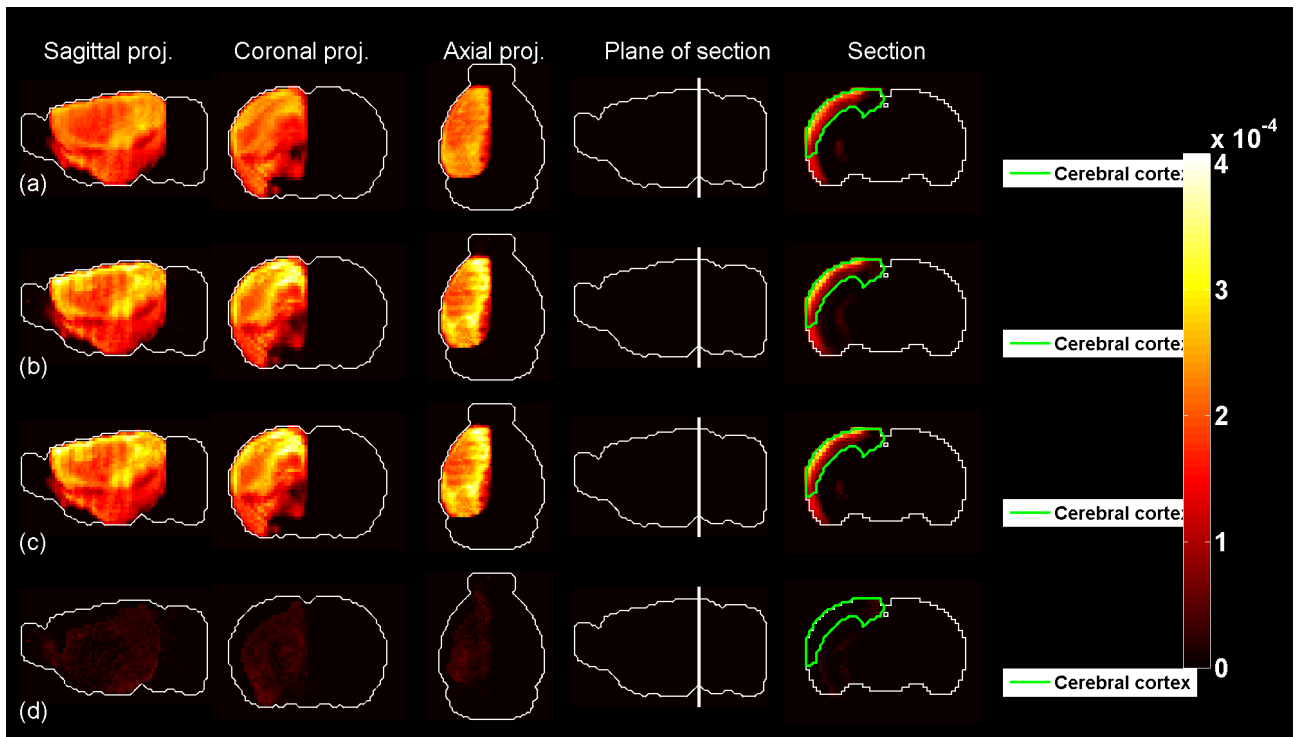


Figure 95: Predicted profile and average sub-sampled profile for  $t = 40$ .

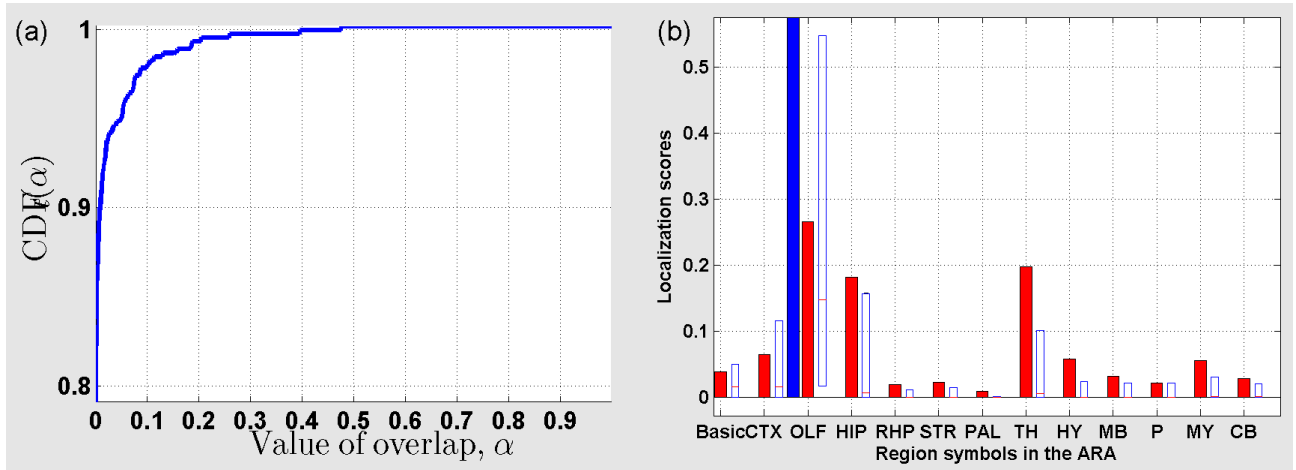


Figure 96: (a) Cumulative distribution function ( $CDF_t$ ) of the overlap between  $\rho_t$  and sub-sampled profiles for  $t = 41$ . (b) Localization scores in the coarsest version of the ARA for  $\rho_t$  (in blue), and  $\bar{\rho}_t$  (in red).

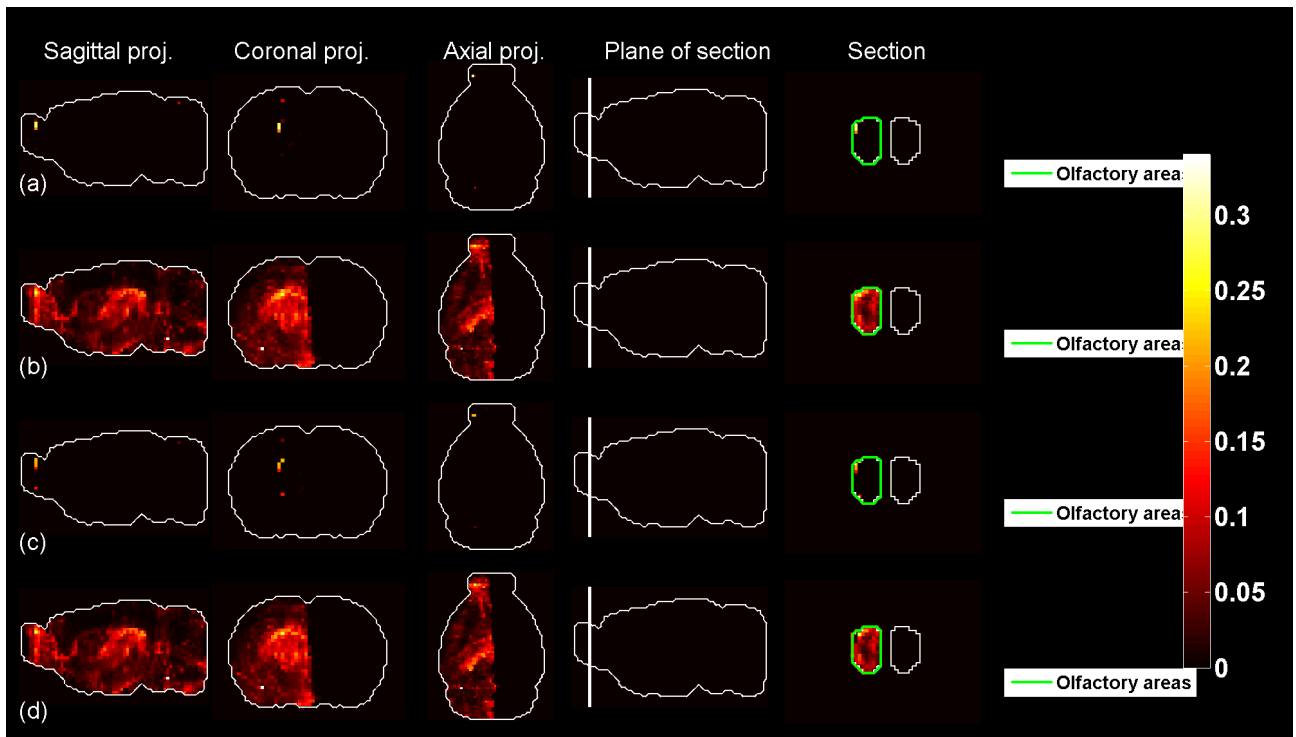


Figure 97: Predicted profile and average sub-sampled profile for  $t = 41$ .

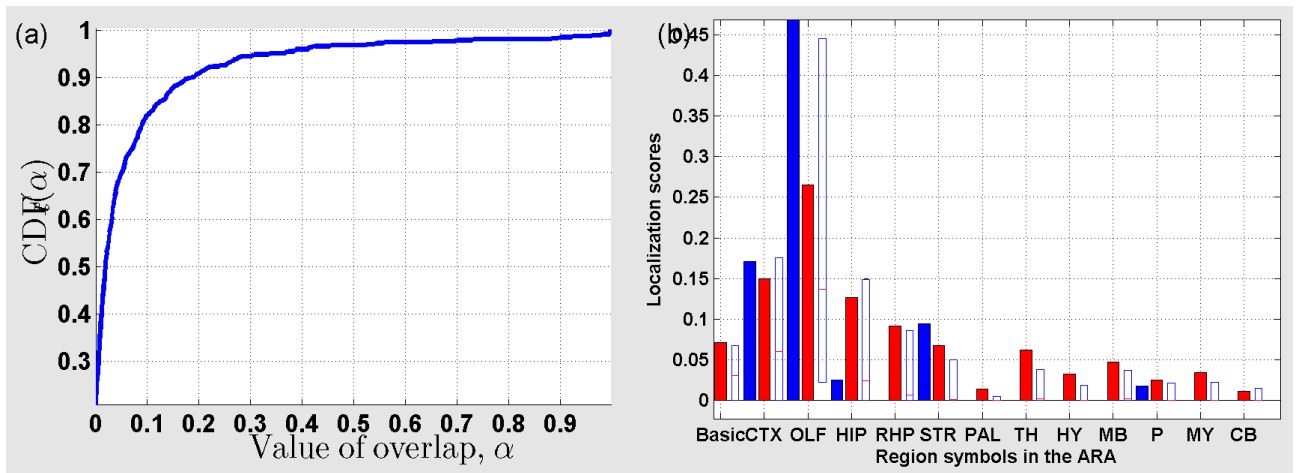


Figure 98: (a) Cumulative distribution function ( $CDF_t$ ) of the overlap between  $\rho_t$  and sub-sampled profiles for  $t = 42$ . (b) Localization scores in the coarsest version of the ARA for  $\rho_t$  (in blue), and  $\bar{\rho}_t$  (in red).

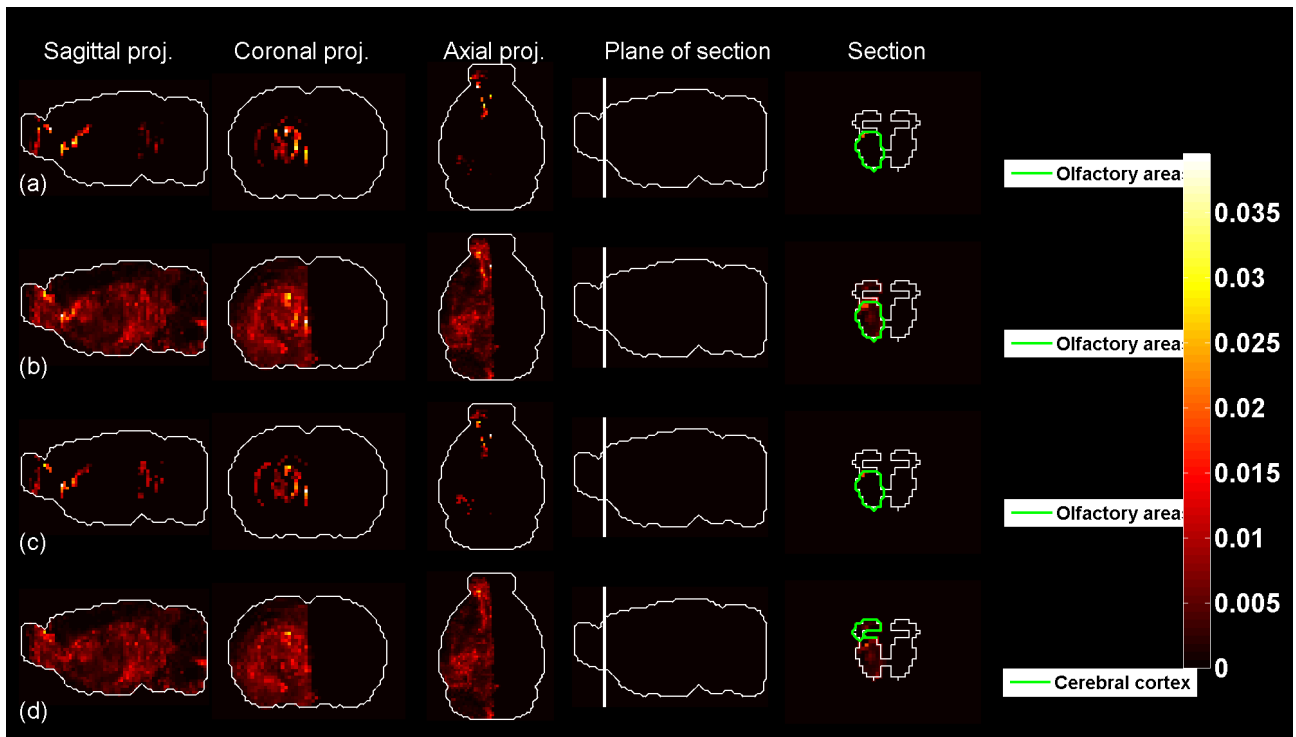


Figure 99: Predicted profile and average sub-sampled profile for  $t = 42$ .

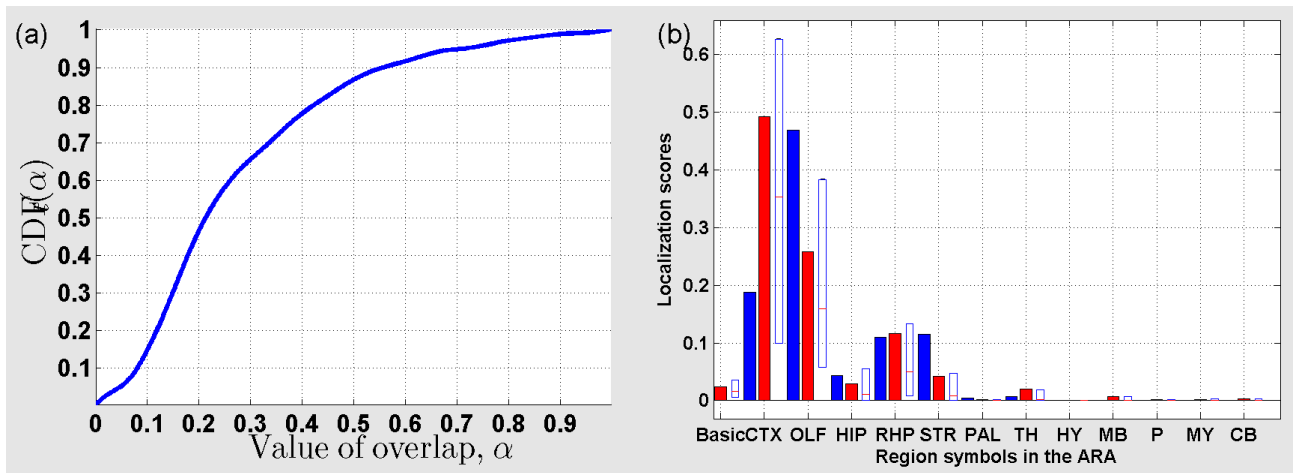


Figure 100: (a) Cumulative distribution function ( $CDF_t$ ) of the overlap between  $\rho_t$  and sub-sampled profiles for  $t = 43$ . (b) Localization scores in the coarsest version of the ARA for  $\rho_t$  (in blue), and  $\bar{\rho}_t$  (in red).

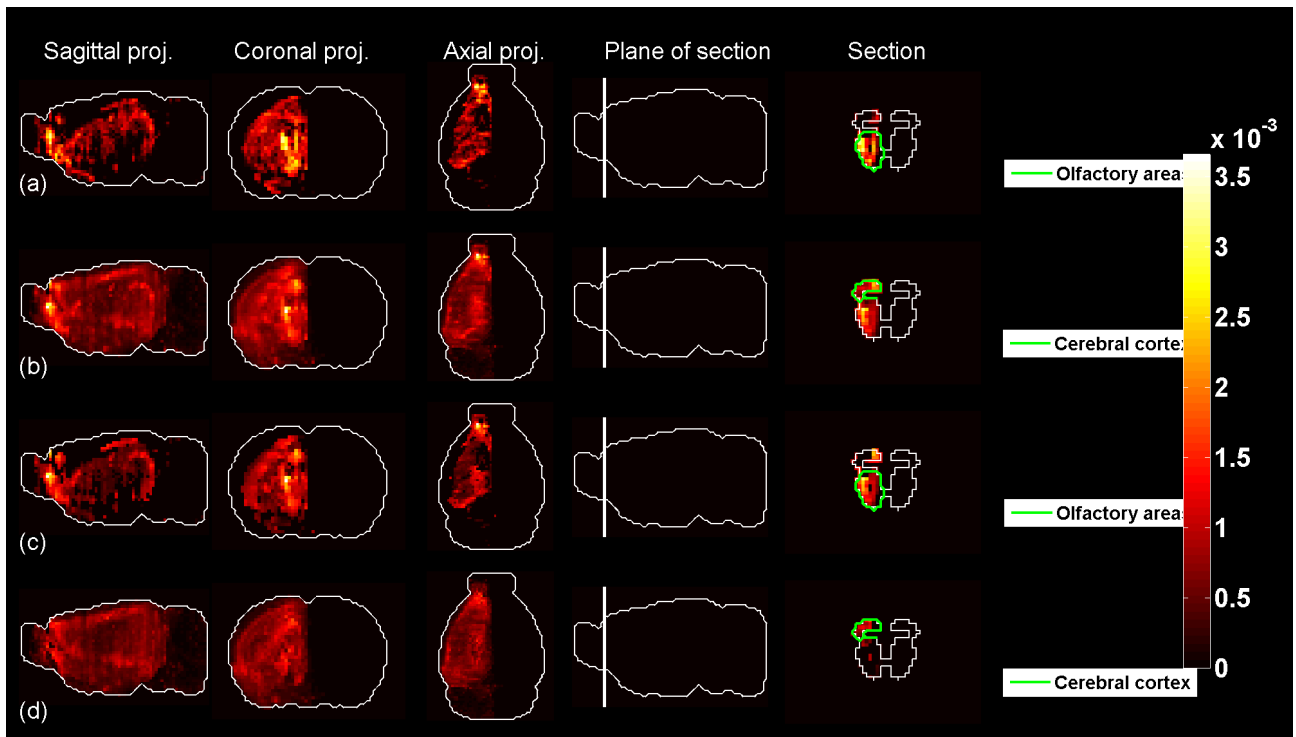


Figure 101: Predicted profile and average sub-sampled profile for  $t = 43$ .

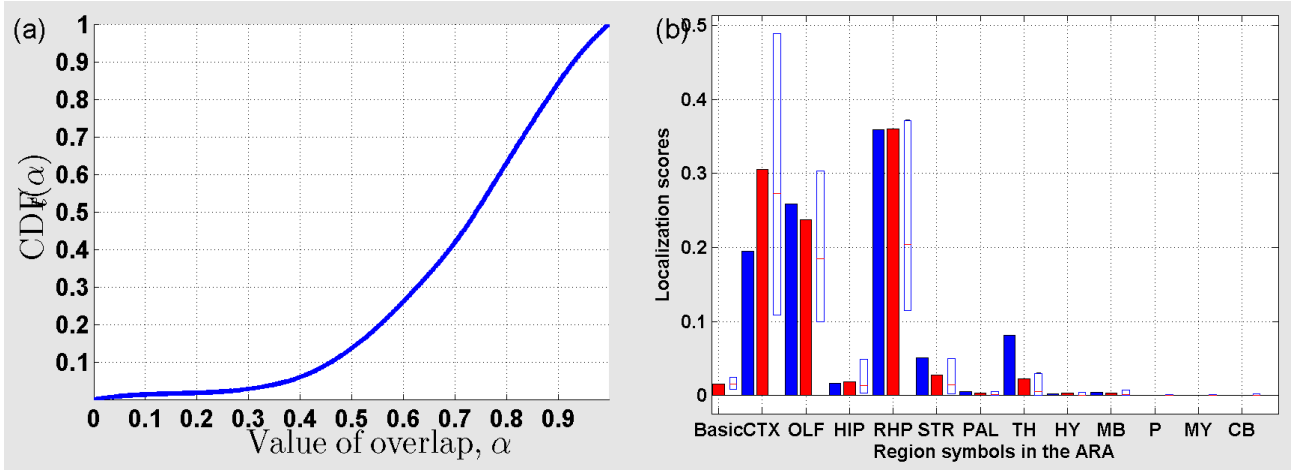


Figure 102: (a) Cumulative distribution function ( $CDF_t$ ) of the overlap between  $\rho_t$  and sub-sampled profiles for  $t = 44$ . (b) Localization scores in the coarsest version of the ARA for  $\rho_t$  (in blue), and  $\bar{\rho}_t$  (in red).

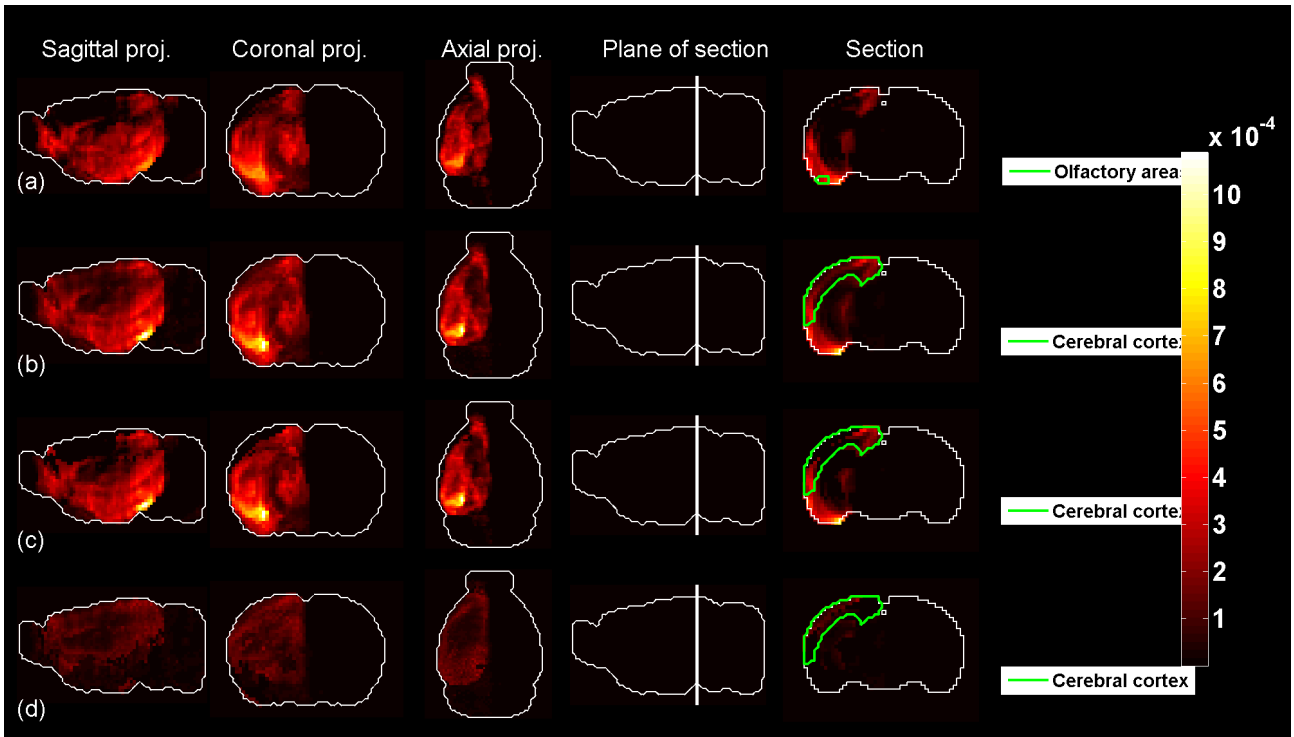


Figure 103: Predicted profile and average sub-sampled profile for  $t = 44$ .

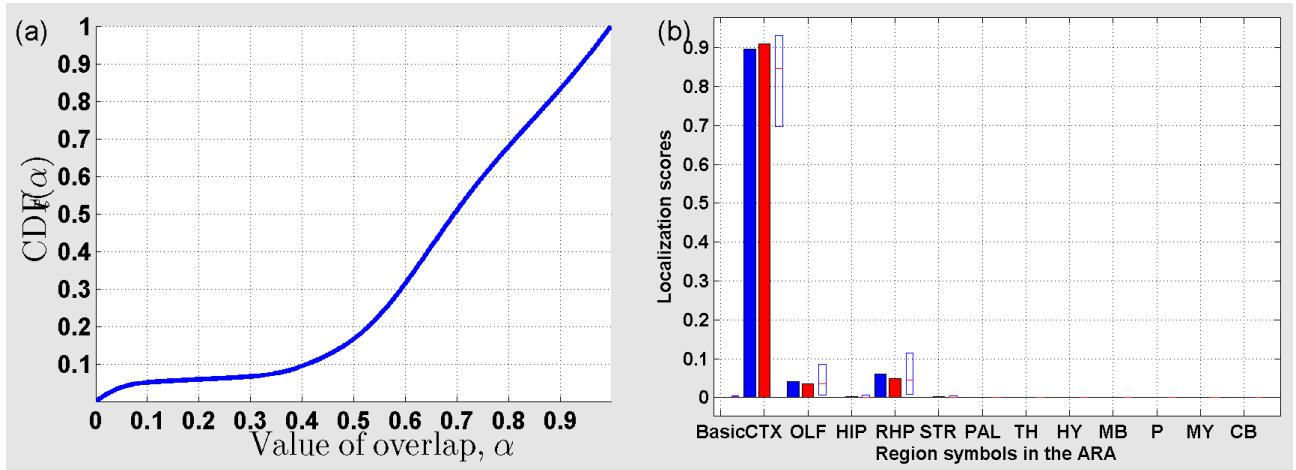


Figure 104: (a) Cumulative distribution function ( $CDF_t$ ) of the overlap between  $\rho_t$  and sub-sampled profiles for  $t = 45$ . (b) Localization scores in the coarsest version of the ARA for  $\rho_t$  (in blue), and  $\bar{\rho}_t$  (in red).

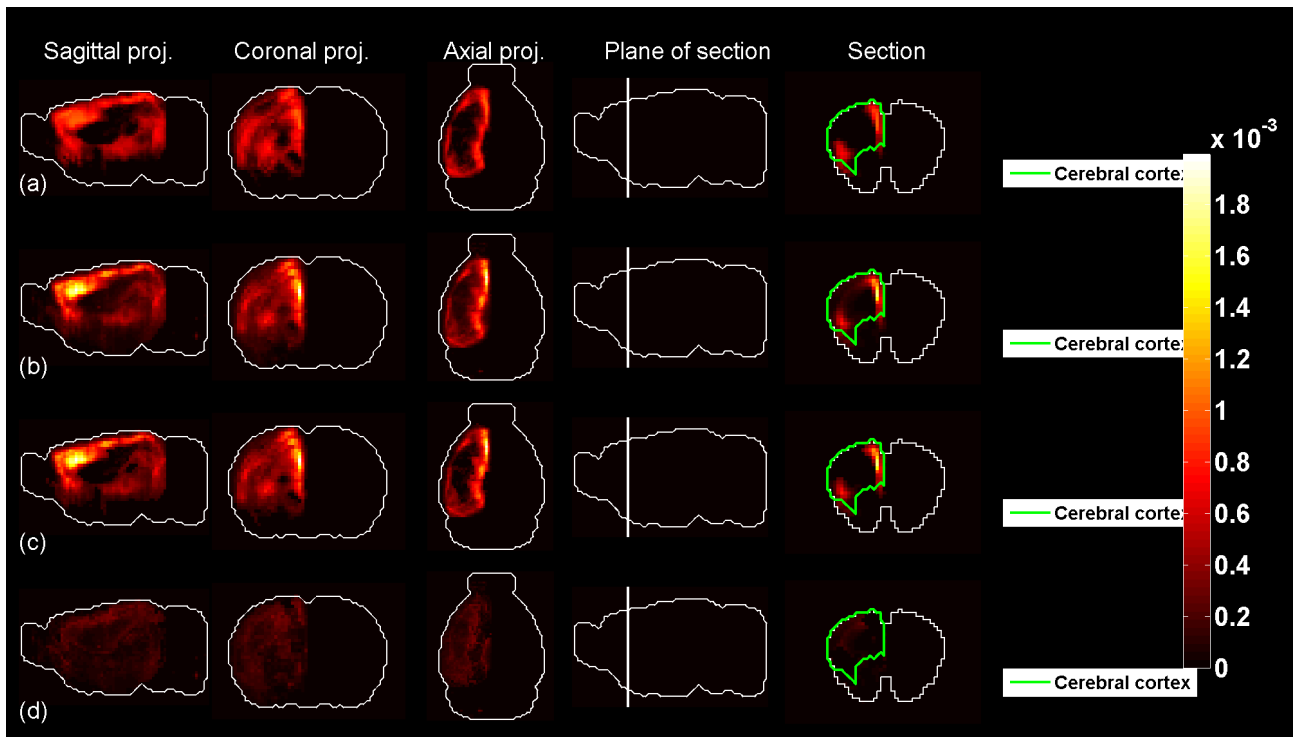


Figure 105: Predicted profile and average sub-sampled profile for  $t = 45$ .

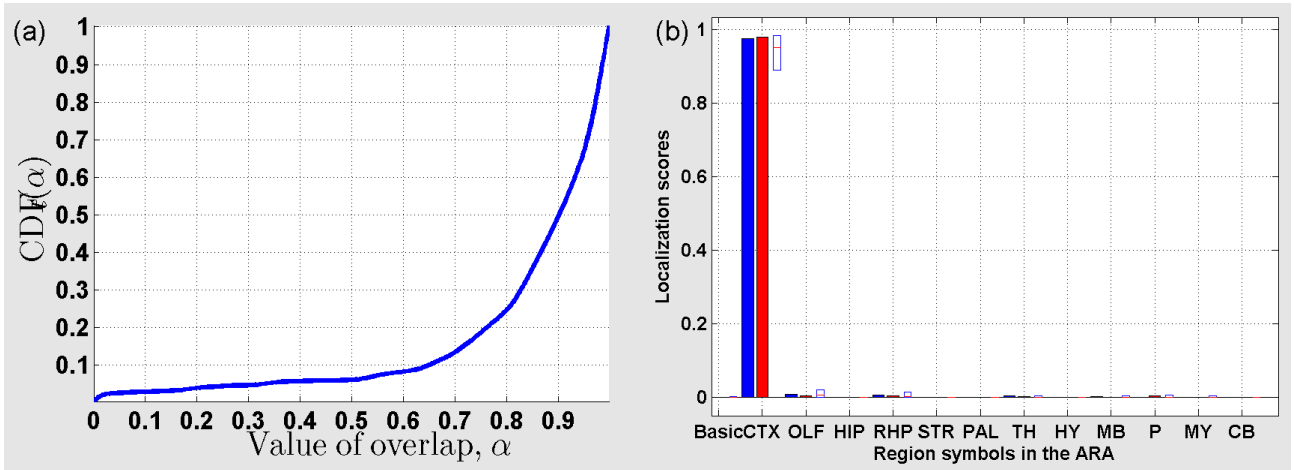


Figure 106: (a) Cumulative distribution function ( $CDF_t$ ) of the overlap between  $\rho_t$  and sub-sampled profiles for  $t = 46$ . (b) Localization scores in the coarsest version of the ARA for  $\rho_t$  (in blue), and  $\bar{\rho}_t$  (in red).

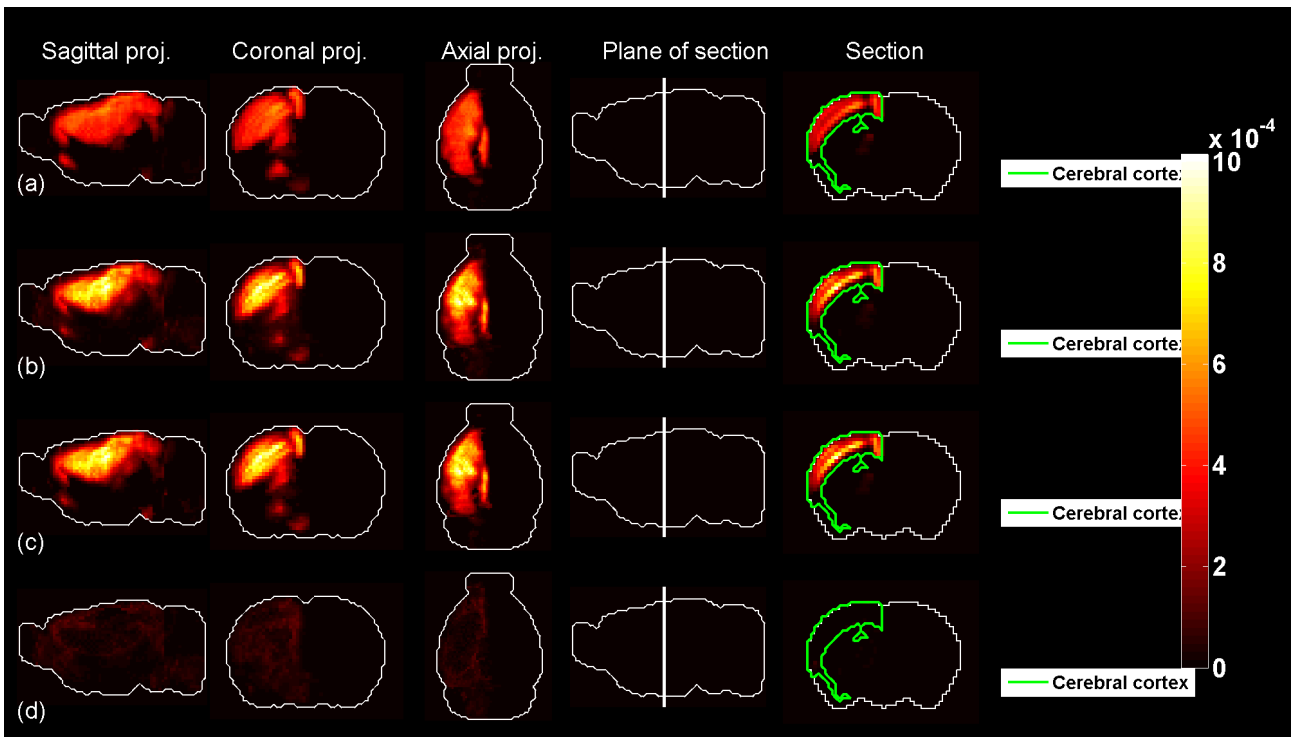


Figure 107: Predicted profile and average sub-sampled profile for  $t = 46$ .

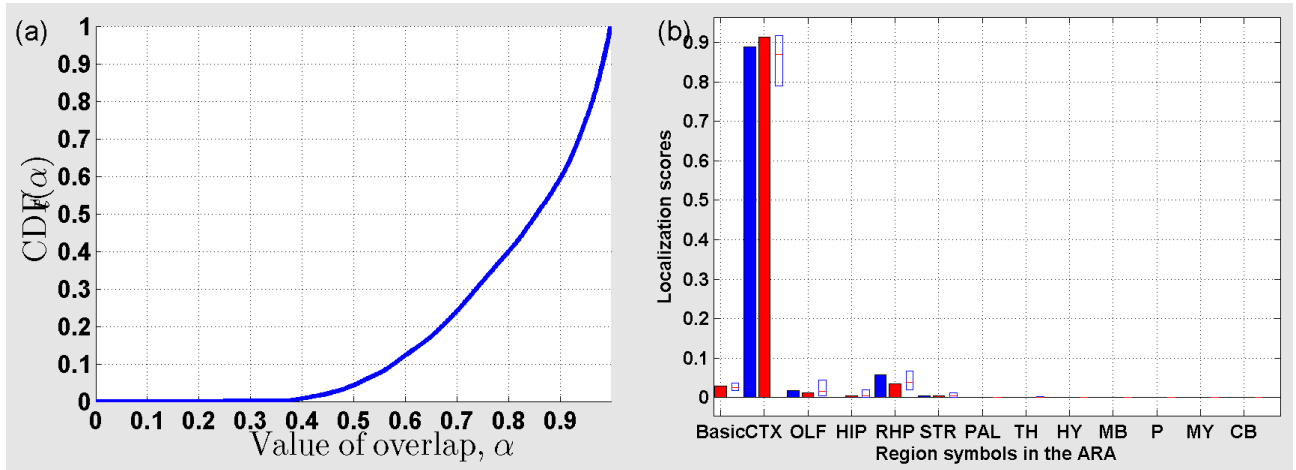


Figure 108: (a) Cumulative distribution function ( $CDF_t$ ) of the overlap between  $\rho_t$  and sub-sampled profiles for  $t = 47$ . (b) Localization scores in the coarsest version of the ARA for  $\rho_t$  (in blue), and  $\bar{\rho}_t$  (in red).

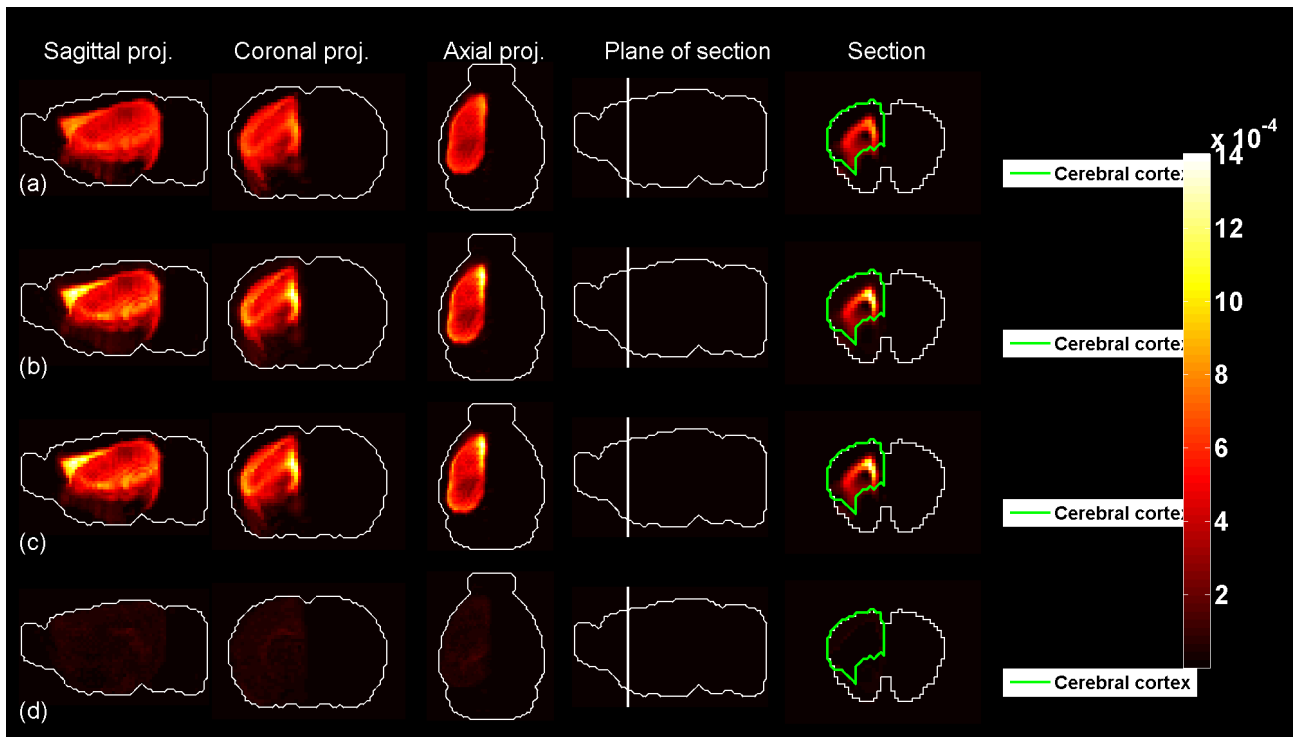


Figure 109: Predicted profile and average sub-sampled profile for  $t = 47$ .

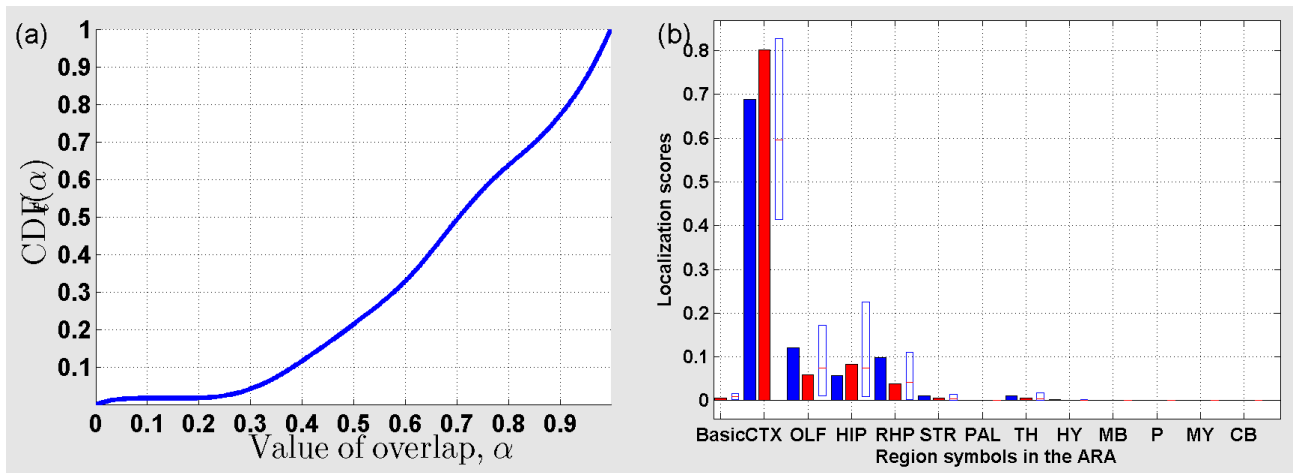


Figure 110: (a) Cumulative distribution function ( $CDF_t$ ) of the overlap between  $\rho_t$  and sub-sampled profiles for  $t = 48$ . (b) Localization scores in the coarsest version of the ARA for  $\rho_t$  (in blue), and  $\bar{\rho}_t$  (in red).

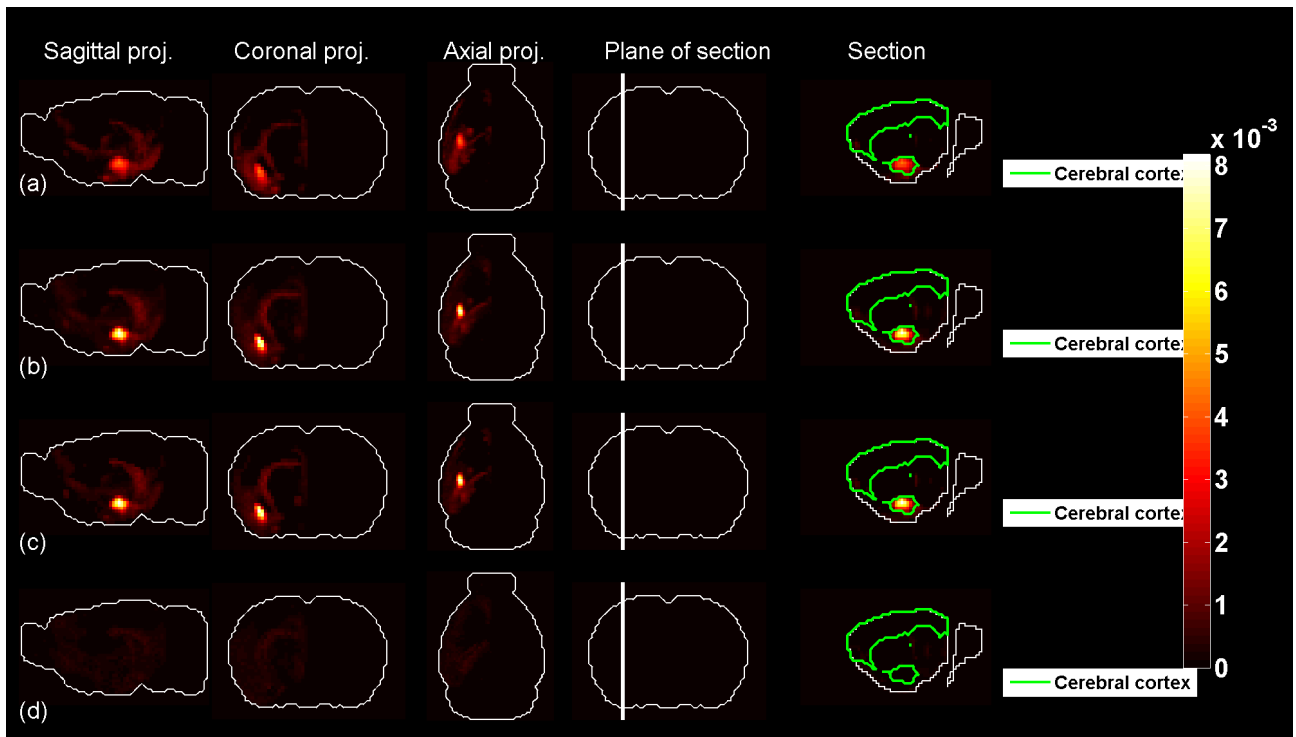


Figure 111: Predicted profile and average sub-sampled profile for  $t = 48$ .

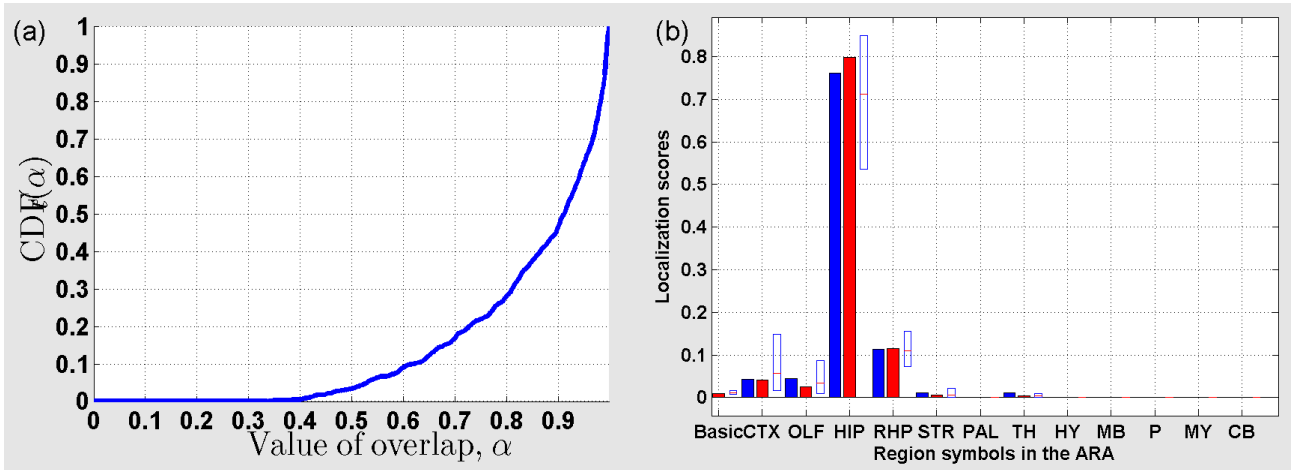


Figure 112: (a) Cumulative distribution function ( $CDF_t$ ) of the overlap between  $\rho_t$  and sub-sampled profiles for  $t = 49$ . (b) Localization scores in the coarsest version of the ARA for  $\rho_t$  (in blue), and  $\bar{\rho}_t$  (in red).

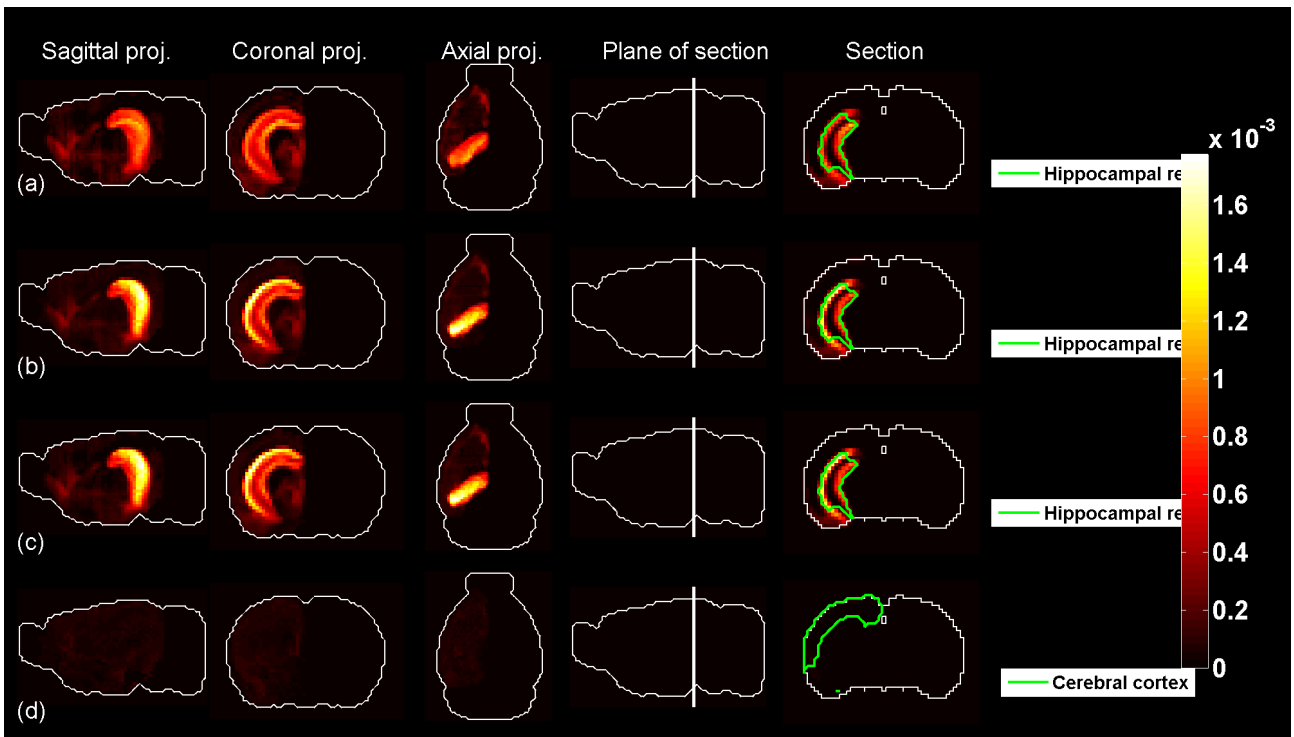


Figure 113: Predicted profile and average sub-sampled profile for  $t = 49$ .

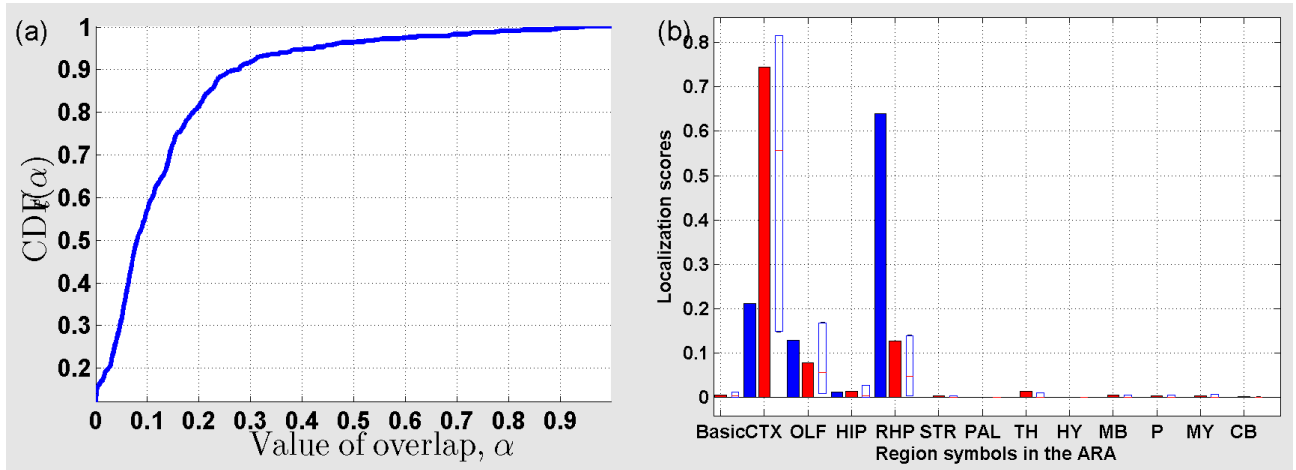


Figure 114: (a) Cumulative distribution function ( $CDF_t$ ) of the overlap between  $\rho_t$  and sub-sampled profiles for  $t = 50$ . (b) Localization scores in the coarsest version of the ARA for  $\rho_t$  (in blue), and  $\bar{\rho}_t$  (in red).

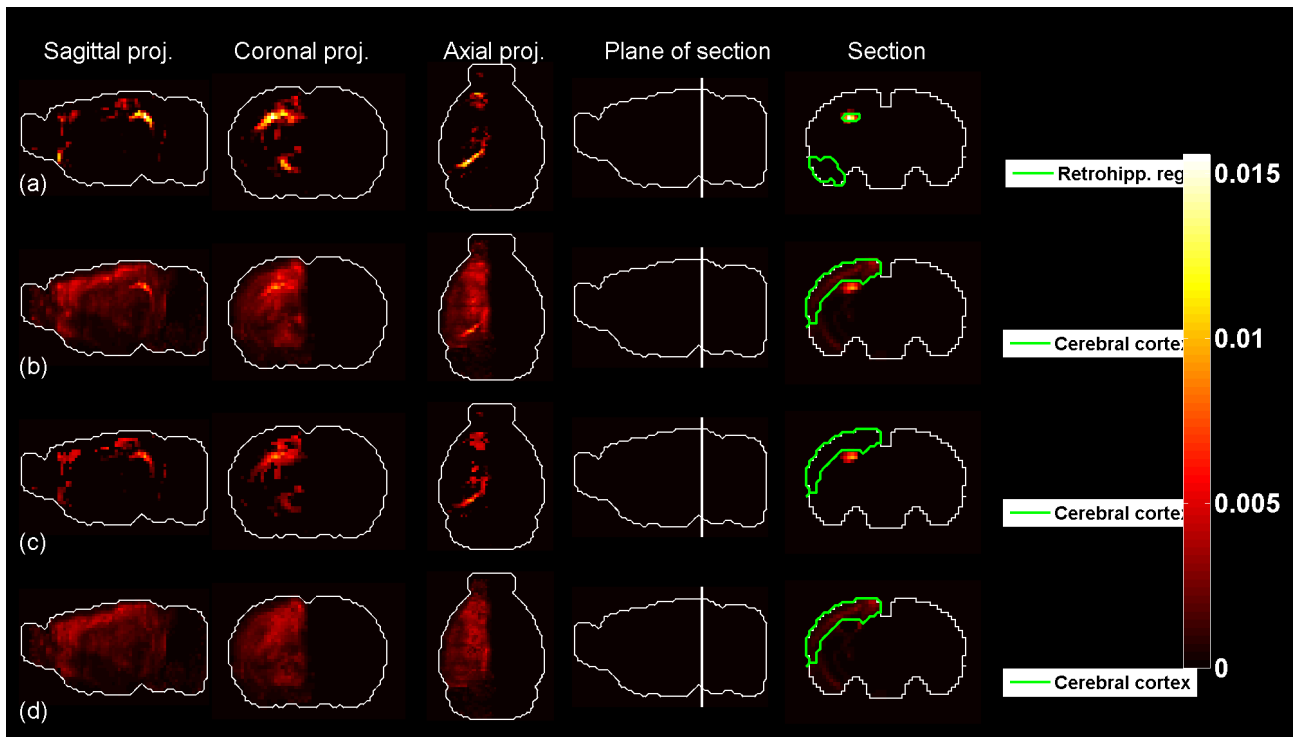


Figure 115: Predicted profile and average sub-sampled profile for  $t = 50$ .

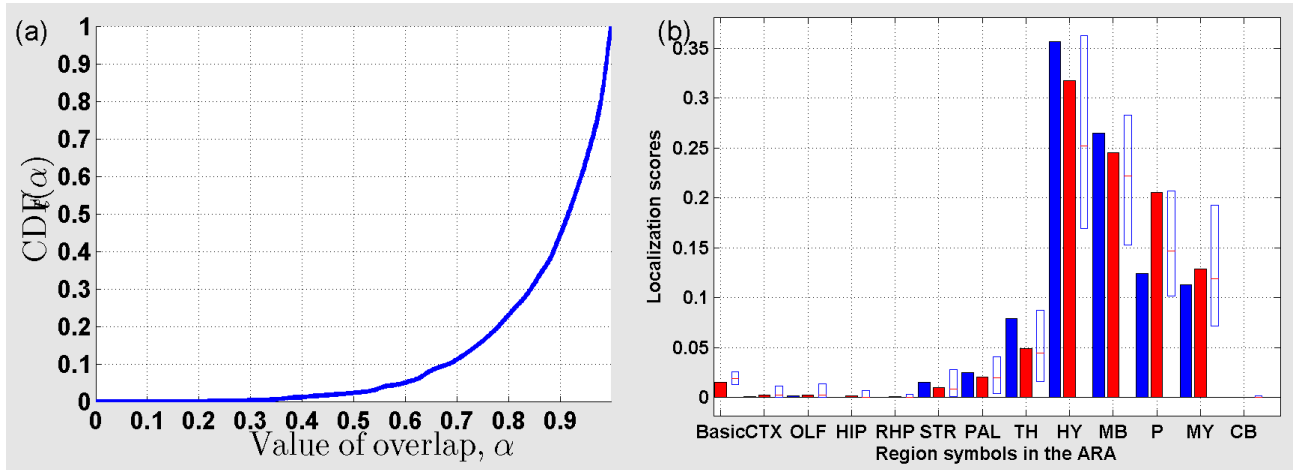


Figure 116: (a) Cumulative distribution function ( $CDF_t$ ) of the overlap between  $\rho_t$  and sub-sampled profiles for  $t = 51$ . (b) Localization scores in the coarsest version of the ARA for  $\rho_t$  (in blue), and  $\bar{\rho}_t$  (in red).

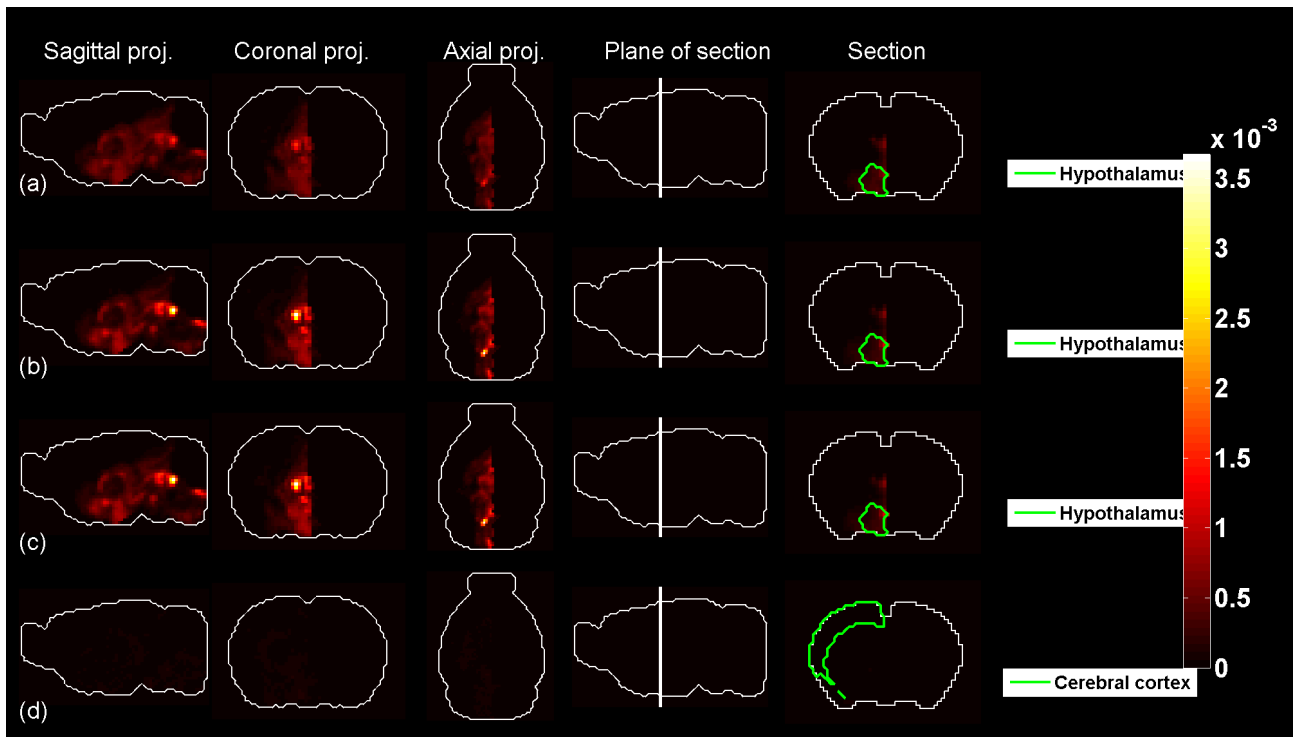


Figure 117: Predicted profile and average sub-sampled profile for  $t = 51$ .

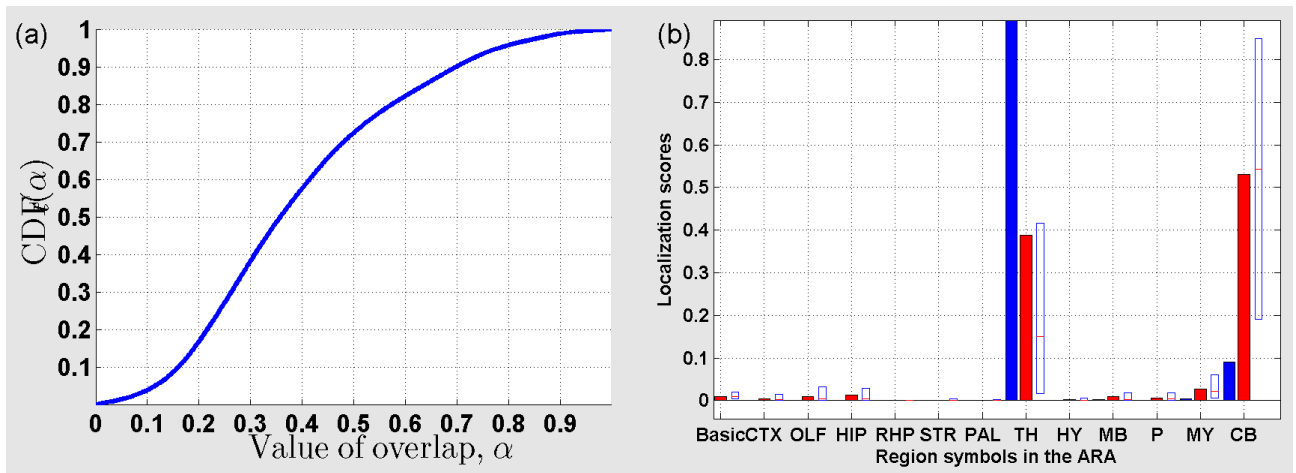


Figure 118: (a) Cumulative distribution function ( $CDF_t$ ) of the overlap between  $\rho_t$  and sub-sampled profiles for  $t = 52$ . (b) Localization scores in the coarsest version of the ARA for  $\rho_t$  (in blue), and  $\bar{\rho}_t$  (in red).

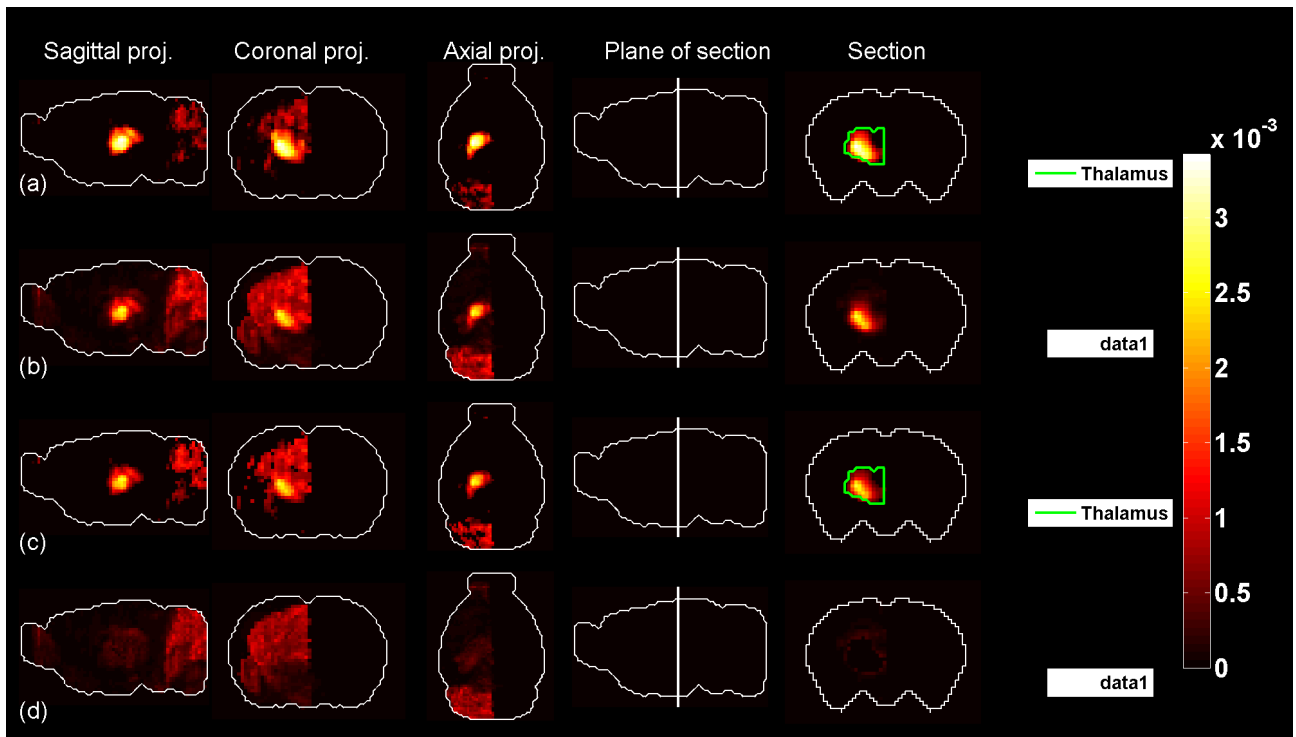


Figure 119: Predicted profile and average sub-sampled profile for  $t = 52$ .

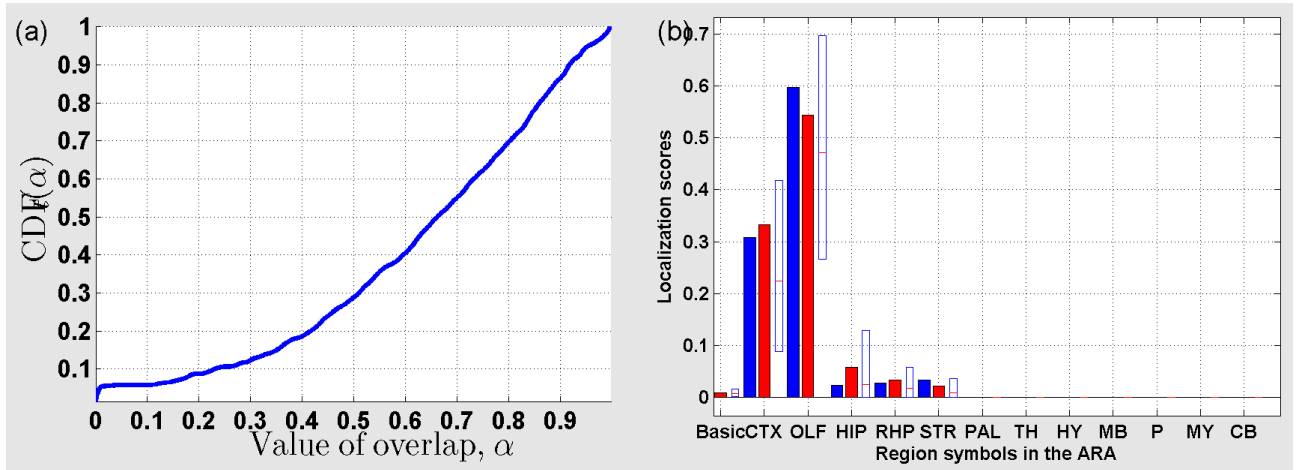


Figure 120: (a) Cumulative distribution function ( $CDF_t$ ) of the overlap between  $\rho_t$  and sub-sampled profiles for  $t = 53$ . (b) Localization scores in the coarsest version of the ARA for  $\rho_t$  (in blue), and  $\bar{\rho}_t$  (in red).

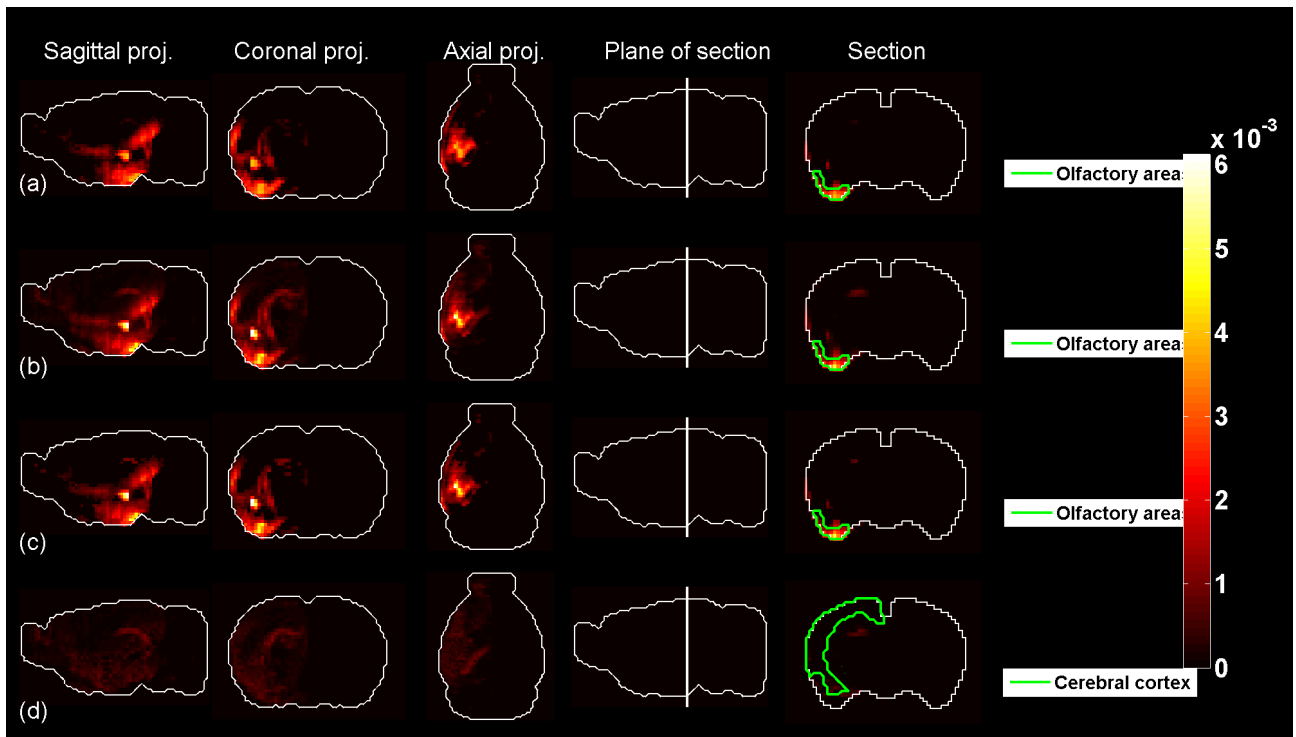


Figure 121: Predicted profile and average sub-sampled profile for  $t = 53$ .

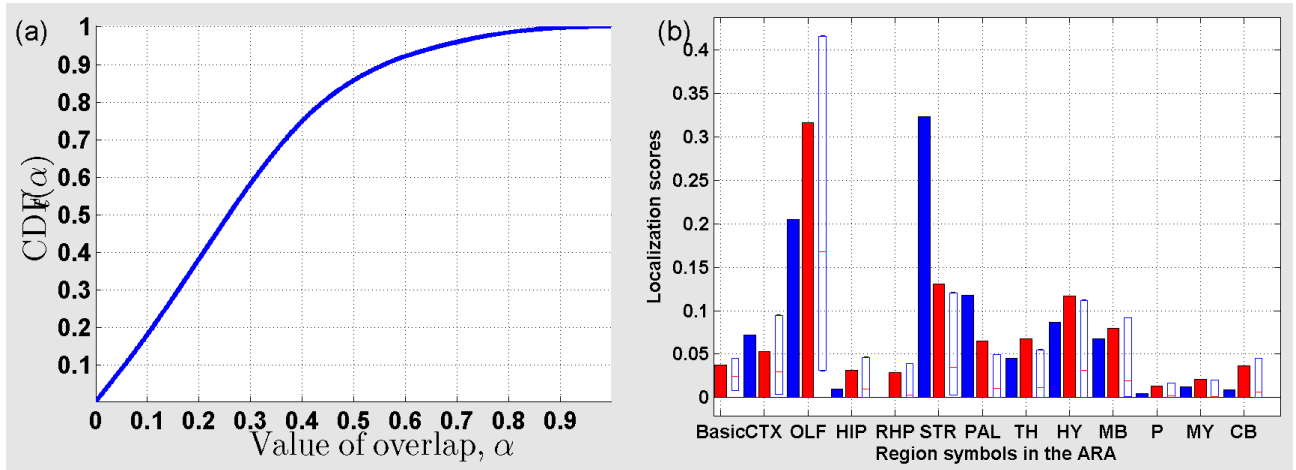


Figure 122: (a) Cumulative distribution function ( $CDF_t$ ) of the overlap between  $\rho_t$  and sub-sampled profiles for  $t = 54$ . (b) Localization scores in the coarsest version of the ARA for  $\rho_t$  (in blue), and  $\bar{\rho}_t$  (in red).

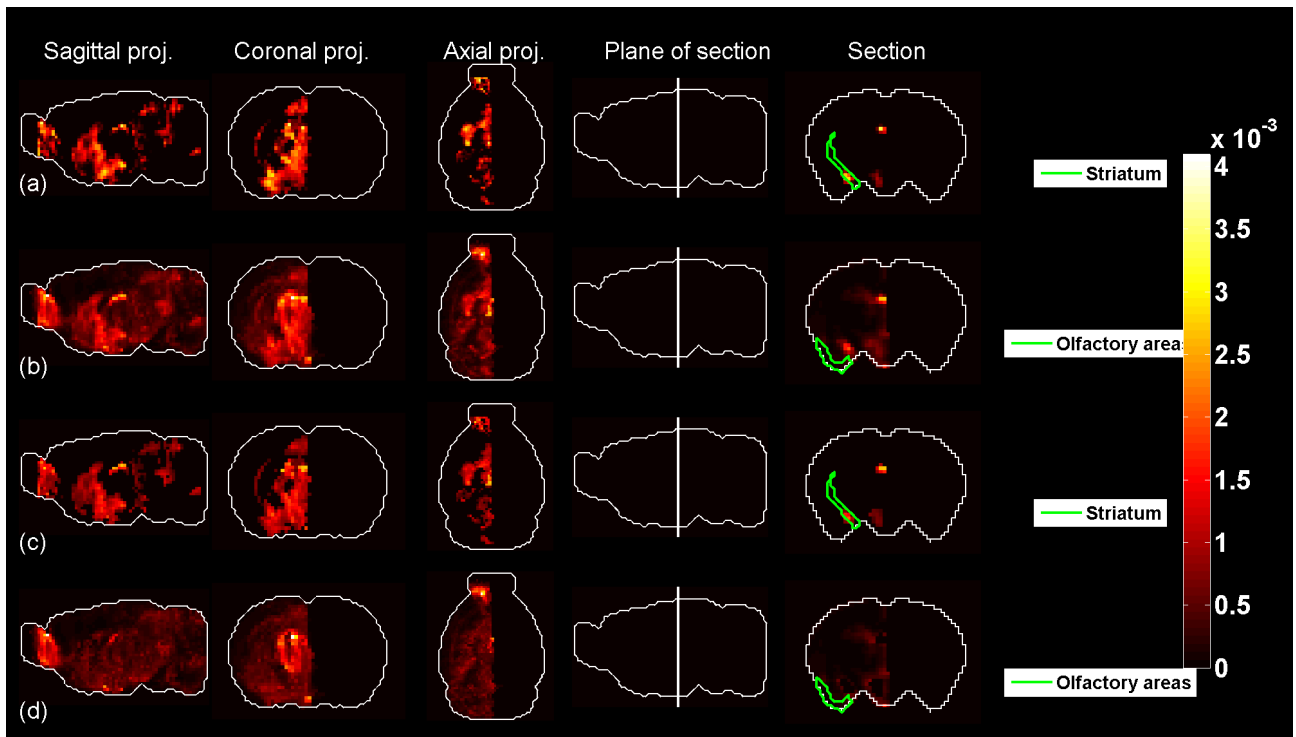


Figure 123: Predicted profile and average sub-sampled profile for  $t = 54$ .

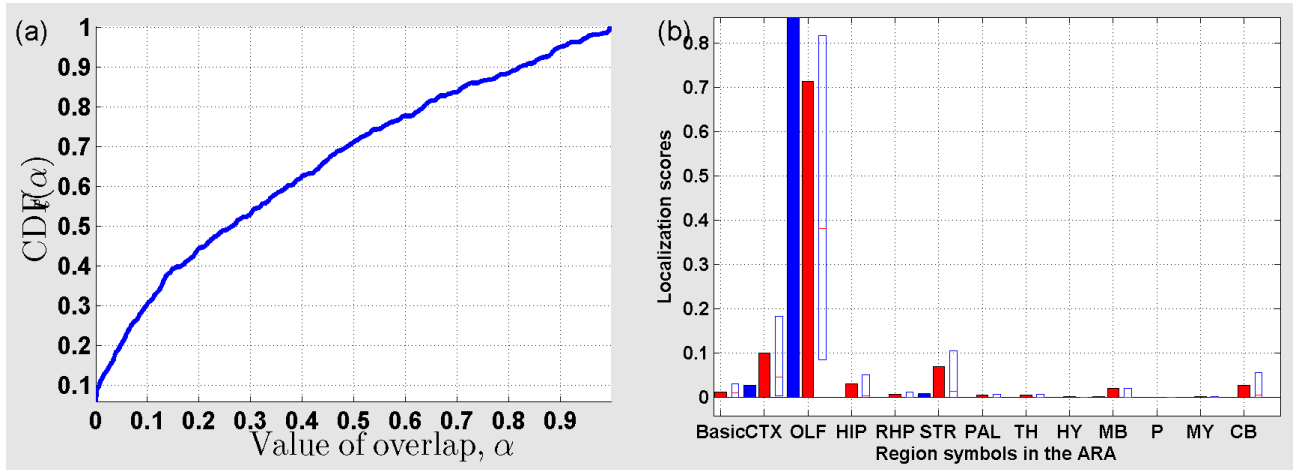


Figure 124: (a) Cumulative distribution function ( $CDF_t$ ) of the overlap between  $\rho_t$  and sub-sampled profiles for  $t = 55$ . (b) Localization scores in the coarsest version of the ARA for  $\rho_t$  (in blue), and  $\bar{\rho}_t$  (in red).

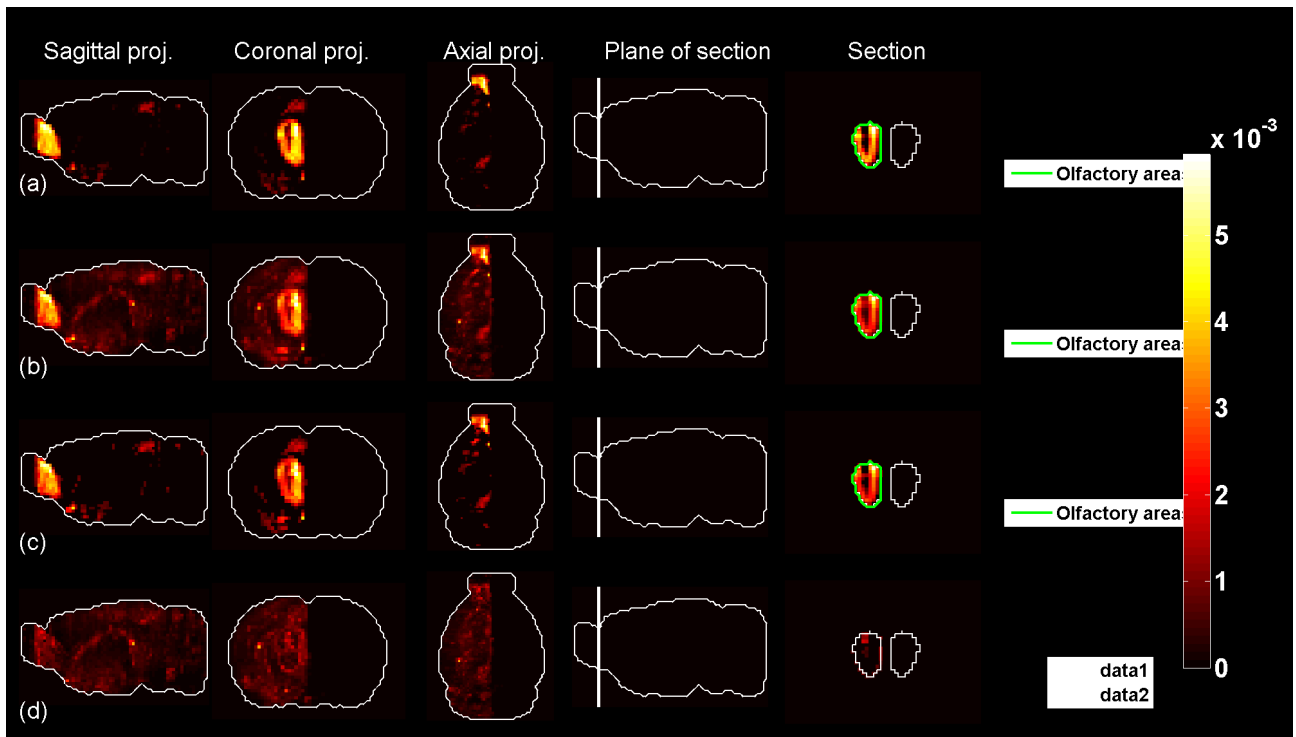


Figure 125: Predicted profile and average sub-sampled profile for  $t = 55$ .

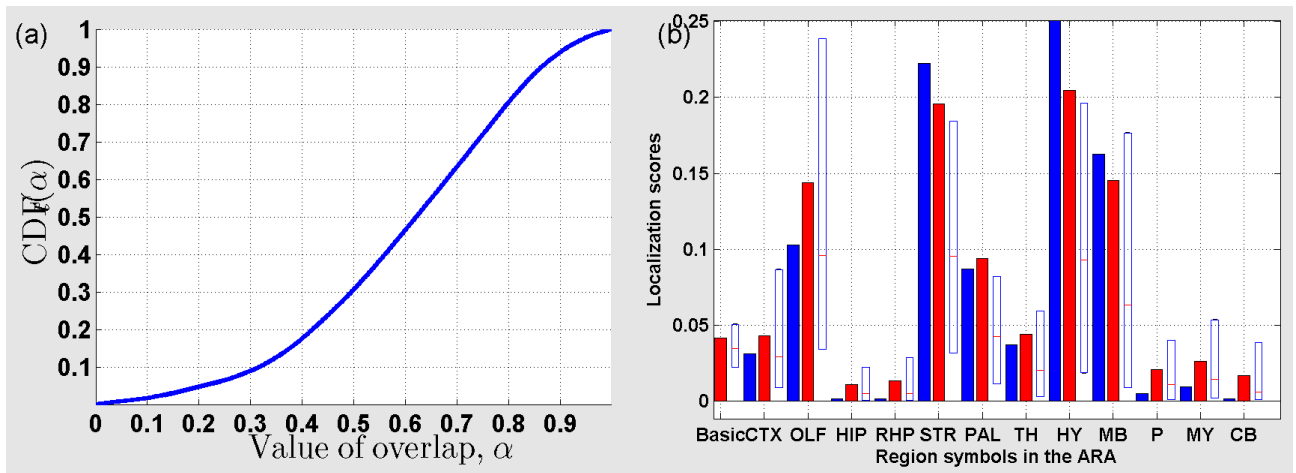


Figure 126: (a) Cumulative distribution function ( $CDF_t$ ) of the overlap between  $\rho_t$  and sub-sampled profiles for  $t = 56$ . (b) Localization scores in the coarsest version of the ARA for  $\rho_t$  (in blue), and  $\bar{\rho}_t$  (in red).

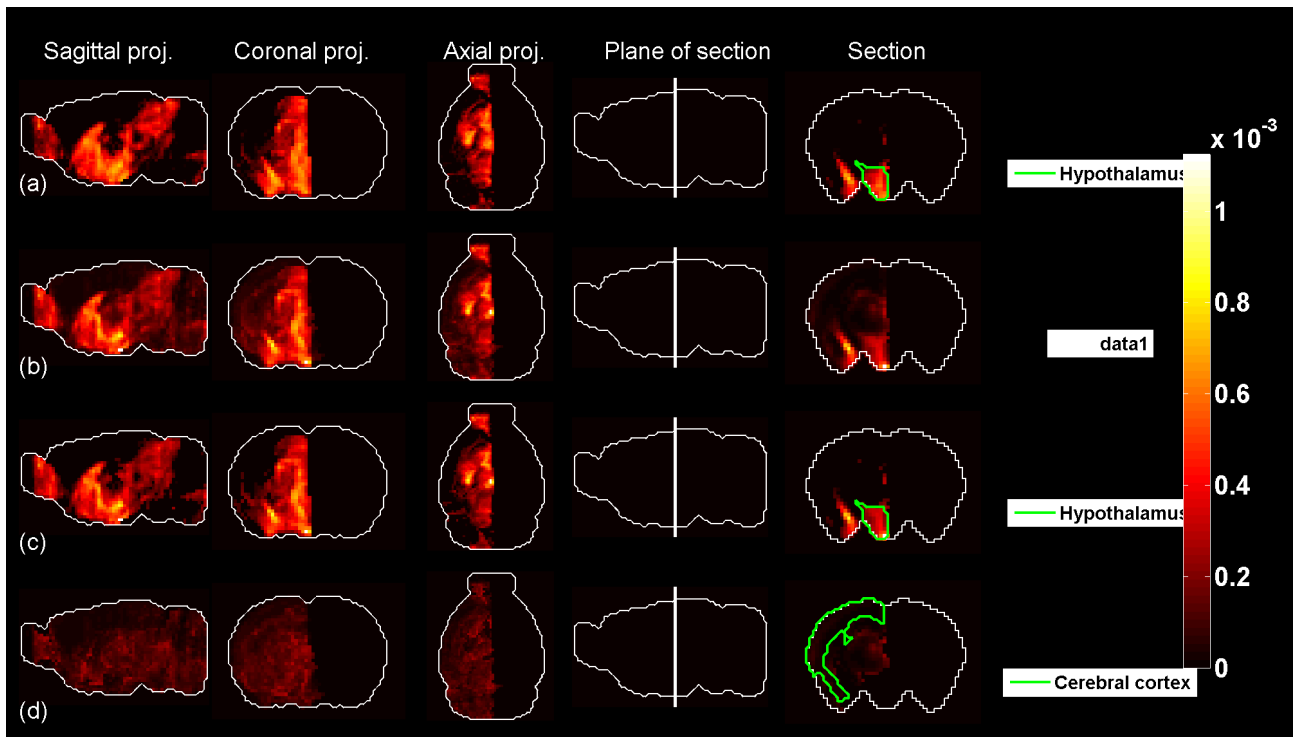


Figure 127: Predicted profile and average sub-sampled profile for  $t = 56$ .

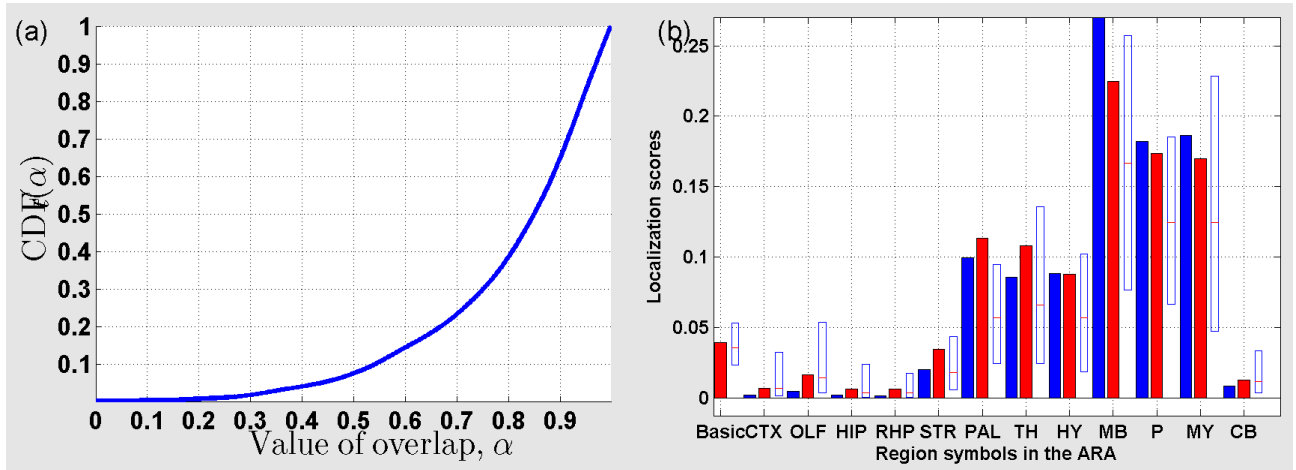


Figure 128: (a) Cumulative distribution function ( $CDF_t$ ) of the overlap between  $\rho_t$  and sub-sampled profiles for  $t = 57$ . (b) Localization scores in the coarsest version of the ARA for  $\rho_t$  (in blue), and  $\bar{\rho}_t$  (in red).

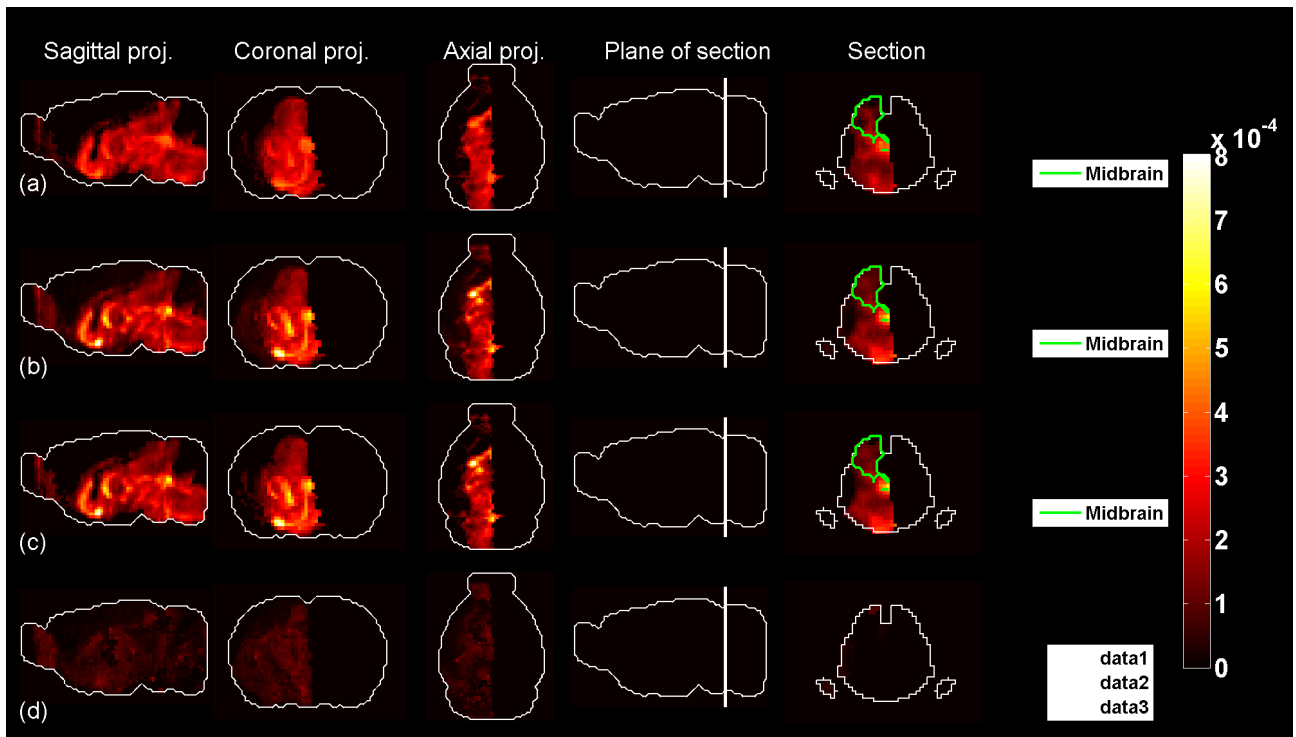


Figure 129: Predicted profile and average sub-sampled profile for  $t = 57$ .

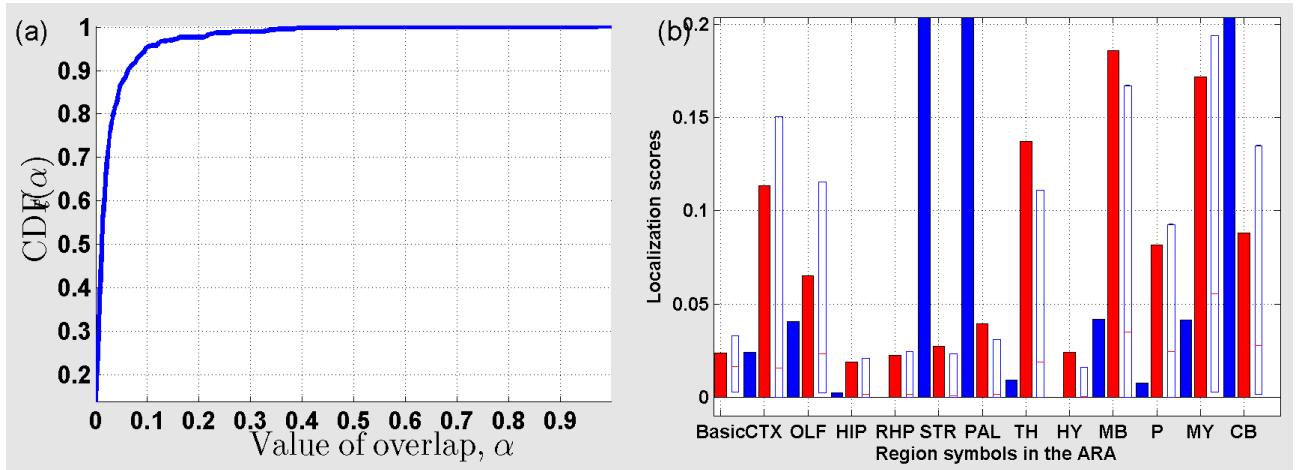


Figure 130: (a) Cumulative distribution function ( $CDF_t$ ) of the overlap between  $\rho_t$  and sub-sampled profiles for  $t = 58$ . (b) Localization scores in the coarsest version of the ARA for  $\rho_t$  (in blue), and  $\bar{\rho}_t$  (in red).

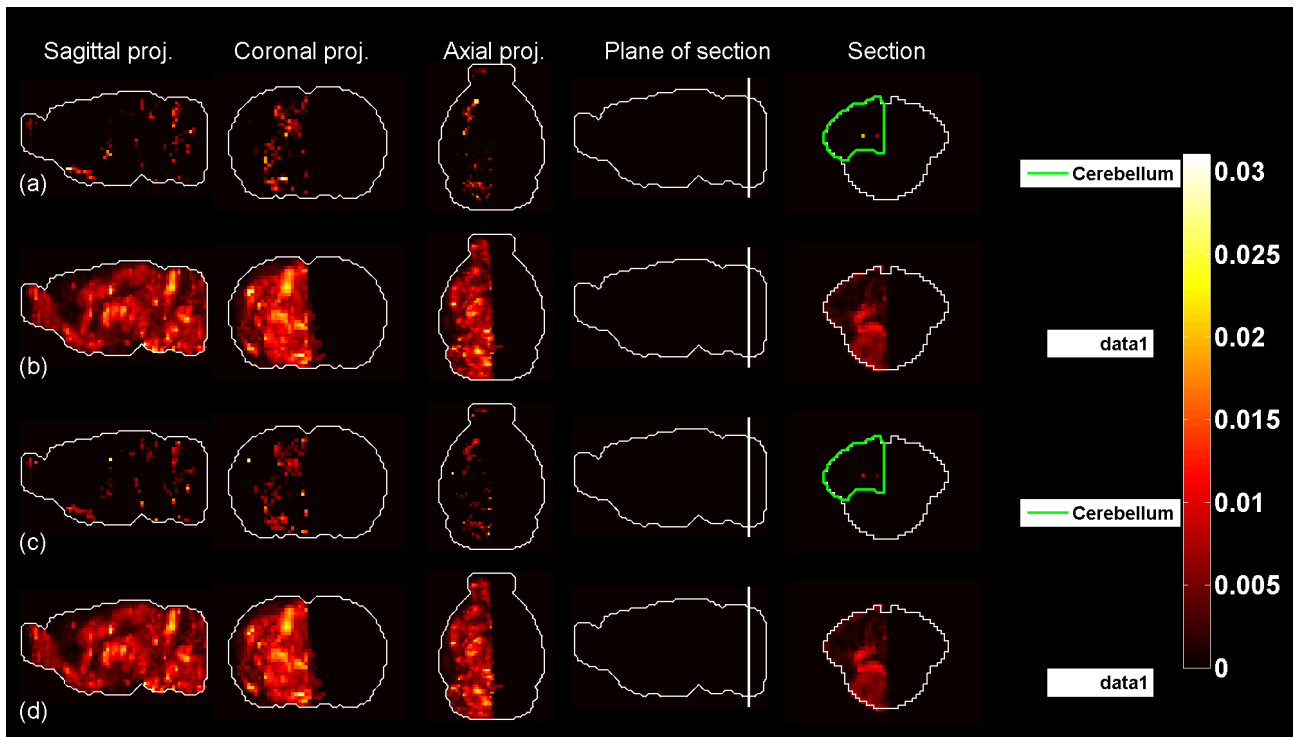


Figure 131: Predicted profile and average sub-sampled profile for  $t = 58$ .

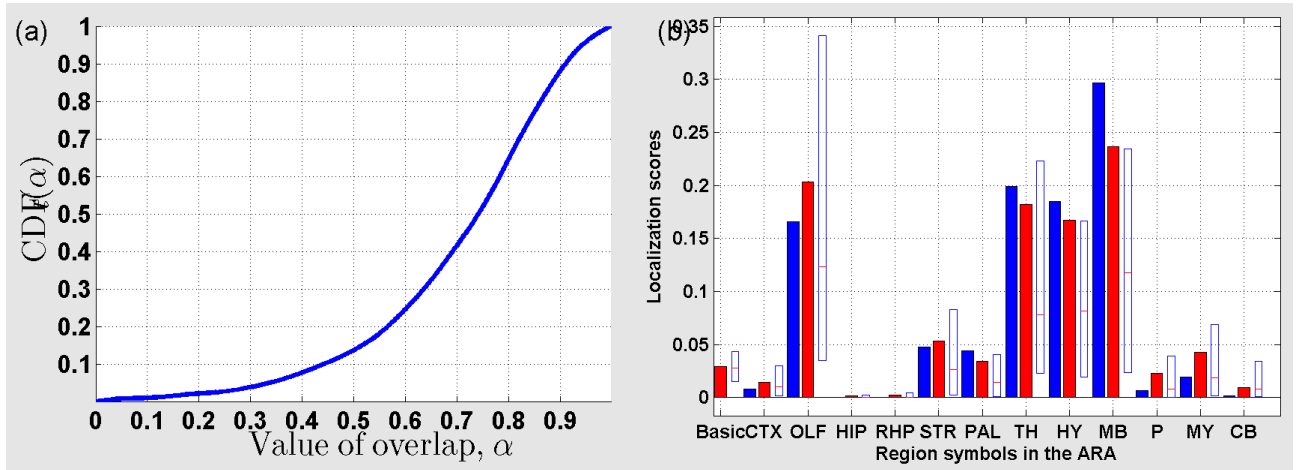


Figure 132: (a) Cumulative distribution function ( $CDF_t$ ) of the overlap between  $\rho_t$  and sub-sampled profiles for  $t = 59$ . (b) Localization scores in the coarsest version of the ARA for  $\rho_t$  (in blue), and  $\bar{\rho}_t$  (in red).

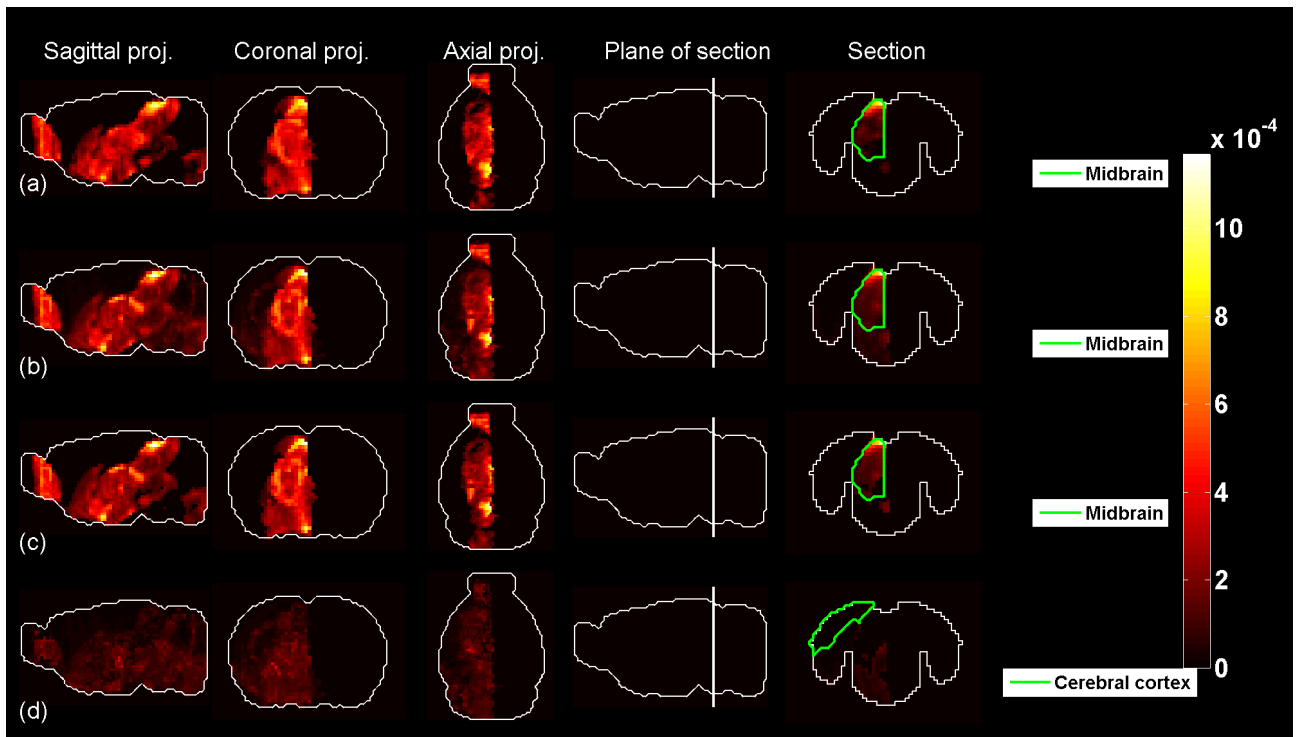


Figure 133: Predicted profile and average sub-sampled profile for  $t = 59$ .

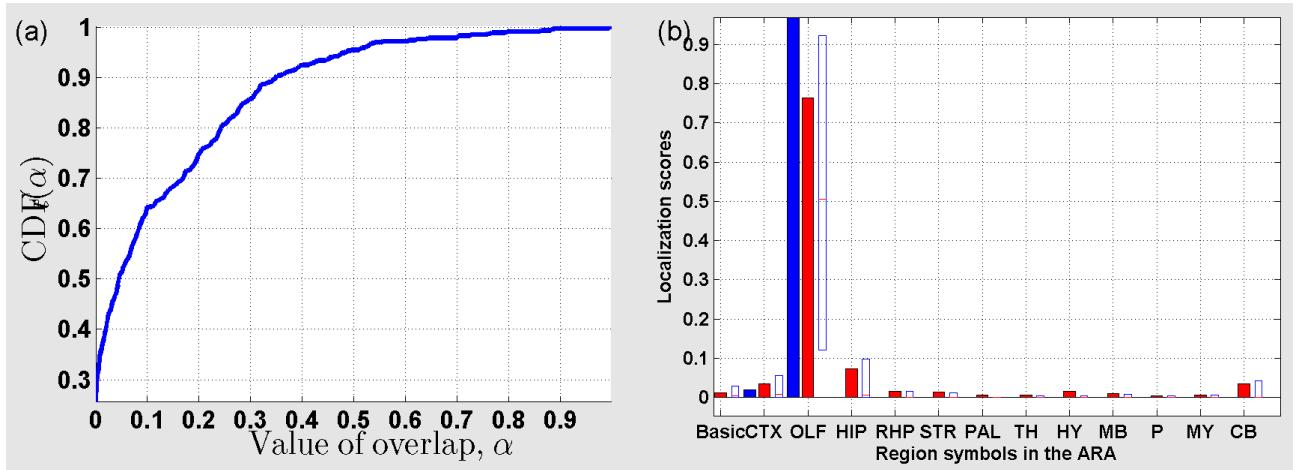


Figure 134: (a) Cumulative distribution function ( $CDF_t$ ) of the overlap between  $\rho_t$  and sub-sampled profiles for  $t = 60$ . (b) Localization scores in the coarsest version of the ARA for  $\rho_t$  (in blue), and  $\bar{\rho}_t$  (in red).

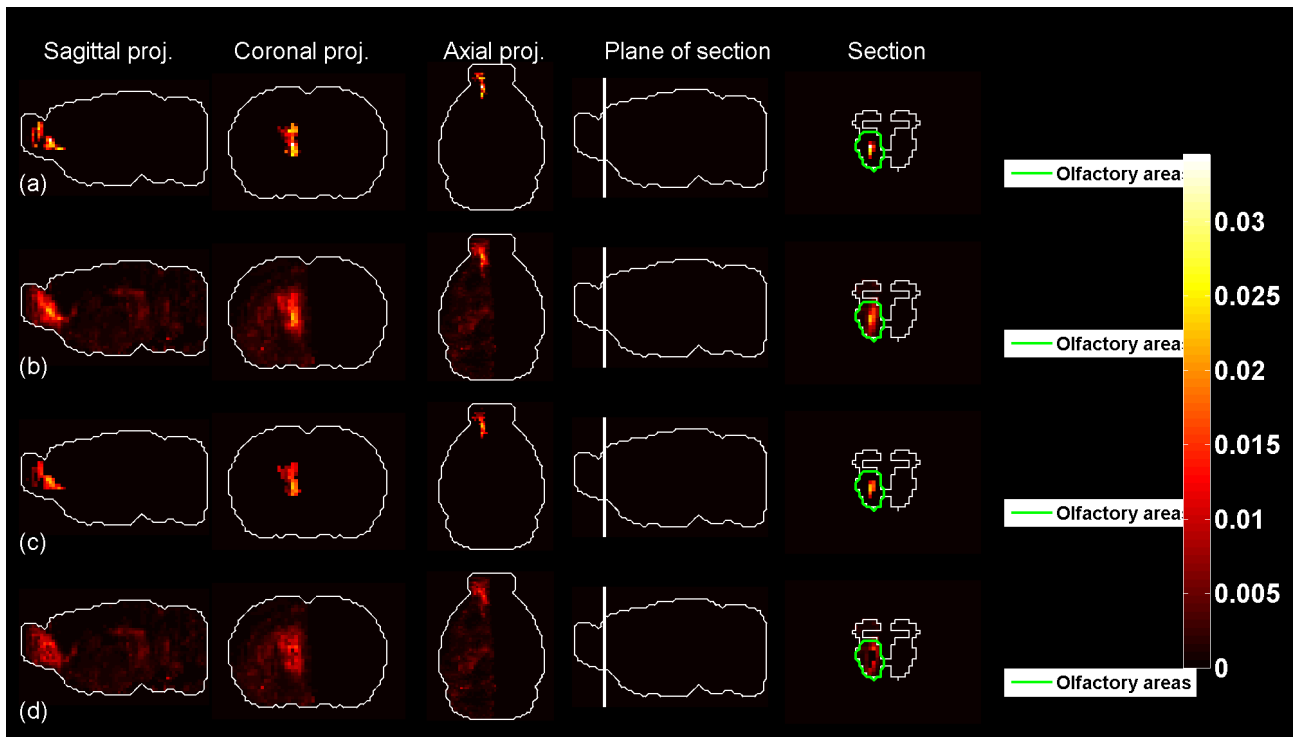


Figure 135: Predicted profile and average sub-sampled profile for  $t = 60$ .

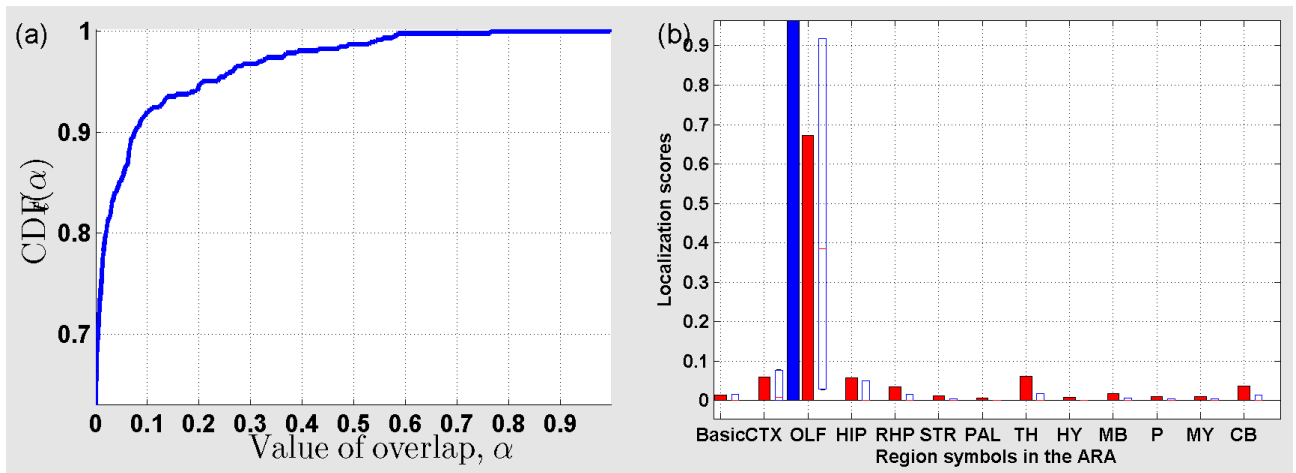


Figure 136: (a) Cumulative distribution function ( $CDF_t$ ) of the overlap between  $\rho_t$  and sub-sampled profiles for  $t = 61$ . (b) Localization scores in the coarsest version of the ARA for  $\rho_t$  (in blue), and  $\bar{\rho}_t$  (in red).

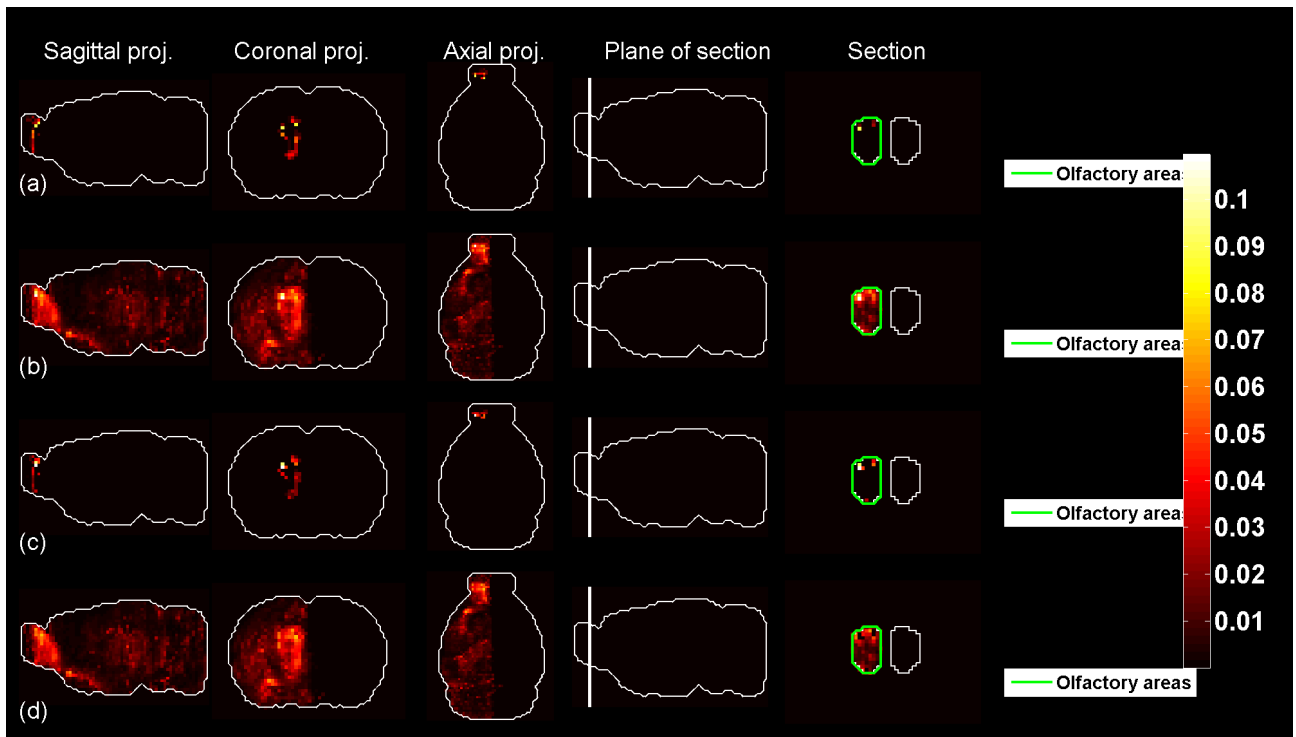


Figure 137: Predicted profile and average sub-sampled profile for  $t = 61$ .

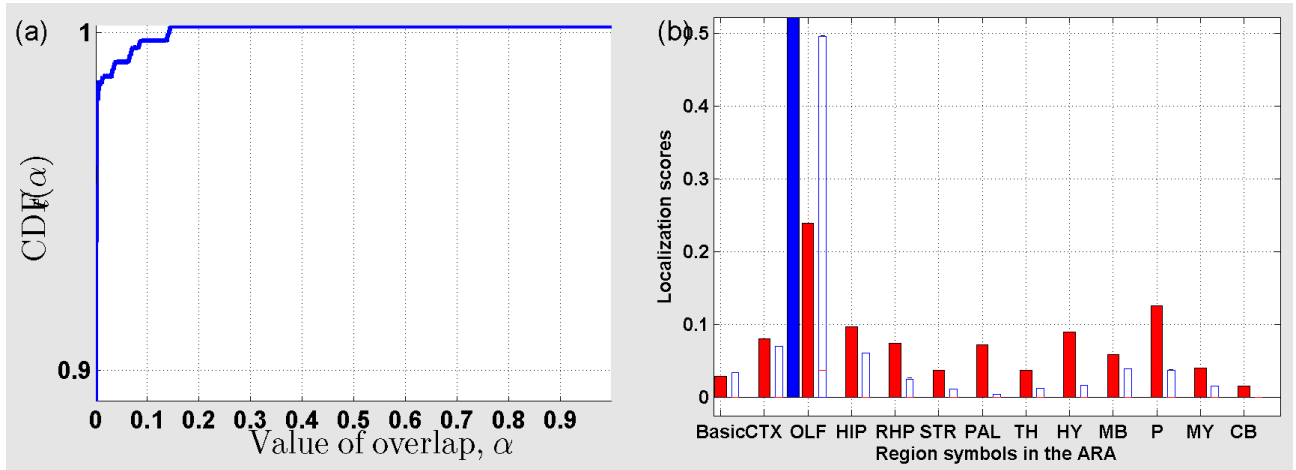


Figure 138: (a) Cumulative distribution function ( $CDF_t$ ) of the overlap between  $\rho_t$  and sub-sampled profiles for  $t = 62$ . (b) Localization scores in the coarsest version of the ARA for  $\rho_t$  (in blue), and  $\bar{\rho}_t$  (in red).

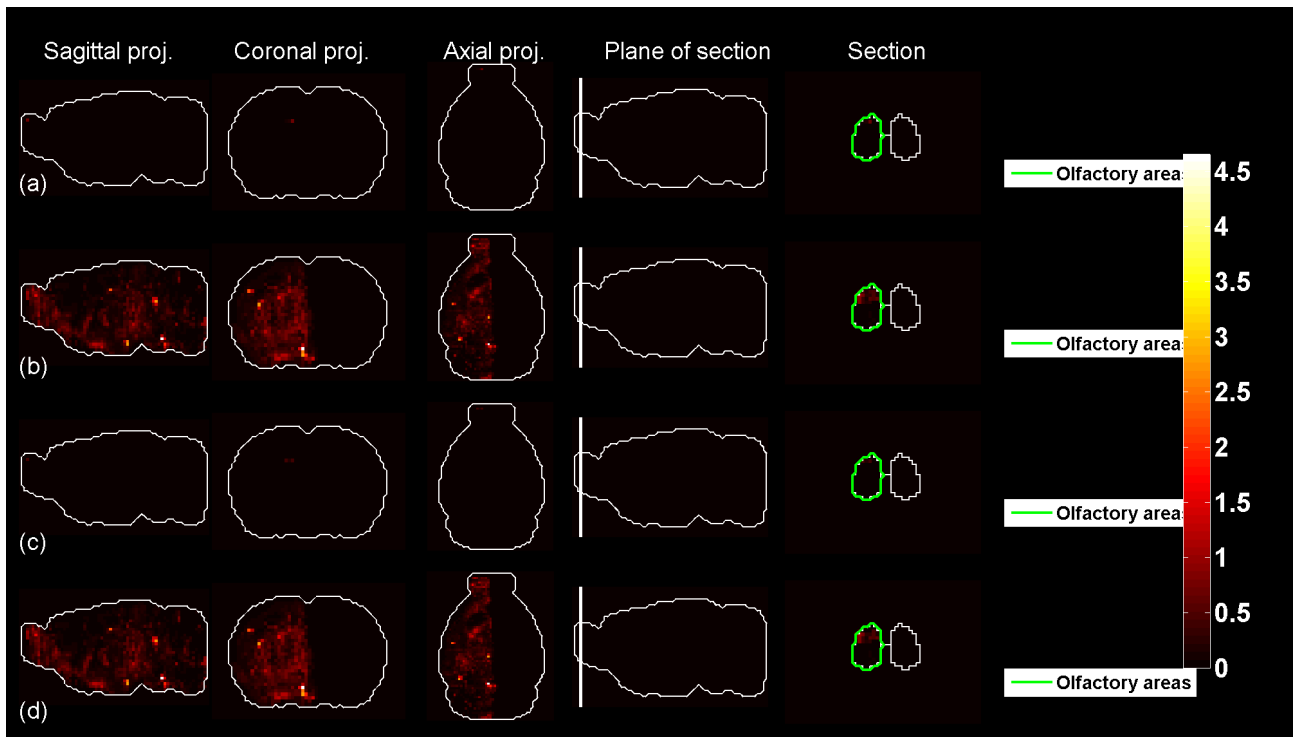


Figure 139: Predicted profile and average sub-sampled profile for  $t = 62$ .

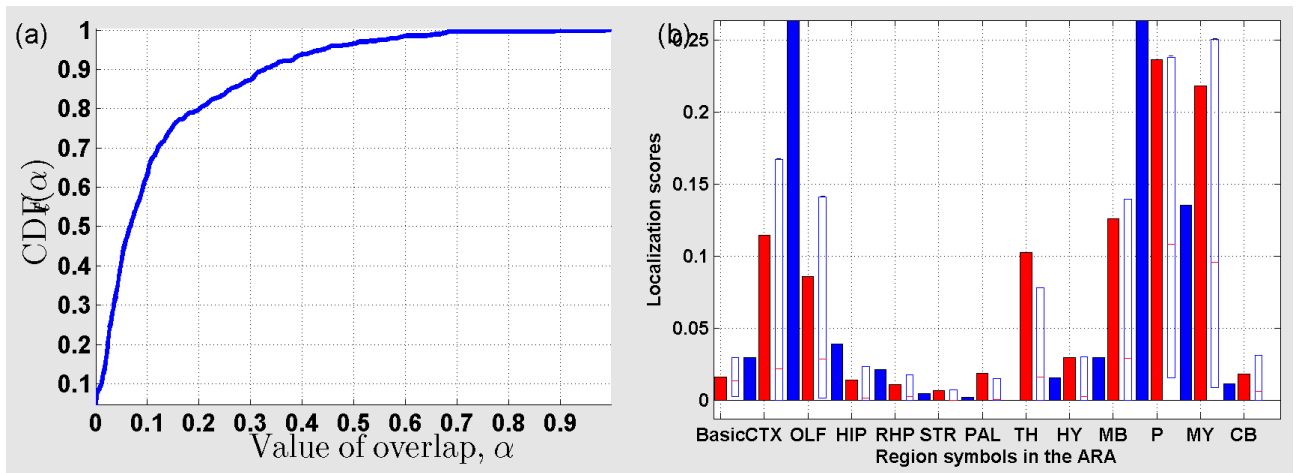


Figure 140: (a) Cumulative distribution function ( $CDF_t$ ) of the overlap between  $\rho_t$  and sub-sampled profiles for  $t = 63$ . (b) Localization scores in the coarsest version of the ARA for  $\rho_t$  (in blue), and  $\bar{\rho}_t$  (in red).

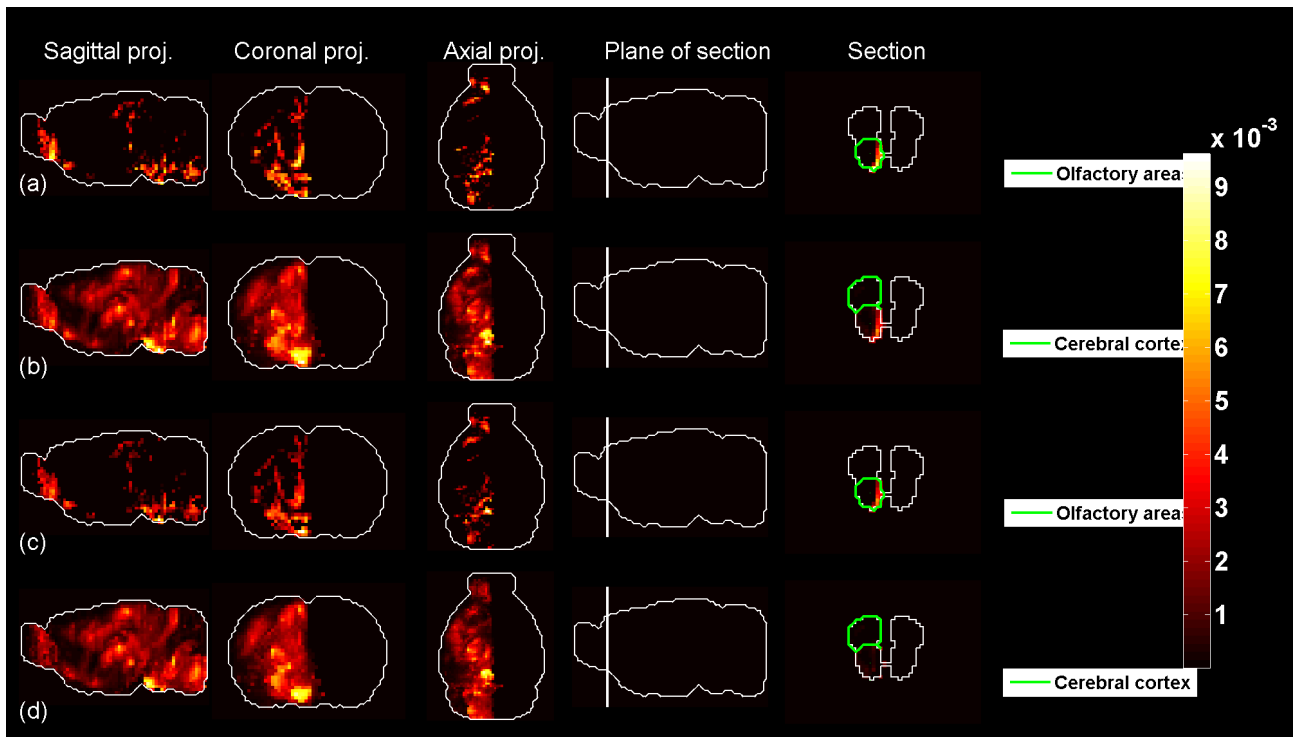


Figure 141: Predicted profile and average sub-sampled profile for  $t = 63$ .

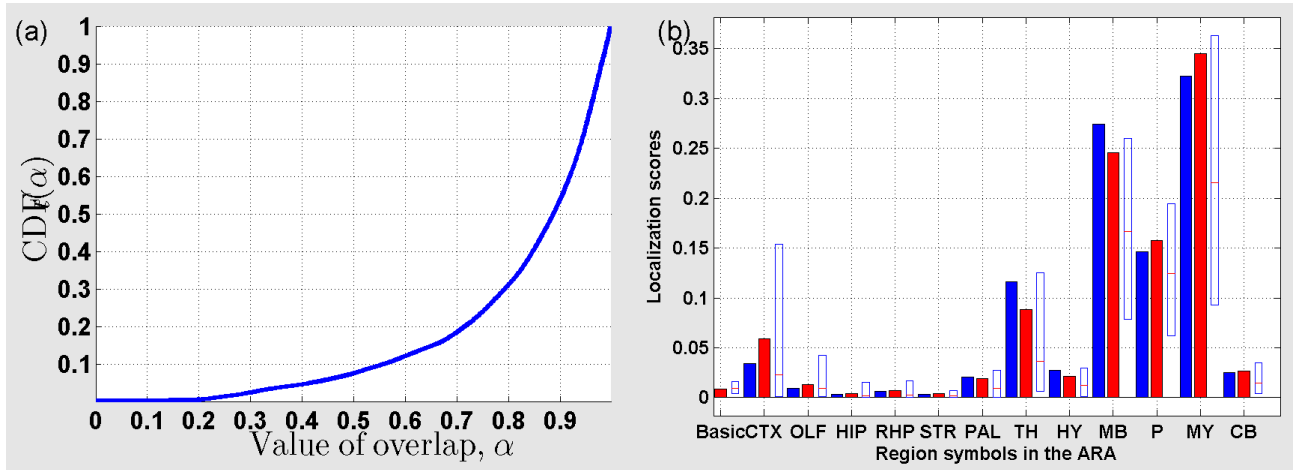


Figure 142: (a) Cumulative distribution function ( $CDF_t$ ) of the overlap between  $\rho_t$  and sub-sampled profiles for  $t = 64$ . (b) Localization scores in the coarsest version of the ARA for  $\rho_t$  (in blue), and  $\bar{\rho}_t$  (in red).

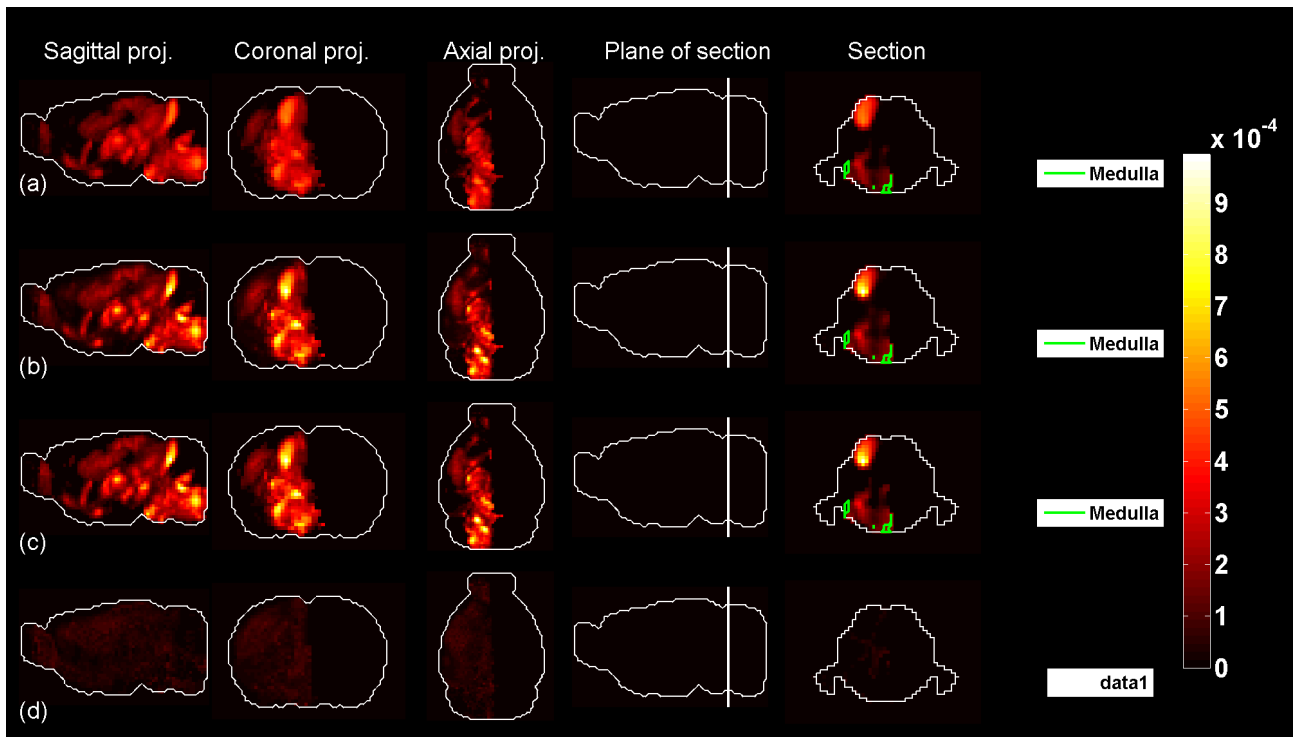


Figure 143: Predicted profile and average sub-sampled profile for  $t = 64$ .

## 7 Figures for sub-sampled profiles (II): random splitting of the genes

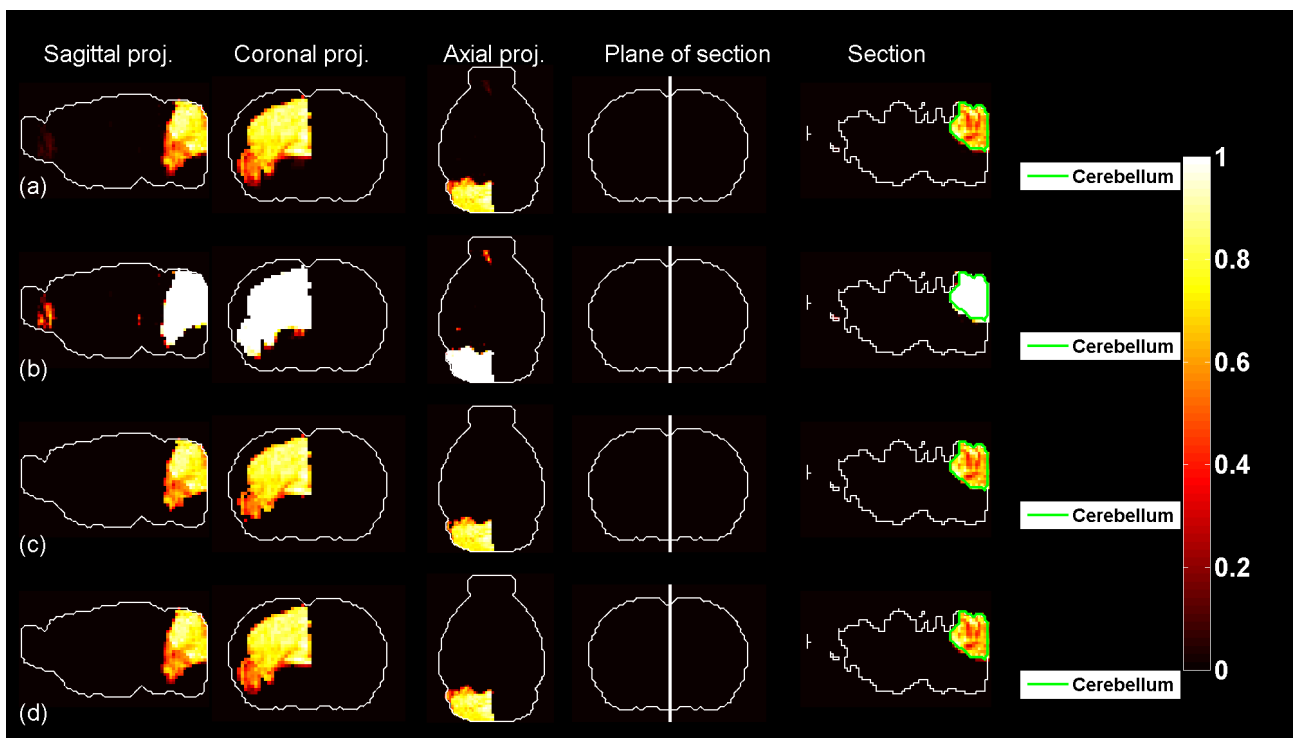


Figure 144: Predicted profile, probability profile and thresholded profiles for  $t = 1$ .

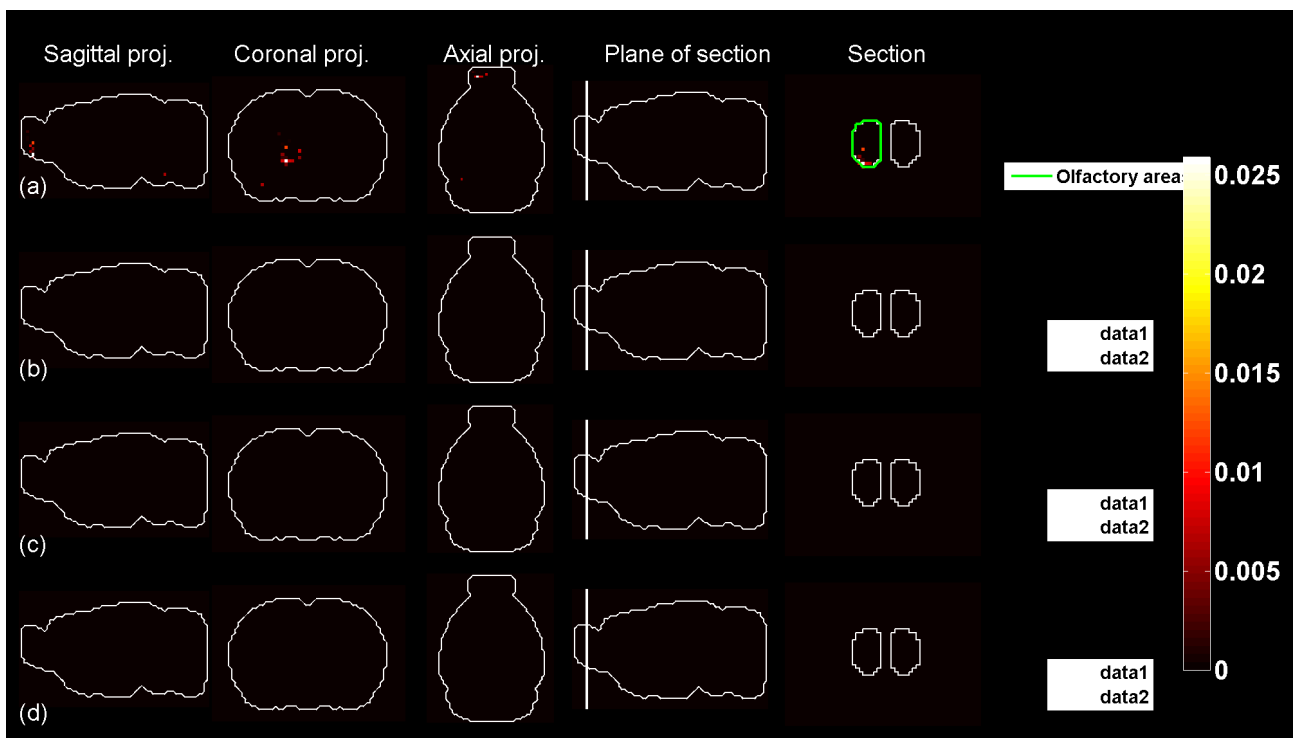


Figure 145: Predicted profile, probability profile and thresholded profiles for  $t = 2$ .

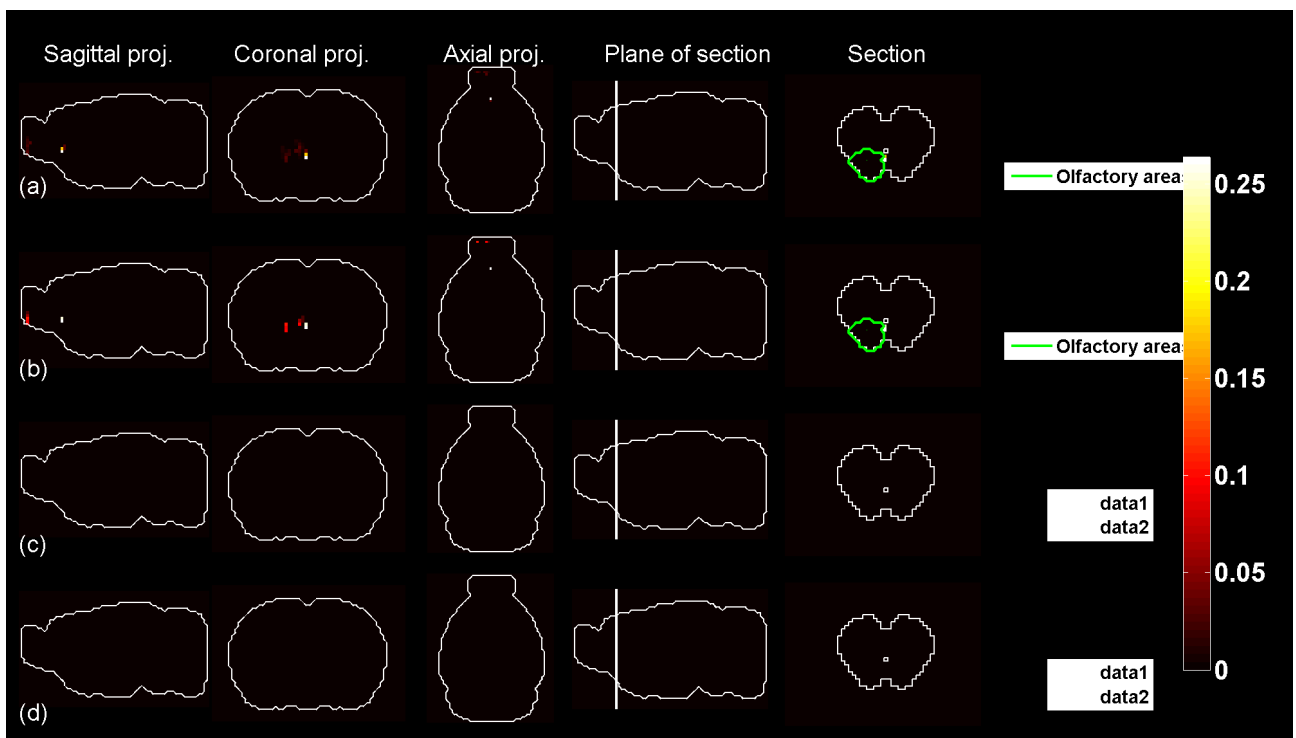


Figure 146: Predicted profile, probability profile and thresholded profiles for  $t = 3$ .

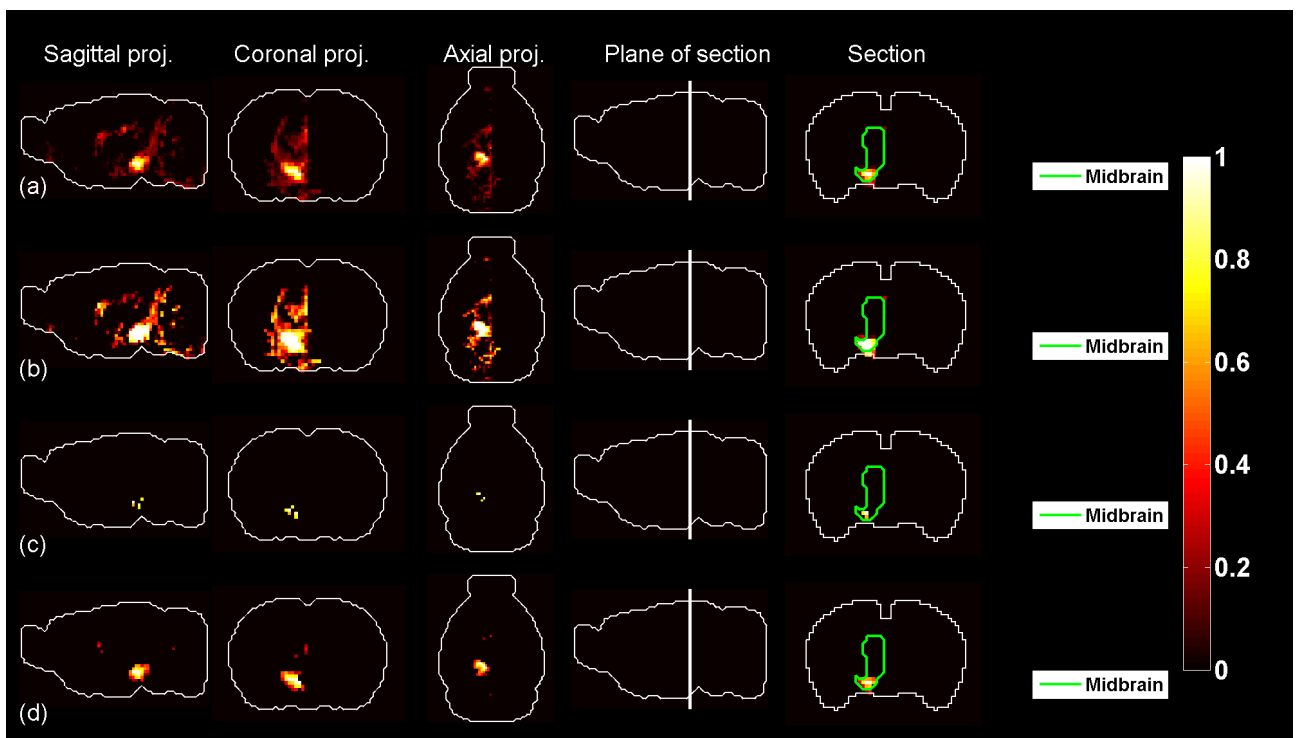


Figure 147: Predicted profile, probability profile and thresholded profiles for  $t = 4$ .

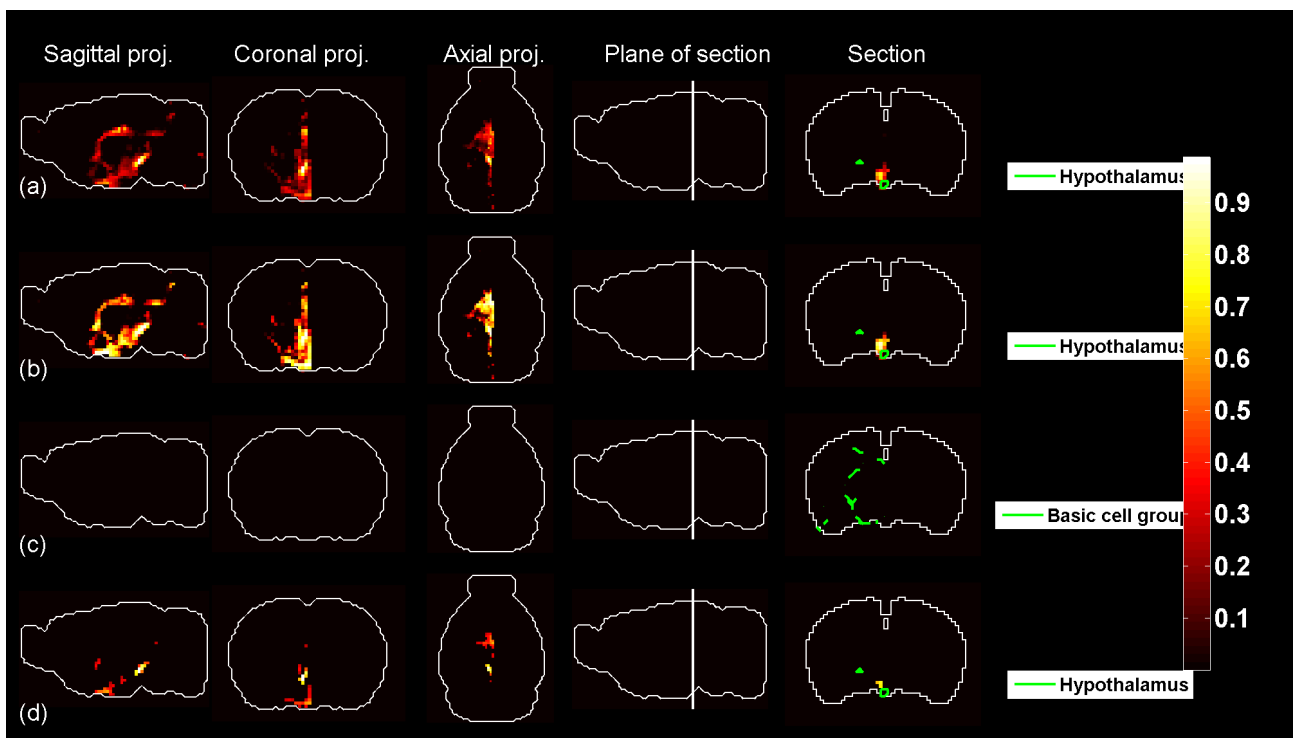


Figure 148: Predicted profile, probability profile and thresholded profiles for  $t = 5$ .

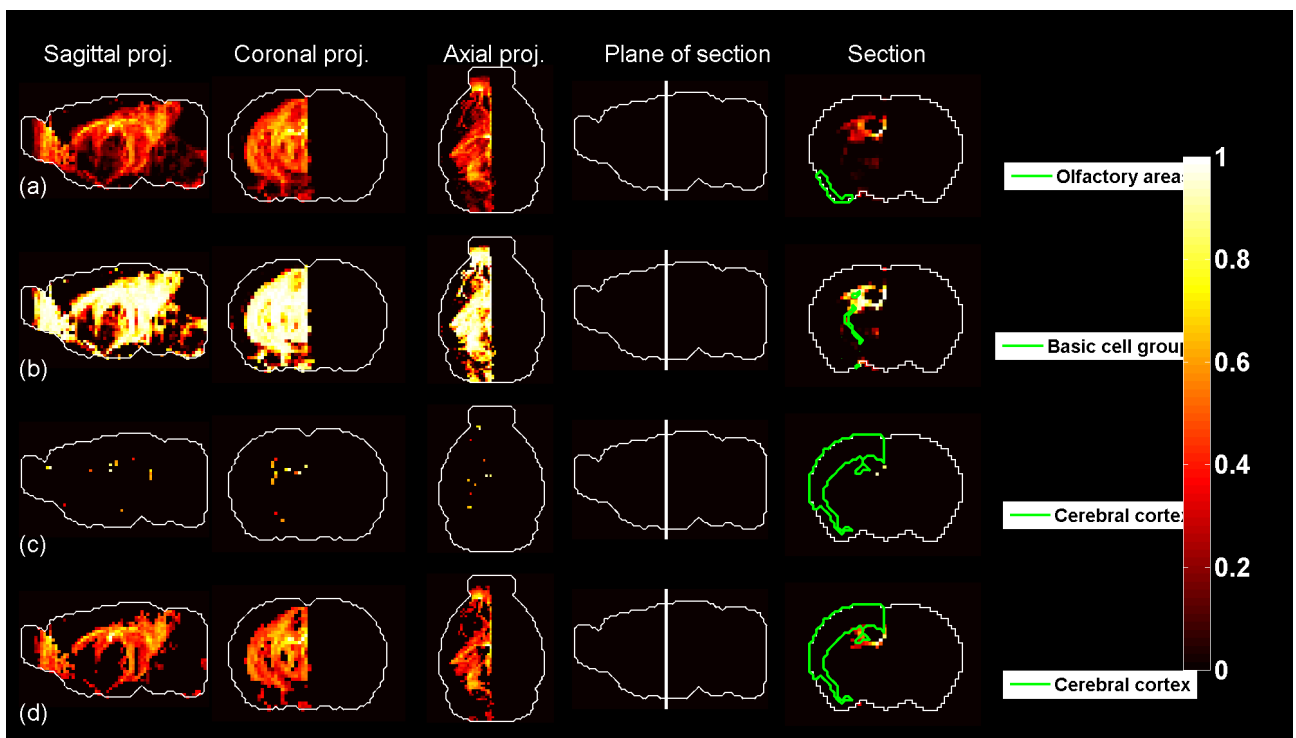


Figure 149: Predicted profile, probability profile and thresholded profiles for  $t = 6$ .

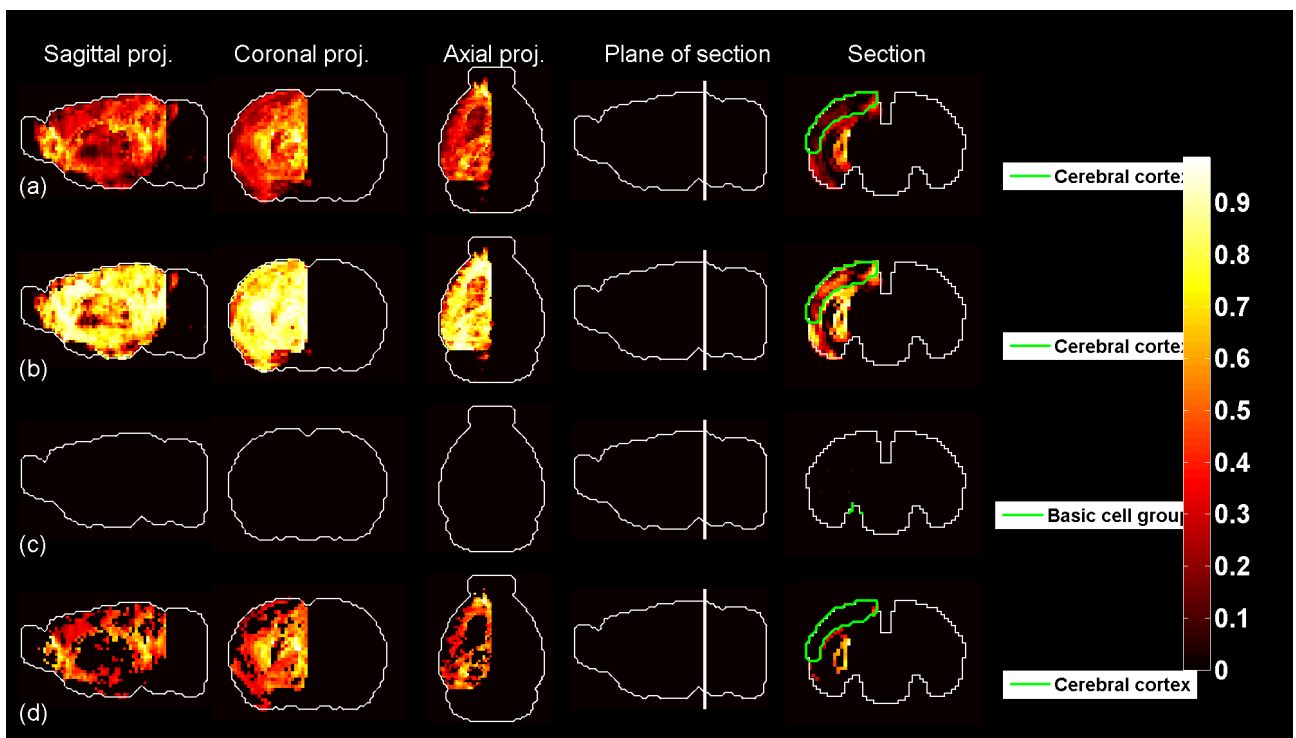


Figure 150: Predicted profile, probability profile and thresholded profiles for  $t = 7$ .

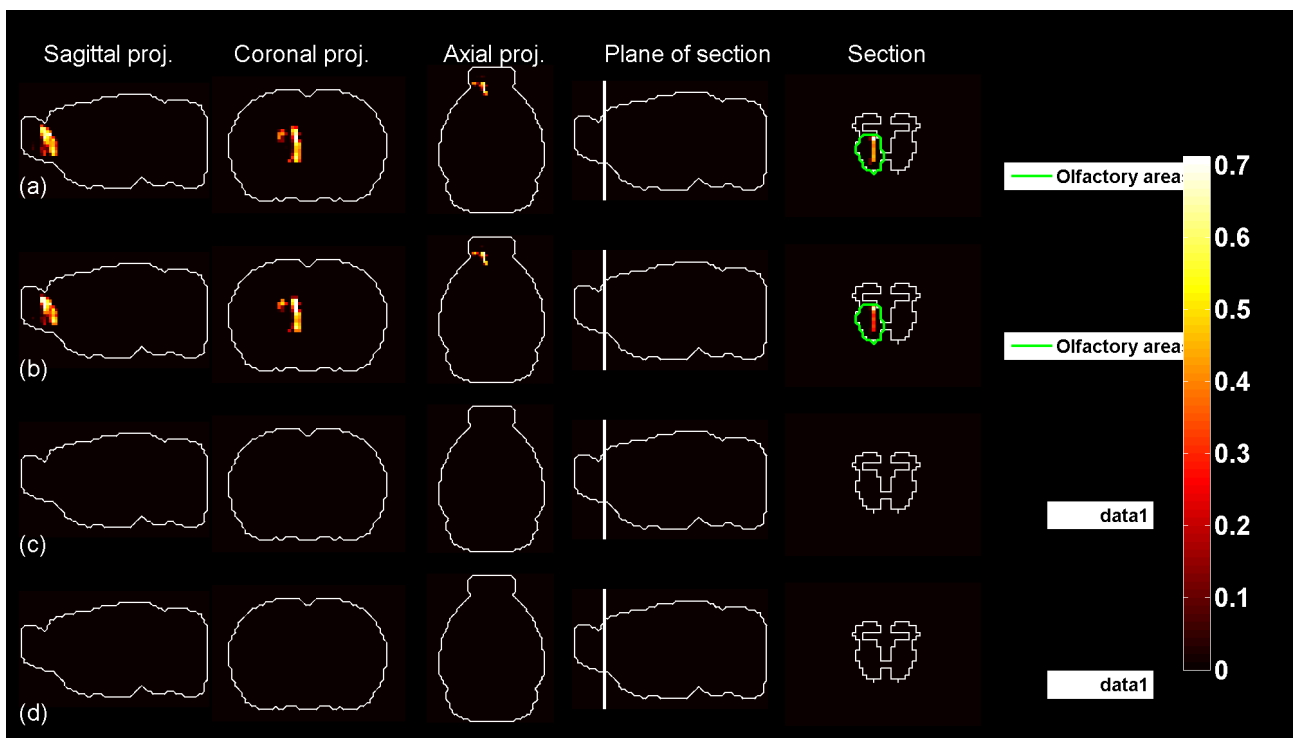


Figure 151: Predicted profile, probability profile and thresholded profiles for  $t = 8$ .

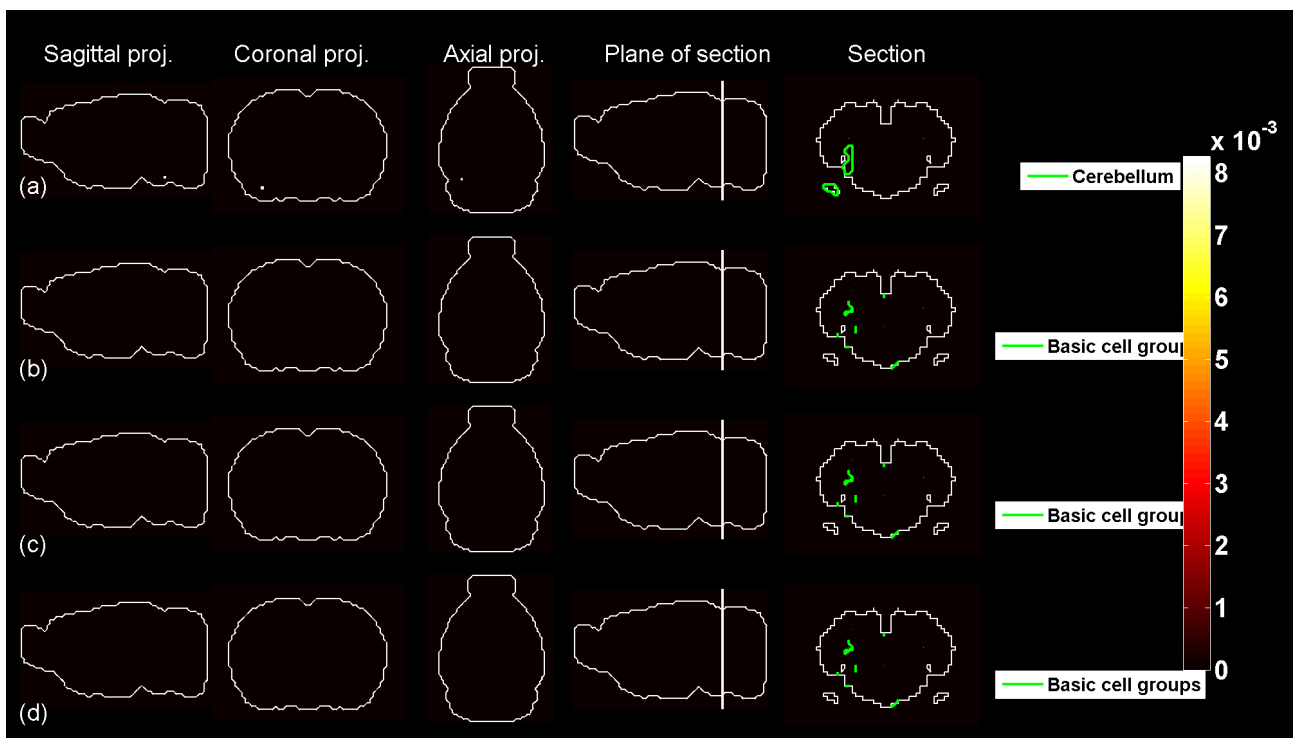


Figure 152: Predicted profile, probability profile and thresholded profiles for  $t = 9$ .

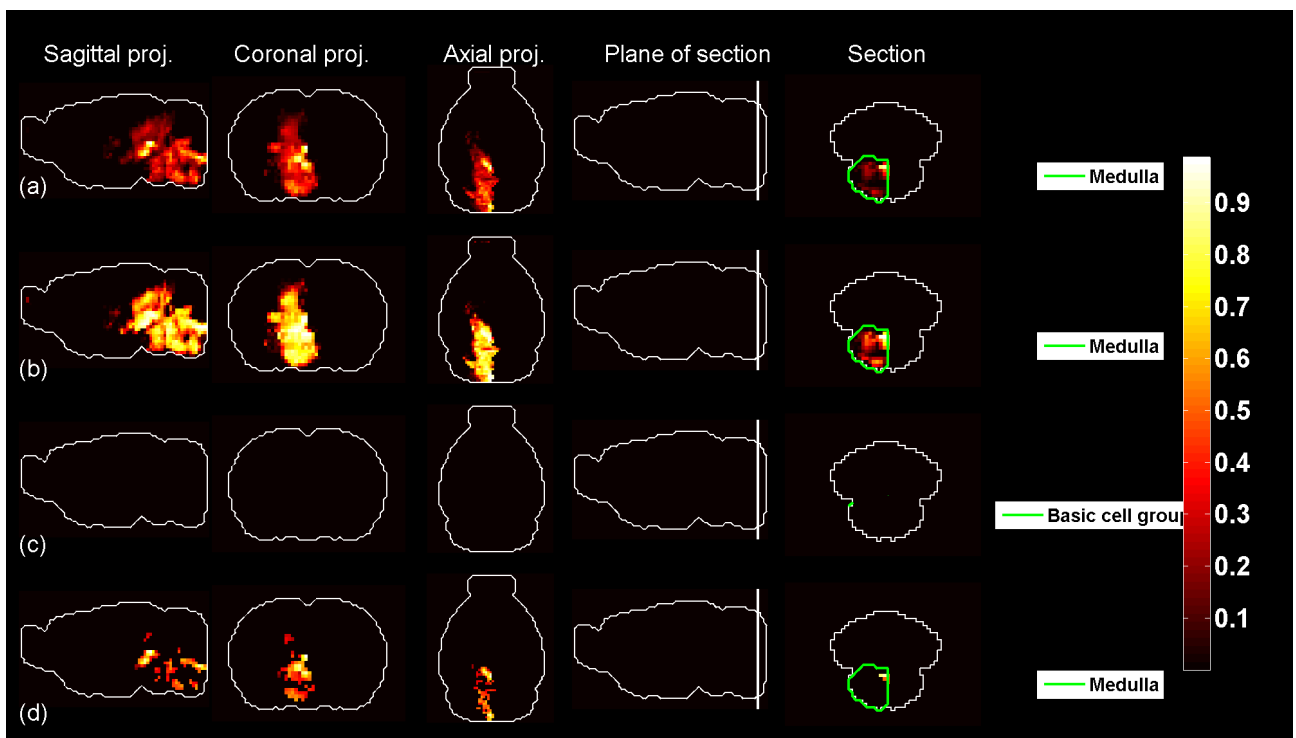


Figure 153: Predicted profile, probability profile and thresholded profiles for  $t = 10$ .

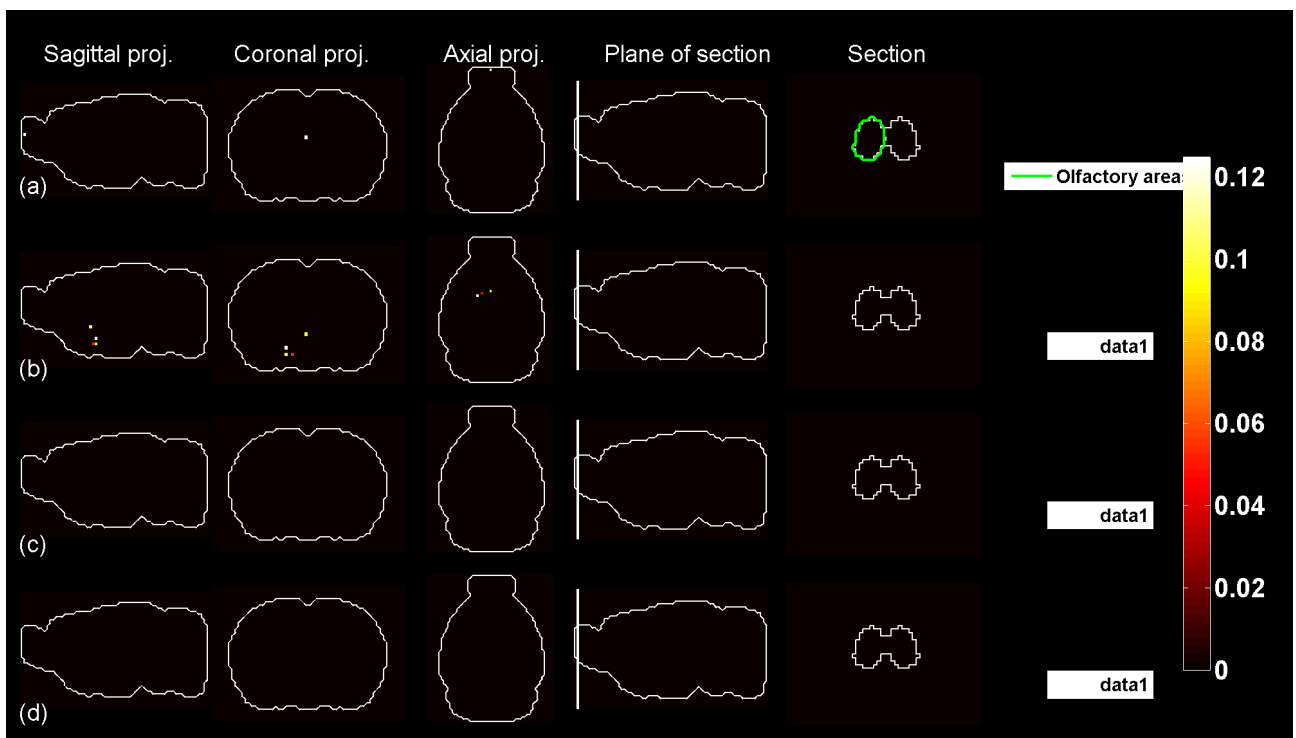


Figure 154: Predicted profile, probability profile and thresholded profiles for  $t = 11$ .

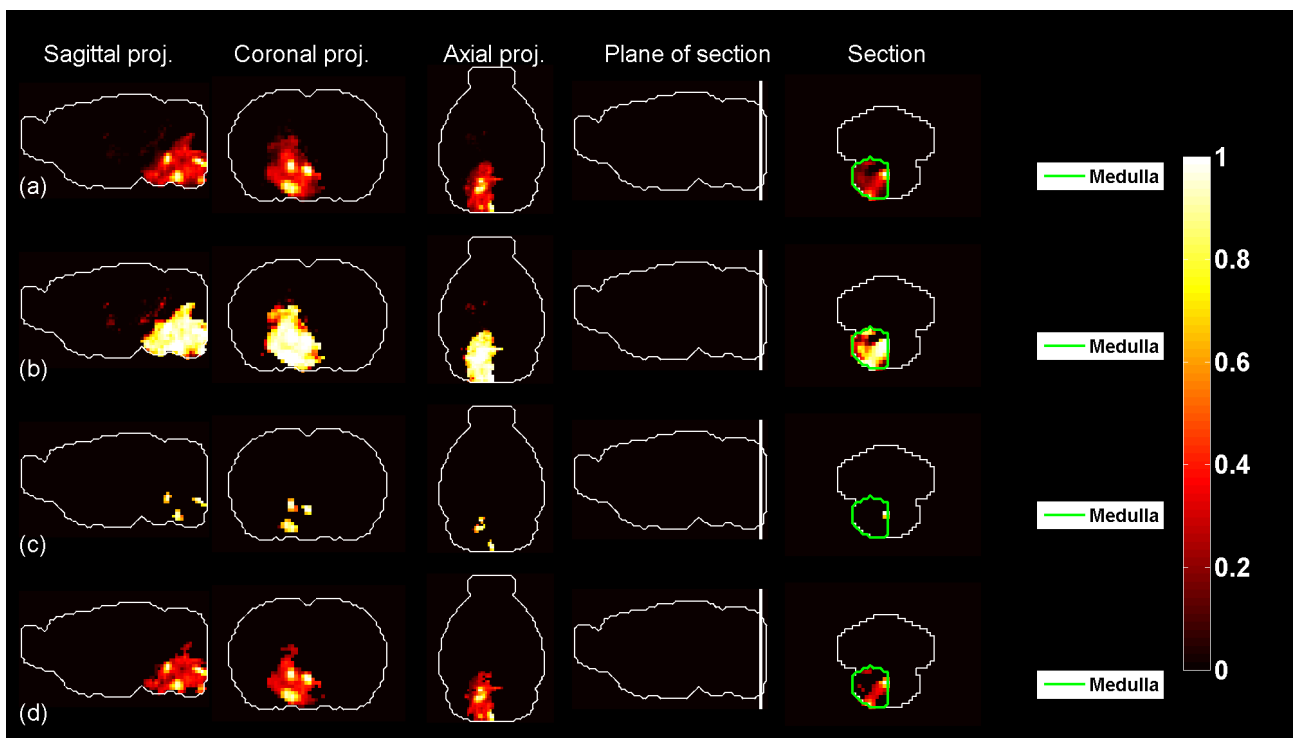


Figure 155: Predicted profile, probability profile and thresholded profiles for  $t = 12$ .

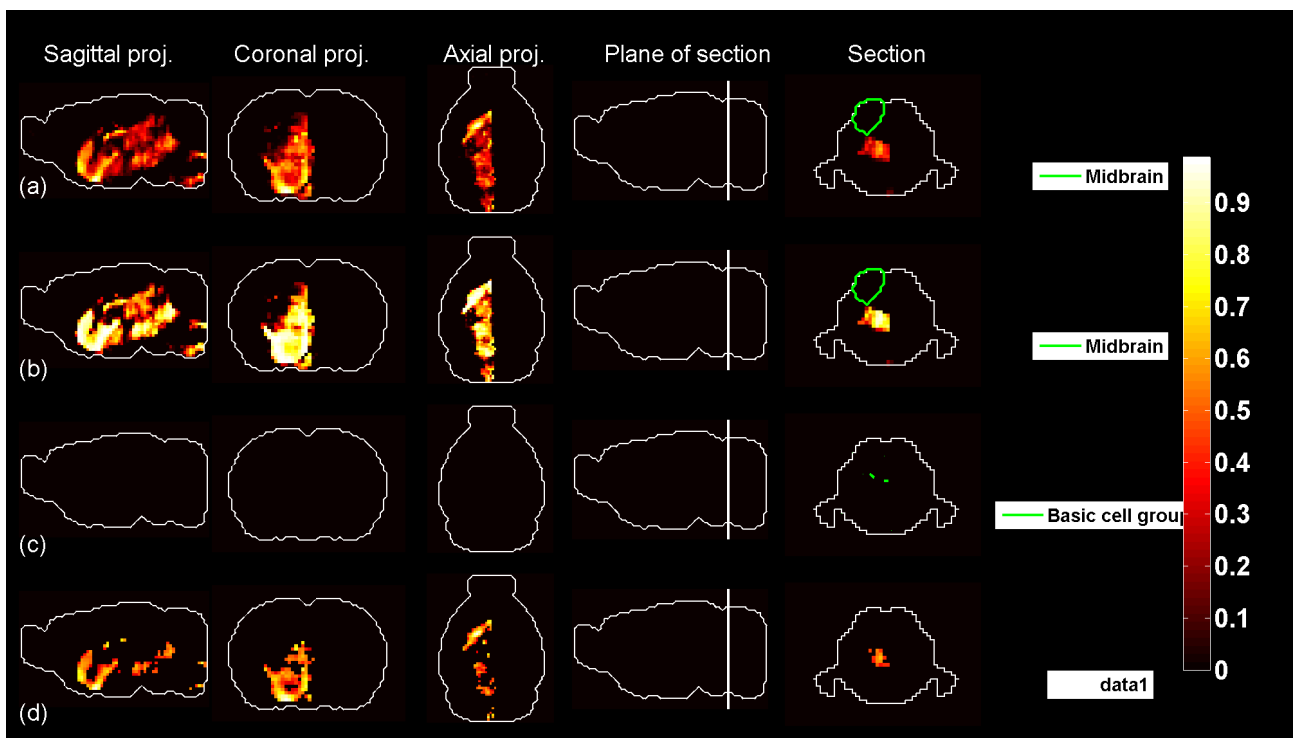


Figure 156: Predicted profile, probability profile and thresholded profiles for  $t = 13$ .

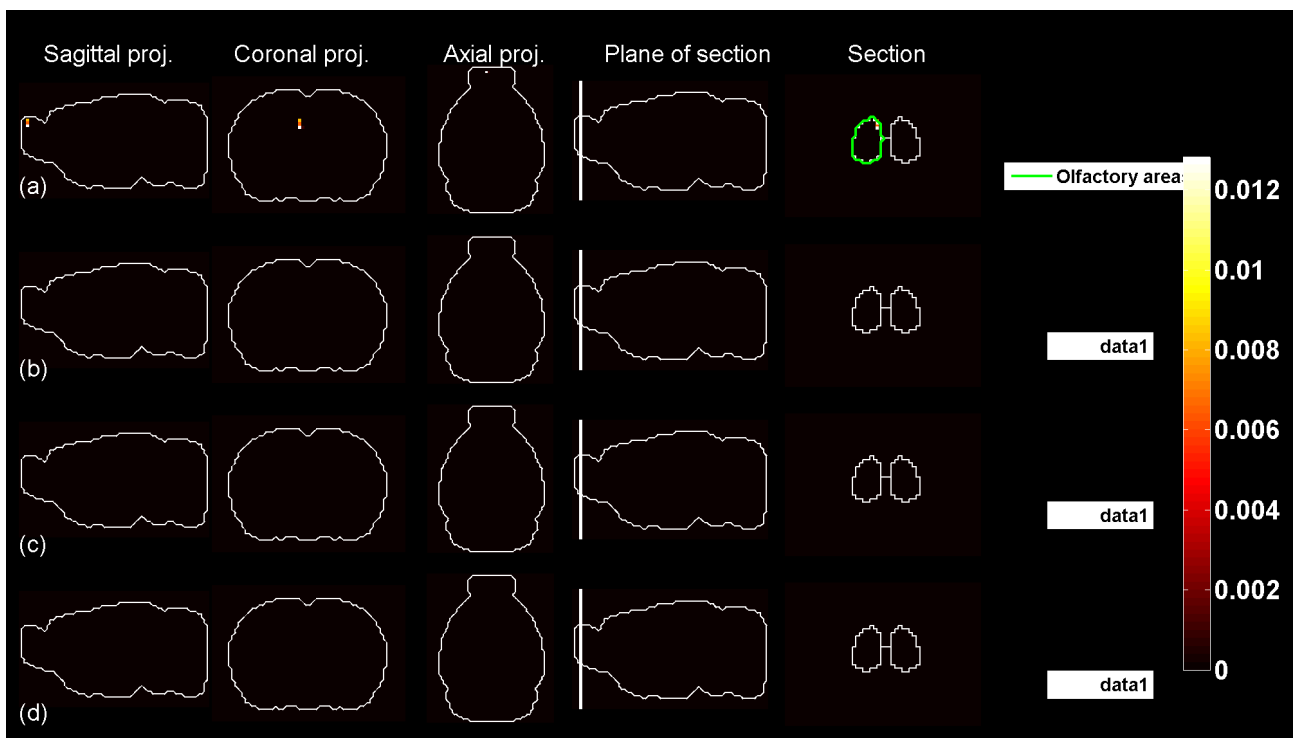


Figure 157: Predicted profile, probability profile and thresholded profiles for  $t = 14$ .

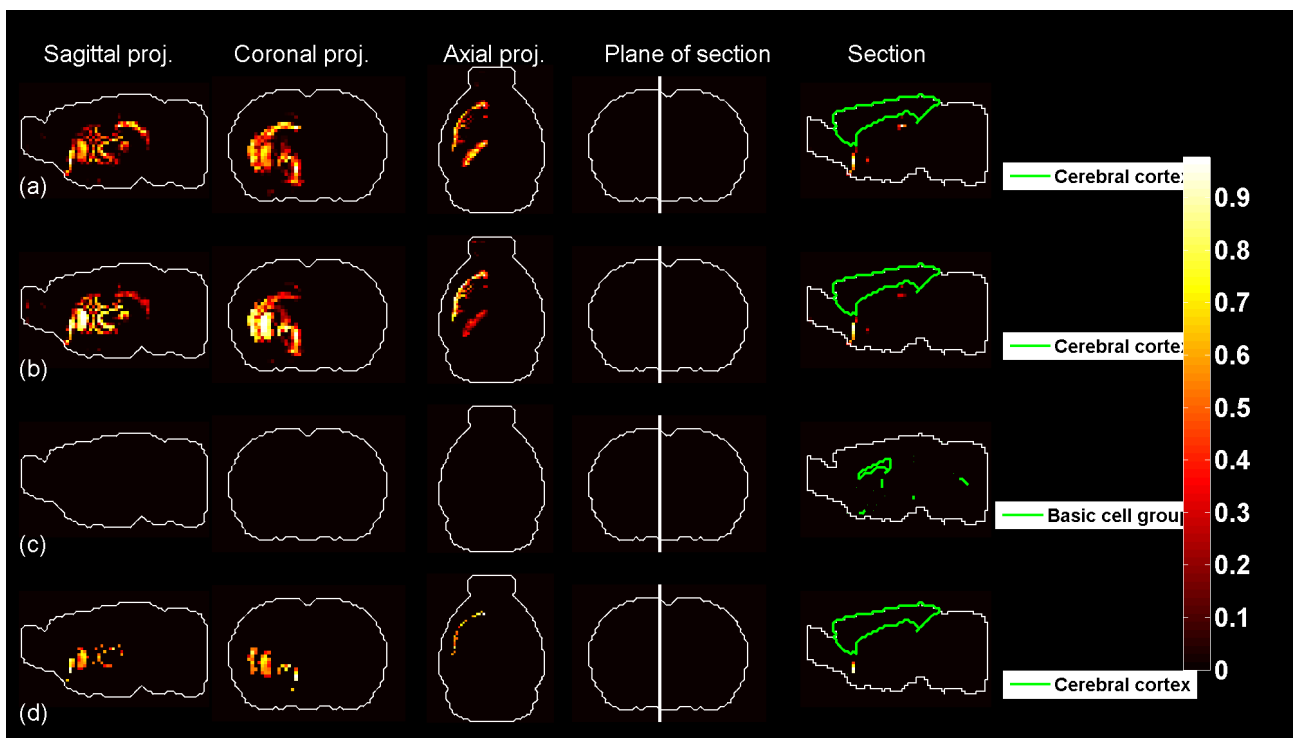


Figure 158: Predicted profile, probability profile and thresholded profiles for  $t = 15$ .

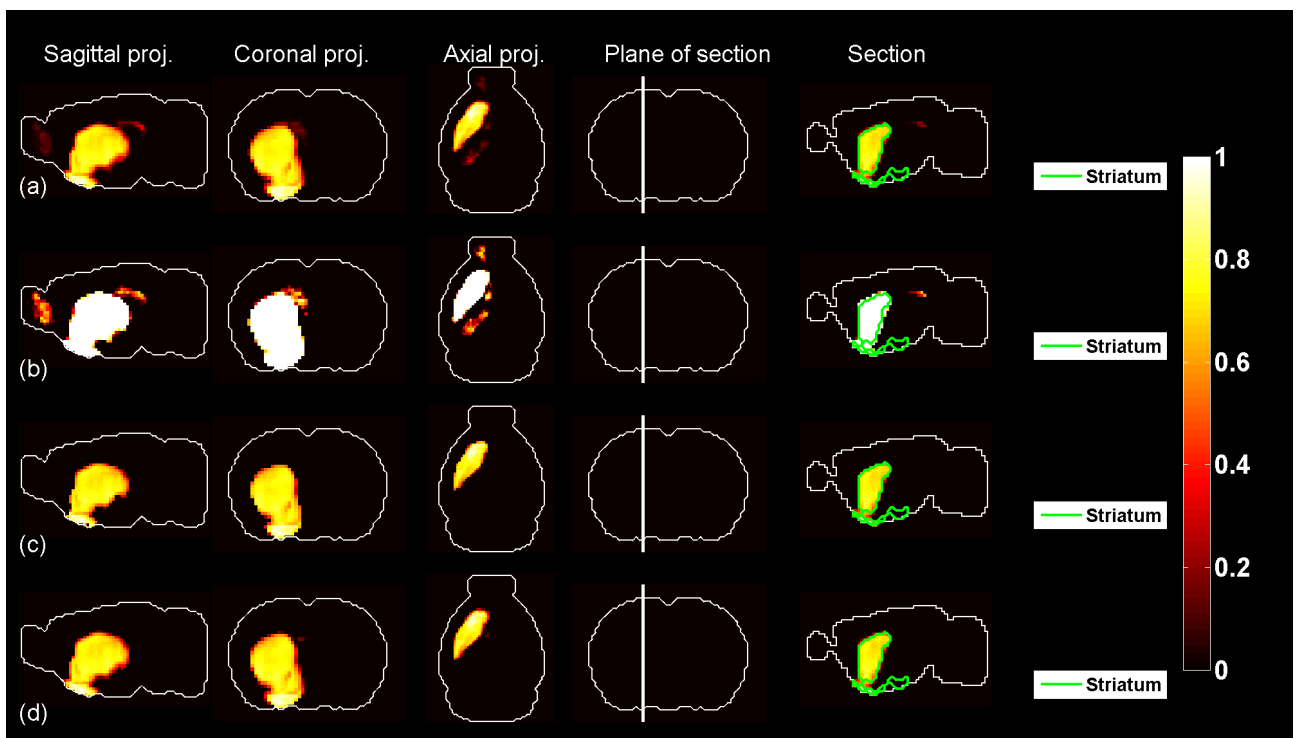


Figure 159: Predicted profile, probability profile and thresholded profiles for  $t = 16$ .

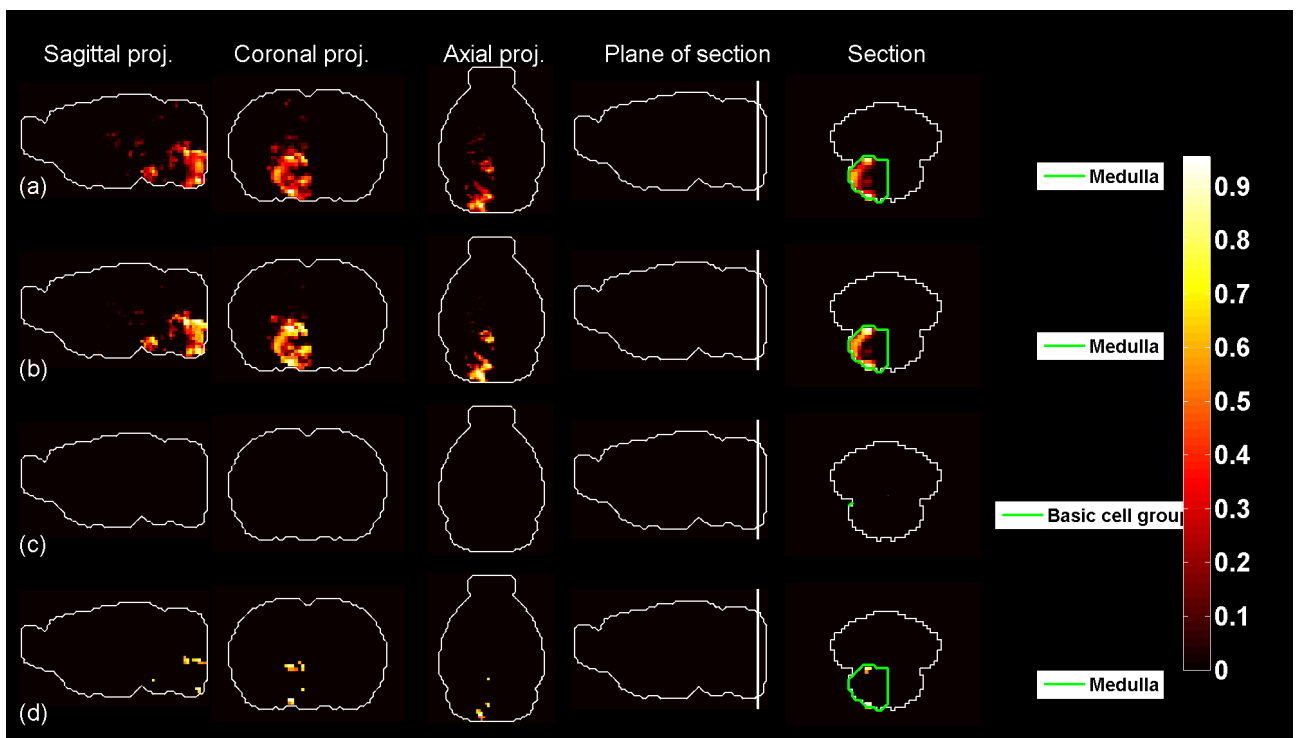


Figure 160: Predicted profile, probability profile and thresholded profiles for  $t = 17$ .

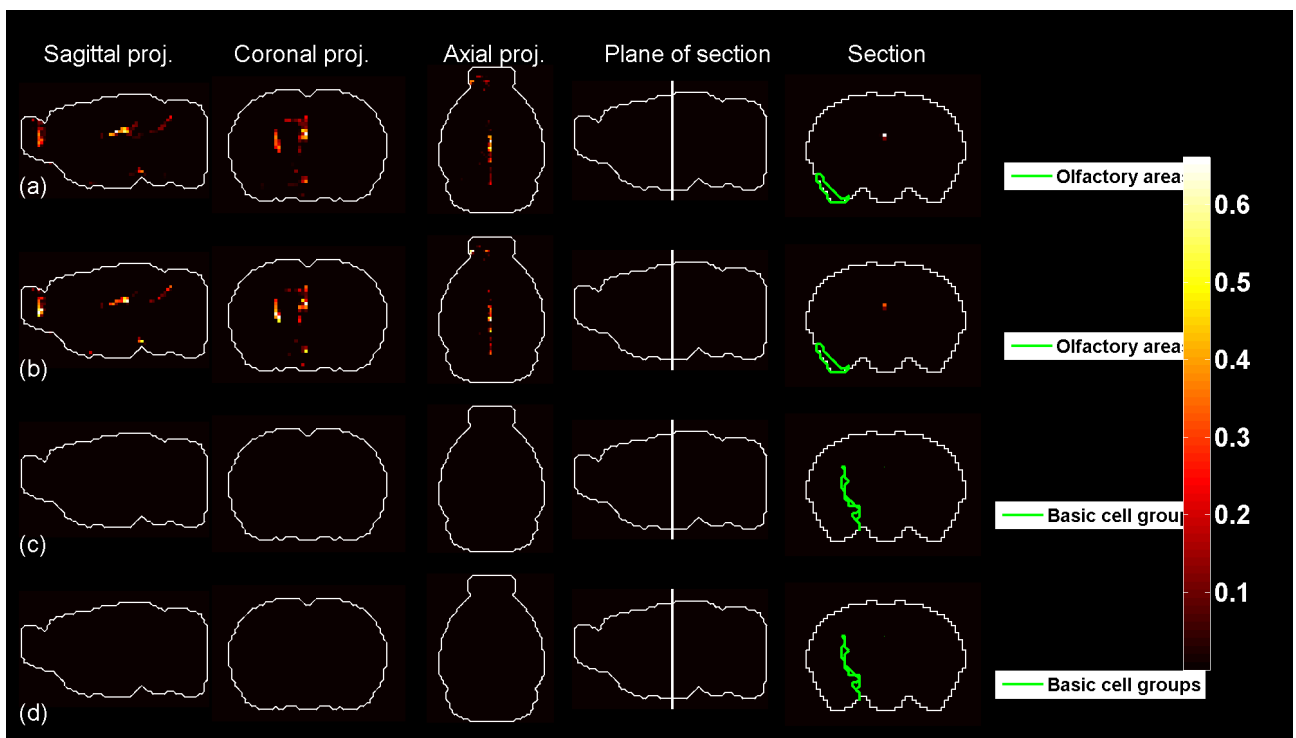


Figure 161: Predicted profile, probability profile and thresholded profiles for  $t = 18$ .

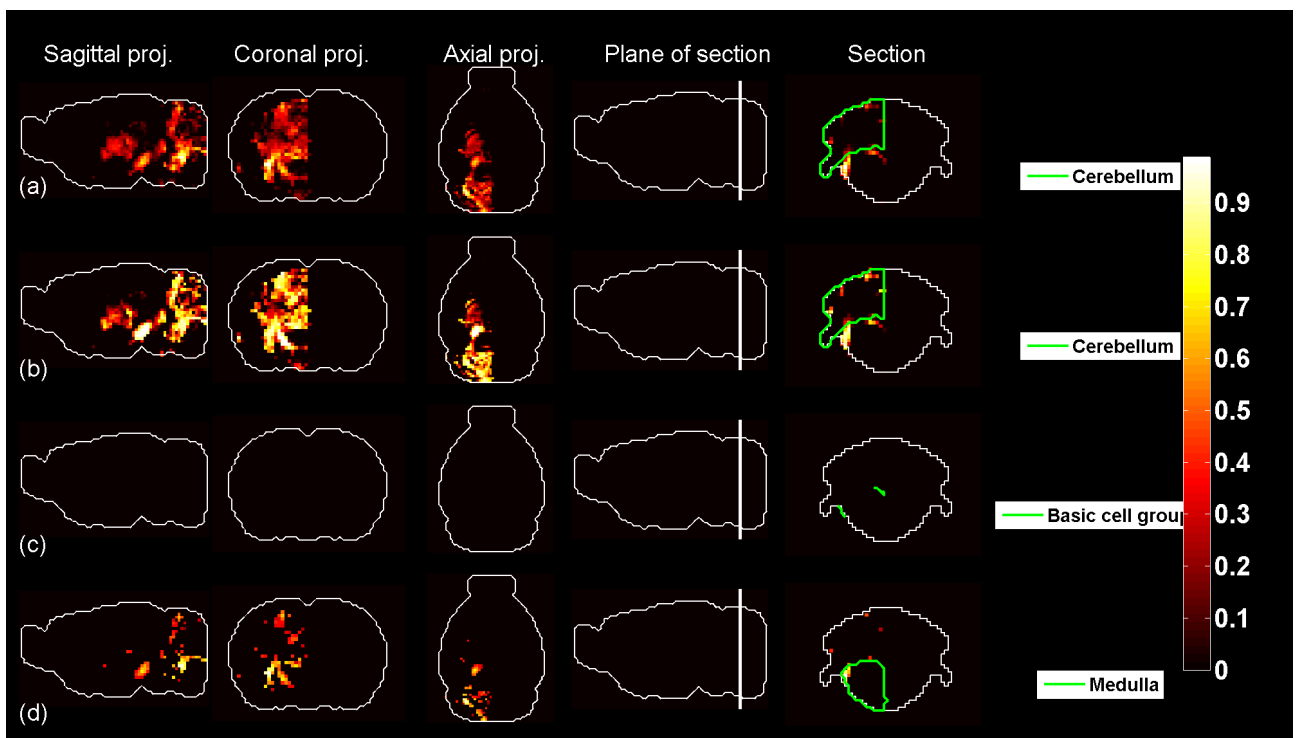


Figure 162: Predicted profile, probability profile and thresholded profiles for  $t = 19$ .

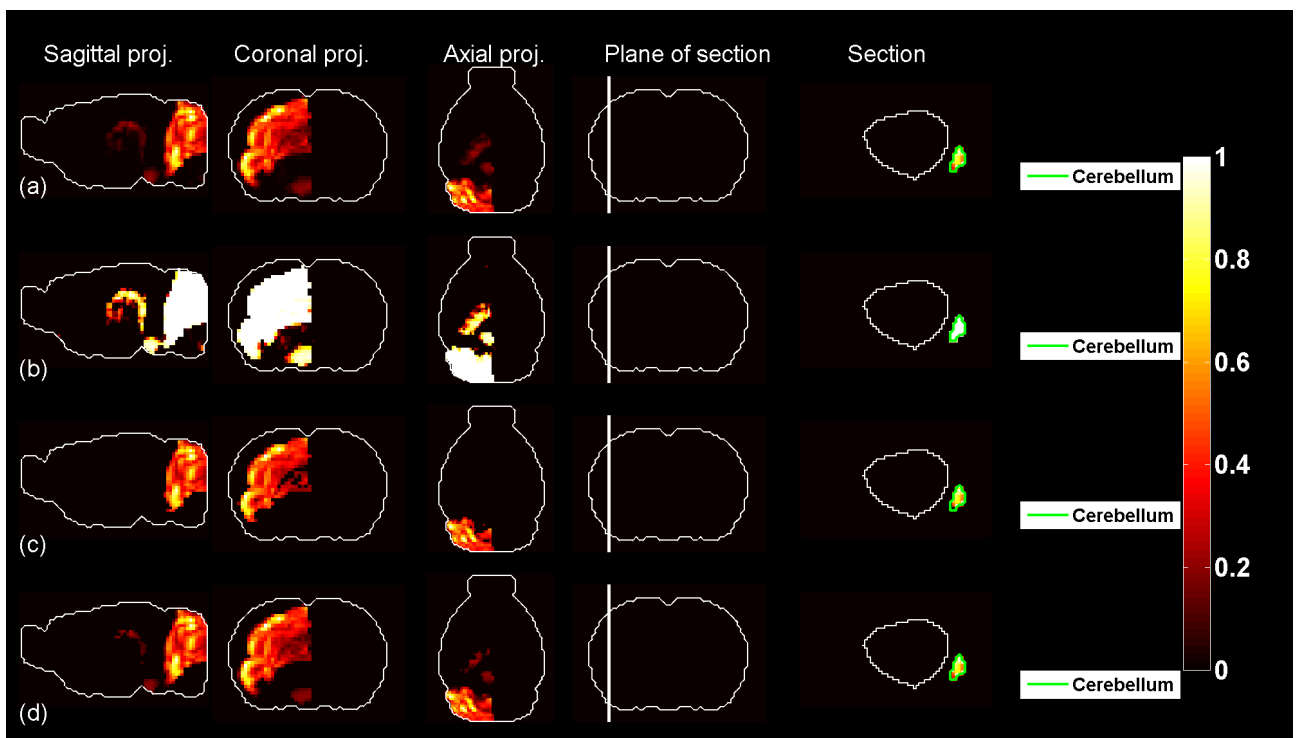


Figure 163: Predicted profile, probability profile and thresholded profiles for  $t = 20$ .

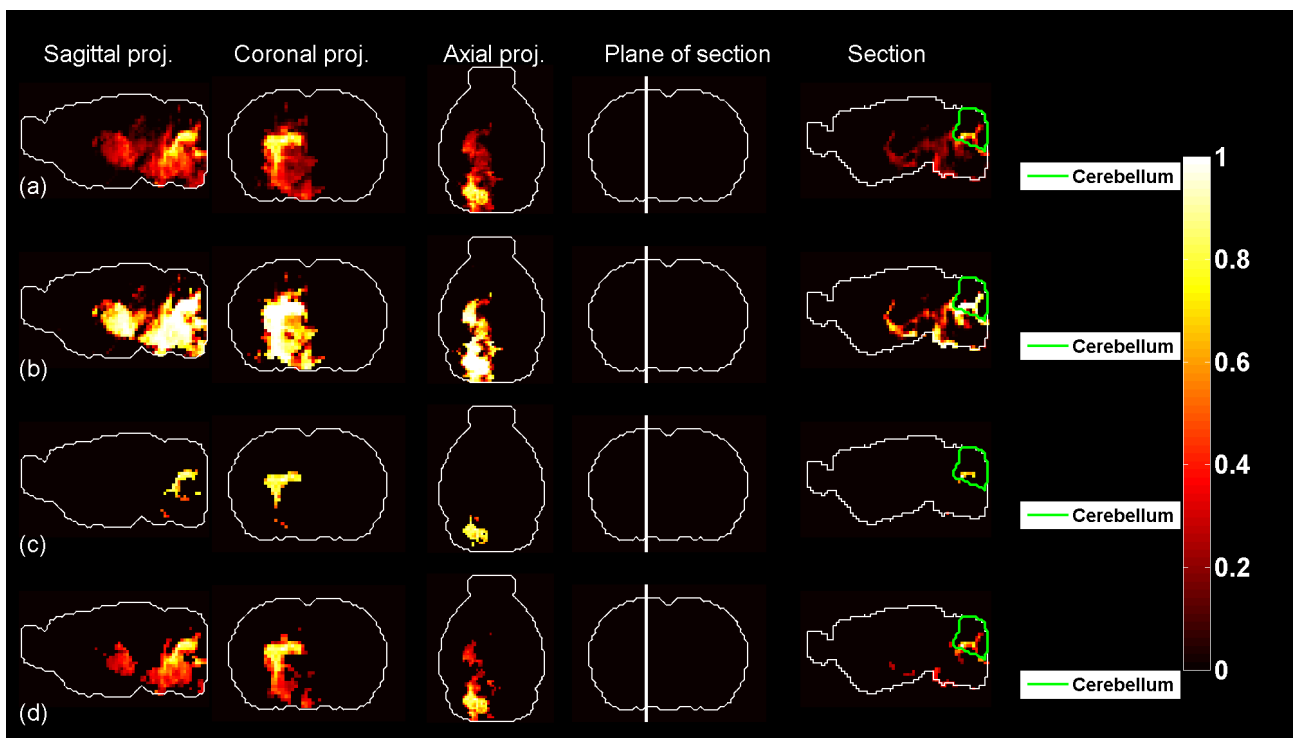


Figure 164: Predicted profile, probability profile and thresholded profiles for  $t = 21$ .

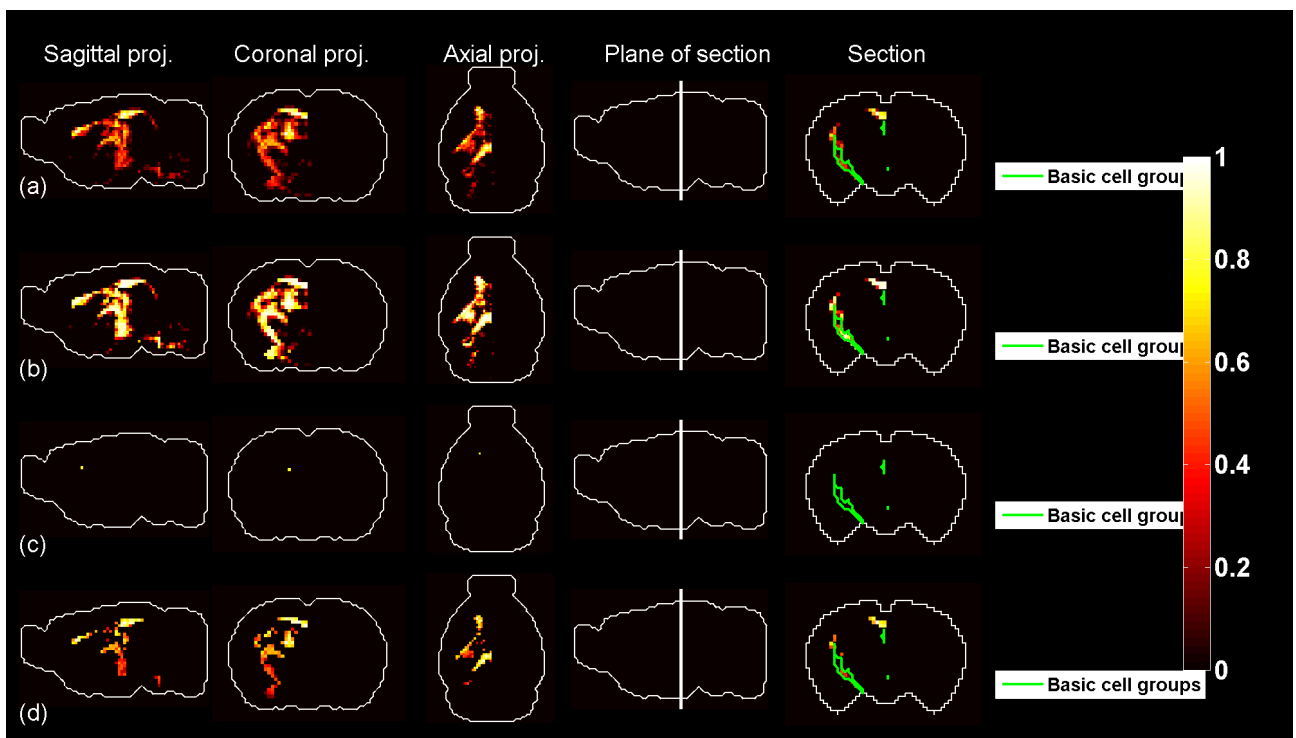


Figure 165: Predicted profile, probability profile and thresholded profiles for  $t = 22$ .

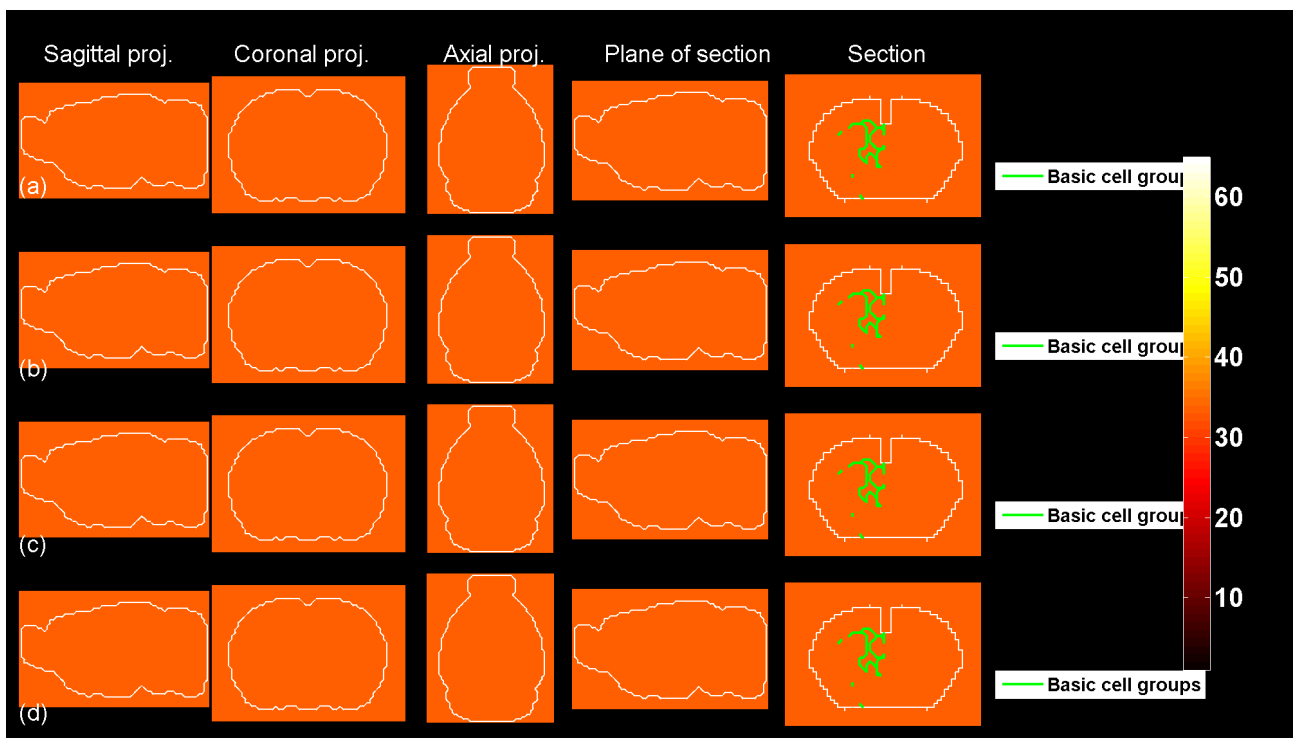


Figure 166: Predicted profile, probability profile and thresholded profiles for  $t = 23$ .

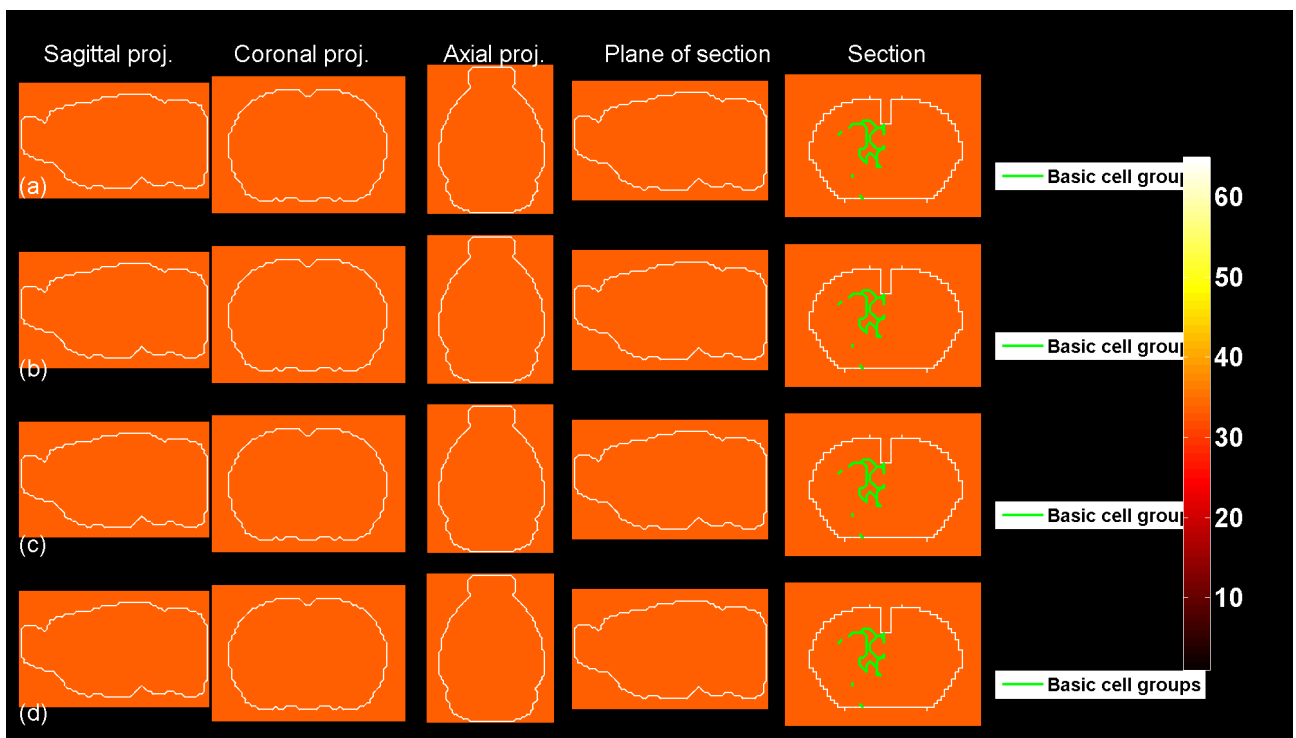


Figure 167: Predicted profile, probability profile and thresholded profiles for  $t = 24$ .

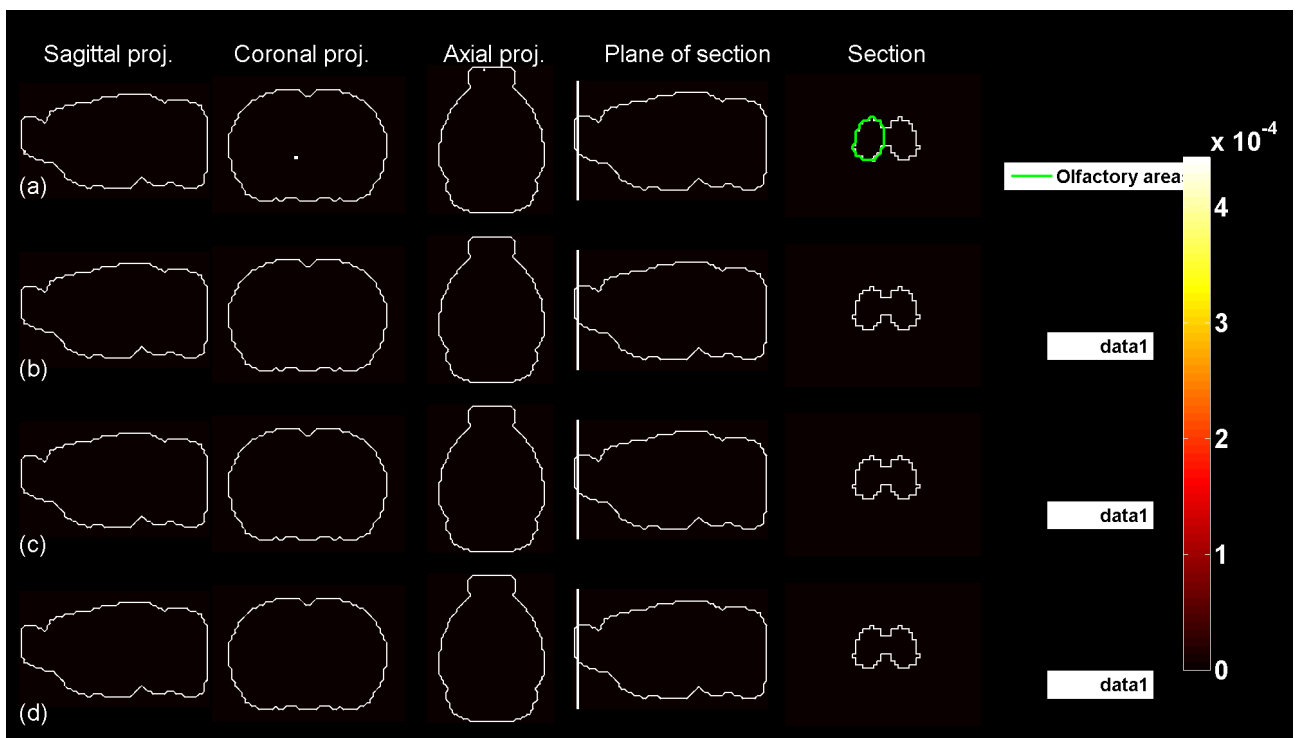


Figure 168: Predicted profile, probability profile and thresholded profiles for  $t = 25$ .

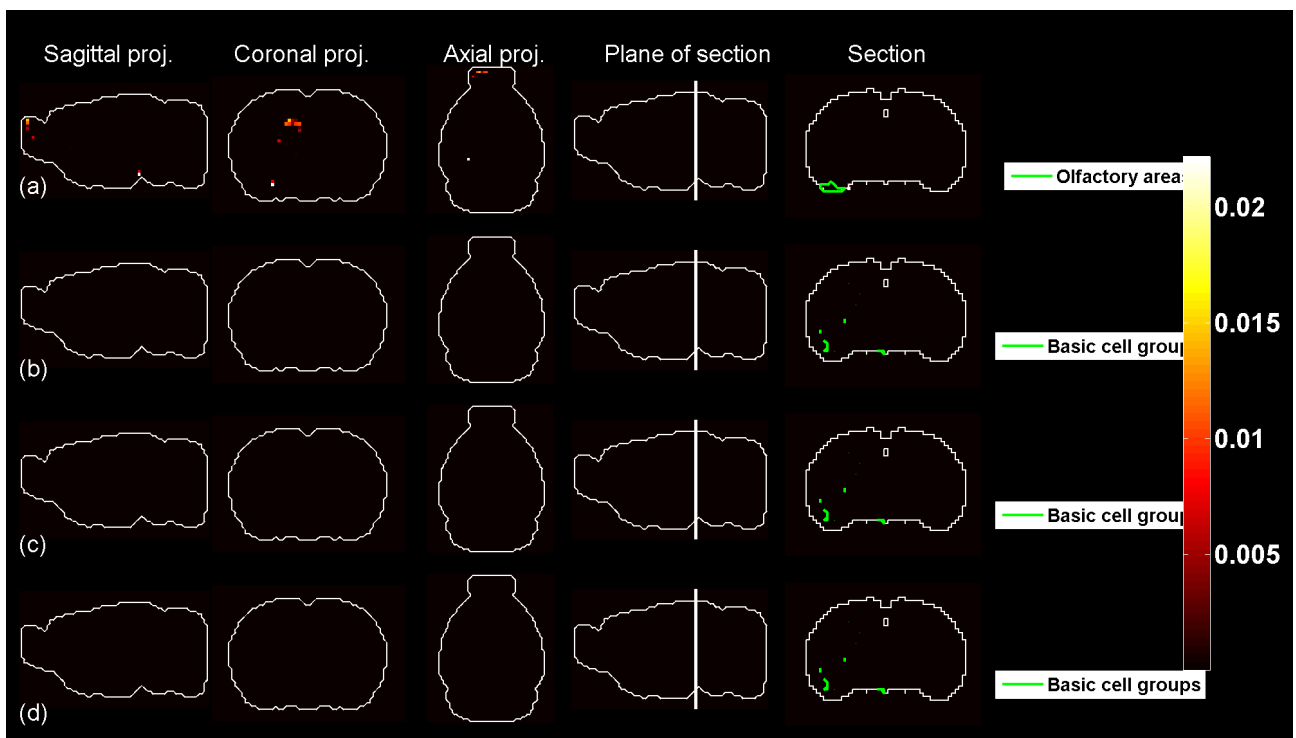


Figure 169: Predicted profile, probability profile and thresholded profiles for  $t = 26$ .

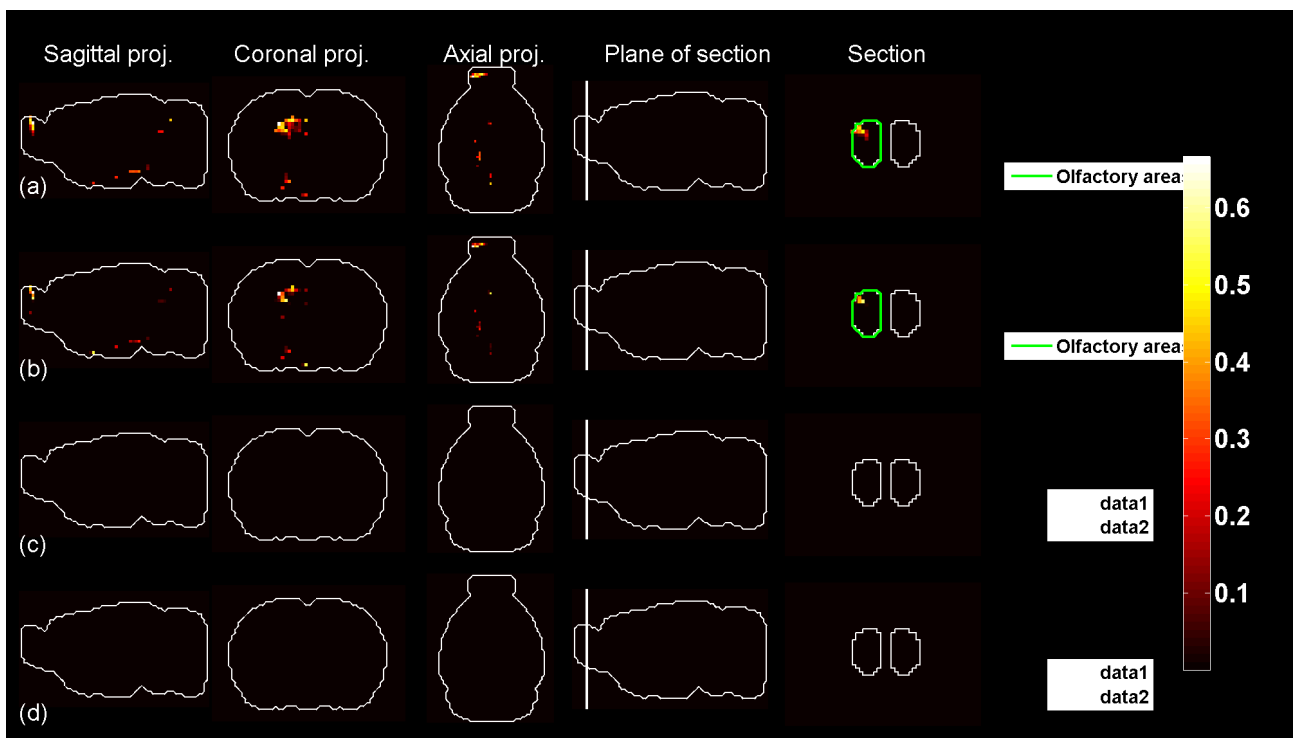


Figure 170: Predicted profile, probability profile and thresholded profiles for  $t = 27$ .

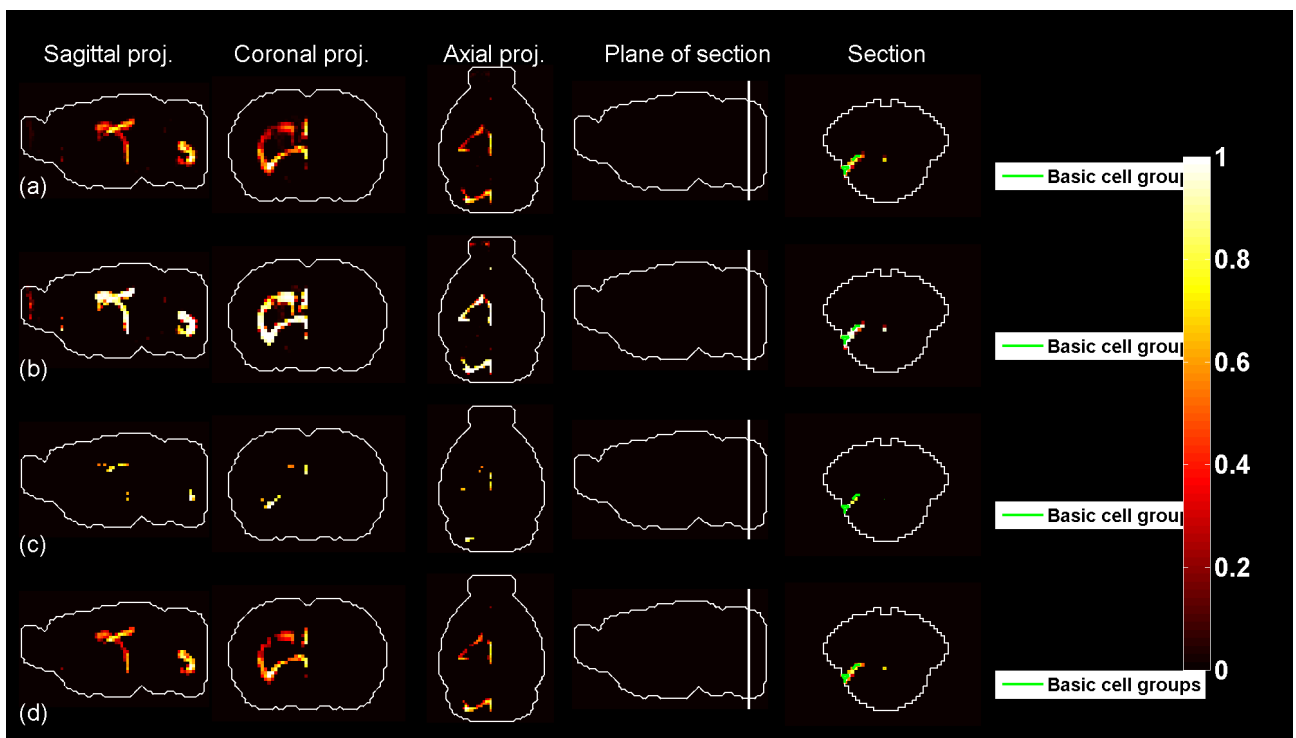


Figure 171: Predicted profile, probability profile and thresholded profiles for  $t = 28$ .

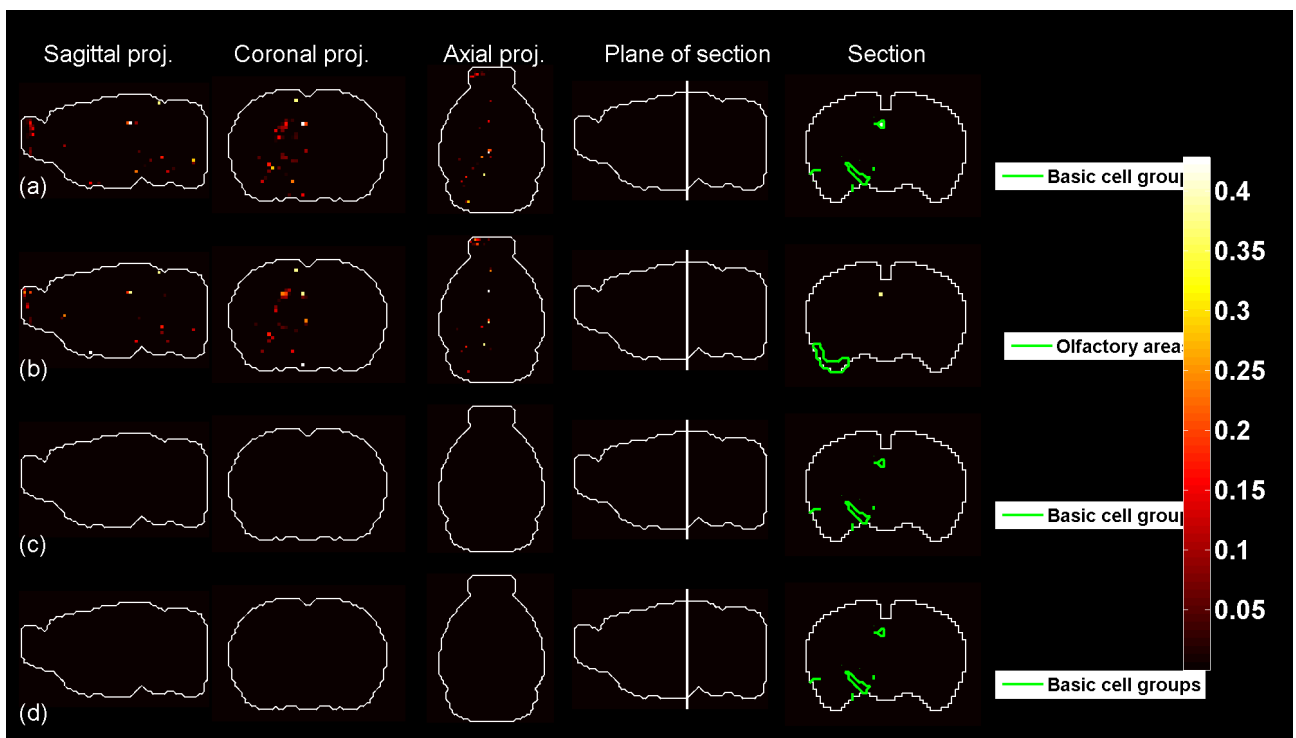


Figure 172: Predicted profile, probability profile and thresholded profiles for  $t = 29$ .

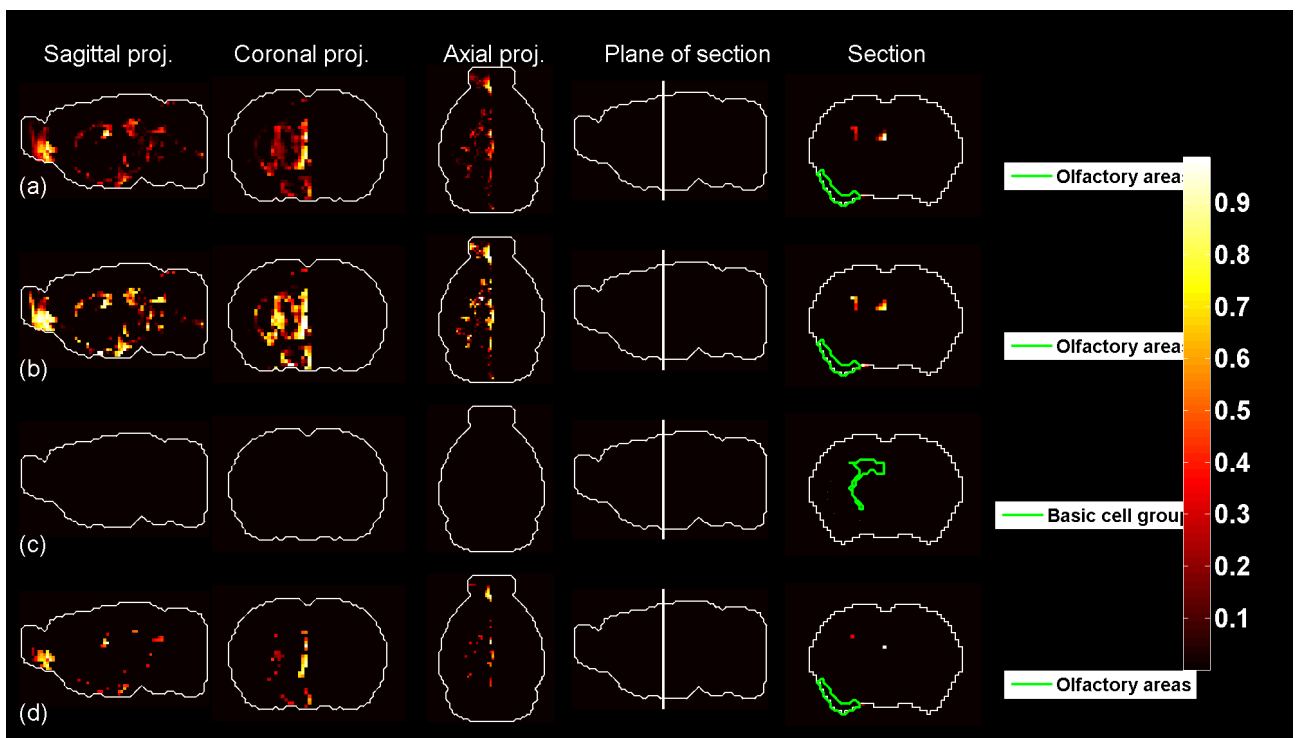


Figure 173: Predicted profile, probability profile and thresholded profiles for  $t = 30$ .

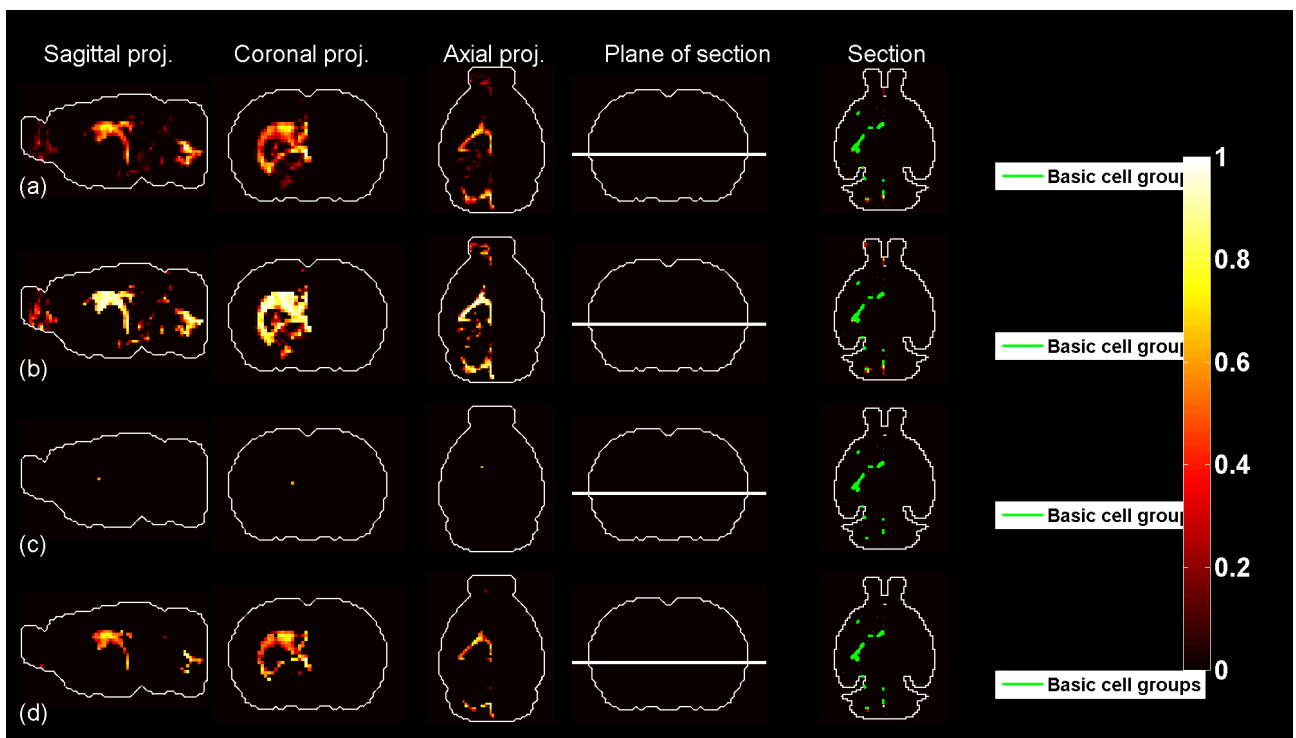


Figure 174: Predicted profile, probability profile and thresholded profiles for  $t = 31$ .

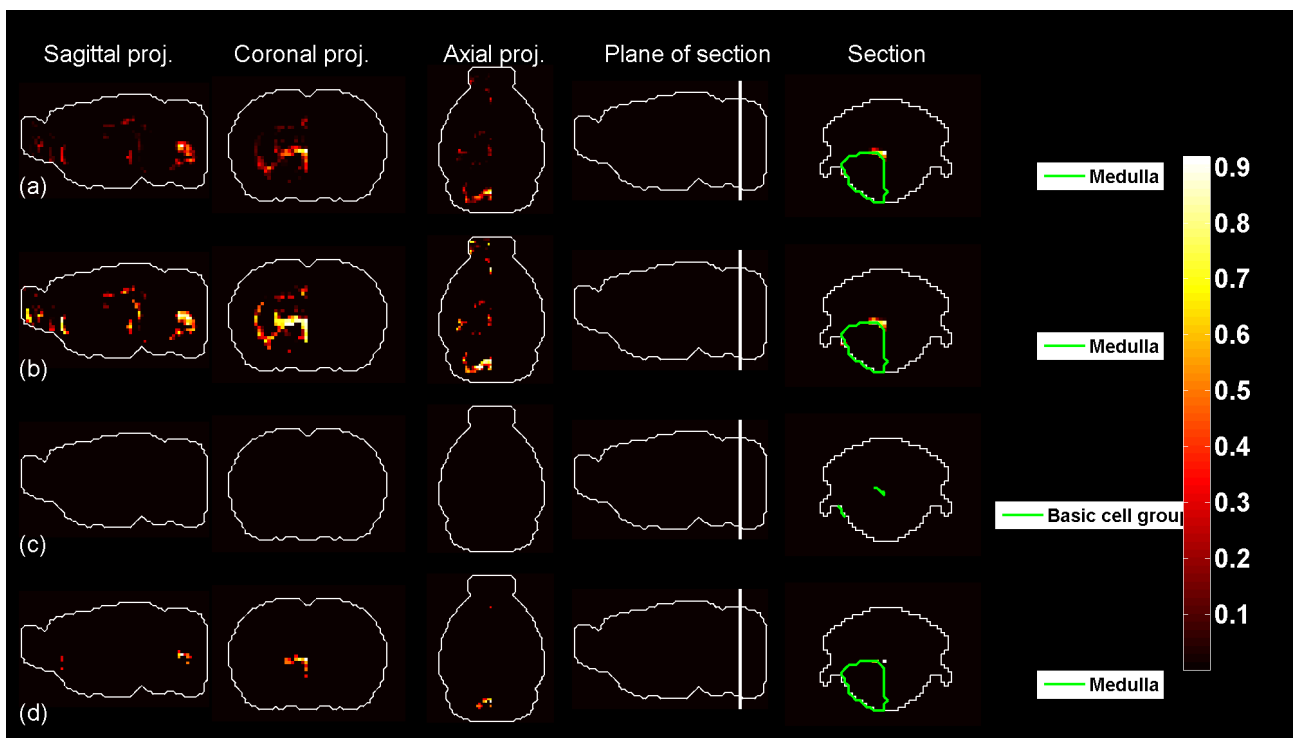


Figure 175: Predicted profile, probability profile and thresholded profiles for  $t = 32$ .

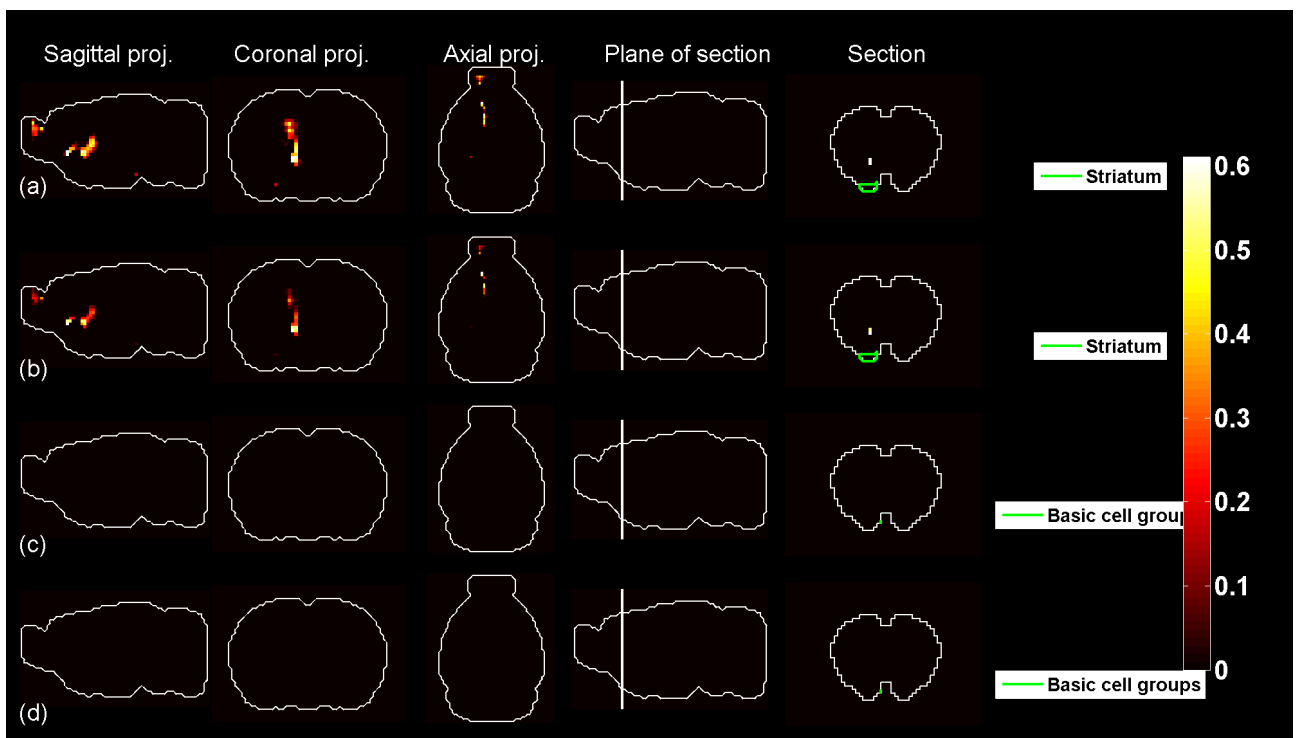


Figure 176: Predicted profile, probability profile and thresholded profiles for  $t = 33$ .

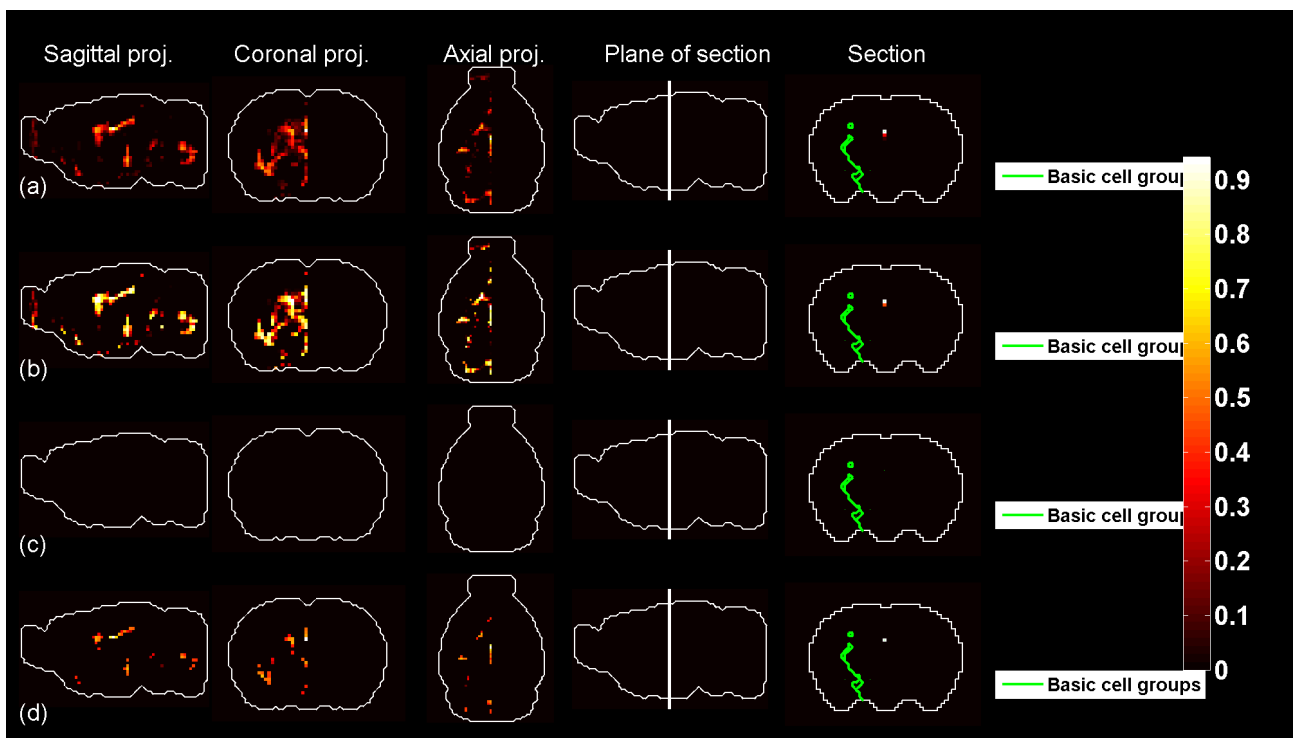


Figure 177: Predicted profile, probability profile and thresholded profiles for  $t = 34$ .

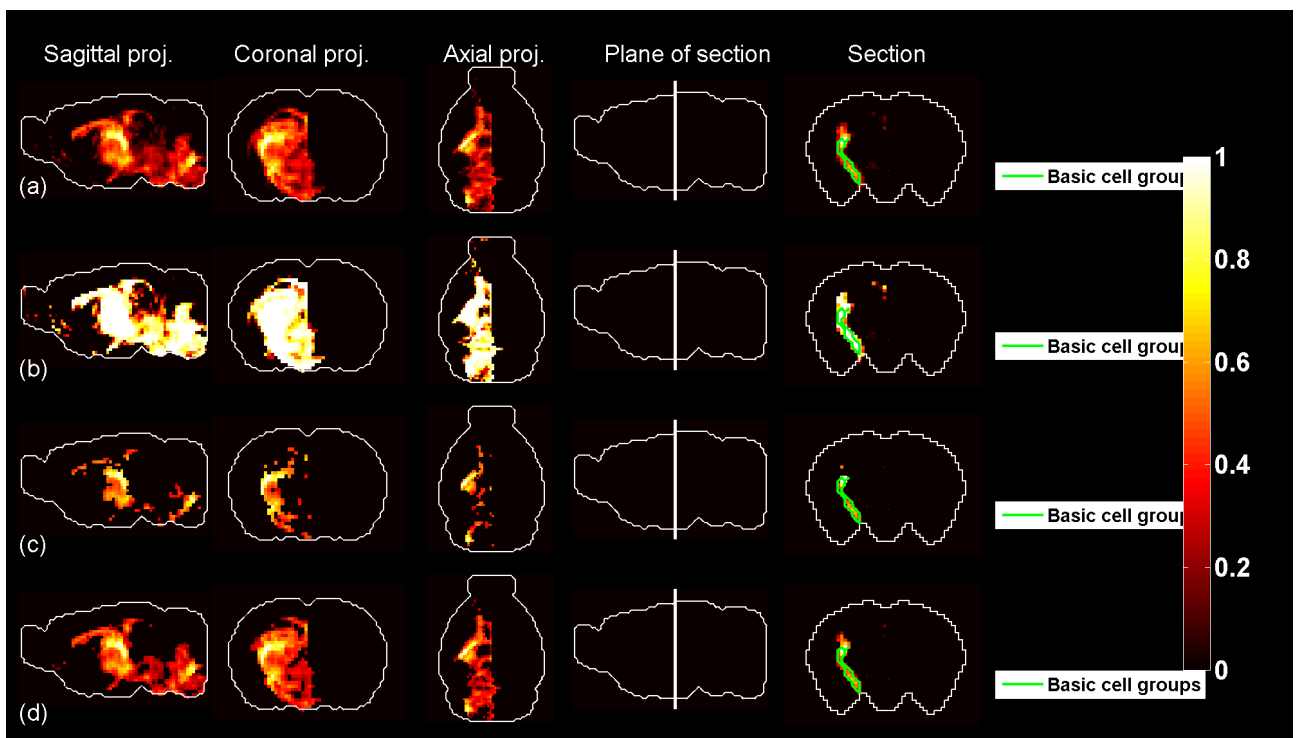


Figure 178: Predicted profile, probability profile and thresholded profiles for  $t = 35$ .

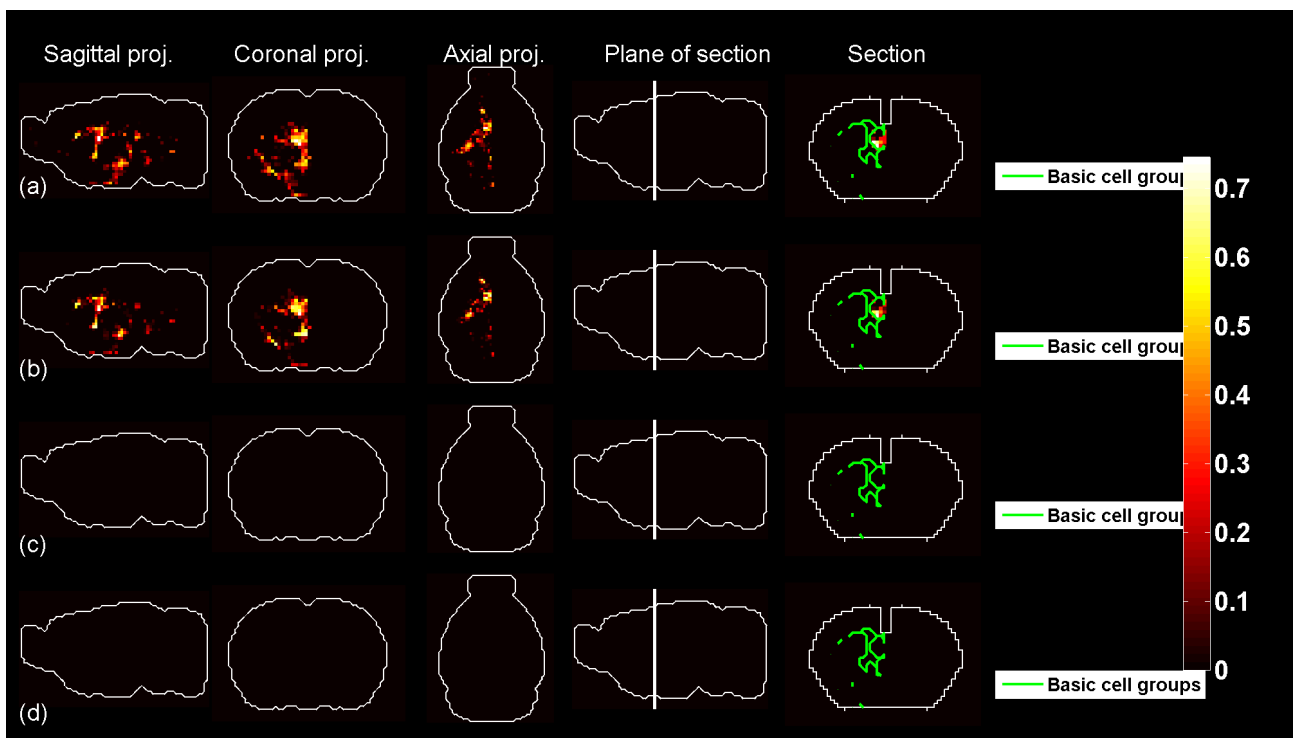


Figure 179: Predicted profile, probability profile and thresholded profiles for  $t = 36$ .

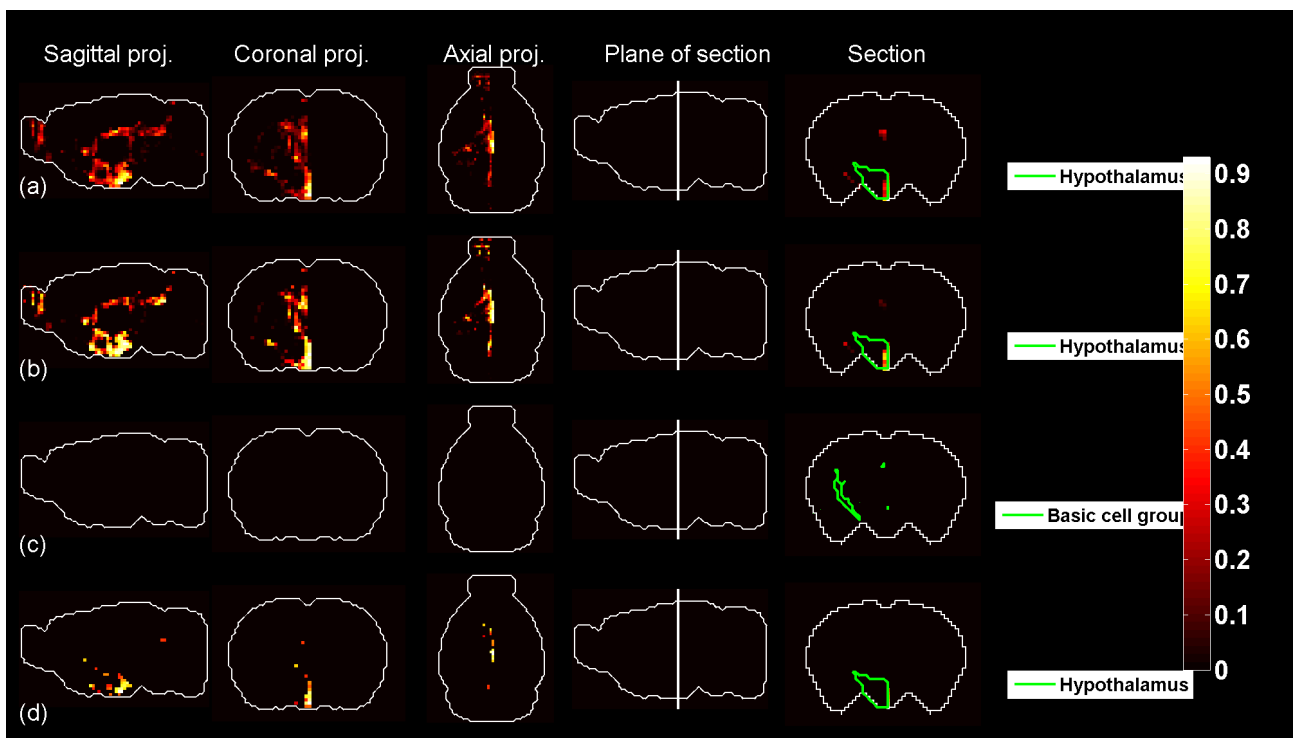


Figure 180: Predicted profile, probability profile and thresholded profiles for  $t = 37$ .

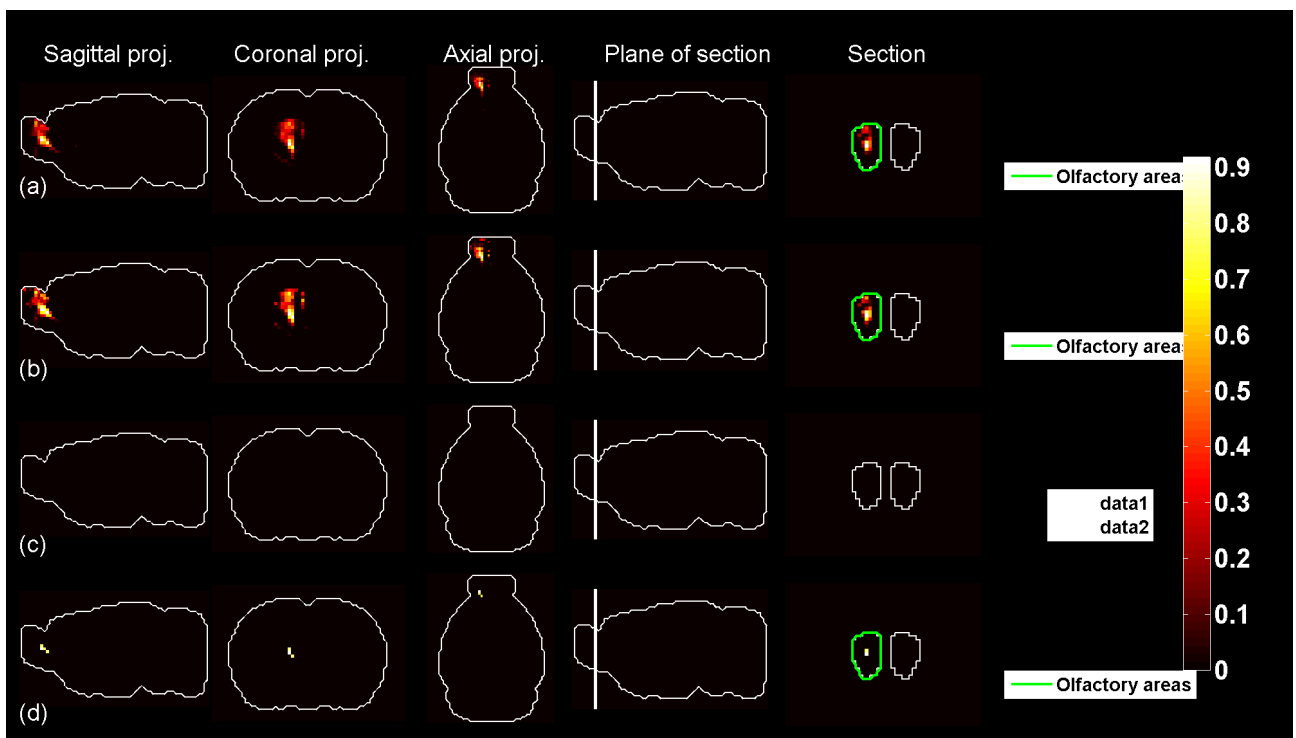


Figure 181: Predicted profile, probability profile and thresholded profiles for  $t = 38$ .

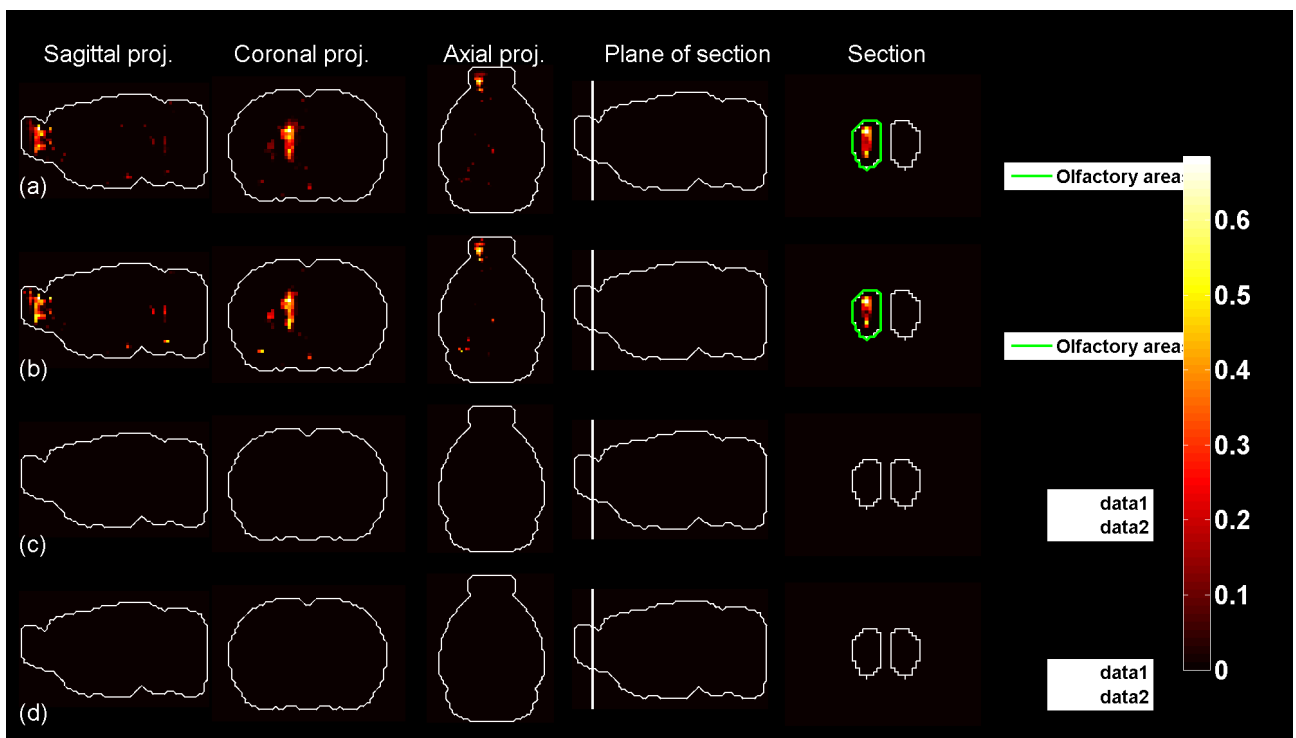


Figure 182: Predicted profile, probability profile and thresholded profiles for  $t = 39$ .

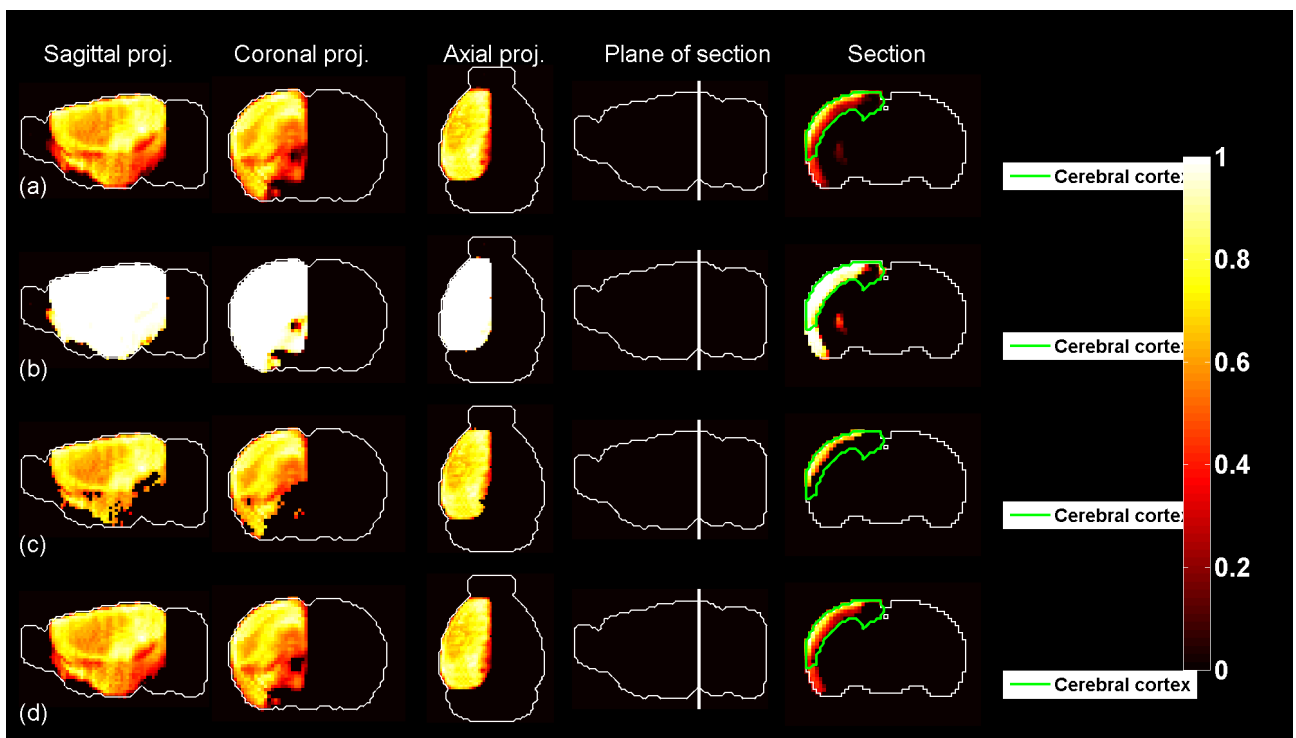


Figure 183: Predicted profile, probability profile and thresholded profiles for  $t = 40$ .

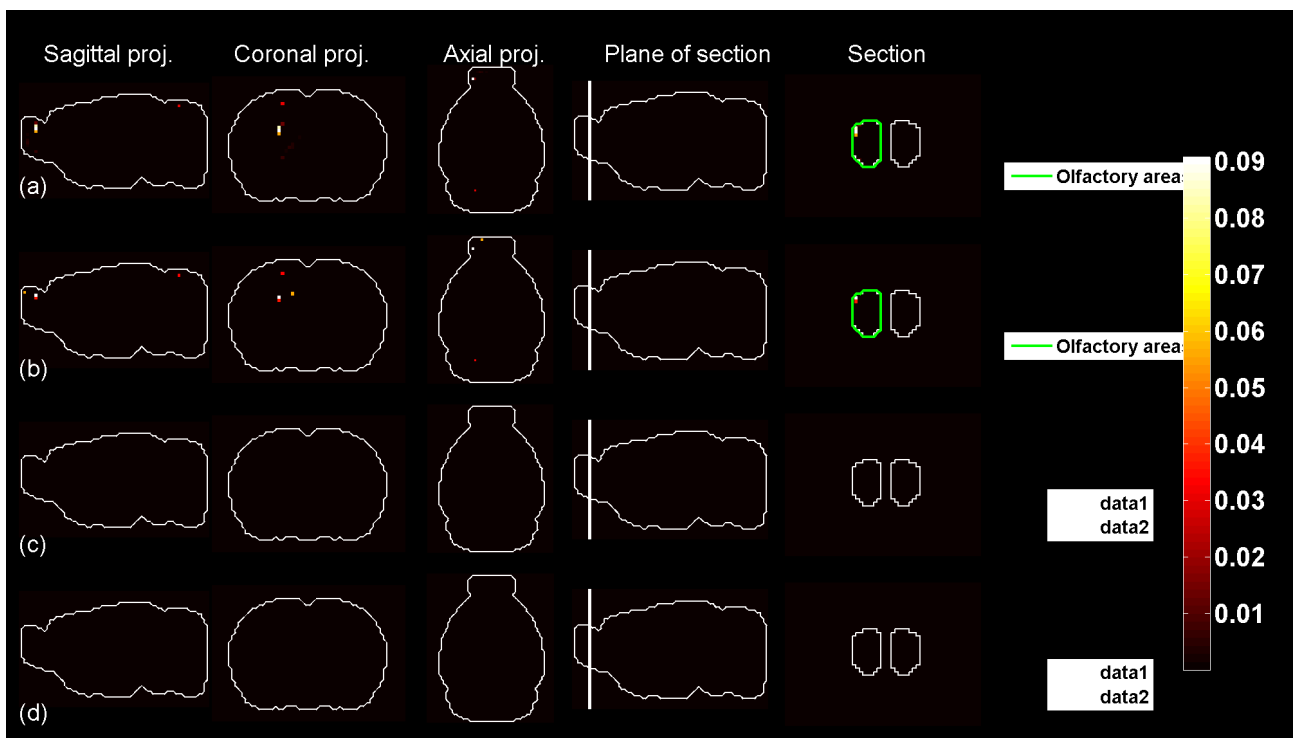


Figure 184: Predicted profile, probability profile and thresholded profiles for  $t = 41$ .

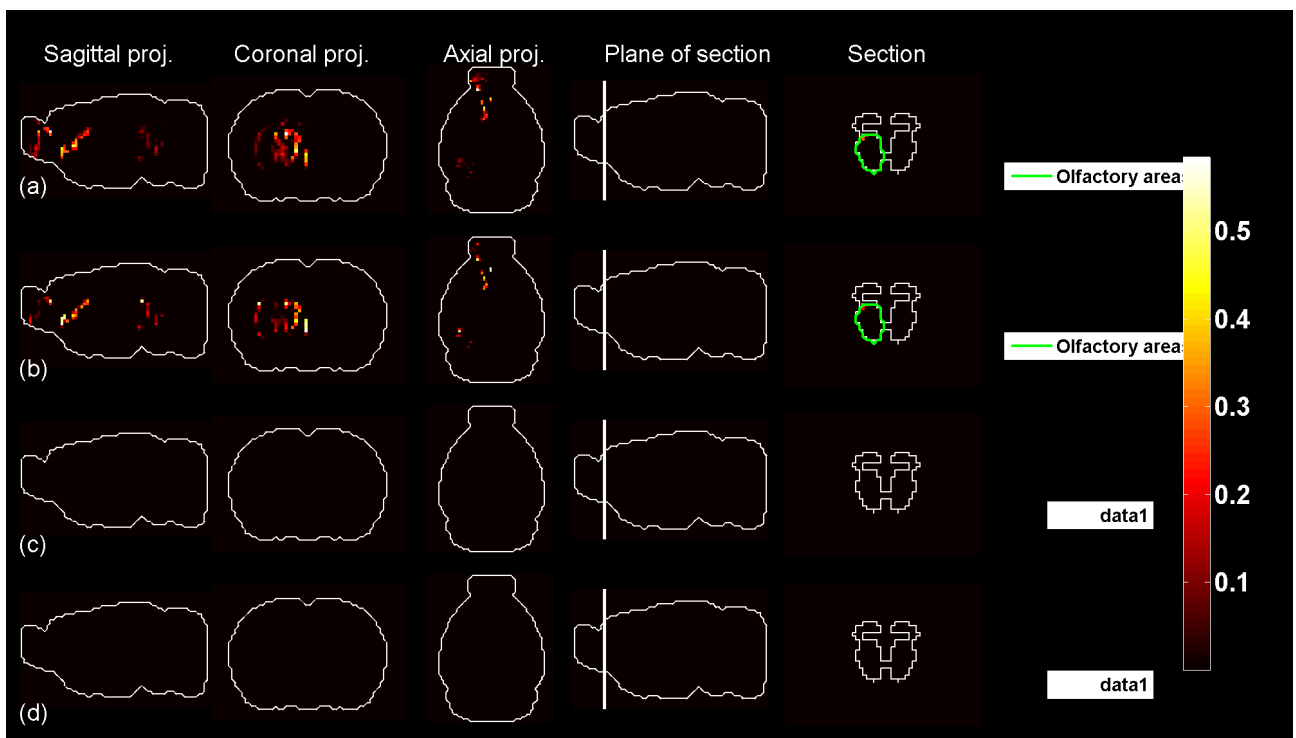


Figure 185: Predicted profile, probability profile and thresholded profiles for  $t = 42$ .

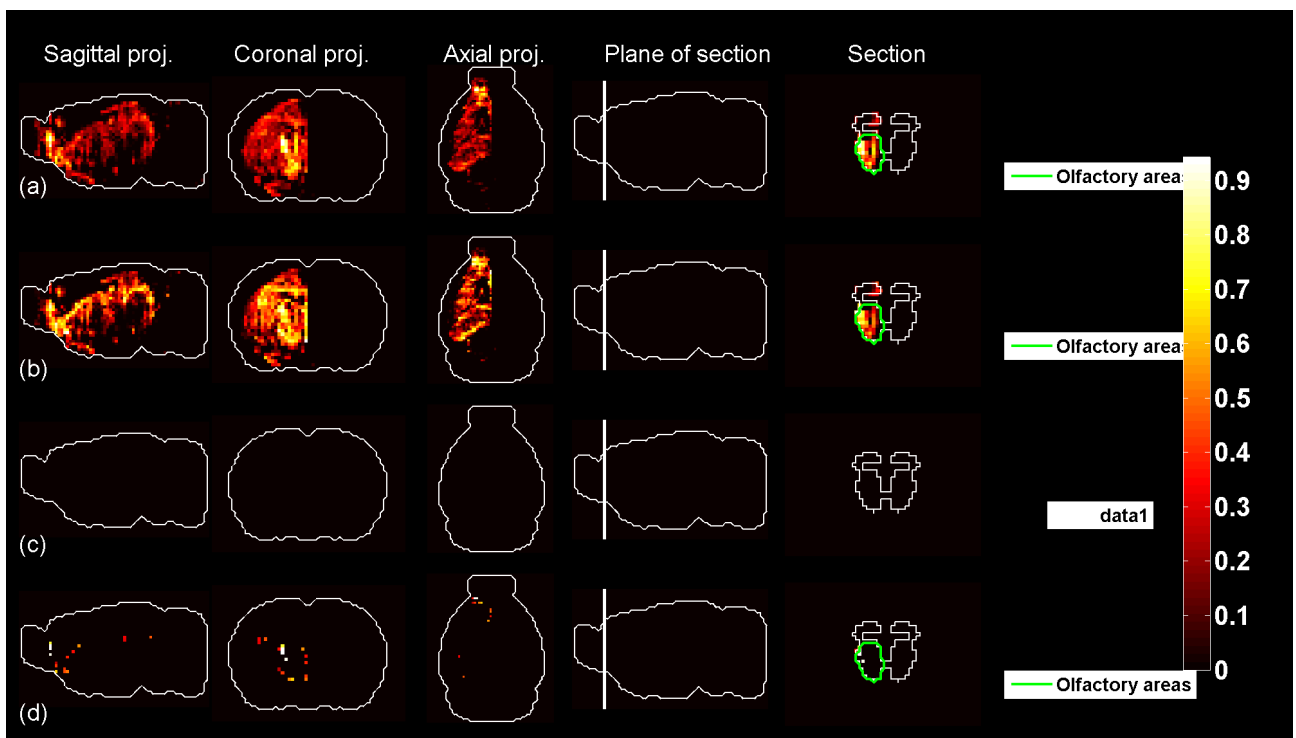


Figure 186: Predicted profile, probability profile and thresholded profiles for  $t = 43$ .

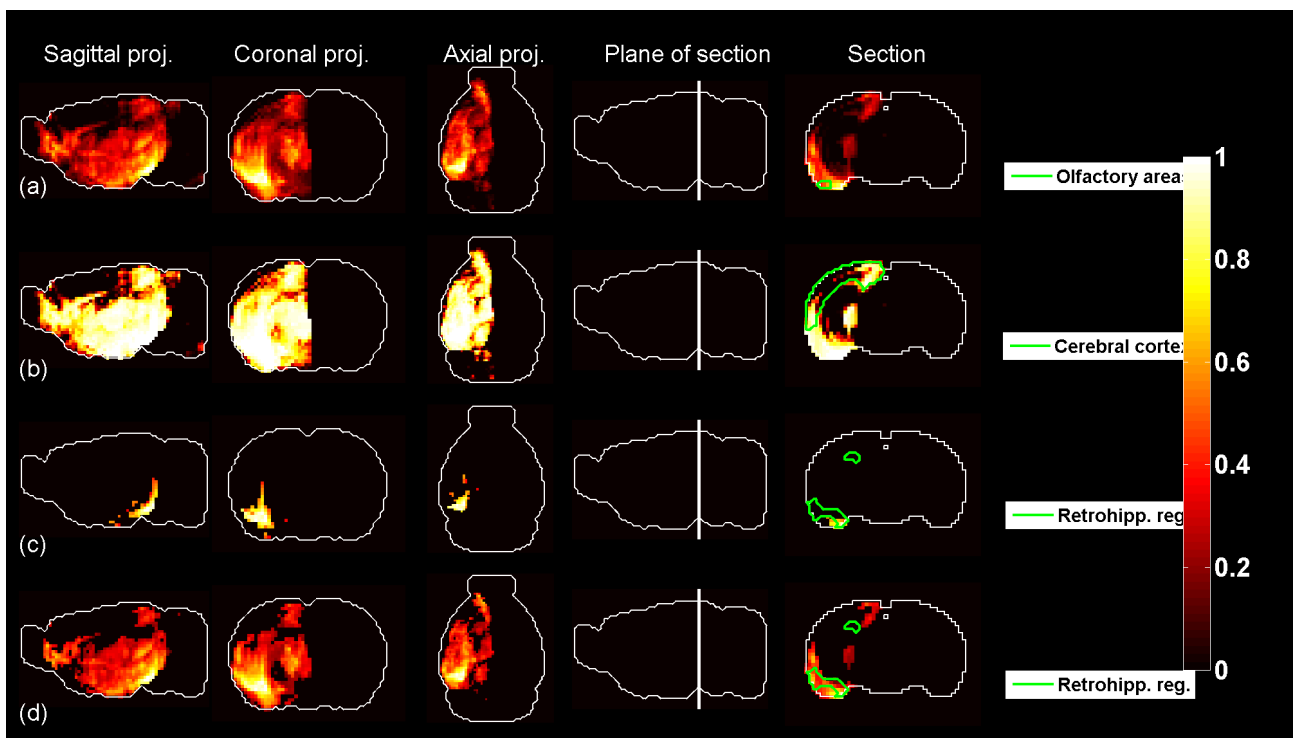


Figure 187: Predicted profile, probability profile and thresholded profiles for  $t = 44$ .

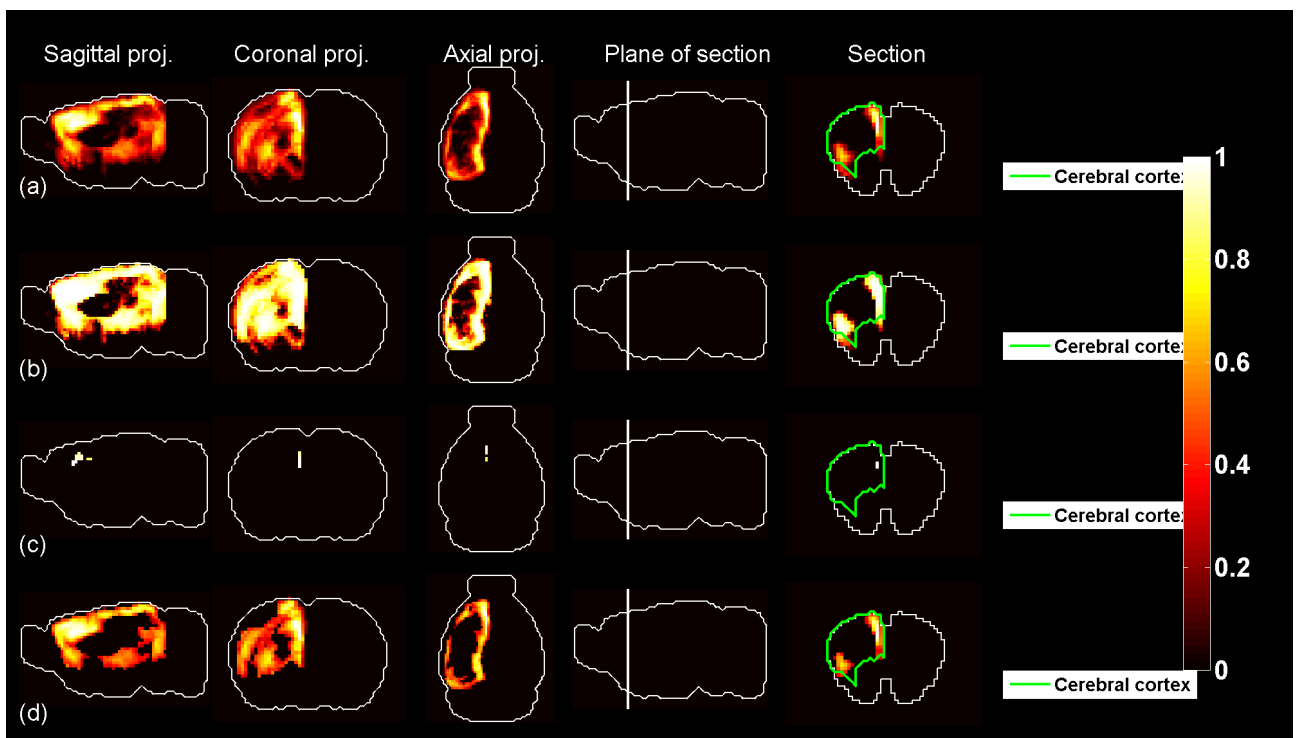


Figure 188: Predicted profile, probability profile and thresholded profiles for  $t = 45$ .

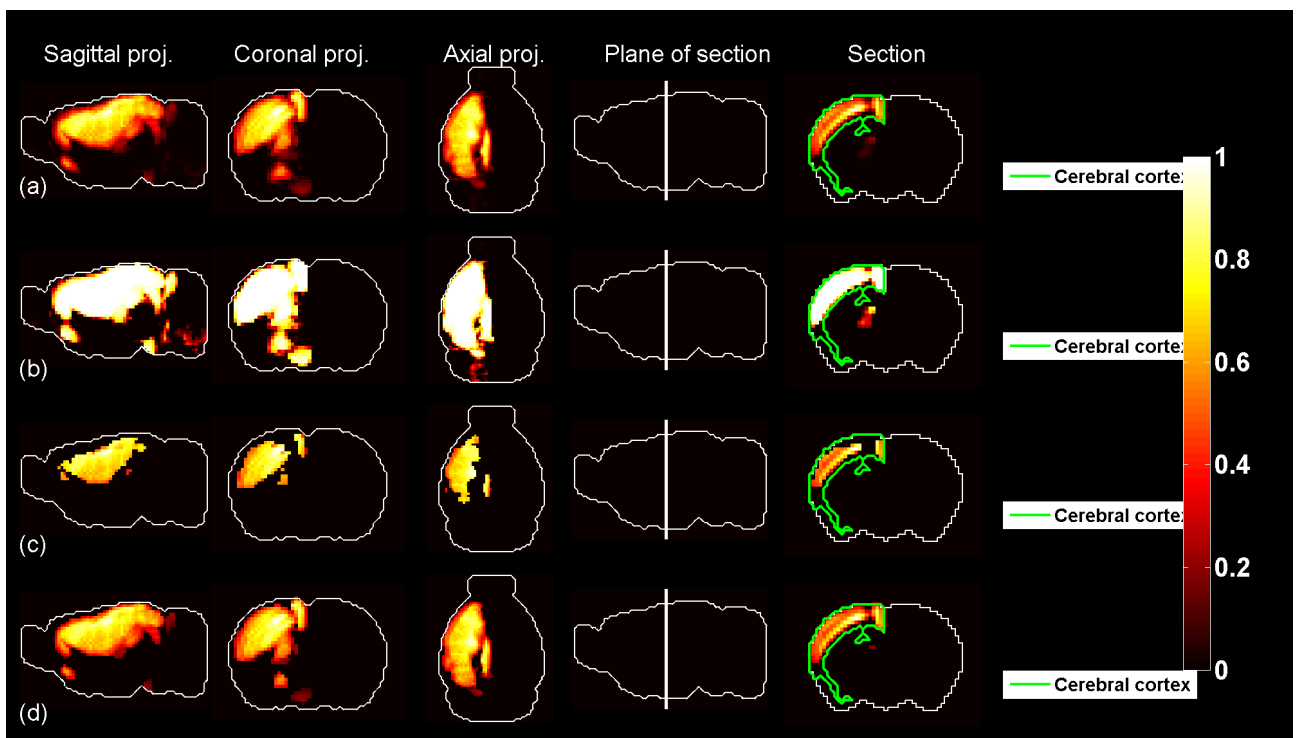


Figure 189: Predicted profile, probability profile and thresholded profiles for  $t = 46$ .

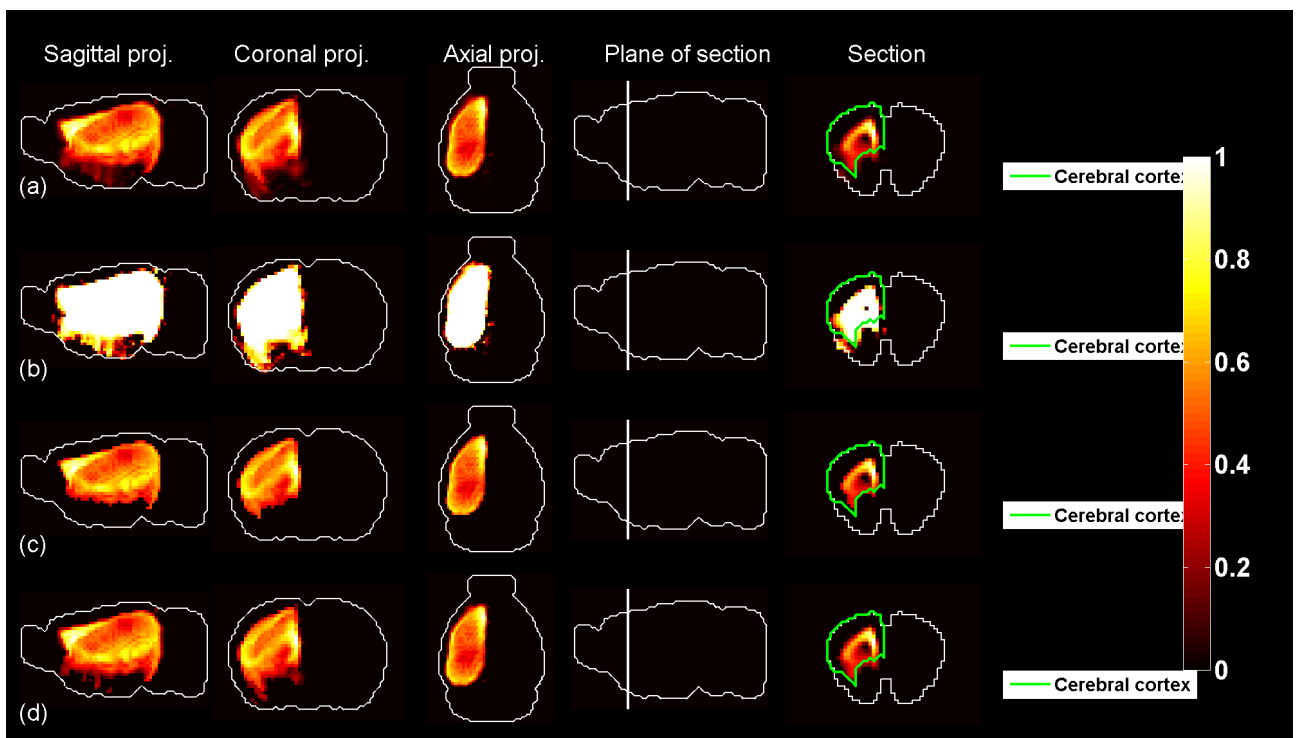


Figure 190: Predicted profile, probability profile and thresholded profiles for  $t = 47$ .

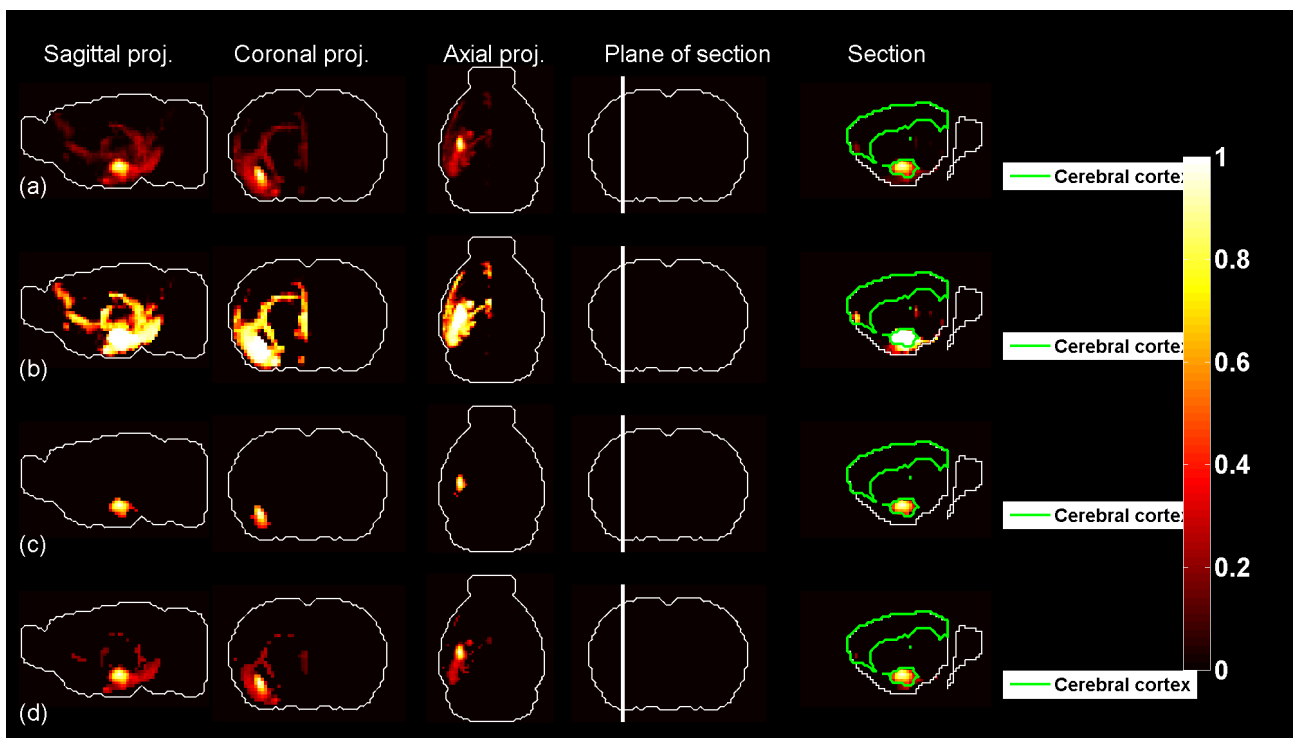


Figure 191: Predicted profile, probability profile and thresholded profiles for  $t = 48$ .

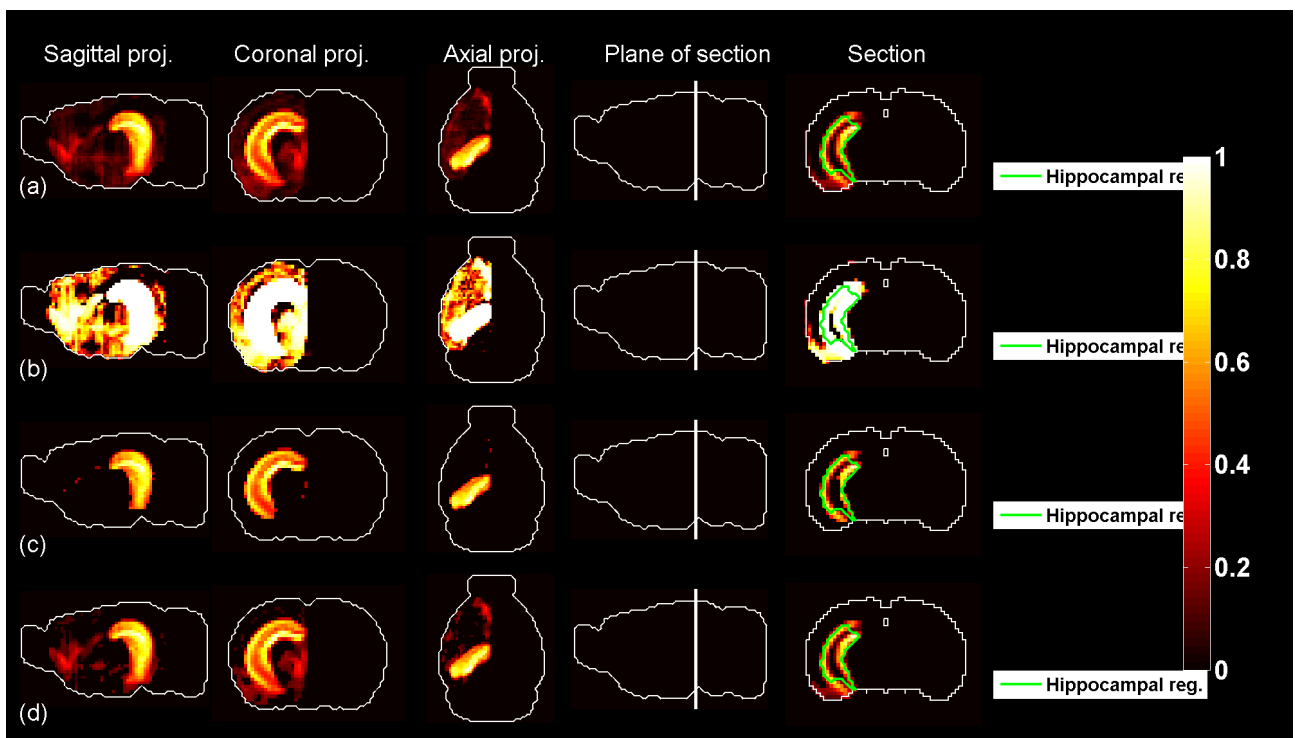


Figure 192: Predicted profile, probability profile and thresholded profiles for  $t = 49$ .

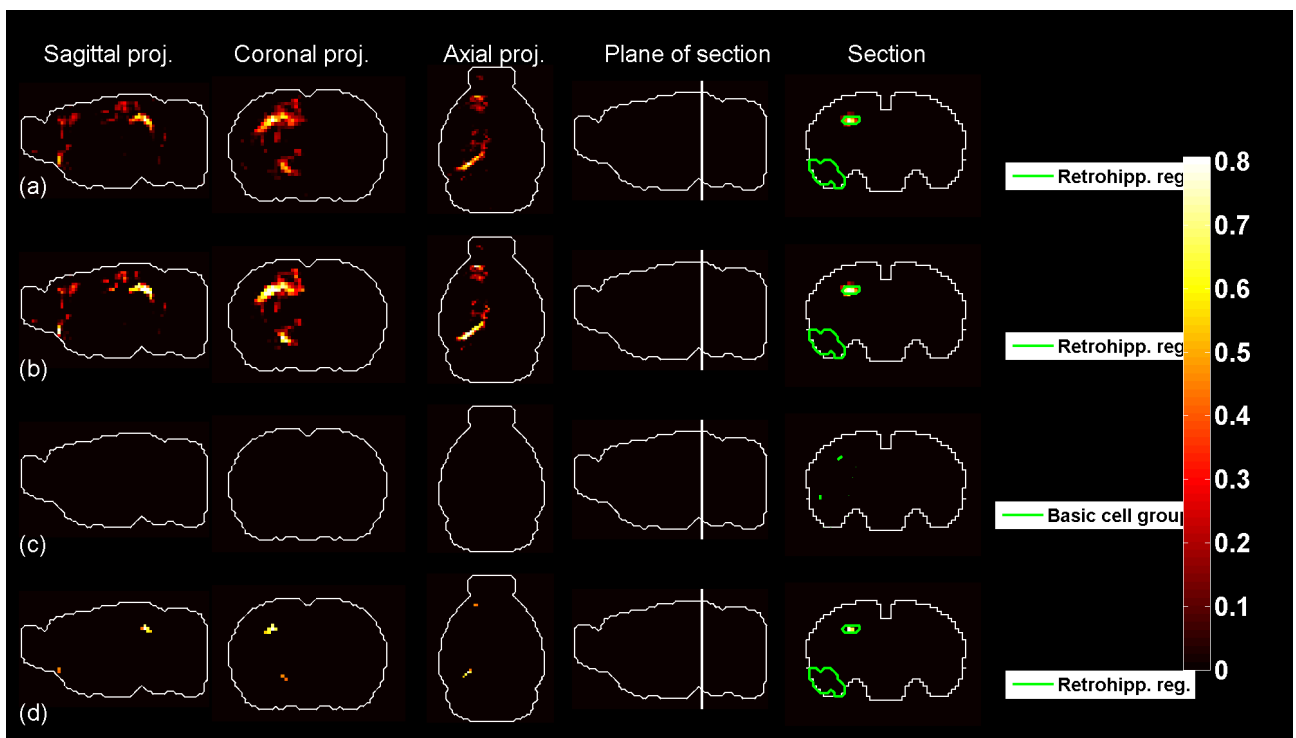


Figure 193: Predicted profile, probability profile and thresholded profiles for  $t = 50$ .

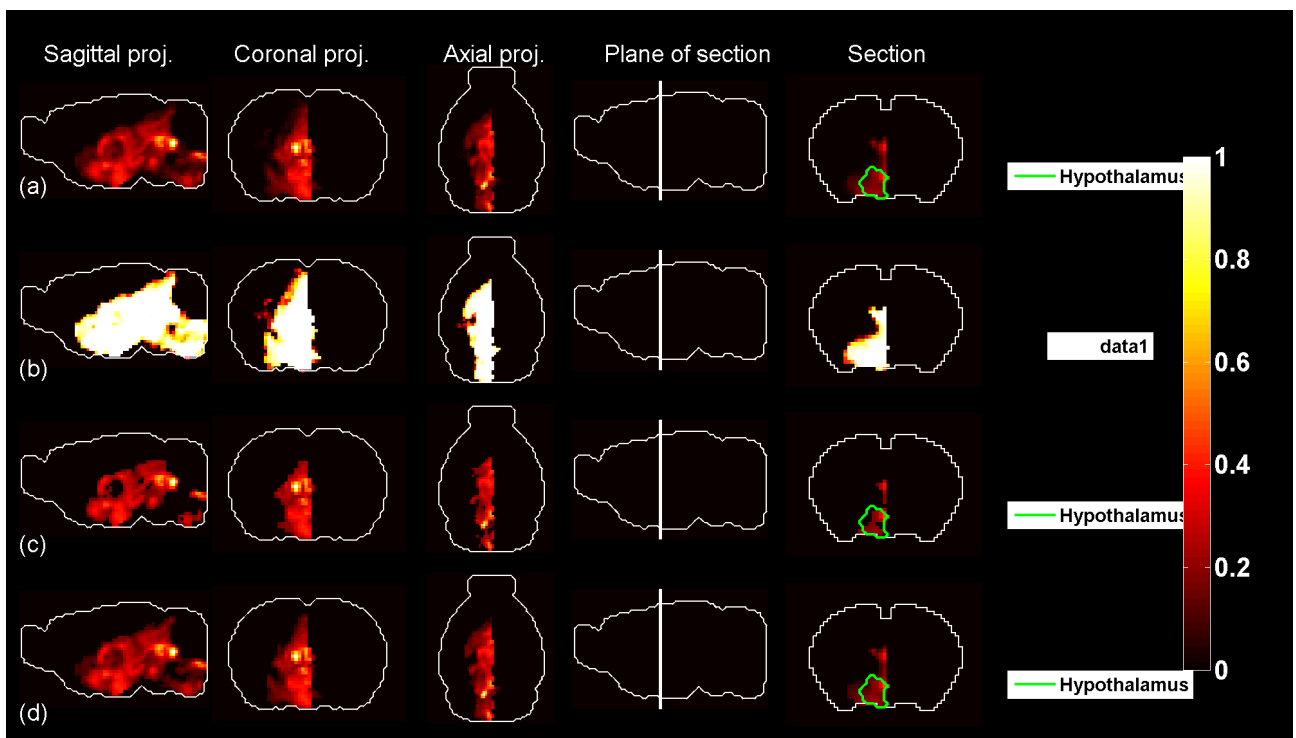


Figure 194: Predicted profile, probability profile and thresholded profiles for  $t = 51$ .

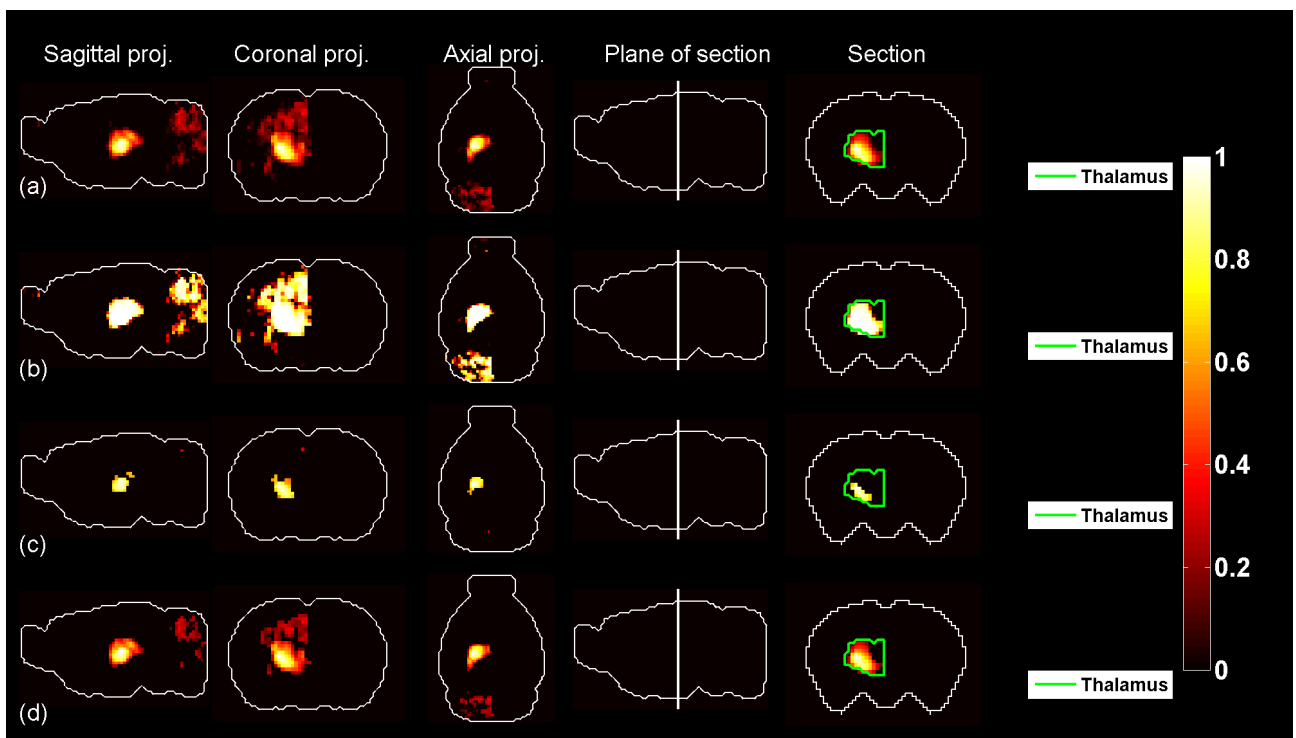


Figure 195: Predicted profile, probability profile and thresholded profiles for  $t = 52$ .

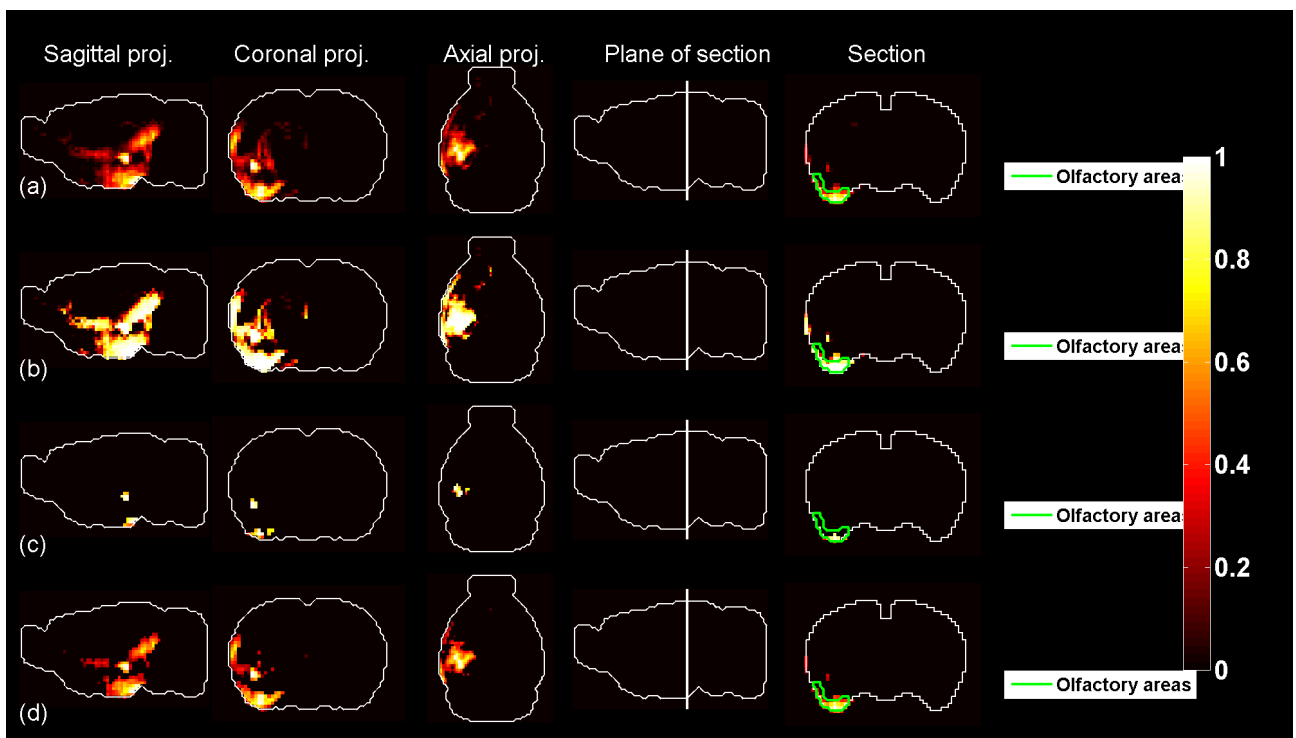


Figure 196: Predicted profile, probability profile and thresholded profiles for  $t = 53$ .

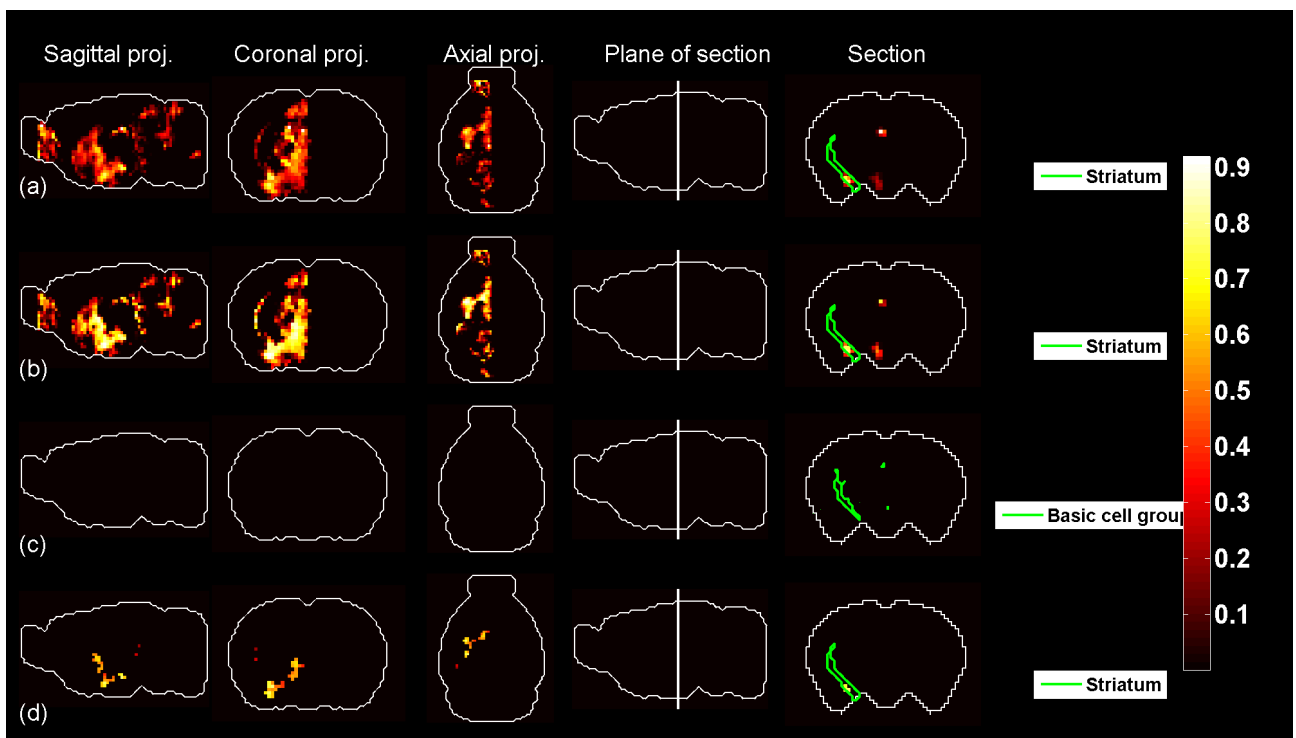


Figure 197: Predicted profile, probability profile and thresholded profiles for  $t = 54$ .

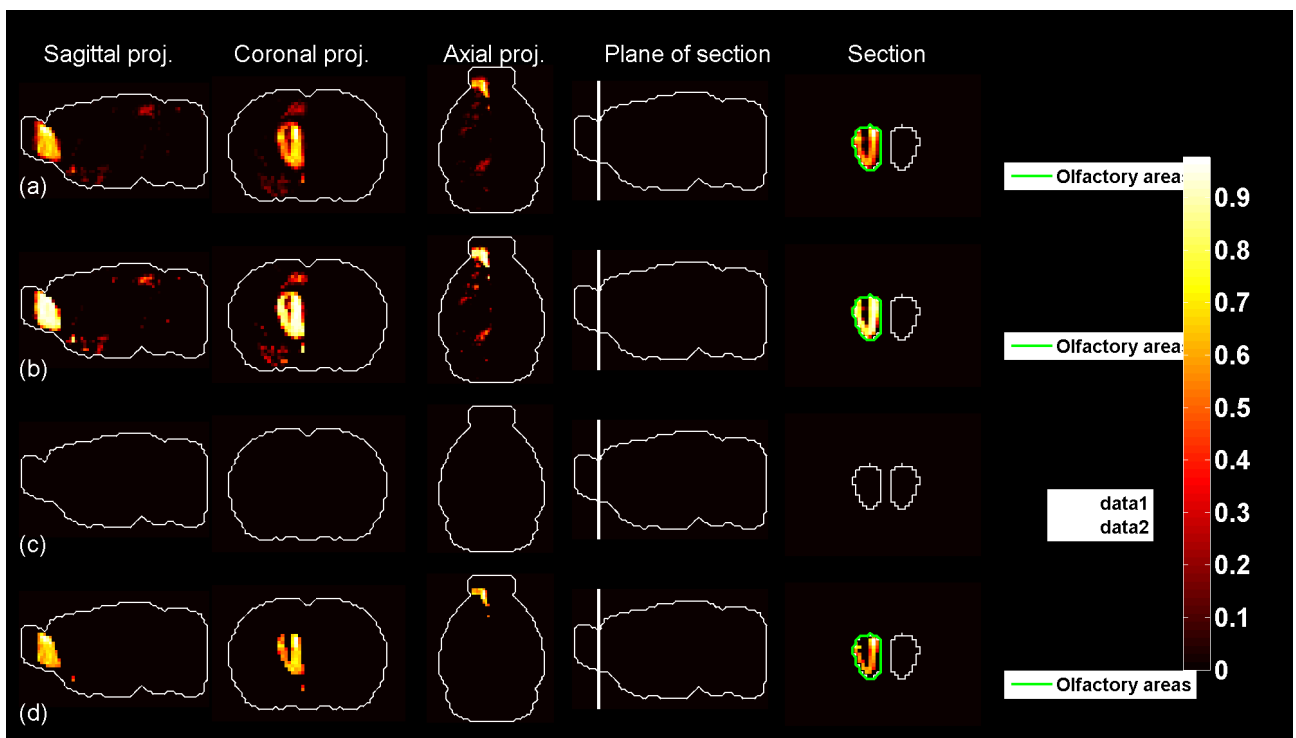


Figure 198: Predicted profile, probability profile and thresholded profiles for  $t = 55$ .

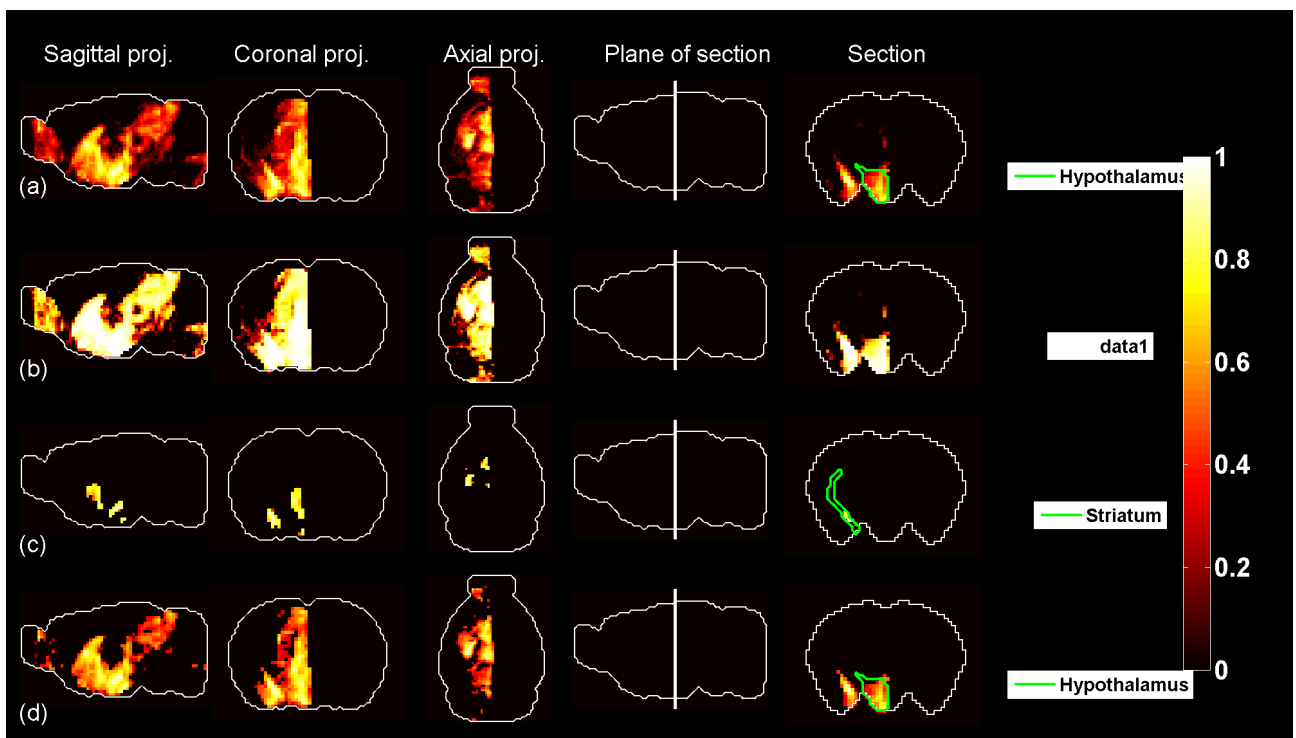


Figure 199: Predicted profile, probability profile and thresholded profiles for  $t = 56$ .

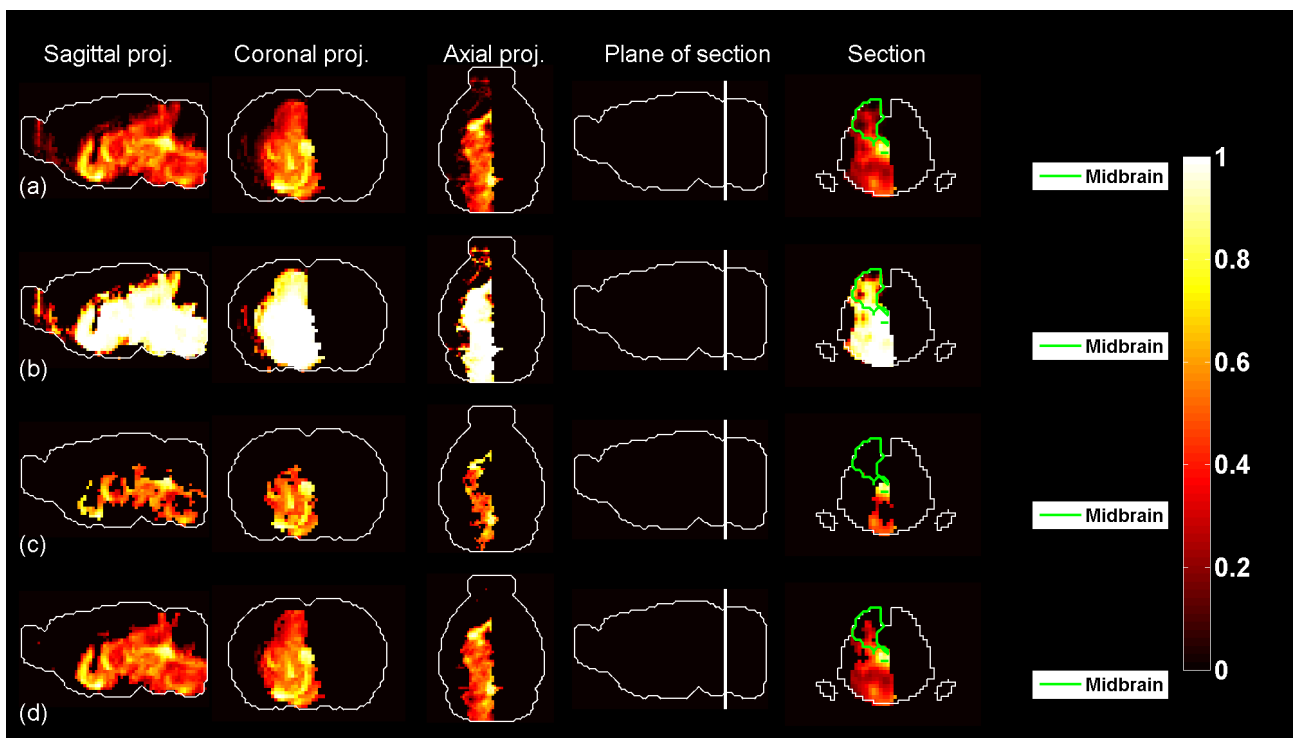


Figure 200: Predicted profile, probability profile and thresholded profiles for  $t = 57$ .

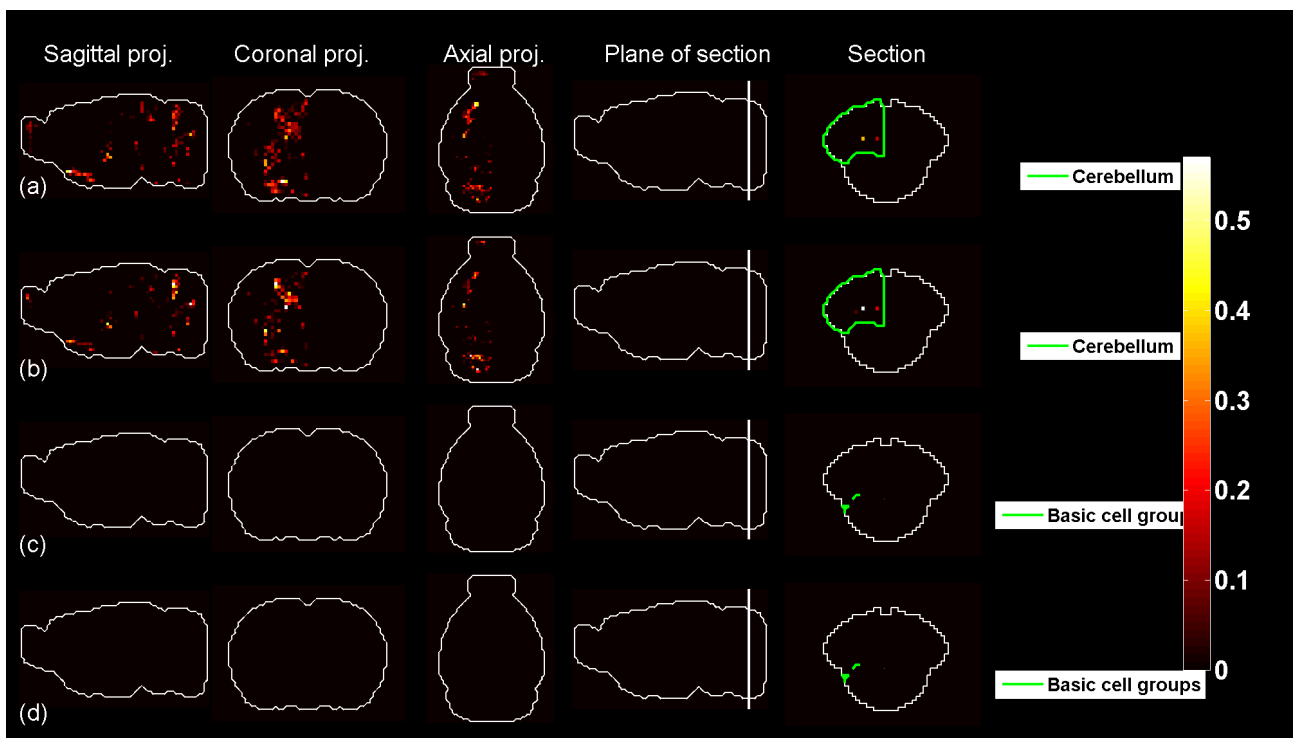


Figure 201: Predicted profile, probability profile and thresholded profiles for  $t = 58$ .

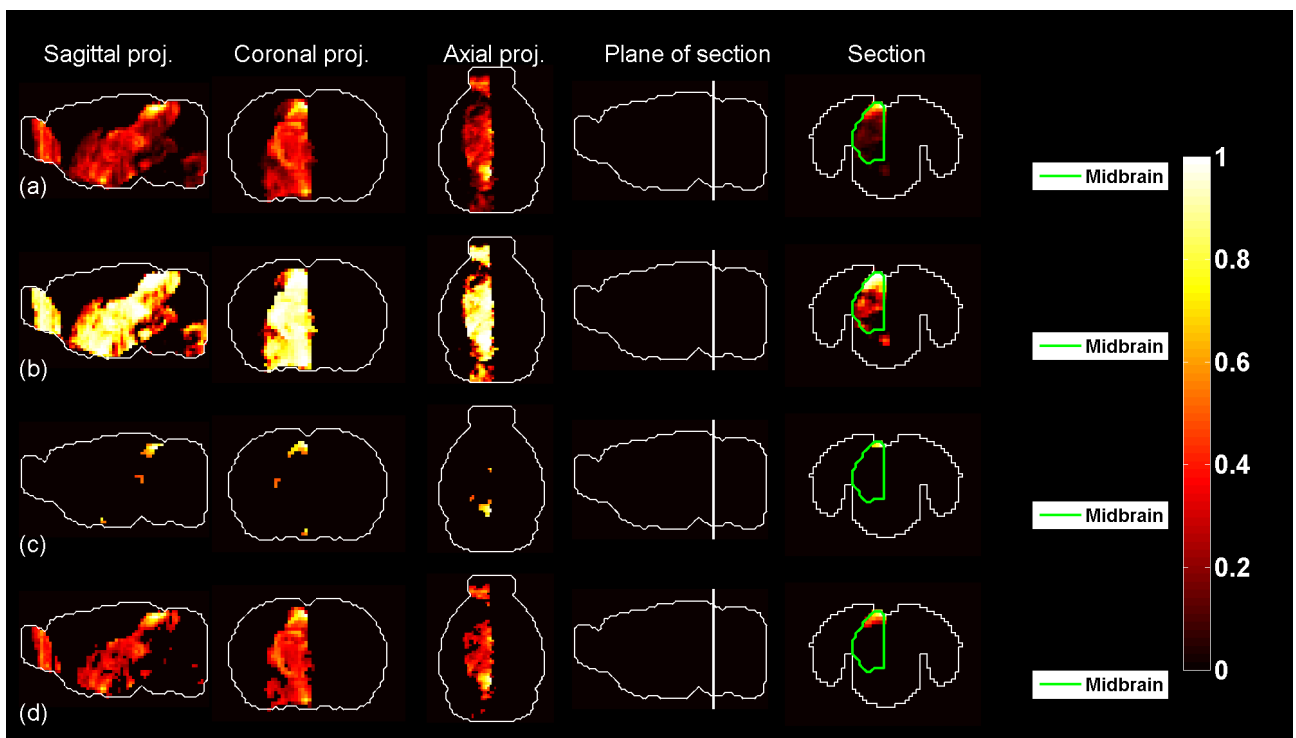


Figure 202: Predicted profile, probability profile and thresholded profiles for  $t = 59$ .

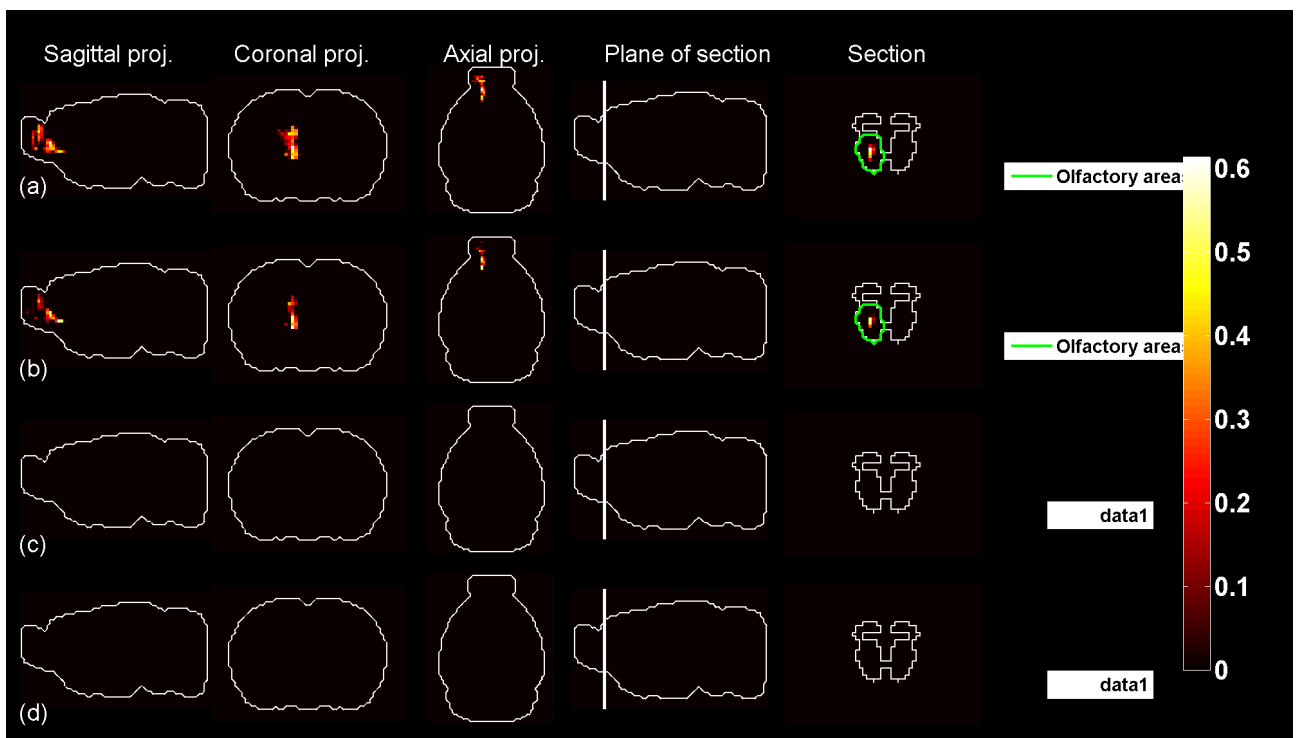


Figure 203: Predicted profile, probability profile and thresholded profiles for  $t = 60$ .

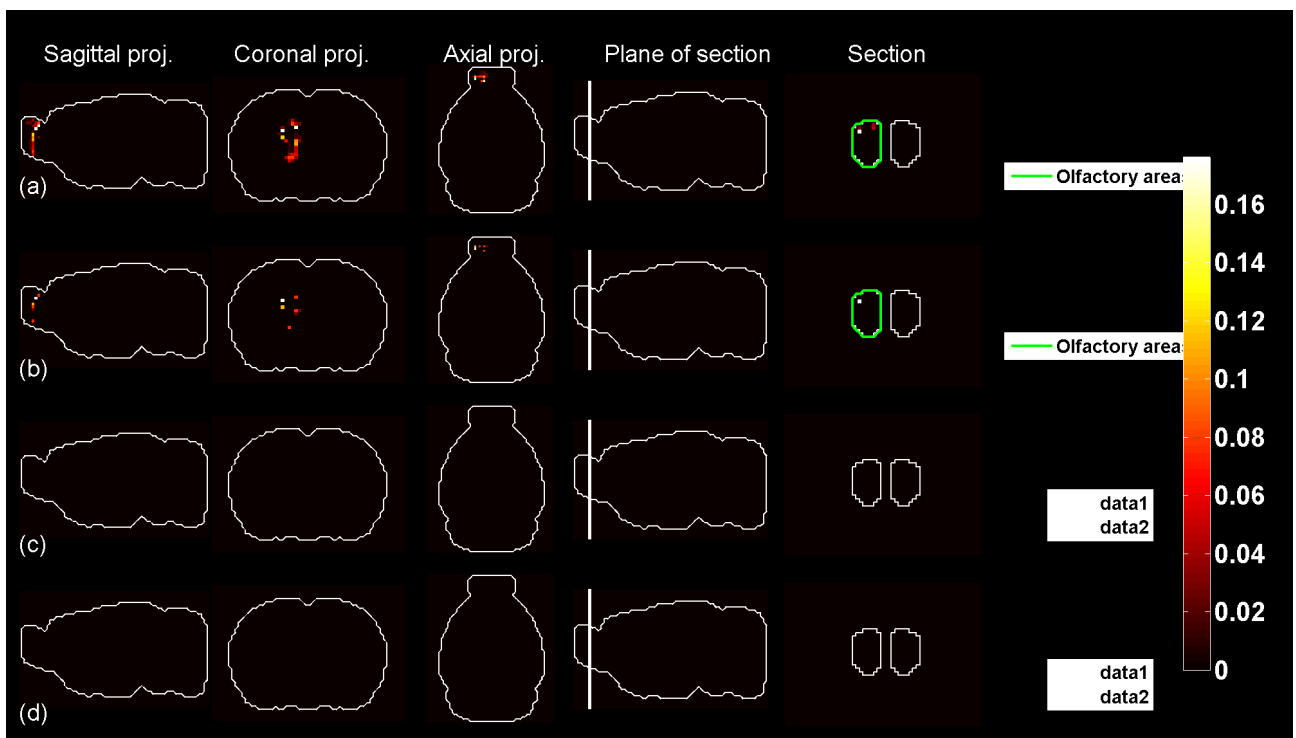


Figure 204: Predicted profile, probability profile and thresholded profiles for  $t = 61$ .

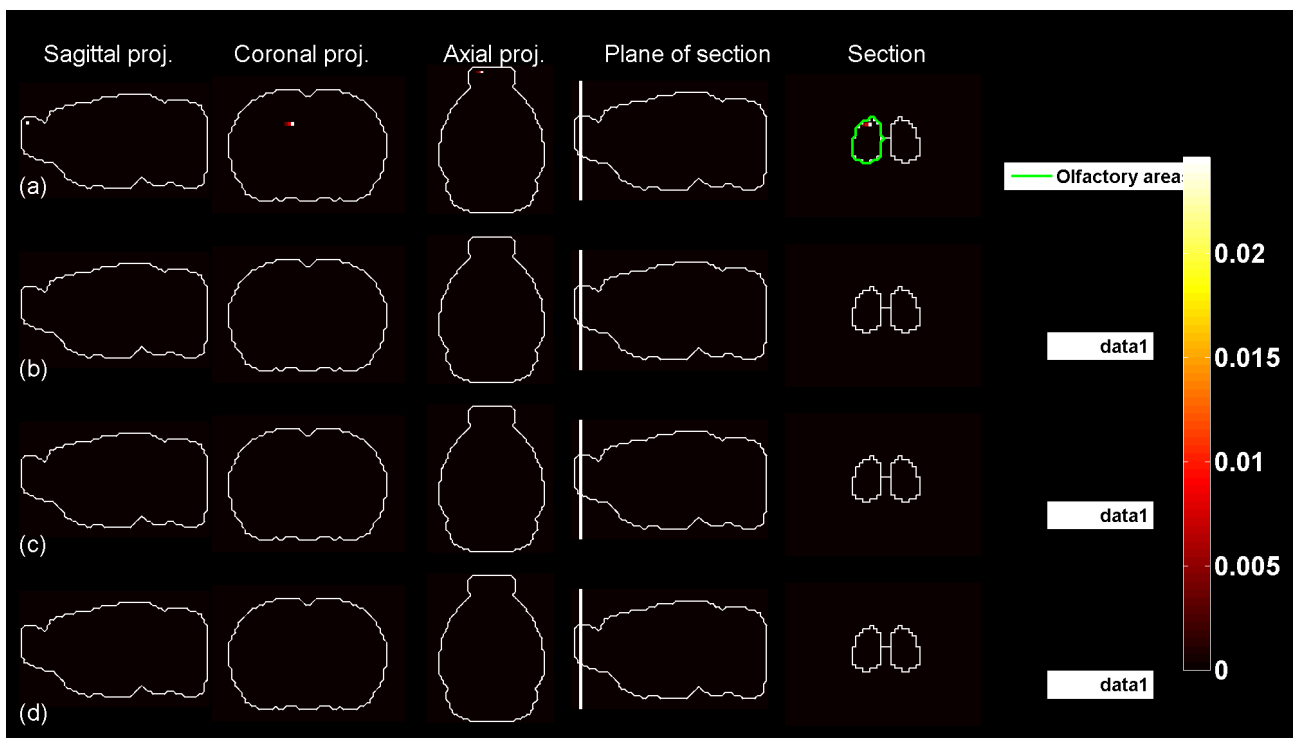


Figure 205: Predicted profile, probability profile and thresholded profiles for  $t = 62$ .

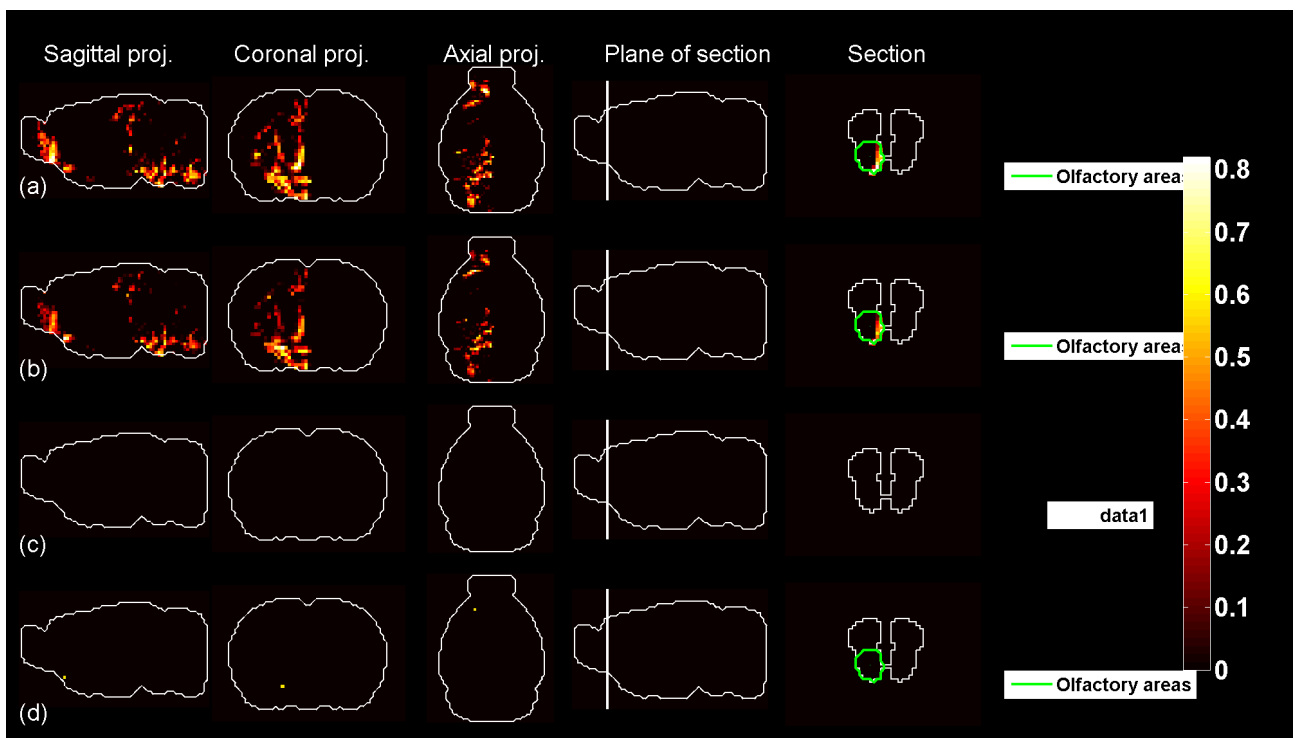


Figure 206: Predicted profile, probability profile and thresholded profiles for  $t = 63$ .

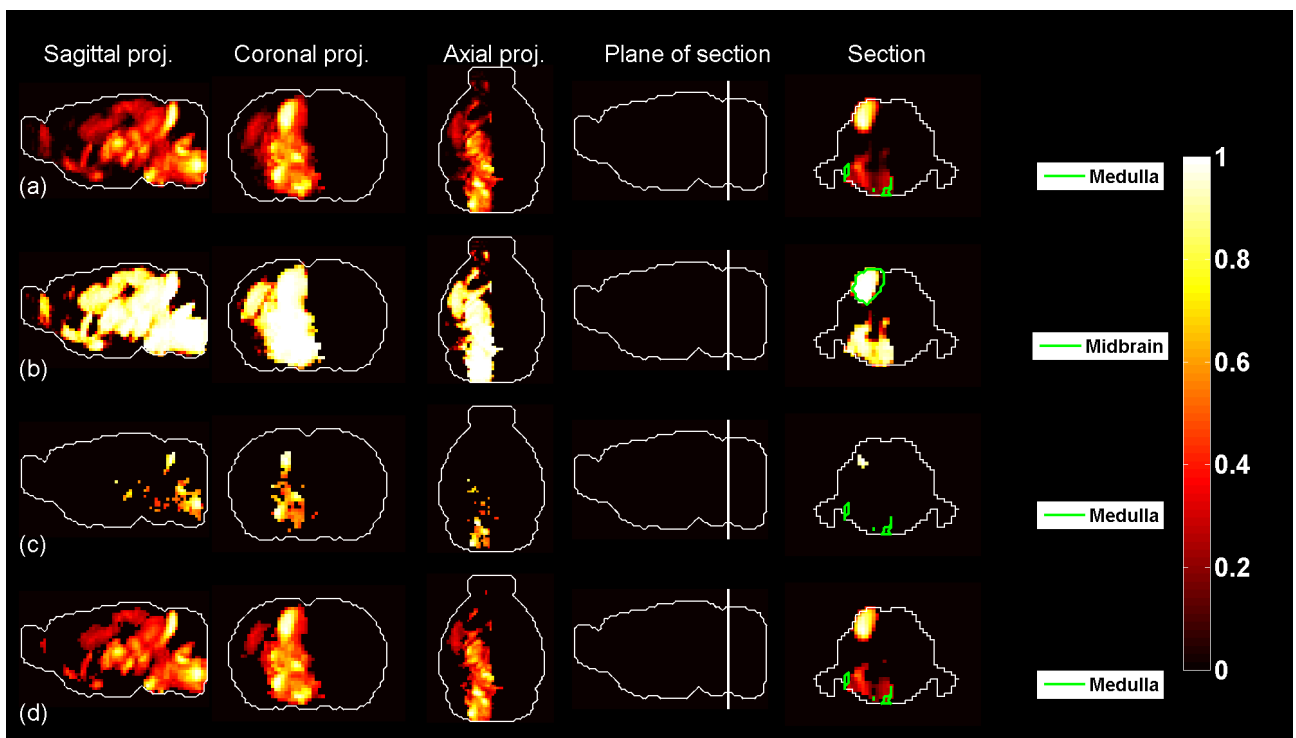


Figure 207: Predicted profile, probability profile and thresholded profiles for  $t = 64$ .

## Acknowledgments

We thank Nicolai Meinshausen and Gregor Havkin for correspondence.

## References

- [1] P. Grange, M. Hawrylycz, P.P. Mitra, *Cell-type-specific microarray data and the Allen atlas: quantitative analysis of brain-wide patterns of correlation and density*, [arXiv:1303.0013].
- [2] M. Bota, H.-W. Dong, L.W. Swanson, *From gene networks to brain networks*, Nature neuroscience (2003) **6** (8), 795–9.
- [3] E.S. Lein, M. Hawrylycz, N. Ao, M. Ayres, A. Bensinger, A. Bernard, A.F. Boe, M.S. Boguski, K.S. Brockway, E.J. Byrnes, L. Chen, L. Chen, T.M. Chen, M.C. Chin, J. Chong, B.E. Crook, A. Czaplinska, C.N. Dang, S. Datta, N.R. Dee, *et al.*, *Genome-wide atlas of gene expression in the adult mouse brain*. Nature **445**, 168–176 (2007).
- [4] L. Ng, M. Hawrylycz, D. Haynor, *Automated high-throughput registration for localizing 3D mouse brain gene expression using ITK*, Insight-Journal (2005).
- [5] S.M. Sunkin and J.G. Hohmann, *Insights from spatially mapped gene expression in the mouse brain*, Human Molecular Genetics, 2007, Vol. 16, Review Issue 2.
- [6] L. Ng, S.D. Pathak, C. Kuan, C. Lau, H. Dong, A. Sodt, C. Dang, B. Avants, P. Yushkevich, J.C. Gee, D. Haynor, E. Lein, A. Jones and M. Hawrylycz, *Neuroinformatics for genome-wide 3D gene expression mapping in the mouse brain*, IEEE/ACM Trans. Comput. Biol. Bioinform. (2007), Jul-Sep **4**(3) 382–93.
- [7] M. Hawrylycz, R.A. Baldock, A. Burger, T. Hashikawa, G.A. Johnson, M. Martone, L. Ng, C. Lau, S.D. Larsen, J. Nissanov, L. Puellas, S. Ruffins, F. Verbeek, I. Zaslavsky1, J. Boline, *Digital Atlasing and Standardization in the Mouse Brain*, PLoS Computational Biology **7** (2) (2011).
- [8] A.R. Jones, C.C. Overly and S.M. Sunkin, *The Allen Brain Atlas: 5 years and beyond*, Nature Reviews (Neuroscience), Volume **10** (November 2009), **1**.
- [9] M. Hawrylycz, L. Ng, D. Page, J. Morris, C. Lau, S. Faber, V. Faber, S. Sunkin, V. Menon, E.S. Lein, A. Jones, *Multi-scale correlation structure of gene expression in the brain*, Neural Networks **24** (2011) 933–942.
- [10] H.-W. Dong, *The Allen reference atlas: a digital brain atlas of the C57BL/6J male mouse*, Wiley, 2007.
- [11] L. Ng, A. Bernard, C. Lau, C.C. Overly, H.-W. Dong, C. Kuan, S. Pathak, S.M. Sunkin, C. Dang, J.W. Bohland, H. Bokil, P.P. Mitra, L. Puellas, J. Hohmann, D.J. Anderson, E.S. Lein, A.R. Jones, M. Hawrylycz, *An anatomic gene expression atlas of the adult mouse brain*, Nature Neuroscience **12**, 356–362 (2009).

- [12] L. Ng *et al.*, *NeuroBlast: a 3D spatial homology search tool for gene expression*, BMC Neuroscience 2007, **8**(Suppl 2):P11.
- [13] P. Grange, J.W. Bohland, M. Hawrylycz and P.P. Mitra, *Brain Gene Expression Analysis: a MATLAB toolbox for the analysis of brain-wide gene-expression data*, [arXiv:1211.6177 [q-bio.QM]].
- [14] The Brain Gene Expression Atlas MATLAB toolbox is downloadable from <http://brainarchitecture.org/allen-atlas-brain-toolbox>.
- [15] P. Grange, M. Hawrylycz, P.P. Mitra, *Computational neuroanatomy and co-expression of genes in the adult mouse brain, analysis tools for the Allen Brain Atlas*, Quantitative Biology (2013), in press, [arXiv:1301.1730 [q-bio.QM]].
- [16] P. Grange, P.P. Mitra, *Computational neuroanatomy and gene expression: optimal sets of marker genes for brain regions*, IEEE, in CISS 2012, 46th annual conference on Information Science and Systems (Princeton).
- [17] B.W. Okaty, M.N. Miller, K. Sugino, C.M. Hempel, S.B. Nelson, *Transcriptional and electrophysiological maturation of neocortical fast-spiking GABAergic interneurons*, J. Neurosci. (2009) **29**(21) 7040-52.
- [18] M.J. Rossner, J. Hirrlinger, S.P. Wichert, C. Boehm, D. Newrzella, H. Hiemisch, G. Eisenhardt, C. Stuenkel, O. von Ahsen, K.A. Nave, *Global transcriptome analysis of genetically identified neurons in the adult cortex*, J. Neurosci. 2006 **26**(39) 9956-66.
- [19] J.D. Cahoy, B. Emery, A. Kaushal, L.C. Foo, J.L. Zamanian, K.S. Christopherson, Y. Xing, J.L. Lubischer, P.A. Krieg, S.A. Krupenko, W.J. Thompson, B.A. Barres, *A transcriptome database for astrocytes, neurons, and oligodendrocytes: a new resource for understanding brain development and function*, J. Neurosci. 2008 **28**(1) 264-78.
- [20] J.P. Doyle, J.D. Dougherty, M. Heiman, E.F. Schmidt, T.R. Stevens, G. Ma, S. Bupp, P. Shrestha, R.D. Shah, M.L. Doughty, S. Gong, P. Greengard, N. Heintz, *Application of a translational profiling approach for the comparative analysis of CNS cell types*, Cell (2008) **135**(4) 749-62.
- [21] C.Y. Chung, H. Seo, K.C. Sonntag, A. Brooks, L. Lin, O. Isacson *Cell type-specific gene expression of midbrain dopaminergic neurons reveals molecules involved in their vulnerability and protection*. Hum. Mol. Genet. (2005) **14**: 1709–1725.
- [22] P. Arlotta, B.J. Molyneaux, J. Chen, J. Inoue, R. Kominami *et al.* (2005) *Neuronal subtype-specific genes that control corticospinal motor neuron development in vivo*, Neuron **45**: 207–221.
- [23] M. Heiman, A. Schaefer, S. Gong, Peterson JD, Day M, Ramsey KE, Surez-Farias M, Schwarz C, Stephan DA, Surmeier DJ, P. Greengard, N. Heintz, (2008) *A translational profiling approach for the molecular characterization of of CNS cell types*, Cell **135**: 738–748.

- [24] K. Sugino, C.M. Hempel, M.N. Miller, A.M. Hattox, P. Shapiro, C. Wu, Z.J. Huang, S.B. Nelson, *Molecular taxonomy of major neuronal classes in the adult mouse forebrain*, Nature Neuroscience **9**, 99-107 (2005).
- [25] B.W. Okaty, K. Sugino, S.B. Nelson, *A Quantitative Comparison of Cell-Type-Specific Microarray Gene Expression Profiling Methods in the Mouse Brain*, PLoS One (2011) **6(1)**.
- [26] C.K. Lee, S.M. Sunkin, C.C. Kuan, C.L. Thompson, S. Pathak, L. Ng, C. Lau, S. Fischer, M. Mortrud, C. Slaughterbeck, A. Jones, E. Lein, M. Hawrylycz, *Quantitative methods for genome-scale analysis of in situ hybridization and correlation with microarray data*, Genome Biol. (2008); **9(1)**: R23.
- [27] Research, Inc. CVX: *Matlab software for disciplined convex programming*, version 2.0 beta. <http://cvxr.com/cvx>, September 2012.
- [28] M. Grant and S. Boyd, *Graph implementations for nonsmooth convex programs*, *Recent Advances in Learning and Control (a tribute to M. Vidyasagar)*, V. Blondel, S. Boyd, and H. Kimura, editors, pages 95-110, Lecture Notes in Control and Information Sciences, Springer, 2008. [http://stanford.edu/~boyd/graph\\_dcp.html](http://stanford.edu/~boyd/graph_dcp.html).
- [29] J.W. Bohland, H. Bokil, C.B. Allen, P.P. Mitra, *The Brain Atlas Concordance Problem: Quantitative Comparison of Anatomical Parcellations*, PLoS ONE (2009).
- [30] J.W. Bohland, H. Bokil, C.-K. Lee, L. Ng, C. Lau, C. Kuan, M. Hawrylycz, P.P. Mitra, *Clustering of spatial gene expression patterns in the mouse brain and comparison with classical neuroanatomy*, Methods, Volume **50**, Issue 2, February 2010, Pages 105-112.
- [31] I. Menashe, P. Grange, E.C. Larsen, S. Banerjee-Basu and P.P. Mitra, *Co-expression profiling of autism genes in the mouse brain*, PLoS Comput. Biol. 9(7): e1003128.
- [32] N. Meinshausen (2013). Sign-constrained least squares estimation for high-dimensional regression. Electronic Journal of Statistics, 7, 1607–1631.